An Investigation of a Jet in a Crosswind

Paul Taylor

Submitted for the Degree of Ph. D. of

The University of Glasgow

May 1976

Acknowledgements

I should like to express my appreciation to Professor T. R. F. Nonweiler and the members of the Department of Aeronautics for their guidance and assistance throughout the course of this study. Special thanks must go to my supervisor Dr. A. W. Babister for his encouragement and help.

The moral and financial support of my wife Elizabeth and the financial assistance of the Science Research Council is acknowledged.

Table of Contents.

List of Tables.

List of Illustrations.

Notation

a	Jet Radius
a_J	Acoustic Velocity at the Jet Exit
A_J	Area of the Jet Exit in a Plane Normal to the Nozzle Centreline
D (Appendix A)	Axis across the Nozzle Exit Plane Normal to the Nozzle Centreline with Distances along the Axis Non-Dimensionalised with respect to the Jet Radius
h	Clearance between Lower Plate Surface and the Working Section Floor
h (Chapter V)	Distance of the Sink from the Origin along the Positive x axis
H	Distance of the Sink from the Origin along the Positive X axis, Non-Dimensionalised with respect to the Jet Radius, $H = h/a$
M	Mach Number
p	pressure
p_R	Static Pressure at the Wall of the Wind Tunnel Reservoir (Section 2.1 and 3.2)
p_W	Static Pressure at the Wall Upstream of the Working Section (Section 2.1 and 3.2)
q	Dynamic Pressure
q (Chapter V)	Complex Velocity, $q = u - iv$
Q	Complex Velocity, $Q = U - iV$
Q_1	Sink Strength
Q_2	Source Strength
r	Radial Distance from the Origin to any point in the xy plane

R	Radial Distance from the Origin to any point in the XY plane, Non-Dimensionalised with respect to the Jet Radius, R = r/a
RR	Upper Limit of Integration representing a Non-Dimensional Radial Distance from the Origin of the XY plane
R_1	Lower Limit of Integration representing a Non-Dimensional Radial Distance from the Origin of the XY plane. Usually represents the Jet Periphery
R_1 (Chapter V)	Radial Distance from the Source to any point in the Z plane, NOn-Dimensionalised with respect to the Jet Radius
R_2	Upper Limit of Integration, identical to RR
R_2 (Chapter V)	Radial Distance from the Sink to any point in the Z plane, Non-Dimensionalised with respect to the Jet Radius
R_3	Radial Distance from the Sink at the Inverse Point to any point in the Z plane, Non-Dimensionalised with respect to the Jet Radius
s	Distance along the Jet Centreline from the origin
S	Distance along the Jet Centreline from the Origin, Non-Dimensionalised with respect to the Jet Radius, S = s/a
u	Component of Velocity in the x direction
U	Component of Velocity in the X direction, Non-Dimensionalised with respect to the Freestream Velocity $U = u/V_\infty$
v	Component of Velocity in the y direction

V (Chapter V)	Component of Velocity in the Y direction, Non-Dimensionalised with respect to the Freestream Velocity $V = v/V_\infty$
V	Velocity
x, y, z	Cartesian Coordinate System with Origin at the Geometrical Centre of the Nozzle Exit plane (fig 2.2)
X, Y, Z	Cartesian Coordinate System Non-Dimensionalised with respect to the Jet Radius; $X = x/a$, $Y = y/a$, $Z = z/a$
X_s, Y_s	Non-Dimensional Cartesian Coordinates of the Stagnation Points S_1 and S_2
z_1	Complex Plane, $z_1 = x + iy$
Z (Chapter V)	Non-Dimensional Complex Plane with respect to the Jet Radius, $Z = X + iY$
α	Plate Angle of Incidence
α (Chapter V)	Angle between the Radial from the Source to any point in the Z plane and the Positive X axis
β	Angle between the Radial from the Sink to any point in the Z plane and the positive X axis
γ	Ratio of Specific Heats
γ (Chapter V)	Angle between the Radial from the Sink at the Inverse Point to any point in the Z plane and the Positive X axis
θ	Angle between the Radial from the Origin to any point in the xy, XY, z_1 or Z plane and the Positive x or X axis
θ_D	Angle of Deflection of the Jet Trajectory at any point. It is given by the angle between the Tangent at that point and the Positive Z axis

θ_s	Angular Position of the Stagnation Points S_1 and S_2 measured from the Positive X axis
ρ	Density
ϕ	Jet Inclination given by the Angle between the Nozzle Centreline and the Positive Z axis
ψ	Stream Function
ω	Complex Potential, ω = function(z_1)
Ω	Non-Dimensional Complex Potential, Ω = function(Z)

Subscripts

A	Ambient Conditions
E	Jet Exit Conditions
J	Jet Conditions or Quantities
m	Minimum Condition or Quantity
0	Stagnation Conditions
0 (Chapter V)	Reference Conditions of Model Parameters
S	Static Conditions in the Jet Plenum Chamber
∞	Freestream Conditions

Definitions

A (Section 5.6)	$\frac{\Delta C_s}{C_{s0}} \times 100$	percentage change in C_s
B (Section 5.6)	$\frac{A}{\frac{\Delta(\text{Model Parameter})}{(\text{Model Parameter})_0} \times 100}$	change in C_s for a 1% change in the model parameter considered
C_F (Chapter IV)	$\int_{R_1}^{R_2} C_p \, R \, dR$	Surface Force
C_F (Chapter V)	$\int_{1}^{RR} C_p \, R \, dR$	Surface Force
C_M (Chapter IV)	$\int_0^{2\pi} \int_{R_1}^{15} C_p \, X \, R \, dR \, d\theta$	Pitching Moment Coefficient

C_p	$\frac{p_{Jet\ On} - p_{Jet\ Off}}{q_\infty}$	Pressure Coefficient
C_s (Chapter IV)	$-\frac{1}{\pi}\int_0^{2\pi}\int_{R_1}^{R_2} C_p\, R\, dR\, d\theta$	Suction Force Coefficient
C_s (Chapter V)	$-\frac{1}{\pi}\int_{\pi/4}^{3\pi/4}\int_1^5 C_p\, R\, dR\, d\theta$	Suction Force Coefficient
K_1 (Chapter V)	$\frac{Q_1}{2\pi a V_\infty}$	Sink Entrainment Parameter
K_2 (Chapter V)	$\frac{Q_2}{2\pi a V_\infty}$	Source Outflow or Blockage Parameter
m	$\sqrt{\frac{\int_{A_J} \rho_J V_J^2 dA}{\rho_\infty V_\infty^2 A_J}}$	which simplifies to (Section A.1)
	$\frac{V_J}{V_\infty}$	Velocity Ratio
$\frac{p_T}{p_E}$	$\frac{p_0 - p_A}{p_{OE} - p_A}$	Total Pressure Coefficient used to determine the Total Pressure Decay along the Jet Centreline
$\bar{X}$ (Chapter IV)	$\frac{\int_0^{2\pi}\int_{R_1}^{15} C_p\, X\, R\, dR\, d\theta}{\int_0^{2\pi}\int_{R_1}^{15} C_p\, R\, dR\, d\theta}$	Centre of Pressure
ΔC_s (Section 5.6)	$C_s - C_{s0}$	

Summary.

Wind tunnel experiments were conducted to determine the complete longitudinal interference characteristics of a turbulent jet exhausting from a flat plate into a turbulent subsonic freestream. The apparatus was designed so that the trends from systematic variations in one parameter, while the others remain fixed, could be established. The variable parameters were jet inclination, the plate incidence and the ratio of the jet exit velocity to the freestream velocity (the velocity ratio.)

The angles of jet inclination, measured from the normal to the plate surface, varied from 0 to 60 degrees downstream in increments of 15 degrees. The angle of incidence of the plate to the freestream direction varied from 0 to 8 degrees in increments of 2 degrees. The values of the velocity ratio ranged from 4 to 12, values that are pertinent to the range of interest for V/STOL aircraft in transitional flight.

The surface pressure distribution about the jet and the jet trajectory, defined as the locus of the maximum total pressure, were measured for each configuration. In addition, the surface pressure distribution was integrated numerically to provide a surface force distribution about the jet, a suction force coefficient, a pitching moment coefficient and the centre of pressure. The results are summarised by presenting the variation of the suction force coefficient, centre of pressure, pitching moment coefficient and jet trajectory with the velocity ratio for a given jet inclination and plate incidence. These curves can be crossplotted to provide the variation of these quantities with the jet inclination or the plate incidence as the independent variable. In addition, selected isobar plots are presented.

The extent of the low pressure field in the lateral and forward regions was reduced as the jet inclination increased. The contribution from these regions to the lift loss and the magnitude of the lift loss

decreased. The centre of pressure moved downstream accordingly. The jet penetrated the freestream less and was deflected less as the jet inclination increased. These observations were attributed to a change in the entrainment rate of the jet. The jet entrainment rate decreased as the jet inclination increased.

The changes in the surface pressure distribution resulting from a change in incidence of the plate were detailed rather then gross. The variation of the lift loss with incidence exhibited a maximum between 4^{o} and 6^{o} incidence. The change in jet penetration and deflection was small. The centre of pressure appeared to be independent of incidence. A change in incidence appeared to cause an effective change in the inclination of the jet. The entrainment rate of the jet was only moderately affected by a change in incidence.

The low pressures spread to the lateral and forward region as the velocity ratio increased. The contribution of these regions to the lift loss increased while that from the wake region decreased. The magnitude of the lift loss increased as the velocity ratio increased. The centre of pressure moved upstream accordingly. Both the lift loss and the centre of pressure showed a weak dependence on the velocity ratio for large values of the velocity ratio. The jet penetrated the freestream more and suffered a less severe initial deflection as the velocity ratio was increased. These observations were attributed to an increase in the entrainment rate of the jet as the velocity ratio increased.

A two-dimensional potential flow model was proposed to predict the surface pressure distribution, the surface force distribution and the suction force coefficient on the flat plate for the normal jet at zero incidence. The model successfully predicted the surface pressures and surface forces close to the jet in the lateral and forward regions,

for velocity ratios less than 10. The agreement between the predicted and experimental value of the suction force coefficient was particularly good for velocity ratios less than 10. The model was unable to allow for the increasing three-dimensional effects at high ratios. The trends in the variation of the model parameters with the velocity ratio agreed well with the experimentally observed trends of the physical characteristics which they represented.

Chapter 1.

Introduction.

The flow fields produced by jets have been investigated for nearly a century. The majority of this earlier work centred on jets exhausting into a quiescent external medium. Jets exhausting into moving streams were restricted to parallel flows. More recently interest in the flow created by jets issuing into a non parallel freestream has been generated. This flow arrangement has several specific practical applications:

1. The discharge and dispersion of effluent either into the atmosphere from chimneys or into rivers and oceans from waste disposal pipes. This application has resulted from pollution considerations.

2. Injection of cooling gases into certain gas turbine engines.

3. Reaction control jets in missile guidance system or certain types of aircraft.

4. Flow fields produced by V/STOL aircraft employing direct jet lift during the transition phase of flight.

This study is primarily aimed at the latter application. Such aircraft suffer significant lift losses in the transition to forward flight, from requiring a vertical component of thrust. These lift losses are accompanied by adverse changes in pitching moments. These effects can be attributed to the aerodynamic interference created by the interaction of the lifting jet and the freestream. This work is aimed at improving the understanding of this phenomenon.

1.1 Literature Review.

1.1.1 Aircraft Configuration Tests.

References 1 to 10 represent the testing that has been conducted to observe the effect of the aerodynamic interference of the jet and freestream on specific aircraft configurations. Gross aerodynamic interference phenomena are reported but add little to the basic understanding

of the problem. References 11 and 12 review the induced effects on the aerodynamics of jet V/STOL aircraft. More fundamental investigations are reviewed below and are divided into surface pressure and jet plume and structure investigations. Details of the experimental configurations are given, in which all dimensions are expressed in jet radii where appropriate.

1.1.2 Surface Pressures.

The surface pressure distribution around a jet exhausting into a freestream has been the subject of several investigations. Most investigations were limited to the normal circular air jet exhausting subsonically into a subsonic freestream. Similar conclusions were stated: the problem was symmetrical about the plate centreline parallel to the freestream direction; the Reynolds Number (based on freestream velocity and jet size) effect was detailed but not gross; the ratio of jet momentum flux to freestream flux, or the effective velocity ratio, was the dominant flow parameter; the relative importance of entrainment increased as the velocity ratio increased; the increased entrainment reduced the maximum pressure and extent of the high pressure region immediately upstream of the jet and increased the extent of the lateral region of low pressures; the pressure recovery in the wake became more rapid and the minimum pressure point moved upstream; the pitching moment changed from nose up to nose down as the velocity ratio increased.

Vogler (ref 13) investigated the pressures induced on a plate of dimensions 80x48 jet radii by a normal jet exhausting into a working section of 168 x 240 jet radii. Pressures were recorded on the plate with both its longer side normal and parallel to the freestream direction. The position of the convergent nozzle exit producingthe jet was 40 and 24 jet radii behind the leading edge. The clearance between the plate and floor was 84 jet radii. No details were given of the uniformity of

the exit profiles or whether the process was isothermal or not. The velocity ratio ranged from 1 to 5. The surface pressure distribution about a cylindrical rod of the same radius as the jet exit was compared to that about the jet. Similarity of the upstream surface pressures with large differences downstream was evident.

Bradbury and Wood (ref 14) conducted a series of fundamental experiments to determine the dominant parameters of the problem. Attention was confined to the normal circular jet exhausting from a flat plate. The plate, dimensions 144 x 168 jet radii, was mounted above the floor boundary layer in a working section 276 x 204 jet radii. The jet exit was at about 60 jet radii from the leading edge. The plate boundary layer was controlled by applying suction to a porous surface upstream of the jet. No details of the nozzle were given except that a pipe connected the nozzle exit to the plate surface. The velocity profile could be expected to have been not unlike that associated with developed pipe flow. No temperature measurements were provided to ascertain whether the process was isothermal or not. Compressibility corrections were applied to the higher values of the velocity ratio which ranged from 2 to 12. The results indicated that the effect of the boundary layer thickness was measurable but was detailed rather than gross and, provided the jet and plate boundary layer were turbulent, the Reynolds Number effect would be small. An integrated surface force and suction force coefficient were defined. The surface force distribution identified the angular region providing the major contribution to the suction force coefficient. This region moved upstream as the velocity ratio increased. The suction force coefficients were found to be of the right order of magnitude to account for the lift loss measured on a direct jet lift VTOL aircraft (ref 4). The suction force coefficient increased with increasing velocity ratio. At higher values of the

velocity ratio, the dependence became weak although the centre of pressure was changing. Bradbury and Wood identified the momentum flux ratio as being the dominant parameter.

Gelb and Martin (ref 15) measured the surface pressure distribution on a plate, 56 x 68 jet radii, mounted in the tunnel ceiling and in the tunnel boundary layer and on a plate, 48 x 48 jet radii, mounted on the tunnel centreline. The height of the plate surface from the floor was 144 and 72 jet radii respectively. The section width was 144 jet radii. The nozzle in the ceiling plate produced a normal jet with a uniform velocity profile, whereas a pipe extending from this nozzle to the centreline plate produced a jet with a velocity profile similar to that produced by developed pipe flow. The range of velocity ratio was from 3 to 63 and no temperature monitoring was recorded. The surface pressures induced on the two plates at the same velocity ratio, but differing freestream and jet velocities, were similar with major differences occurring only far from the jet exit resulting from a Reynolds Number effect. Impingement of the jet on the floor occurred at the higher values of velocity ratio.

Mosher (ref 16,17,18) extended the investigation to non-circular jets in an attempt to isolate the entrainment effect and the so-called blockage effect of the jet on the freestream. Considerations were limited to normal jets. The jets exhausted through a plate of dimensions 48 x 66 jet radii, mounted 12 jet radii above the wind tunnel floor, into a circular section 108 jet radii diameter. The jet was positioned at 24 jet radii behind the leading edge. The turbulence factor of the freestream was 1.04 and the jet exit total pressure was uniform to within 1% across its span. The exit conditions were determined by assuming an isothermal process, however, the jet temperature settled at 160° F. The velocity ratio ranged from 4 to 12. Mosher concluded that the

surface pressure distribution induced was a combined result of the blocking and entraining properties of the jet with entrainment becoming more dominant as the velocity ratio increased. This dominance brought about an attenuation of lift loss and caused a rise in the low pressures in the wake region.

Fricke, Wooler and Ziegler (ref 19) extended the investigation to include surface pressures induced by an inclined jet and multiple jets. The effects of sideslip were also included. The single jet data was obtained by exhausting a jet through a circular plate, diameter 96 jet radii mounted above the floor boundary layer, into a section 168 x 240 jet radii. The jet exit was positioned 40 jet radii behind the leading edge. Because the contraction ratio of the circular nozzle was 1.866 to 1, it would be expected that the velocity profile would resemble that resulting from developed pipe flow. The angles of inclination varied from 30° upstream to 30 degrees downstream in increments of 15 degrees. The jet velocity was sonic and no temperature data was provided. The surface pressures were found to decrease in magnitude and shift downstream as the angle of inclination changed from an upstream to downstream direction. This is the only data for the surface pressure distribution induced by an inclined jet. Unfortunately, the surface pressure contours were not given.

Fearn and Weston (ref 20) investigated the surface pressure distribution induced by a normal circular jet. The jet exhausted from a plate, 48 x 54 jet radii and mounted above the floor, into a section 87 x 130.5 jet radii. The nozzle was designed to give a uniform velocity profile and employed a 20:1 contraction ratio. A pipe extended from the nozzle to the plate surface. The exit was 18 jet radii behind the leading edge. The range of velocity ratio was from 2 to 10 and the jet temperature was adjusted to ensure an isothermal process. It was observed

that a slower pressure recovery in the wake occurred at a velocity ratio of 4 than for the other values of velocity ratio tested. Measurements of the boundary layer indicated that the leading edge should be at least 16 to 20 jet radii upstream of the jet for a stable boundary layer to exist in the region of interest. A comprehensive comparison with other works showed that the agreement was generally good close to the jet. The difference between the position of low magnitude contours was found to be two jet radii at most, but the error increased as $|C_p|$ decreased.

The link between the idealised infinite flat plate and the jet lift model is provided by the two dimensional wing with exhausting jet. Peake (ref 21) measured the pressure distribution induced on a wing surface by a jet issuing normal to the freestream. Non circular and circular jets were tested. The wind tunnel section was 60 x 120 effective jet radii and the wing was positioned 60 jet radii from the floor. The jet exhausted 13.5 jet radii from the circular leading edge. The flow from the plenum chamber passed through a bellmouth and a pipe to the jet orifice. No details of the uniformity of the exit profile or whether the process was isothermal or not were given. The velocity ratio ranged from 2 to 8. Peake concluded that the increase in Reynolds Number (increase in jet scale or freestream velocity) had a negligible effect.

Mikolowsky (ref 22,23) conducted a series of experiments to investigate the aerodynamic interference resulting from a jet issuing normal to the chordal plane of a NACA 0021 wing in crossflow. Measurements were made of the surface pressure distribution and the gross interference force and moment coefficients for a variation of jet exit location, exit areas and wing incidence. This is the only existing data for the effect of incidence on the surface pressure distribution. The circular wind tunnel section varied from a diameter of 72 to 144 jet radii. The wing chord varied from 10 to 20 jet radii and the position of the jet from 2.5 to

13 jet radii behind the leading edge. The exit velocity profile was uniform but no temperature monitoring was performed. The angle of incidence ranged from 0 to 9 degrees and the velocity ratio ranged from 2 to 8. A comparison between the interference surface pressures on the wing and flat plate revealed good qualitive agreement at higher values of the velocity ratio (in that authors' opinion). The dissimilarity increased as the velocity ratio decreased because of the growth of an extensive high pressure region upstream of the jet which had no counterpart on the flat plate. This provided a noticeable lift augmentation for a velocity ratio less than 6. Attention was also drawn to the different flow field characteristics at high and low velocity ratios. The pressure recovery in the wake was slower at a velocity ratio of 6 than for the other cases.

1.1.3 Jet Plume and Structure (fig 1.1)

Numerous experiments to determine the jet trajectroy and to investigate the flow structure have been reported. Some investigations have been concerned with determining only the jet path but the definitions of the jet centreline have ranged from the locus of the maximum total pressure in the planes normal to the freestream direction to a median drawn between the boundaries of the jet as observed from flow visualisation studies. Other investigations have been concerned with a particular experimentally determined characteristic to enable the evaluation of an empirical or analytical model. The velocity ratio emerged as the dominant parameter determining the position of the jet path.

Jordinson (ref 24) determined the path and shape of the plume with a series of total pressure traverses downstream of the jet. The stream inclination was also measured. The circular jet exhausted normally from a plate, mounted above the floor boundary layer, into a section 120 x 24 and 240 x 48 jet radii. The jet exit was 3 and 6 jet radii behind the

leading edge. No data for the exit profile or temperature of the jet was provided. The velocity ratio ranged from 4 to 8. The results indicated that the cross-section was horse-shoe shaped away from the orifice. The pressure difference across the jet orifice was thought to be responsible for the initial deflection of the jet but, within a few radii of travel from the exit, the effect of entrainment was predominant. The floor boundary layer might be expected to considerably influence the flow beneath the plume. Jordinson observed a region, behind and below the plume, with a total pressure lower than that of the freestream; air was being drawn up from the boundary layer in this region. The stream inclination indicated that the flow had a component opposed to the freestream direction in this region. Entrainment of the boundary layer immediately in front of the jet was also observed.

Gordier (ref 25) investigated the jet trajectory and lateral spread of a circular water jet exhausting normally to a water flow. The nozzles, consisting of bellmouths, were positioned in the floor 28 jet radii from the working section entrance. The jets exhausted into a section 48 x 72 jet radii. The penetration and lateral spread of the jet were measured from photographs of coloured water jets. Total pressure surveys were also conducted to determine the jet shape. A comparison of the results with those of ref 24 (for air jets) revealed a virtual independence of Reynolds Number. Measurements of the potential core showed that the core length decreased with decreasing velocity ratio. Gordier observed that the external fluid was entrained only through the wake at low velocity ratio, whereas, at high velocity ratio, fluid was entrained from all sides. Entrainment from the wake of the jet proceeded in a periodic manner. Gordier concluded that the pressure field induced and the trajectory were dependent on the velocity ratio.

Keffer, Baines, Platten and Pratte (ref 26 to 29) conducted a series

of experiments to determine the structure of the flow. A series of analytical models were introduced to aid the interpretation of the results. Keffer and Baines (ref 26) investigated the flow of a circular jet directed normal to a uniform crosswind. The jet exhausted from a circular plate, 32 jet radii diameter, into a section 248 x 496 jet radii. The plate was mounted 16 jet radii above the floor and the jet was positioned 16 jet radii behind the leading edge. No details were given of the jet exit profile or temperature. The velocity ratio ranged from 4 to 8. Mean velocity contours were obtained using a hotwire anemometer. Keffer and Baines observed that the length of the potential core increased as the velocity ratio increased but was always less than that of the free jet and that the axial velocity decayed more rapidly than that of a free jet.

Pratte and Baines (ref 27) investigated the bulk profile characteristics of the far field or vortex zone of the flow. Oil aerosol was injected into circular jets exhausting normally from a circular plate varying from 66 to 152 jet radii in diameter into a section varying from 530 x 260 to 1230 x 595 jet radii. The height of the plate varied from 44 to 102 jet radii and the position of the jet varied from 33 to 76 jet radii behind the leading edge. The velocity profile was uniform and the process was isothermal. The smoke jet was photographed and the jet centreline was assumed to be midway between the jet boundaries measured normal to the centreline. The potential core length was found to be strongly affected by the crossflow and approached the freejet value slowly as the velocity ratio increased. The length also increased with orifice size suggesting a Reynolds Number effect (which was small). The results indicated the onset of the vortex zone at a value of S/m of 10 or Z/m of 6.4.

Platten and Keffer (ref 28) investigated the entrainment of inclined

jets exhausting into a crossflow. An analytical model was proposed to simulate the two entrainment mechanisms (freejet and vorticity) observed in the experiments. The jets exhausted from a 96 jet radii diameter circular plate into a section of 768 x 384 jet radii. The turbulence level of the uniform crossflow was 1%. The plate was positioned 48 jet radii above the floor and the jet exit was 48 jet radii behind the leading edge. The jet exit tube was 20 jet radii long and the exit profile could be assumed to be that of developed pipe flow. The process was isothermal, the angles of inclination ranged from 45^0 upstream to 45^0 downstream in increments of 15^0 and the velocity ratio ranged from 4 to 8. The maximum and average initial jet velocities of the various inclined jets were constant. Velocities were measured with hotwire anemometers. The results of the analysis applied to the experimental data indicated that the vortex entrainment coefficient so defined was an order of magnitude greater than that of the freejet coefficient. The vortex induced velocity exhibited an initial finite value for zero deflection and increased to a maximum as the deflection increased (at $\theta_D \simeq 30^\circ$) and then decreased to zero at $\theta_D \simeq 90^\circ$. It was evident from the measured trajectories that the jet inclined at 15^0 in the upstream direction experienced the largest deflection of its initial centre line. The model demonstrated that the observed vortex pair was responsible for this secondary and more significant mechanism of entrainment. Pratte and Keffer (ref 29) extended the investigation to swirling turbulent jets in order to study the mechanism of this vortex entrainment. The entrainment rate and angle of spread of the swirling jet was found to be about twice that of a non swirling jet.

Patrick (ref 30) determined the trajectory of a normal circular jet exhausting from the tunnel floor into a section varying from $91\frac{1}{2}$ x $30\frac{1}{2}$ to 282 x 94 jet radii using velocity and concentration measuring

techniques and the Schlieren method of flow visualisation. The jet temperature was raised by 50 degrees C to obtain the Schlieren photographs. The three techniques resulted in three different trajectories.

Reilly (ref 31) studied the flow structure of non circular jets exhausting normally into a crossflow. Smoke was injected into the jet and the resulting flow was photographed. The jets exhausted from a plate, 56 x 80 effective jet radii mounted 14 jet radii above the floor, into a section 60 x 60 jet radii. The jet exit total pressure profile varied by 1% over 85% of the jet span and the jet was positioned 24 jet radii behind the leading edge. A temperature correction was applied and the velocity ratio varied from 1 to 5. A jet centreline was defined by drawing a media line between the jet boundaries. The photographs revealed the existence of two distinct groups of eddies shed periodically from different regions of the plume. The first group was shed alternately from each side of the jet and appeared to merge with the main jet body 10 radii downstream. The formation and periodicity of these eddies suggested an analogy to the von Karman Street shed from a solid body. The second and larger group appeared to be shed over the top of the jet having been formed about 2 to 3 radii above the exit. Two eddies (clockwise and anti-clockwise) were shed simultaneously and caused the flow field to be unsteady in the vicinity of the jet.

Margason (ref 32) measured the paths of a jet exhausting into a section 168 x 240 jet radii at inclinations varying from 90^{0} upstream to 60^{0} downstream. The jet consisted of a mixture of water and compressed air. The paths were determined from photographs. The exit profile of the jet was not particularly uniform and no temperature measurements were recorded. The velocity ratio ranged from 2 to 10. An empirical formula was fitted to the data obtained. The reported trajectories to date were summarised and Margason's formula generally

described the mean path of all these results. Considerable scatter was evident, which was not surprising, considering the different definitions employed to determine the jet path.

McAllister (ref 33) investigated the flow structure of a water jet exhausting into a crossflow. The boundaries of a jet exhausting into a section 16 x 24 and 32 x 48 jet radii were made visible by the injection of red ink. The jet centreline was determined from photographs of the flow. The exit profile of the circular jet was that of developed pipe flow and no temperature monitoring was noted. A strong vortex street was observed to be shed alternately from each side of the jet. Most of the entrained fluid was observed to enter the rear of the jet, induced by the strong attached vortices existing alternately each side of the jet.

Confusion arises between the reported flow phenomenon of refs 26 to 29 and that of ref 31 and 33. Keffer and Baines observed a strongly attached pair of vortices formed just above the jet exit and travelling in the jet direction. Reilly and McAllister observed vortices being shed alternately from each side of the jet. McMahon, Hester and Palfrey (ref 34) investigated the wake behind the jet to resolve the confusion. Their results indicated that vortex shedding occurred and that the characteristics of the vortex system were in qualitative agreement with those corresponding to that behind a bluff body. The shed vortices appeared to be travelling in a downstream direction along the plate surface, rather than in the jet direction.

In this author's opinion the two systems observed by Reilly appear to be feasible. The difficulty with smoke visualisation is that the velocities must be reduced considerably such that the mainstream is laminar. Otherwise the turbulence rapidly diffuses the smoke and obliterates the resulting flow field. At the low Reynolds Numbers necessary

for visualisation tests, the smoke probably depicts the turbulent fluctuations,which are more apparent, and makes the vortices appear detached or, on the other hand,the vortices appear attached by virtue of the fact that they travel in the jet direction. In addition, the smoke in the jet will not mix into the mainstream sufficiently to make the freestream eddies visible and, also, the jet entrains the wake fluid. Therefore, it is difficult to determine whether the vortices shed from the sides of the jet are composed of freestream fluid as they must be for this vortex system to be a von Karman street. Some of these vortices will be entrained into the jet as observed by Reilly,while others will escape the influence of the jet and travel downstream.

Extensive experiments (of which ref 35 and 36 are representative) have been conducted into the detailed structure of the circulatory flow downstream of the jet. The distributions of velocity, temperature and turbulence intensity have been measured and the results used as an aid to analytical modelling of the vortex flow field produced by the jet. The vortex curve or centreline was found to be below the total pressure centreline (ref 36) and it is tne vortex centreline which is probably measured in flow visualisation techniques.

1.2 Research Objective.

The above experimental configurations exhibit a number of shortcomings. Confusion has arisen over the definition of a nozzle and of an orifice. The determination of the exit characteristics of the jets have rarely been mentioned. The degree of uniformity of the exit profiles improves as the nozzle length increases; this increases the penetration of the jet. This can be qualitatively explained by examining the direction the fluid particles must have as they exhaust from the plenum chamber. The fluid exhausting from a nozzle has a more ordered direction because of the guiding effect of the nozzle walls. Data for

nozzles of varying length to radius ratios indicate that as the length of the nozzle decreases the range of uniformity of the total pressure profile over the nozzle width at exit decreases (ref 31). The less the range of uniformity the less the jet penetrates the freestream because the mean momentum at exit is less, ie. a nozzle flow penetrates further into the freestream than an orifice flow for identical mass flows and exit velocities.

The potential core length of the jet depends on the exit Reynolds Number (not strongly) and this can be expected to influence the initial deflection of the centreline. In view of the results of ref 20, it is doubtful if the boundary layer was stable in the region of interest. The surface conditions surrounding the exit affect the data reported. For instance, a thicker boundary layer around the jet exit will provide more fluid with a lower momentum and more susceptible to being entrained into the jet and hence affecting the initial deflection. Any small change in the initial deflection results in a larger shift in the jet trajectory with increasing distance from the exit. Care must be exercised in the definition employed in determining the centreline. For instance, the vortex centreline lies below the velocity centreline.

The determination of the exit conditions is rarely mentioned. The temperature difference between the jet and freestream could incur significant errors in the quoted velocity ratio if expansion to freestream static conditions is assumed, constant density being implicit. The resulting effective velocity ratio change could lead to the wrong conclusion as to the observed trends.

The surface pressures induced appear not to be greatly affected by these difficulties but the scatter of data evident from the comparisons of jet centreline data strongly suggest the reverse. These shortcomings make the development of a theoretical model to describe

the longitudinal characteristics of the problem difficult. There is a need for an experimental programme to be conducted under the same laboratory conditions using carefully determined jet exit characteristics. There is a lack of data in specific areas: more surface pressure measurements are required for inclined jets; the surface pressure distribution on a flat plate at incidence and the jet centrelines require investigating.

Experimental tests were conducted under identical laboratory conditions to determine the complete longitudinal interference characteristics of a subsonic turbulent jet exhausting through a plate into a turbulent subsonic freestream. The apparatus (described in chapter II) was designed so that the trends from systematic variations in one parameter while the others remain fixed could be established. The angle of inclination varies from 0 to 60 degrees downstream in increments of 15 degrees; the angle of incidence of the plate varies from 0 to 8 degrees in increments of 2 degrees with restrictions for inclinations of 30, 45 and 60 degrees, the incidence being limited to 6, 4 and 2 degrees respectively; the range of interest for V/STOL aircraft suggested velocity ratios in the range of 4 to 12. The surface pressure distributions and jet centreline (the locus of maximum total pressure) is measured for each configuration.

The surface pressure distribution is integrated to provide a surface force distribution, a suction force coefficient, a centre of pressure about the exit and a pitching moment coefficient. These quantities are compared to those previously reported where applicable. Trends are established for the variation of these quantities with each parameter.

The ultimate aim of this research is to be able to predict, in some sense, the longitudinal characteristics of a V/STOL aircraft employing direct jet lift. The experimental results should provide consistent and coherent data for evaluating and assessing future theoretical models

which do attempt to describe these characteristics.

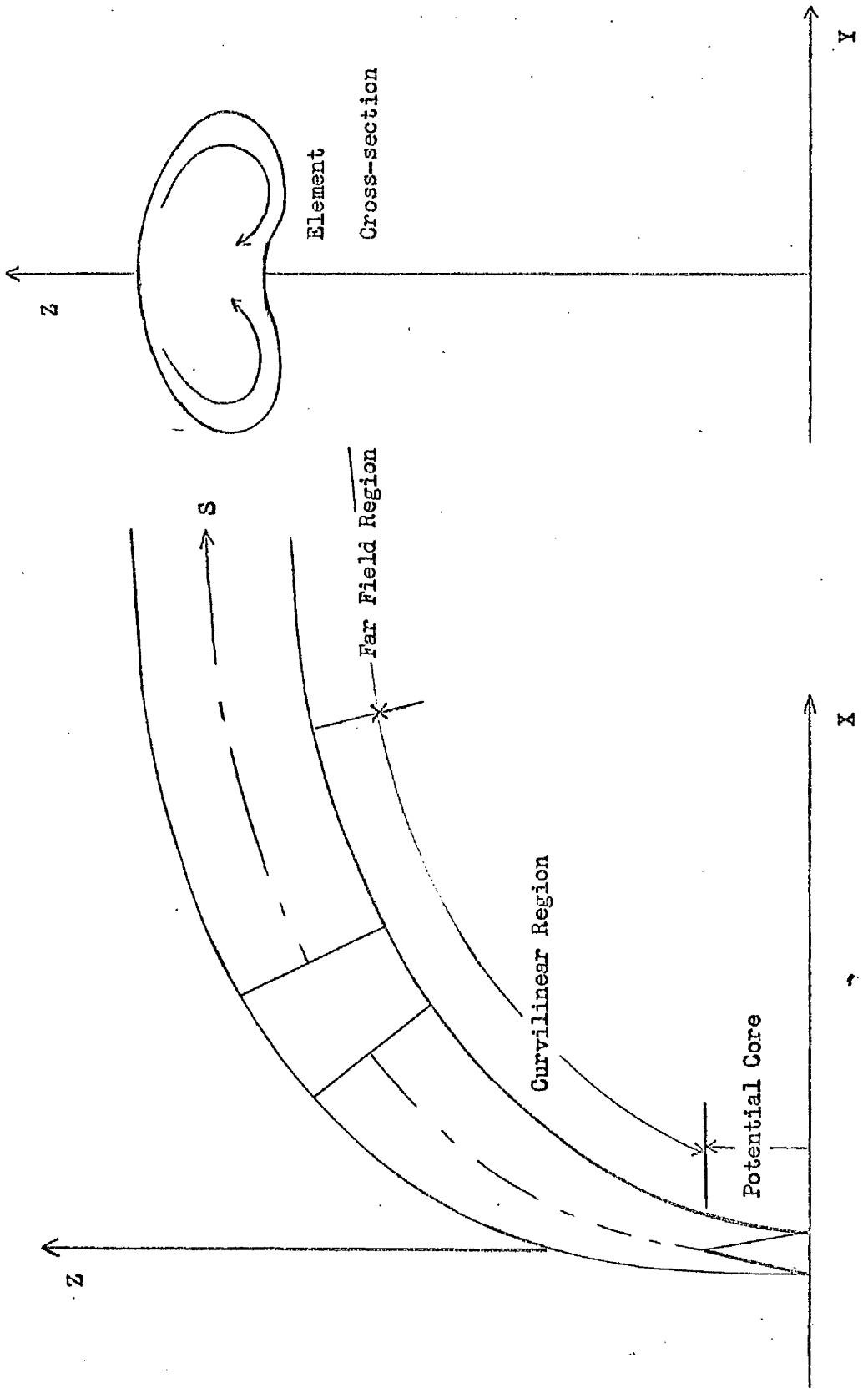

Figure 1.1. Schematic Representation of the Jet Flow

Chapter 11.

Equipment and Installation.

The experimental apparatus described in this chapter consisted of a flat plate of variable incidence equipped with a jet exhausting at various angles to the freestream. All dimensions are expressed in jet radii where appropriate, the jet radius being 0.25 inches (see sections 2.5 and 2.6).

2.1 Wind Tunnel.

The closed return wind tunnel had a working section 132 jet radii high and 180 jet radii wide. The working section velocity was continuously variable with a maximum speed of 100 feet per second. The setting of the turbulence grids at the entrance to the working section gave a turbulence level of 4.4% at the leading edge of the plate.

The wind tunnel was equipped with two static pressure taps to enable the working section dynamic pressure to be monitored without the use of a pitot-static tube in the working section. One tap was situated in the wall of the settling chamber and the other in the wall immediately upstream of the working section.

2.2 Air Supply.

The crossflow was provided by the uniform stream of the wind tunnel. The jet air was supplied by two tanks, of 750 cubic feet capacity each, initially pressurised to 250 psi. The air passed through a regulating valve, used to control the jet exit conditions, and into a 0.75 inch internal diameter flexible hose connected to the jet plenum chamber. The exit conditions required a low mass flow such that the change in exit conditions was negligible for the duration of the test.

2.3 General Test Arrangement. (plate 2.1 and 2.2, fig 2.1)

Several factors determined the general arrangement of the apparatus and limited the number of configurations that could be tested. The

situation of the force balance under the working section floor dictated the mounting of the flat plate and jet plenum chamber in the working section ceiling. It was considered desirable to position the jet plenum chamber outside of the working section to minimise the flow disturbance for all configurations. An increase in jet inclination angle required an increase in the length of the jet pipe. The height restriction above the working section required that the jet chamber and nozzle block be pivotted about the support plate (section 2.5) rather than about the jet exit plane as originally intended. Each nozzle block required a jet pipe of a different length.

A large angle of incidence together with a large jet inclination angle entailed a considerable lowering of the plate. This was considered to be undesirable as it would interfere with the flow conditions within the working section and consequently, a limit was imposed on the maximum angle of incidence for a given jet inclination angle.

The plate was kept as close as possible to the working section ceiling to minimise any floor interference effects on the jet flow. The empirical formula from ref 32 was used to decide on the range of magnitude of jet radii that could be employed within the given working section. Having decided on a jet radius (section 2.6), the formula was utilised to determine the maximum height above the working section floor at which the plate could be positioned so that the jet did not impinge on the floor. These considerations placed the jet exit plane at 26 jet radii below the working section ceiling. At this postion, it was felt that if the topside of the plate was kept reasonably 'clean', that is, the pressure lines were kept to one deep and attached firmly to the plate, then the only blockage incurred would be that arising from the plate thickness, supports and jet pipe; the flow over the plate surface would

then not be interfered with.

The plate and its associated support and jet pipe fairings were installed in the working section. A test was conducted with the jet off and at zero incidence to verify that in the region of interest ($-20 < X < 48, -40 < Y < 40$) the flow over the plate surface was uniform. The test revealed that this was so (see also Appendix B).

Further tests were conducted to determine how sensitive the surface pressure distribution was to very small changes in pitch and bank of the plate. These tests revealed that the actual pressure readings were very insensitive and zero incidence was defined as the postion of the plate when its XY plane was perfectly horizontal as determined by a clinometer. The flow over the plate in this position was uniform (see also Appendix B).

The boundary layer was measured on the plate surface (at X= -7, Y= 3) and was found to be approximately 3.0 jet radii thick with a typical one-seventh power profile.

2.4 Flat Plate. (Plates 2.1, 2.2)

The dimensions of the flat plate were 144 jet radii spanwise and 192 jet radii chordwise. The plate material was 0.5 inch thick perspex suitably stiffened with two chordwise aluminium angle bars. These bars provided attachments for the supports and pressure lines. The jet exhausted at a position 40 jet radii from the leading edge and on the plate centreline. A leading edge trip was fitted.

The plate was supported by four legs each of 0.5 inch diameter screwed rod. The screw pitch was 0.05inch. Each leg was fitted through a hole in the wind tunnel roof and with the aid of adjusting nuts, the plate could be set to some desired angle of incidence up to a maximum of approximately 8 degrees. The two front legs were each housed in a NACA 0025 fairing of chord 24 jet radii (co-ordinates from ref 37). The portion of the jet pipe protruding below the working section ceiling

and the nozzle block pressure lines were housed in a NACA 0025 fairing of chord 40 jet radii. The fairing around the rear legs and pressure lines from the plate was a NACA 0030 of chord 60 jet radii.

2.5 Jet Plenum Chamber (Plate 2.1, 2.2 and fig 2.1)

The jet plenum chamber was designed to be positioned outside of the working section for all configurations to minimise the blockage between the top side of the plate and the ceiling. The chamber consisted of a 4 inch internal diameter steel cylinder. The transition from the 4 inch diameter chamber to the 0.5" diameter exit was achieved by using one of the family of curves, slightly modified, from ref 38. The other end of the chamber contained the fitting for the flexible hose. The chamber contained screens to aid flow uniformity at exit, a static pressure tap (internal diameter 0.040 inch) and a thermocouple.

The chamber supporting plate was slotted so that the chamber could be rotated to a desired position and clamped by means of a bolt passing through one of these slots and a bracket attached to the chamber.

The supporting plate was able to slide along an angle bar carefully positioned in a plane parallel to the plane containing the plate centreline to ensure that the jet exhausted symmetrically with respect to the plate.

2.6 Jet Nozzles (fig 2.1)

Each jet nozzle block consisted of a block of perspex 11 jet radii chordwise and 7 jet radii spanwise and was machined to be a tight fit in an existing recess in the plate. No leakage was detected through the discontinuity in the plate surface.

The copper jet pipe of 0.5 inch internal diameter was fixed in the nozzle block which had been previously drilled at the required angle for the given jet inclination. Care was taken to ensure that the pipe was flush with the surface of the nozzle block and that its centreline was

at the specified angle to the Z axis in the XZ plane of the plate and that the projection of the pipe centreline onto the YZ plane of the plate was parallel to the Z axis (i.e. the pipe was not yawed). The length of the jet pipe was determined by the position of the plenum chamber. The jet pipe was attached to the plenum chamber by means of a gas fitting nut bearing down on to a flange at the end of the pipe. The various characteristics of the jets are given in Appendix A.

2.7 Pressure Measurement Instrumentation.

The working section dynamic pressure was monitored on a water micromanometer. The working section was calibrated with the model in position and for each model configuration. The freestream stagnation temperature was measured using a bulb type mercury thermometer and the ambient atmospheric pressure was measured using a Fortin barometer.

The plenum chamber pressure tap was monitored with a Prandtl manometer (range 0 to 600mm). This tap was located immediately upstream of the convergence to the exit plane (fig 2.1). A vacrum-eureka thermocouple was installed in the plenum chamber to monitor the stagnation temperature. Melting ice was used at the reference junction and the output was displayed on a digital voltmeter.

The plate was instrumented with 357 static taps. The pressure taps were located on a rectangular grid of variable spacing, that is the spacing distance decreases with decreasing distance from the jet exit (see Table 2.1.1). This was to allow for the large pressure gradients in the immediate vicinity of the jet. The important factor in locating the taps was to ensure that adequate interference pressure contours and sufficient points on contours further away from the jet could be obtained. A rectangular grid fulfills these conditions more satisfactorily than a polar grid. Pressure taps were also provided to check the symmetry and the uniformity of flow conditions and to aid the installation of a given configuration (see end of Table 2.1.6).

The pressure taps consisted of P.V.C. tubing (internal diameter 0.035 inch, outside diameter 0.060 inch) inserted into a hole drilled through the perspex, initially undersize then opened out using a taper drill. Care was taken to ensure that the hole was normal to the plate surface. A special P.V.C./perspex adhesive was applied to bond the tubing to the plate. The protruding end of the tube was sliced flush with the plate surface. The taps were observed under a microscope to check that no burred edges existed. The P.V.C. tubing was sufficiently flexible to undergo a 90 degree bend of small curvature without any adverse effects. The tubes were attached, one deep, to the plate upper surface and led to the nearest stiffener. The tubes were routed along the stiffeners to the rear legs and out of the tunnel.

The static pressure taps were positioned as close as was physically possible on the nozzle blocks and to the jet periphery but still maintaining the correct grid position (Tables 2.1.2 to 2.1.6). The nozzle block pressure lines were routed along the outside of the jet pipe and out of the tunnel.

All the pressure lines were fed into the rear of a 'pressure' console. The purpose of this console was to facilitate the handling of a large number of pressure taps. The console consisted of 14 rows of holes, each row containing 36 holes in 4 banks of 9 holes. Each bank was sealed with a blank cover. Four 'connecting blocks', each of 9 connections, were connected to hexane multitube tilting manometer. The incoming pressure lines were arranged so that the taps giving the various distributions (end of Table 2.1.6) for symmetry and uniformity of flow conditions could be observed together. The jet characteristics and the jet penetration into the crossflow were measured with a total pressure probe. This pressure was monitored on a Prandtl manometer.

2.8 Traversing Mechanism (Plate 2.2)

The total pressure probe (dimensions: 0.031 inch diameter head and reinforced stem of 0.125 inch diameter) was supported by a traversing mechanism so that its stem was parallel to the plane of the plate and perpendicular to the freestream direction. The probe head was parallel to the freestream direction. The probe could be moved vertically along a lead screw (20 turns to the inch or a pitch of 0.2 jet radii) and rotated about its stem. The number of revolutions of the lead screw and the angle of rotation of the probe determined the vertical position of the probe head relative to the plate.

A small rail was attached to the plate surface at a position Y = -21.125 jet radii, parallel to the X axis. This rail provided extra stability to the mechanism. The rail was drilled every 2 jet radii and thumb screws were used to fix the mechanism at a particular position along the X direction. The other end of the traversing mechanism passed through a slot in the wind tunnel floor. This end was clamped to the floor of the working section and, using the clinometer, the clamp was positioned such that the axis of the mechanism was always normal to the plate surface (i.e. parallel to the Z axis). The horizontal position of the probe head was determined from the position of the mechanism along the rail and the angle of rotation of the probe.

The range of operation of the traversing mechanism was as follows: horizontal movement $-6 \leq X \leq 18$ depending on the angle of incidence of the plate; vertical movement $6.25 \leq Z \leq 102$; rotation through approximately 150 degrees.

Table 2.1.1. Static Pressure Tap Locations: Flat Plate

Tap Number	X	Y	Tap Number	X	Y	Tap Number	X	Y
1	-32	0	28	-16	8	55	-12	20
2	-32	8	29	-16	10	56	-12	24
3	-32	16	30	-16	12	57	-12	60
4	-32	24	31	-16	14	58	-10	0
5	-32	32	32	-16	16	59	-10	2
6	-32	40	33	-16	20	60	-10	4
7	-32	60	34	-16	24	61	-10	6
8	-24	0	35	-16	32	62	-10	8
9	-24	4	36	-16	40	63	-10	10
10	-24	8	37	-14	0	64	-10	12
11	-24	12	38	-14	2	65	-10	14
12	-24	16	39	-14	4	66	-10	16
13	-24	20	40	-14	6	67	-8	0
14	-24	24	41	-14	8	68	-8	2
15	-24	32	42	-14	10	69	-8	4
16	-24	40	43	-14	12	70	-8	6
17	-20	0	44	-14	14	71	-8	8
18	-20	4	45	-14	16	72	-8	10
19	-20	8	46	-12	0	73	-8	12
20	-20	12	47	-12	2	74	-8	14
21	-20	16	48	-12	4	75	-8	16
22	-20	20	49	-12	6	76	-8	20
23	-20	24	50	-12	8	77	-8	24
24	-16	0	51	-12	10	78	-8	32
25	-16	2	52	-12	12	79	-8	40
26	-16	4	53	-12	14	80	-6	1
27	-16	6	54	-12	16	81	-6	2

Table 2.1.1. Continued.

Tap Number	X	Y	Tap Number	X	Y	Tap Number	X	Y
82	-6	3	109	-3	5	136	0	20
83	-6	4	110	-3	6	137	0	24
84	-6	5	111	-3	7	138	0	32
85	-6	6	112	-3	8	139	0	40
86	-6	7	113	-2	4	140	1	4
87	-6	8	114	-2	5	141	1	5
88	-6	10	115	-2	6	142	1	6
89	-6	12	116	-2	7	143	1	7
90	-6	14	117	-2	8	144	1	8
91	-6	16	118	-2	10	145	2	4
92	-5	4	119	-2	12	146	2	5
93	-5	5	120	-2	14	147	2	6
94	-5	6	121	-2	16	148	2	7
95	-5	7	122	-1	4	149	2	8
96	-5	8	123	-1	5	150	2	10
97	-4	4	124	-1	6	151	2	12
98	-4	5	125	-1	7	152	2	14
99	-4	6	126	-1	8	153	2	16
100	-4	7	127	0	4	154	3	4
101	-4	8	128	0	5	155	3	5
102	-4	10	129	0	6	156	3	6
103	-4	12	130	0	7	157	3	7
104	-4	14	131	0	8	158	3	8
105	-4	16	132	0	10	159	4	4
106	-4	20	133	0	12	160	4	5
107	-4	24	134	0	14	161	4	6
108	-3	4	135	0	16	162	4	7

Table 2.1.1. Continued.

Tap Number	X	Y	Tap Number	X	Y	Tap Number	X	Y
163	4	8	190	7	2	217	9	2
164	4	10	191	7	3	218	9	3
165	4	12	192	7	4	219	9	4
166	4	14	193	7	5	220	9	5
167	4	16	194	7	6	221	9	6
168	4	20	195	7	7	222	9	7
169	4	24	196	7	8	223	9	8
170	5	4	197	8	0	224	10	0
171	5	5	198	8	1	225	10	1
172	5	6	199	8	2	226	10	2
173	5	7	200	8	3	227	10	3
174	5	8	201	8	4	228	10	4
175	6	0	202	8	5	229	10	5
176	6	1	203	8	6	230	10	6
177	6	2	204	8	7	231	10	7
178	6	3	205	8	8	232	10	8
179	6	4	206	8	10	233	10	10
180	6	5	207	8	12	234	10	12
181	6	6	208	8	14	235	10	14
182	6	7	209	8	16	236	10	16
183	6	8	210	8	20	237	11	0
184	6	10	211	8	24	238	11	1
185	6	12	212	8	32	239	11	2
186	6	14	213	8	40	240	11	3
187	6	16	214	8	60	241	11	4
188	7	0	215	9	0	242	11	5
189	7	1	216	9	1	243	11	6

Table 2.1.1. Continued.

Tap Number	X	Y	Tap Number	X	Y	Tap Number	X	Y
244	11	7	271	16	12	298	24	4
245	11	8	272	16	16	299	24	6
246	12	0	273	16	20	300	24	8
247	12	1	274	16	24	301	24	12
248	12	2	275	16	32	302	24	16
249	12	3	276	16	40	303	24	20
250	12	4	277	18	0	304	24	24
251	12	5	278	18	2	305	24	32
252	12	6	279	18	4	306	24	40
253	12	7	280	18	6	307	48	0
254	12	8	281	18	8	308	48	8
255	12	10	282	20	0	309	48	16
256	12	12	283	20	2	310	48	24
257	12	14	284	20	4	311	48	32
258	12	16	285	20	6	312	48	40
259	12	20	286	20	8	313	48	60
260	12	24	287	20	12	314	148	0
261	14	0	288	20	16	315	148	20
262	14	2	289	20	20	316	148	40
263	14	4	290	20	24	317	148	60
264	14	6	291	22	0	318	28	60
265	14	8	292	22	2	319	68	60
266	16	0	293	22	4	320	88	60
267	16	2	294	22	6	321	108	60
268	16	4	295	22	8	322	128	60
269	16	6	296	24	0	323	-32	-8
270	16	8	297	24	2	324	-32	-16

Table 2.1.1. Continue.

Tap Number	X	Y	Tap Number	X	Y	Tap Number	X	Y
325	-32	-24	336	0	-12	347	48	-24
326	-32	-32	337	0	-14	348	48	-32
327	-32	-40	338	0	-16	349	48	-40
328	-32	-60	339	0	-20	350	48	-60
329	-12	-60	340	0	-24	351	68	-60
330	0	-4	341	0	-32	352	88	-60
331	0	-5	342	0	-40	353	108	-60
332	0	-6	343	8	-60	354	128	-60
333	0	-7	344	28	-60	355	148	-20
334	0	-8	345	48	-8	356	148	-40
335	0	-10	346	48	-16	357	148	-60

Table 2.1.2. Static Pressure Tap Locations: Nozzle Block, $\phi = 0°$.

Tap Number	X	Y	Tap Number	X	Y	Tap Number	X	Y
358	-5	0	385	-3.5	3.0	412	-1.5	2.5
359	-5	0.5	386	-3	0	413	-1.5	3.0
360	-5	1.0	387	-3	0.5	414	-1	1.0
361	-5	1.5	388	-3	1.0	415	-1	1.5
362	-5	2.0	389	-3	1.5	416	-1	2.0
363	-5	2.5	390	-3	2.0	417	-1	2.5
364	-5	3.0	391	-3	2.5	418	-1	3.0
365	-4.5	0	392	-3	3.0	419	-0.5	1.5
366	-4.5	0.5	393	-2.5	0	420	-0.5	2.0
367	-4.5	1.0	394	-2.5	0.5	421	-0.5	2.5
368	-4.5	1.5	395	-2.5	1.0	422	-0.5	3.0
369	-4.5	2.0	396	-2.5	1.5	423	0	1.5
370	-4.5	2.5	397	-2.5	2.0	424	0	2.0
371	-4.5	3.0	398	-2.5	2.5	425	0	2.5
372	-4	0	399	-2.5	3.0	426	0	3.0
373	-4	0.5	400	-2	0	427	0.5	1.5
374	-4	1.0	401	-2	0.5	428	0.5	2.0
375	-4	1.5	402	-2	1.0	429	0.5	2.5
376	-4	2.0	403	-2	1.5	430	0.5	3.0
377	-4	2.5	404	-2	2.0	431	1	1.0
378	-4	3.0	405	-2	2.5	432	1	1.5
379	-3.5	0	406	-2	3.0	433	1	2.0
380	-3.5	0.5	407	-1.5	0	434	1	2.5
381	-3.5	1.0	408	-1.5	0.5	435	1	3.0
382	-3.5	1.5	409	-1.5	1.0	436	1.5	0
383	-3.5	2.0	410	-1.5	1.5	437	1.5	0.5
384	-3.5	2.5	411	-1.5	2.0	438	1.5	1.0

Table 2.1.2. Continued.

Tap Number	X	Y	Tap Number	X	Y	Tap Number	X	Y
439	1.5	1.5	457	3	0	475	4	2.0
440	1.5	2.0	458	3	0.5	476	4	2.5
441	1.5	2.5	459	3	1.0	477	4	3.0
442	1.5	3.0	460	3	1.5	478	4.5	0
443	2	0	461	3	2.0	479	4.5	0.5
444	2	0.5	462	3	2.5	480	4.5	1.0
445	2	1.0	463	3	3.0	481	4.5	1.5
446	2	1.5	464	3.5	0	482	4.5	2.0
447	2	2.0	465	3.5	0.5	483	4.5	2.5
448	2	2.5	466	3.5	1.0	484	4.5	3.0
449	2	3.0	467	3.5	1.5	485	5	0
450	2.5	0	468	3.5	2.0	486	5	0.5
451	2.5	0.5	469	3.5	2.5	487	5	1.0
452	2.5	1.0	470	3.5	3.0	488	5	1.5
453	2.5	1.5	471	4	0	489	5	2.0
454	2.5	2.0	472	4	0.5	490	5	2.5
455	2.5	2.5	473	4	1.0	491	5	3.0
456	2.5	3.0	474	4	1.5	492	0	-2.0

Table 2.1.3. Static Pressure Tap Locations: Nozzle Block, $\phi = 15°$.

Tap Number	X	Y	Tap Number	X	Y	Tap Number	X	Y
358	-5	0	385	-3.5	3.0	415	-1.0	1.5
359	-5	0.5	386	-3	0	416	-1.0	2.0
360	-5	1.0	387	-3	0.5	417	-1.0	2.5
361	-5	1.5	388	-3	1.0	418	-1.0	3.0
362	-5	2.0	389	-3	1.5	419	-0.5	1.5
363	-5	2.5	390	-3	2.0	420	-0.5	2.0
364	-5	3.0	391	-3	2.5	421	-0.5	2.5
365	-4.5	0	392	-3	3.0	422	-0.5	3.0
366	-4.5	0.5	393	-2.5	0	423	0	1.5
367	-4.5	1.0	394	-2.5	0.5	424	0	2.0
368	-4.5	1.5	395	-2.5	1.0	425	0	2.5
369	-4.5	2.0	396	-2.5	1.5	426	0	3.0
370	-4.5	2.5	397	-2.5	2.0	427	0.5	1.5
371	-4.5	3.0	398	-2.5	2.5	428	0.5	2.0
372	-4	0	399	-2.5	3.0	429	0.5	2.5
373	-4	0.5	400	-2	0	430	0.5	3.0
374	-4	1.0	401	-2	0.5	431	1	1.0
375	-4	1.5	402	-2	1.0	432	1	1.5
376	-4	2.0	403	-2	1.5	433	1	2.0
377	-4	2.5	404	-2	2.0	434	1	2.5
378	-4	3.0	405	-2	2.5	435	1	3.0
379	-3.5	0	406	-2	3.0	436	1.5	0
380	-3.5	0.5	409	-1.5	1.0	437	1.5	0.5
381	-3.5	1.0	410	-1.5	1.5	438	1.5	1.0
382	-3.5	1.5	411	-1.5	2.0	439	1.5	1.5
383	-3.5	2.0	412	-1.5	2.5	440	1.5	2.0
384	-3.5	2.5	413	-1.5	3.0	441	1.5	2.5

Table 2.1.3. Continued.

Tap Number	X	Y	Tap Number	X	Y	Tap Number	X	Y
442	1.5	3.0	459	3	1.0	476	4	2.5
443	2	0	460	3	1.5	477	4	3.0
444	2	0.5	461	3	2.0	478	4.5	0
445	2	1.0	462	3	2.5	479	4.5	0.5
446	2	1.5	463	3	3.0	480	4.5	1.0
447	2	2.0	464	3.5	0	481	4.5	1.5
448	2	2.5	465	3.5	0.5	482	4.5	2.0
449	2	3.0	466	3.5	1.0	483	4.5	2.5
450	2.5	0	467	3.5	1.5	484	4.5	3.0
451	2.5	0.5	468	3.5	2.0	485	5	0
452	2.5	1.0	469	3.5	2.5	486	5	0.5
453	2.5	1.5	470	3.5	3.0	487	5	1.0
454	2.5	2.0	471	4	0	488	5	1.5
455	2.5	2.5	472	4	0.5	489	5	2.0
456	2.5	3.0	473	4	1.0	490	5	2.5
457	3	0	474	4	1.5	491	5	3.0
458	3	0.5	475	4	2.0	492	0	-2.0

Table 2.1.4. Static Pressure Tap Locations: Nozzle Block, $\phi = 30°$.

Tap Number	X	Y	Tap Number	X	Y	Tap Number	X	Y
358	-5	0	385	-3.5	3.0	421	-0.5	2.5
359	-5	0.5	386	-3	0	422	-0.5	3.0
360	-5	1.0	387	-3	0.5	423	0	1.5
361	-5	1.5	388	-3	1.0	424	0	2.0
362	-5	2.0	389	-3	1.5	425	0	2.5
363	-5	2.5	390	-3	2.0	426	0	3.0
364	-5	3.0	391	-3	2.5	427	0.5	1.5
365	-4.5	0	392	-3	3.0	428	0.5	2.0
366	-4.5	0.5	395	-2.5	1.0	429	0.5	2.5
367	-4.5	1.0	396	-2.5	1.5	430	0.5	3.0
368	-4.5	1.5	397	-2.5	2.0	431	1	1.0
369	-4.5	2.0	398	-2.5	2.5	432	1	1.5
370	-4.5	2.5	399	-2.5	3.0	433	1	2.0
371	-4.5	3.0	403	-2	1.5	434	1	2.5
372	-4	0	404	-2	2.0	435	1	3.0
373	-4	0.5	405	-2	2.5	436	1.5	0
374	-4	1.0	406	-2	3.0	437	1.5	0.5
375	-4	1.5	410	-1.5	1.5	438	1.5	1.0
376	-4	2.0	411	-1.5	2.0	439	1.5	1.5
377	-4	2.5	412	-1.5	2.5	440	1.5	2.0
378	-4	3.0	413	-1.5	3.0	441	1.5	2.5
379	-3.5	0	415	-1	1.5	442	1.5	3.0
380	-3.5	0.5	416	-1	2.0	443	2	0
381	-3.5	1.0	417	-1	2.5	444	2	0.5
382	-3.5	1.5	418	-1	3.0	445	2	1.0
383	-3.5	2.0	419	-0.5	1.5	446	2	1.5
384	-3.5	2.5	420	-0.5	2.0	447	2	2.0

Table 2.1.4. Continued.

Tap Number	X	Y	Tap Number	X	Y	Tap Number	X	Y
448	2	2.5	463	3	3.0	478	4.5	0
449	2	3.0	464	3.5	0	479	4.5	0.5
450	2.5	0	465	3.5	0.5	480	4.5	1.0
451	2.5	0.5	466	3.5	1.0	481	4.5	1.5
452	2.5	1.0	467	3.5	1.5	482	4.5	2.0
453	2.5	1.5	468	3.5	2.0	483	4.5	2.5
454	2.5	2.0	469	3.5	2.5	484	4.5	3.0
455	2.5	2.5	470	3.5	3.0	485	5	0
456	2.5	3.0	471	4	0	486	5	0.5
457	3	0	472	4	0.5	487	5	1.0
458	3	0.5	473	4	1.0	488	5	1.5
459	3	1.0	474	4	1.5	489	5	2.0
460	3	1.5	475	4	2.0	490	5	2.5
461	3	2.0	476	4	2.5	491	5	3.0
462	3	2.5	477	4	3.0	492	0	-2.0

Table 2.1.5. Static Pressure Tap Locations: Nozzle Block, $\phi = 45°$.

Tap Number	X	Y	Tap Number	X	Y	Tap Number	X	Y
358	-5	0	390	-3	2.0	427	0.5	1.5
359	-5	0.5	391	-3	2.5	428	0.5	2.0
360	-5	1.0	392	-3	3.0	429	0.5	2.5
361	-5	1.5	396	-2.5	1.5	430	0.5	3.0
362	-5	2.0	397	-2.5	2.0	431	1	1.0
363	-5	2.5	398	-2.5	2.5	432	1	1.5
364	-5	3.0	399	-2.5	3.0	433	1	2.0
365	-4.5	0	403	-2	1.5	434	1	2.5
366	-4.5	0.5	404	-2	2.0	435	1	3.0
367	-4.5	1.0	405	-2	2.5	438	1.5	1.0
368	-4.5	1.5	406	-2	3.0	439	1.5	1.5
369	-4.5	2.0	410	-1.5	1.5	440	1.5	2.0
370	-4.5	2.5	411	-1.5	2.0	441	1.5	2.5
371	-4.5	3.0	412	-1.5	2.5	442	1.5	3.0
372	-4	0	413	-1.5	3.0	443	2	0
373	-4	0.5	415	-1	1.5	444	2	0.5
374	-4	1.0	416	-1	2.0	445	2	1.0
375	-4	1.5	417	-1	2.5	446	2	1.5
376	-4	2.0	418	-1	3.0	447	2	2.0
377	-4	2.5	419	-0.5	1.5	448	2	2.5
378	-4	3.0	420	-0.5	2.0	449	2	3.0
381	-3.5	1.0	421	-0.5	2.5	450	2.5	0
382	-3.5	1.5	422	-0.5	3.0	451	2.5	0.5
383	-3.5	2.0	423	0	1.5	452	2.5	1.0
384	-3.5	2.5	424	0	2.0	453	2.5	1.5
385	-3.5	3.0	425	0	2.5	454	2.5	2.0
389	-3	1.5	426	0	3.0	455	2.5	2.5

Table 2.1.5. Continued.

Tap Number	X	Y	Tap Number	X	Y	Tap Number	X	Y
456	2.5	3.0	469	3.5	2.5	482	4.5	2.0
457	3	0	470	3.5	3.0	483	4.5	2.5
458	3	0.5	471	4	0	484	4.5	3.0
459	3	1.0	472	4	0.5	485	5	0
460	3	1.5	473	4	1.0	486	5	0.5
461	3	2.0	474	4	1.5	487	5	1.0
462	3	2.5	475	4	2.0	488	5	1.5
463	3	3.0	476	4	2.5	489	5	2.0
464	3.5	0	477	4	3.0	490	5	2.5
465	3.5	0.5	478	4.5	0	491	5	3.0
466	3.5	1.0	479	4.5	0.5	492	0	-2.0
467	3.5	1.5	480	4.5	1.0			
468	3.5	2.0	481	4.5	1.5			

Table 2.1.6. Static Pressure Tap Locations: Nozzle Block, $\phi = 60°$.

Tap Number	X	Y	Tap Number	X	Y	Tap Number	X	Y
360	-5	1.0	405	-2	2.5	439	1.5	1.5
361	-5	1.5	406	-2	3.0	440	1.5	2.0
362	-5	2.0	410	-1.5	1.5	441	1.5	2.5
363	-5	2.5	411	-1.5	2.0	442	1.5	3.0
364	-5	3.0	412	-1.5	2.5	445	2	1.0
368	-4.5	1.5	413	-1.5	3.0	446	2	1.5
369	-4.5	2.0	415	-1	1.5	447	2	2.0
370	-4.5	2.5	416	-1	2.0	448	2	2.5
371	-4.5	3.0	417	-1	2.5	449	2	3.0
375	-4	1.5	418	-1	3.0	450	2.5	0
376	-4	2.0	419	-0.5	1.5	451	2.5	0.5
377	-4	2.5	420	-0.5	2.0	452	2.5	1.0
378	-4	3.0	421	-0.5	2.5	453	2.5	1.5
382	-3.5	1.5	422	-0.5	3.0	454	2.5	2.0
383	-3.5	2.0	423	0	1.5	455	2.5	2.5
384	-3.5	2.5	424	0	2.0	456	2.5	3.0
385	-3.5	3.0	425	0	2.5	457	3	0
389	-3	1.5	426	0	3.0	458	3	0.5
390	-3	2.0	427	0.5	1.5	459	3	1.0
391	-3	2.5	428	0.5	2.0	460	3	1.5
392	-3	3.0	429	0.5	2.5	461	3	2.0
396	-2.5	1.5	430	0.5	3.0	462	3	2.5
397	-2.5	2.0	432	1	1.5	463	3	3.0
398	-2.5	2.5	433	1	2.0	464	3.5	0
399	-2.5	3.0	434	1	2.5	465	3.5	0.5
403	-2	1.5	435	1	3.0	466	3.5	1.0
404	-2	2.0	438	1.5	1.0	467	3.5	1.5

Table 2.1.6. Continued.

Tap Number	X	Y	Tap Number	X	Y	Tap Number	X	Y
468	3.5	2.0	477	4	3.0	486	5	0.5
469	3.5	2.5	478	4.5	0	487	5	1.0
470	3.5	3.0	479	4.5	0.5	488	5	1.5
471	4	0	480	4.5	1.0	489	5	2.0
472	4	0.5	481	4.5	1.5	490	5	2.5
473	4	1.0	482	4.5	2.0	491	5	3.0
474	4	1.5	483	4.5	2.5	492	0	-2.0
475	4	2.0	484	4.5	3.0			
476	4	2.5	485	5	0			

Notes.

1. Taps 328, 327, 326, 325, 323, 1, 2, 3, 4, 5, 6 and 7 provided the leading edge pressure distribution.
2. Taps 357, 356, 355, 317, 316, 315 and 314 provided the trailing edge pressure distribution.
3. Taps 350, 349, 348, 347, 346, 345, 307, 308, 309, 310, 311, 312 and 313 provided the spanwise pressure distribution at X = 48.
4. The chordwise pressure distribution at the plate tips was given by taps 7, 57, 214, 318, 313, 319, 320, 321, 322 and 317 at Y = 60, and by 328, 329, 343, 344, 350, 351, 352, 353, 354 and 357 at Y = -60.
5. The spanwise pressure distribution along the Y axis was given by taps 342, 341, 340, 339, 338, 337, 336, 335, 334, 333, 332, 331, 330, 492, 423, 424, 425, 426, 127, 128, 129, 130, 131, 132, 133, 134, 135, 136, 137, 138 and 139.
6. Taps 1, 8, 17, 24, 37, 46, 58, 67, 358, 365, 372, 379, 386, 393, 400, 407, 436, 443, 450, 457, 464, 471, 478, 485, 175, 188, 197, 215, 224, 237, 246, 261, 266, 277, 282, 291 and 296 provided

Notes. Continued.

the plate centreline pressure distribution.

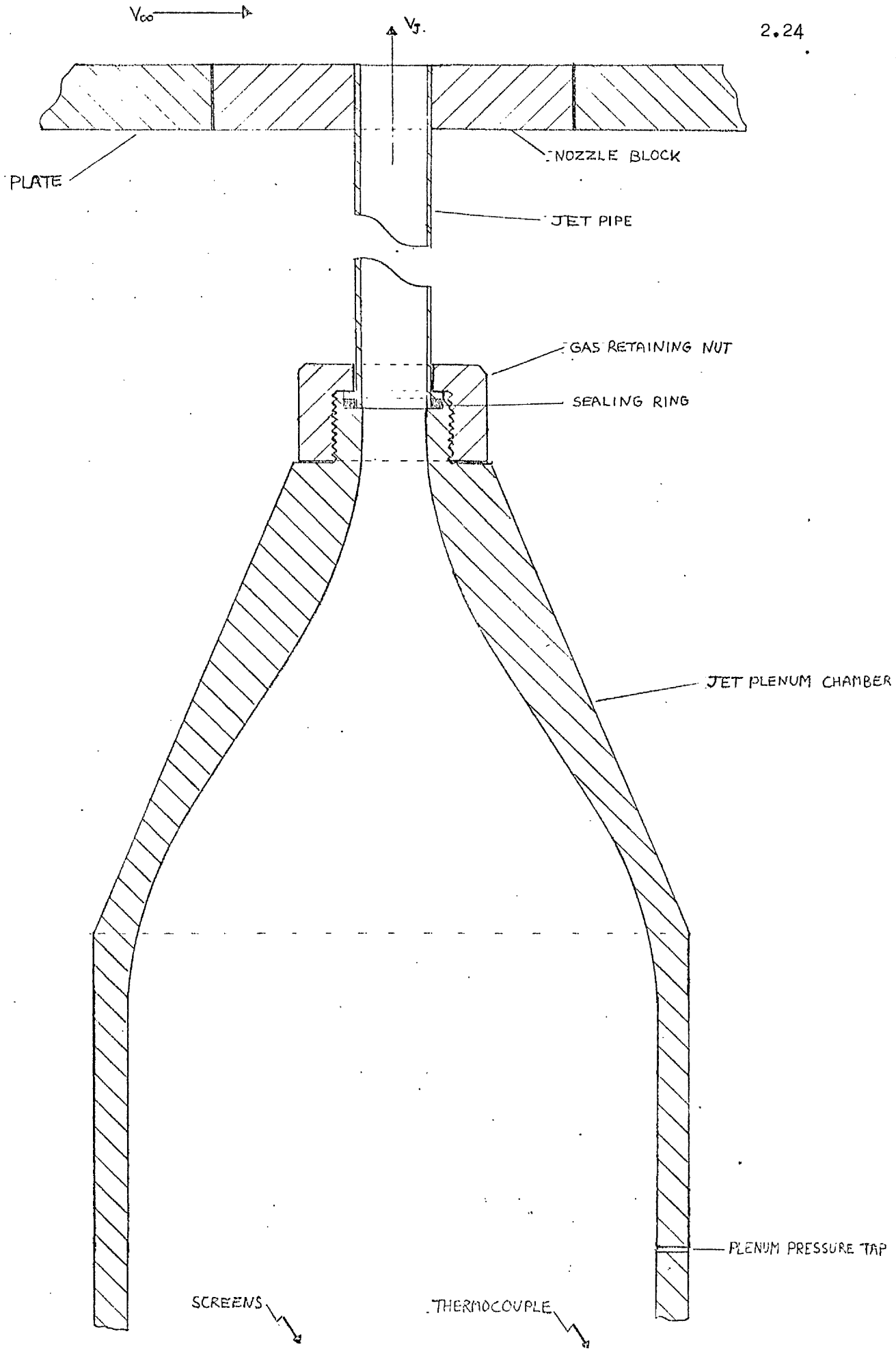

Figure 2.1. Cross-section of the Plenum Chamber and Nozzle Block.

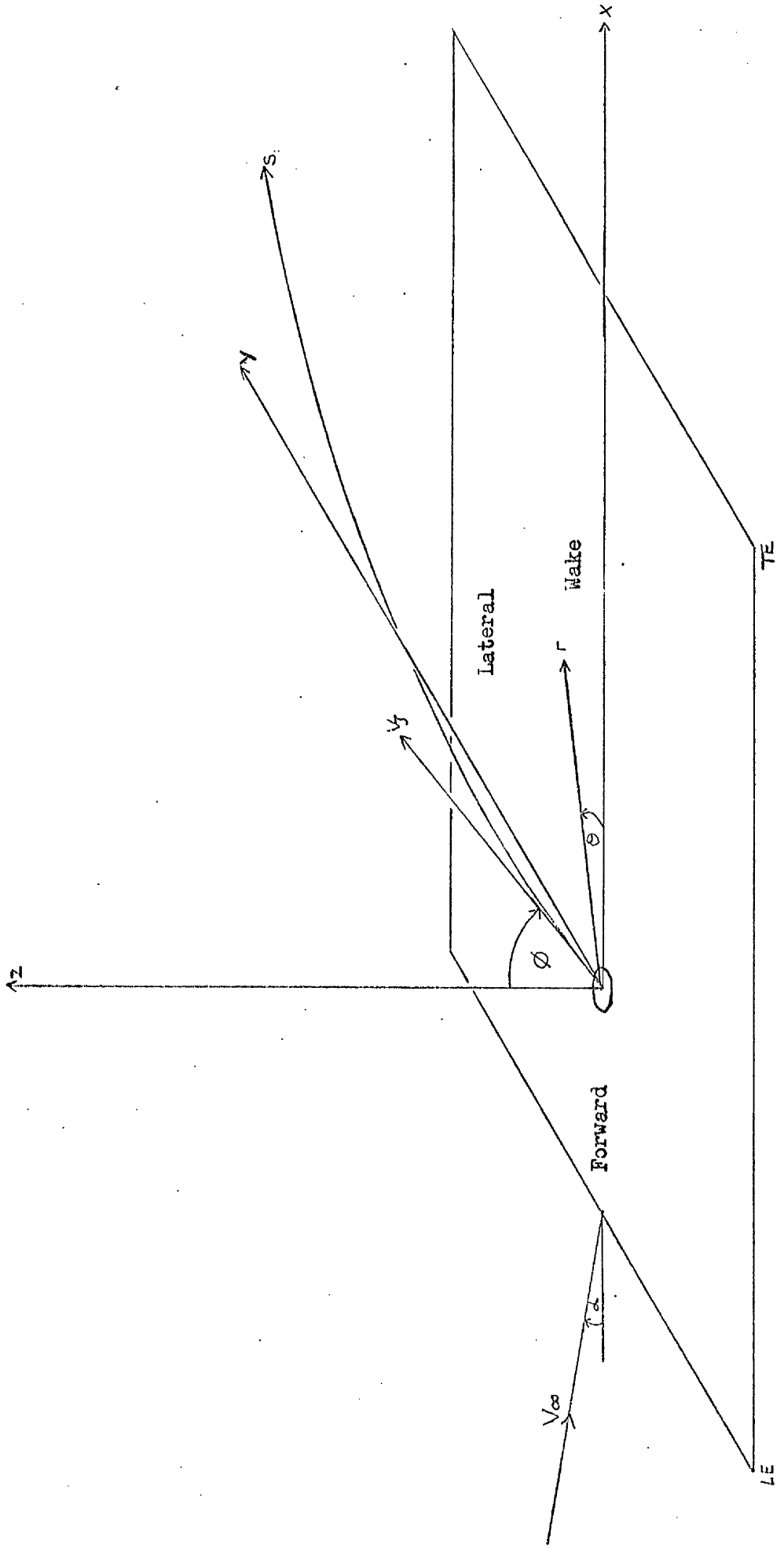

Figure 2.2. Definition of Axes and Flow Regions.

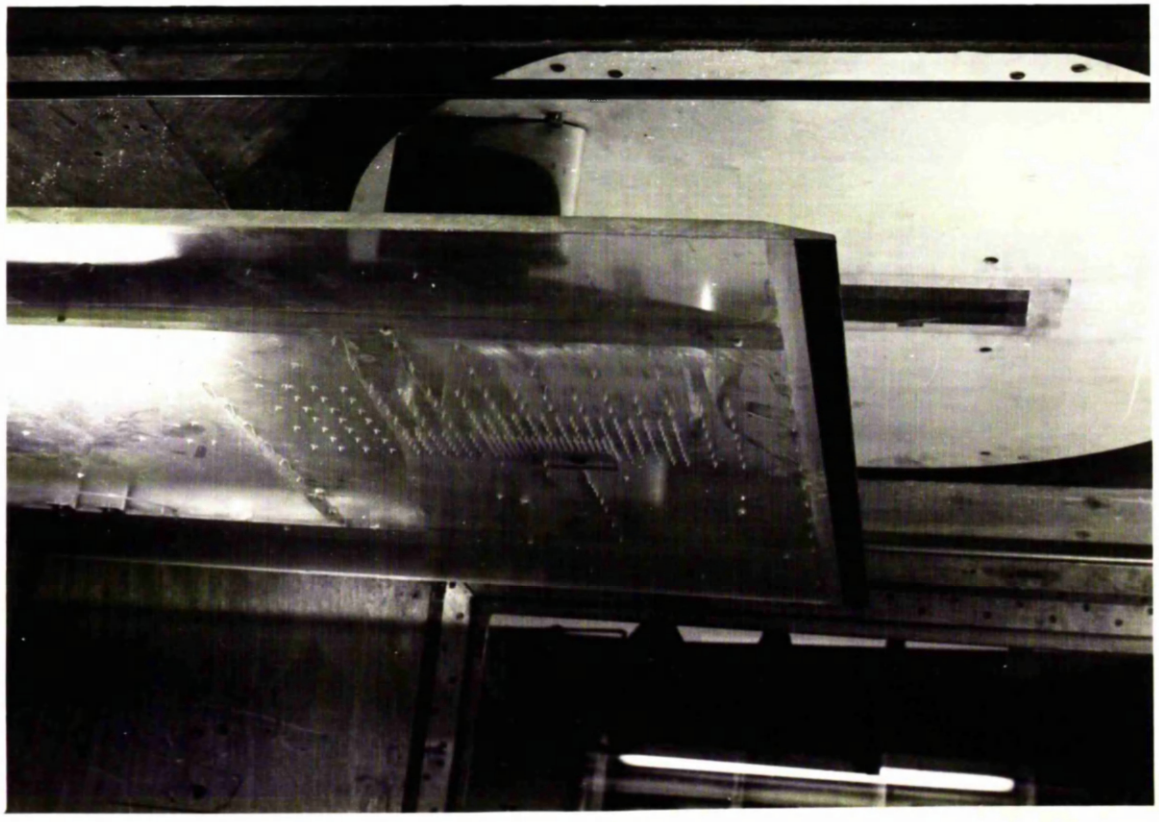

Plate 2.1. The plate mounted in the working section showing the positioning of the pressure taps and the nozzle block. The front leg and fairing are also visible.

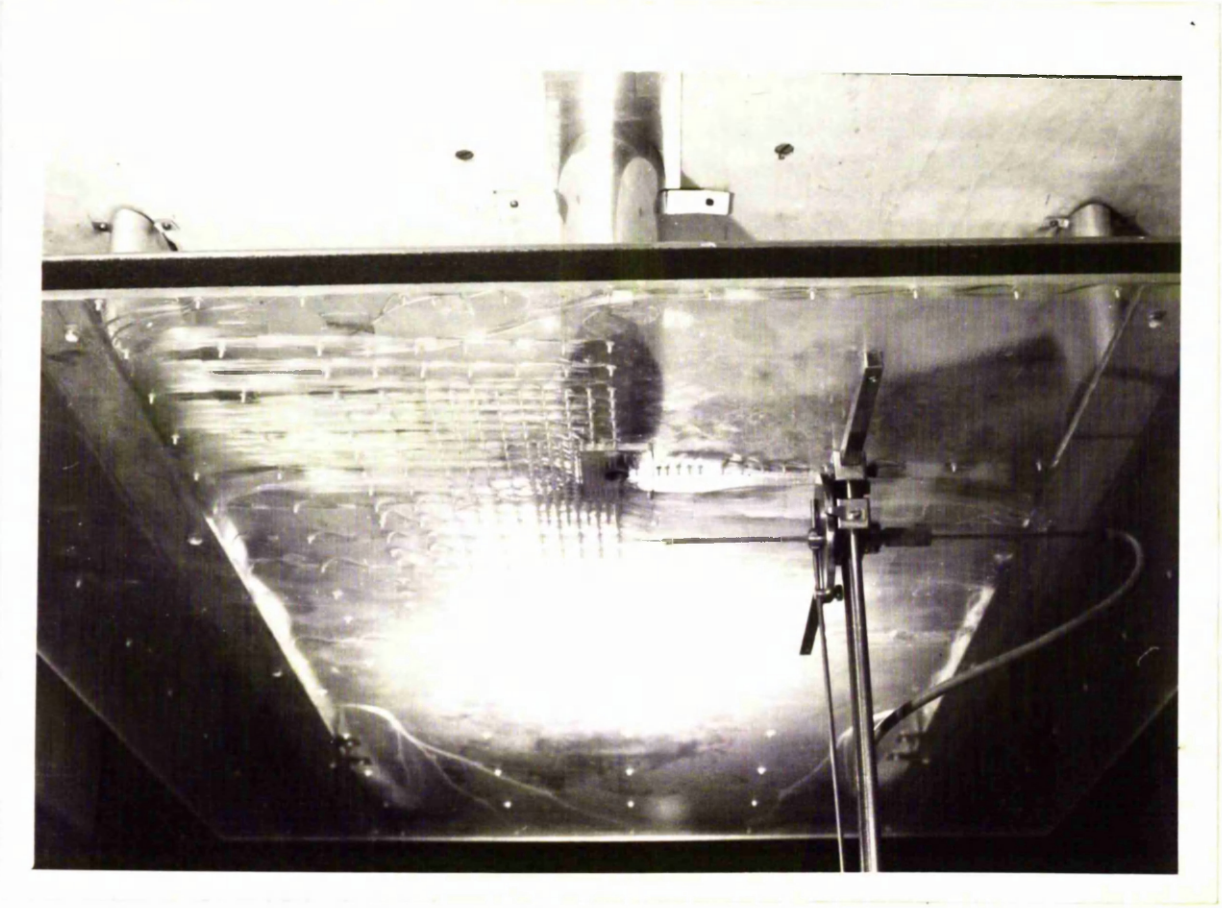

Plate 2.2. The plate mounted in the working section with the traversing mechanism and support rail in position. The jet pipe fairing is also visible.

Chapter III

Experimental method and Accuracy

3.1 Configuration.

The plate was adjusted to the required angle of incidence by lowering the rear legs. The nozzle block was inserted. The jet plenum chamber was rotated to the required angle, set by the clinometer, and clamped to the support plate. The support plate was moved along the roof of the tunnel and the jet chamber was offered up to the flanged end of the jet pipe (fig 2.1). Further adjustments were made to the plate supports until the jet pipe flange was located within the recess in the jet chamber. The plate was finally adjusted to the correct incidence and height. The nozzle block surface was now flush with the plate surface.

3.2 Test Conditions.

The required pressure difference (P_R-P_W) was taken from the corresponding calibration chart for the given configuration and for a dynamic pressure of 0.576 inch of water. This pressure difference was monitored on a water micromanometer and the wind tunnel speed brought up accordingly.

The atmospheric pressure was measured by a Fortin barometer and the value of P_{OE}-P_A was taken from the curve of P_{OE}-P_A versus P_A for the required velocity ratio. (see Appendix A). The pressure difference (P_S - P_A) in the jet plenum chamber was read from the calibration of P_{OE}-P_A versus P_S-P_A for the jet under consideration. This pressure difference was monitored by a Prandtl manometer.

The tunnel freestream dynamic pressure and the jet plenum pressure were constantly monitored. The change in mass flow rate after the jet plenum temperature had stabilised at ambient was negligible. The use of storage tanks for the jet air supply obviated the unwanted temperature

increase which would have arisen if the air was fed directly from a compressor.

3.3 Surface Pressures.

All data from the plate surface was measured on the multitube manometer inclined at 20 degrees to the horizontal. This data was stored on melinex sheets.

The first wind tunnel run was to determine the jet off pressure distribution on the plate surface. The second run was to determine the interference pressure distribution. The raw data had the form

$$(P_{\text{Jet on}} - P_A) - (P_{\text{Jet off}} - P_A)$$

and was inputted into a computer programme (Appendix B) which reduced the data, calculated the interference pressure contours, integrated the pressure distribution and plotted the contours, various selected pressure distributions and integrated distributions.

3.4 Jet Penetration.

The plate and nozzle block surfaces were covered with a self adhesive sheet. The traversing mechanism support rail was attached to the plate surface (see Plate 2.2). The mechanism was initially positioned on the rail such that the probe head was as close to the nozzle exit as possible. The lateral position of the probe was adjusted such that the probe head lay in the XZ plane which, from symmetrical considerations, was assumed to contain the jet centreline. A search was made to determine the X and Z co-ordinate, relative to the plate axes, at which the total pressure was a maximum. The traversing mechanism was then moved to the next position along the rail, a distance 2 jet radii downstream.

3.5 Accuracy.

The clinometer could be read to the nearest 0.5 of a minute. The Prandtl manometer and the Fortin barometer were accurate to $\pm$ 0.01 mm of

mercury. The calibration chart of dynamic pressure in the working section versus the pressure difference across the two pressure taps fitted to the tunnel wall ($p_R - p_W$) as mentioned in Section 2.1 could be read to $\pm$ 0.002 inch of water. The working section was calibrated with a standard pitot-static tube, the error involved being 0.5% of V_∞ or 1% of q_∞ (ref 39).

Static pressure taps introduce an error because of their finite size. Ref 40 suggests that the error is of the order of $\pm$ 0.005 q_∞. Turbulence also affects the accuracy of the mean static pressure measurement (ref 41). This reference suggests that the error is of the same order as that incurred by the finite diameter taps.

The response time was of the order of 60 secs. This was felt to be reasonable considering the physical restrictions involved because of the size of the pressure lines and taps. No fluctuation band of the readings was evident even in the wake region.

The order of accuracy of the multitube manometer was difficult to estimate. The distance along any tube was measured to the nearest 0.016 inch. However, the angle of tilt did introduce errors. Since the manometer was viewed from above, then the further the meniscus was from the eyes, the greater was the amount by which the pressure was underread. However, the pressure reading was greater the further away from the position of the eyes, so in all probability the percentage error introduced was virtually constant. In converting the pressures to inches of vertical height, these multitube manometer errors were reduced by a factor proportional to the size of the angle of tilt (in this case about 0.33).

Figures 3.1 to 3.3 show the effect on the surface pressure distribution and the surface force distribution (see introduction to Chapter IV) of the uncertainty in the multitube readings. These figures were

obtained by varying the readings by $\pm$ 0.016 inch either side of the recorded reading. The error band increases as $|C_p|$ decreases and as the distance from the jet increases. The error band is larger for the upstream surface pressures than those in the lateral or wake regions. The error band of the surface force distribution over an area of five jet radii is negligible. The corresponding changes in the suction force coefficient over an area of five and ten jet radii were $\mp$ 3% and $\mp$ 4.5% respectively and the changes in centre of pressure and pitching moment coefficient were $\mp$ 5.5% and $\mp$ 11% respectively (see introduction to Chapter IV for definitions).

No wind tunnel wall corrections were made in this work. It has been suggested that the parameter ma/h (where m is the velocity ratio, a is the jet radius and h is the clearance between the lower surface of the plate and the working section floor) can act as an appropriate wall effect criterion (ref 42). For a jet inclined at 8 degrees upstream (corresponding to a plate incidence of 8 degrees) a value of $ma/h \leq 0.4$ was required to prevent separation of the free-stream flow on the wind tunnel walls forward of the model. With a velocity ratio of 12 and a clearance of 105 jet radii (i.e. 105a) then ma/h = 0.11. Since this criterion is considered to be conservative it was assumed that adverse wall effects would be insignificant.

The calibration of the working section for the various model configurations jet off, was aimed at allowing for blockage effects incurred for the basic model. The only other blockage arises from the potential core of the jet and the separated region behind the jet. Using a one-dimensional approach, that is

$$\frac{V_{correct}}{V_{indicated}} = 1 + \xi \quad \text{where} \quad \xi = \frac{\text{frontal area of core and wake}}{\text{working section area - frontal area}}$$

with a very conservative estimate of the frontal area of the potential

core and separated region from ref 24, ε is of the order of 0.004.

The repeatability of readings from one test to the next was found to be within 0.08 of the C_p values. This was expressed as a mean relative error such that the repeatability was much better than this value nearer the jet where the magnitude of the readings was higher. Far away from the jet the error band of the readings was greater than the actual magnitude (for $|C_p| < 0.1$) so that the position of pressure contours of low magnitude was not reliable (see also fig 3.1). The repeatability in these regions was also bad. Figures 3.4 to 3.6 show a comparison of the pressure distribution and surface force distribution obtained from two separate tests under identical conditions. The symmetry was found to be within 0.04 of the C_p value (checked along the Y axis). Again this was expressed as a mean relative error and the above comments are applicable. Figure 4.89 shows a comparison of the surface pressure distribution obtained from this work with that of reference 14 and 20.

The total pressure reading fluctuation within the jet plume was of the order of 0.001 of the reading. The total head probe was insensitive to a rotation of $\pm$ 5 degrees within the plume and figure 3.7 shows a typical plot from which the plume centreline was determined. The uncertainty in determining the plume centreline increased with increasing distance from the nozzle exit as the total pressure decreased and was a maximum of $\pm$ 0.5 jet radii. The determination of the jet plume was repeatable from one test to another (see fig 3.8). During the freejet tests (Appendix A) the head of the probe when placed at the centre of the nozzle exit plane with a jet exit velocity of 600 feet per second, was found to be displaced by about 0.2 jet radii. The fluctuation in the jet chamber static pressure tap reading ($P_s - P_A$) was typically of the order of 0.005 of the reading.

Figure 4.102 shows a comparison of the jet plume measurements from this work with that of references 19,24,27 32 for a normal jet. A comparison of the inclined jet centreline with that of reference 28 is made in figure 4.56.

Figure 3.9 shows the effect of the vertical support and probe holder on the total pressure reading with the jet off. At a position within the XZ plane the effect of the mechanism was to reduce the total head by about 3%. However, the interference calibration was for a uniform and essentially incompressible flow. The effect on the probe reading of the mechanism in an incompressible region and the probe head within a compressible region of the flow field was not known. Reference 41 suggests that the compressibility effects of the total pressure reading would be negligible except when the Mach number was close to unity. As the compressible region of the flow was considered to be more dominant, it was assumed that the mechanism interference could be ignored.

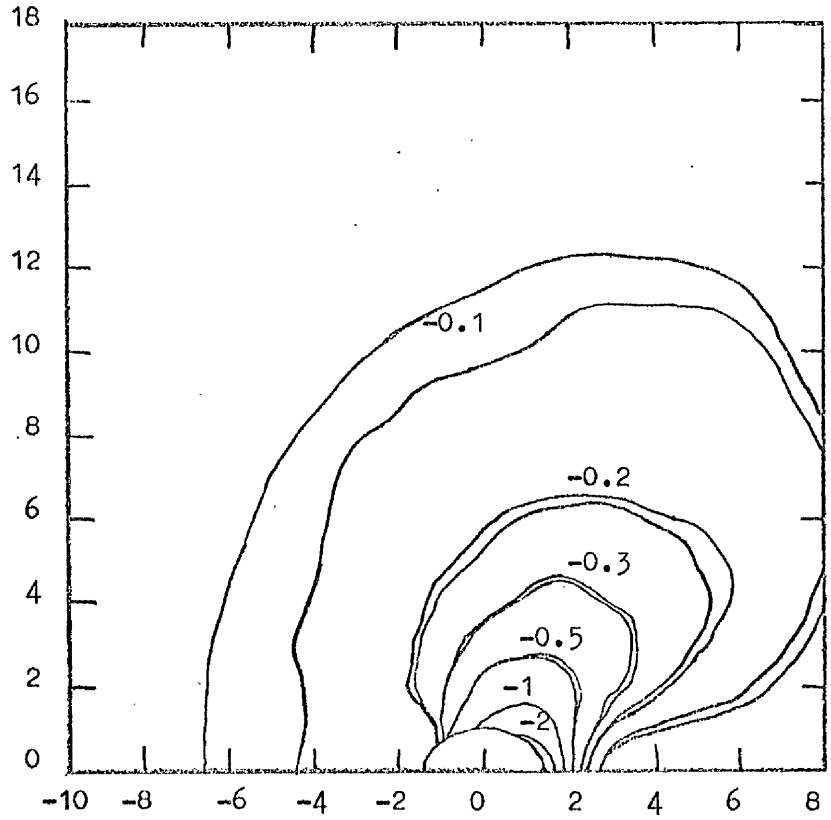

Figure 3.1. Surface Pressure Distribution Error Band (ϕ = 45°, α = 0°, m = 12).

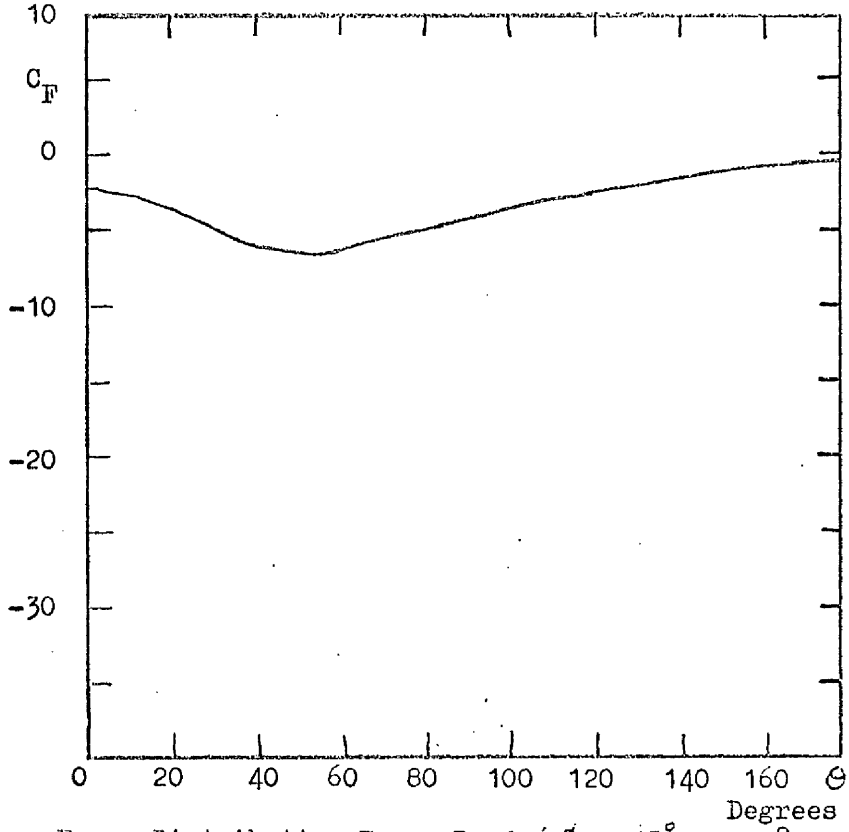

Figure 3.2. Surface Force Distribution Error Band (ϕ = 45°, α = 0°, m = 12, R_2 = 5).

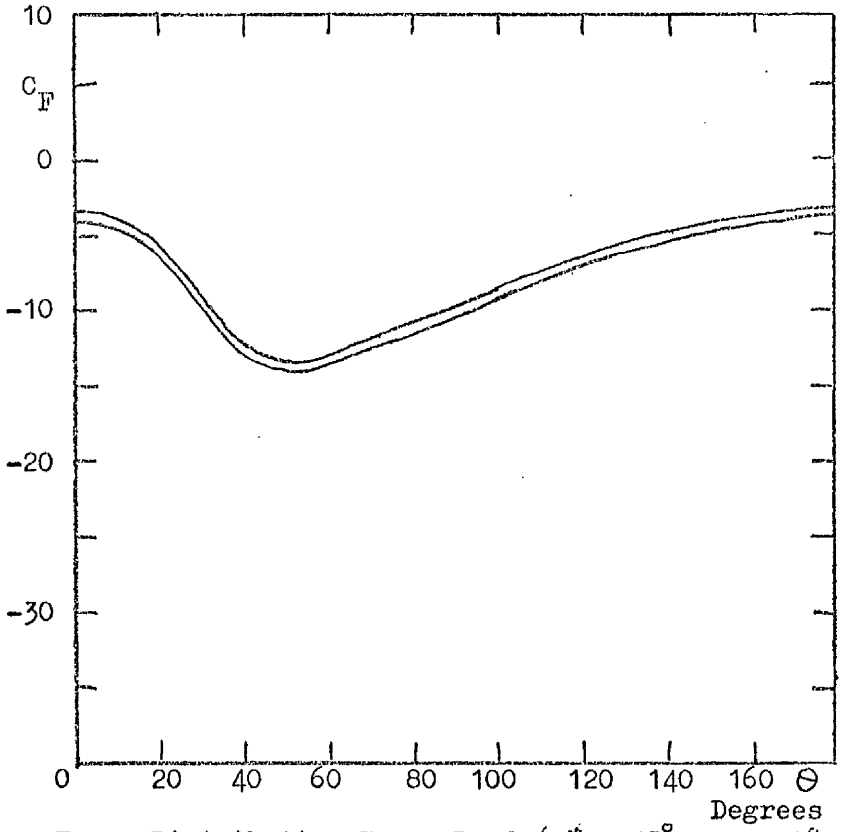

Figure 3.3. Surface Force Distribution Error Band ($\phi = 45°$, $\alpha = 0°$, $m = 12$, $R_2 = 10$).

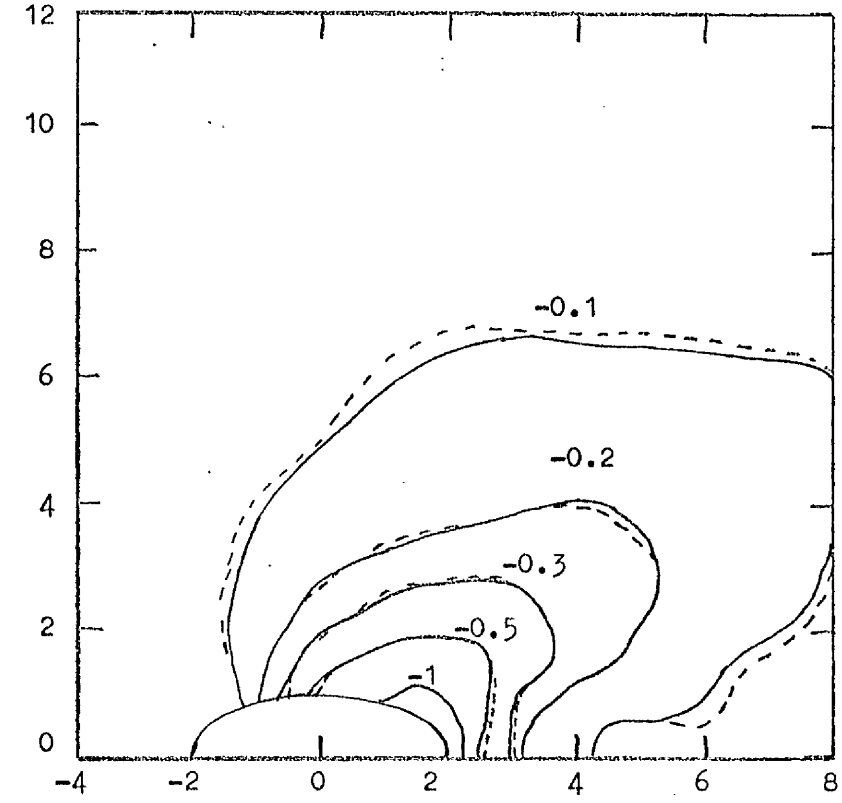

Figure 3.4. Surface Pressure Distribution Repeatibility ($\phi = 60°$, $\alpha = 0°$, $m = 8$).

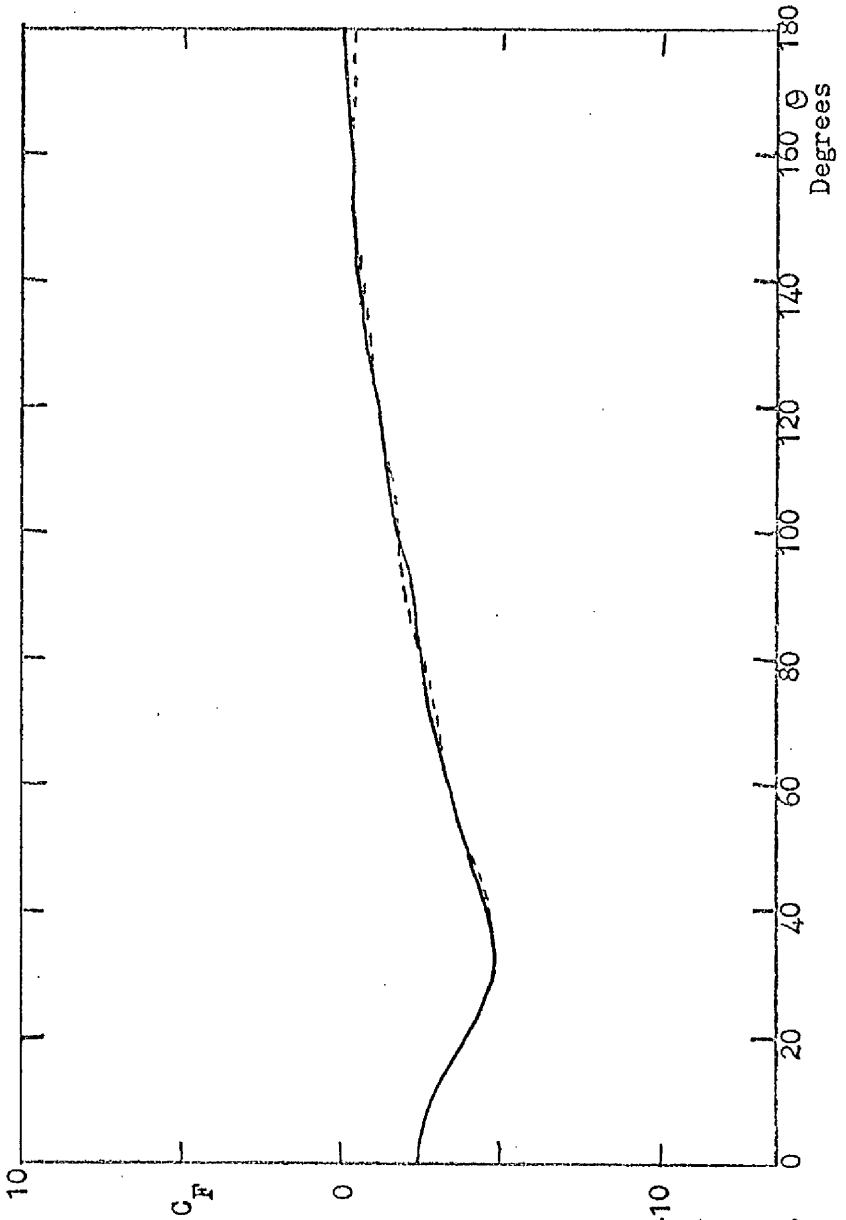

Figure 3.5. Surface Force Distribution Repeatibility ($\phi = 60^{\circ}$, $\alpha = 0^{\circ}$, $m = 8$, $R_2 = 5$).

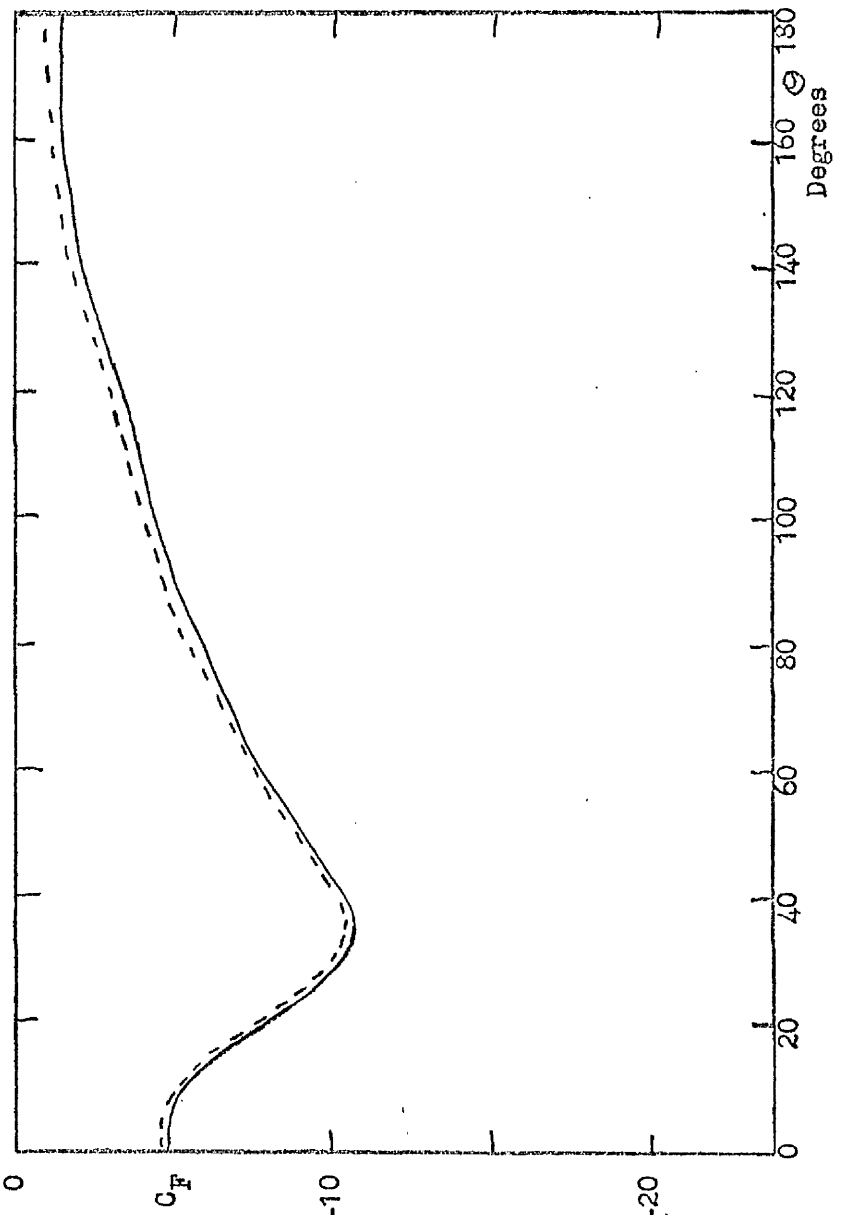

Figure 3.6. Surface Force Distribution Repeatibility ($\phi = 60^{\circ}$, $\alpha = 0^{\circ}$, $m = 8$, $R_2 = 10$).

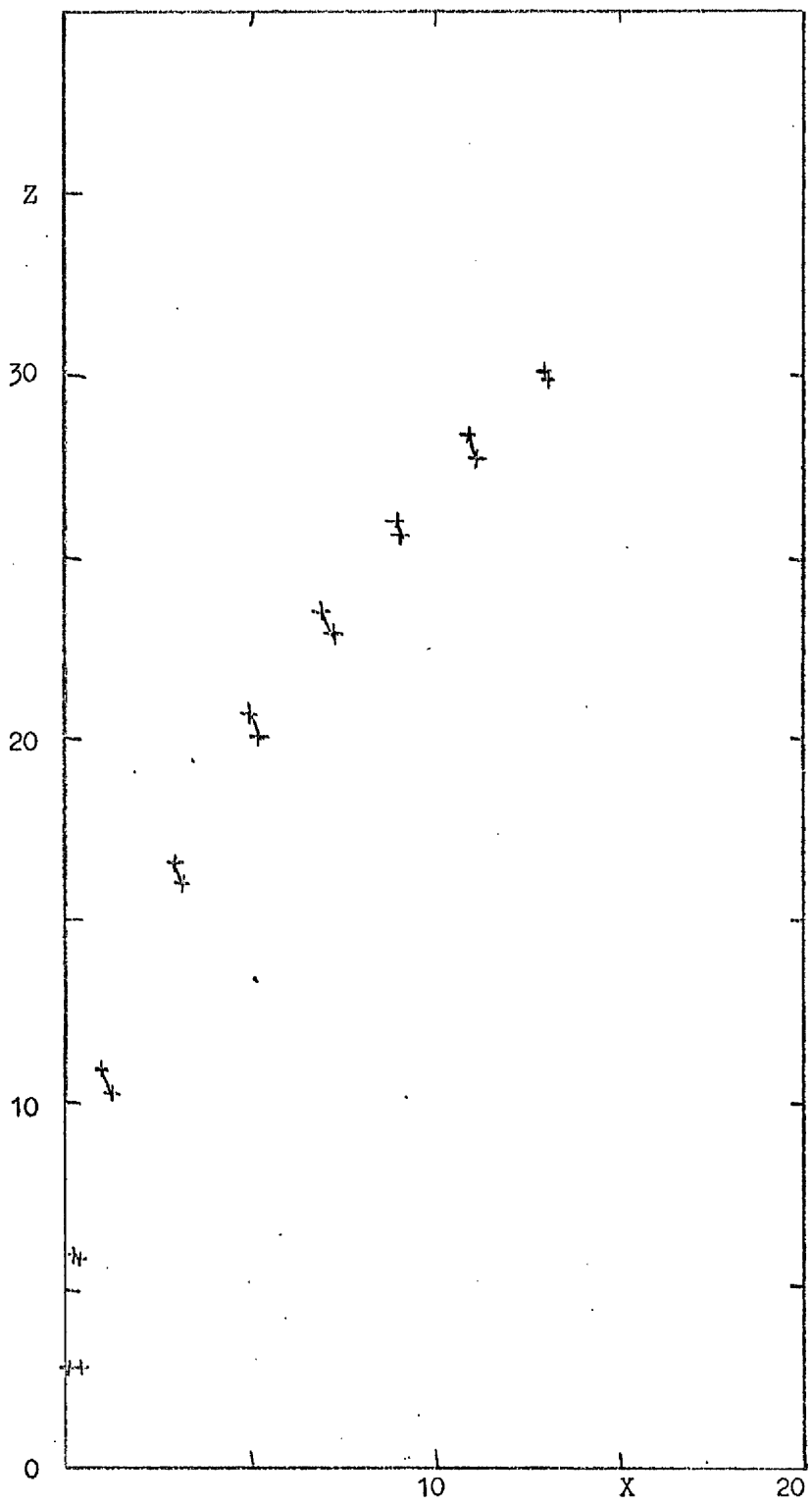

Figure 3.7. Total Pressure fluctuation in Jet Plume

($\phi = 0^{\circ}$, $\alpha = 2^{\circ}$, m = 12).

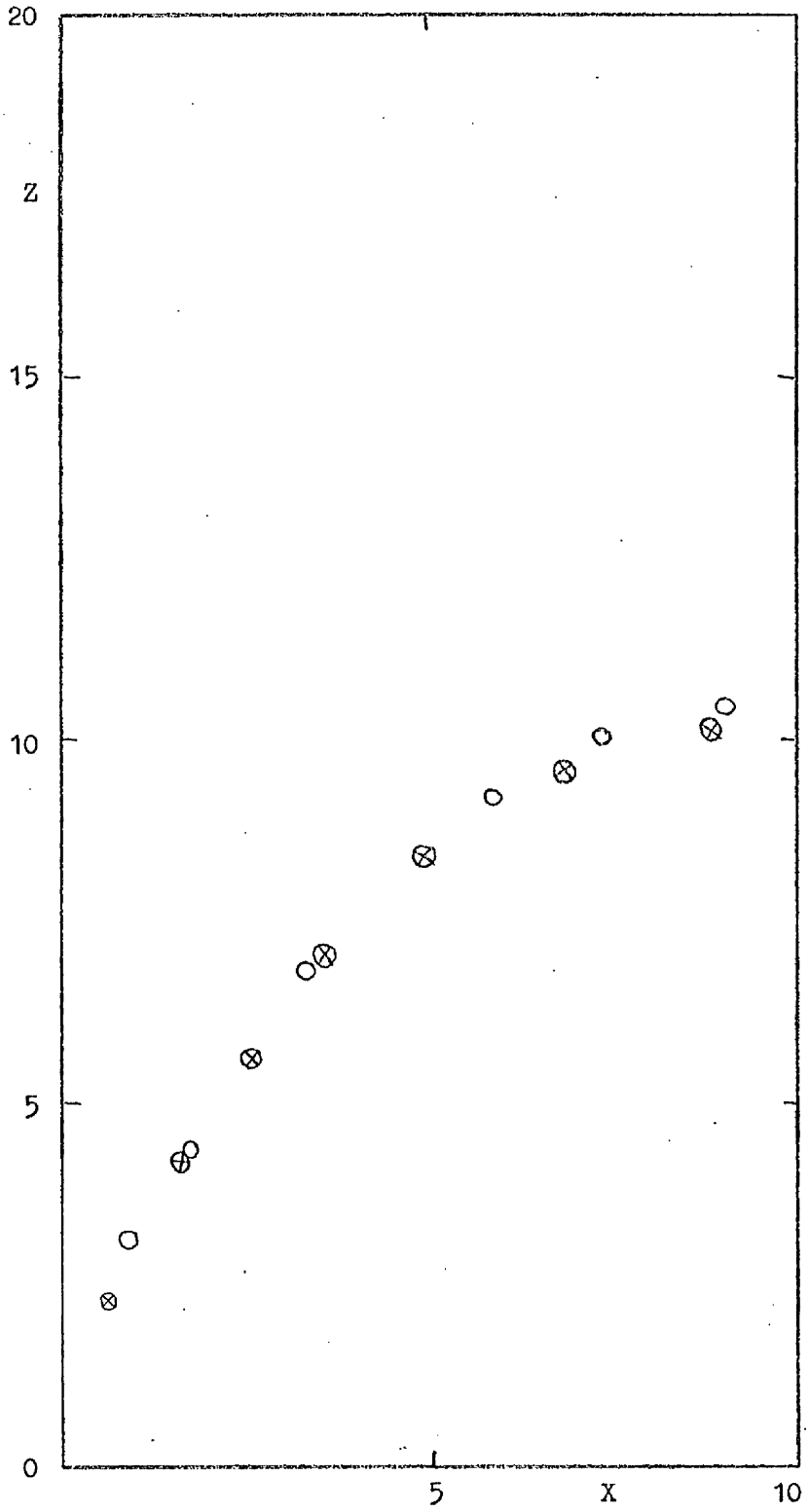

Figure 3.8. Repeatibility of the Jet Centreline ($\phi = 0^{\circ}$, $\alpha = 0^{\circ}$, m = 4).

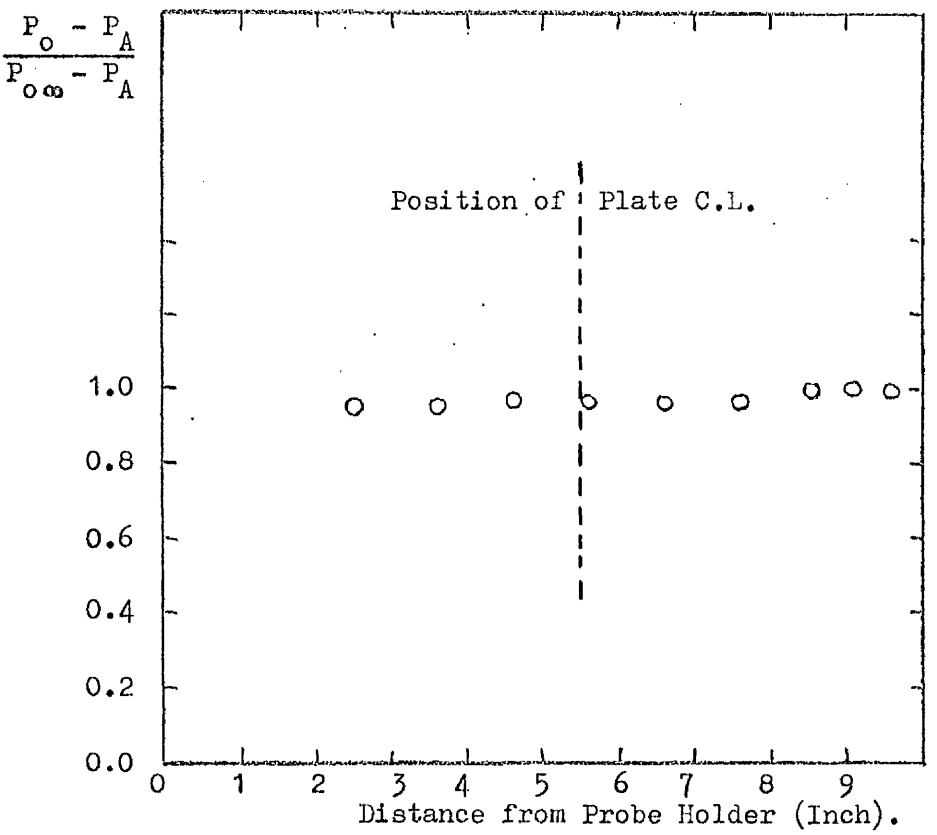

Figure 3.9. Effect of Traversing Mechanism on the Freestream Total Pressure.

Chapter IV
Results and Discussion

Table 4.1 summarises the collected data. The data was obtained for a systematic variation of each parameter (jet inclination ϕ, plate incidence α, velocity ratio, m) while the other parameters remained fixed. The surface force distribution, suction force coefficient and centre of pressure were derived from the surface pressure distribution. These quantities are defined below. The surface pressure distribution is presented in the form of isobar plots.

The surface force along a radial is denoted by C_F, where

$$C_F = \int_{R_1}^{R_2} C_p \, R \, dR$$

, where C_p is the interference pressure coefficient

R is the radial distance from the jet exit centre, non-dimensionalised with respect to the jet radius.

The lower limit of integration , R_1, represents the jet periphery and varies with the exit geometry, e.g for the normal jet, R_1 is unity. The upper limit of integration, R_2 was assigned two values, 5 and 10. Both R_1 and R_2 are non-dimensionalised with respect to the jet radius. The surface force distribution refers to the variation of C_F with increasing Θ, where Θ is the angular displacement in degrees from the positive X axis (see fig 2.2).

The suction force coefficient is denoted by C_s, where

$$C_s = \frac{-1}{\pi} \int_0^{2\pi} C_F \, d\Theta$$

$$= \frac{-2}{\pi} \int_0^{\pi} \int_{R_1}^{R_2} C_p \, R \, dR \, d\Theta$$

The upper limit of integration, R_2, was 10. The suction force can be thought of as the force obtained by integrating the surface pressure distribution over a circular area with a radius of 10 jet radii (but excluding the jet exit area) and a centre coinciding with the jet exit centre. The variation of the suction force coefficient with increasing velocity ratio for each angle of inclination and incidence is summarised in Figures 4.1 to 4.5. These curves can be crossplotted to give the variation of the suction force coefficient with angle of incidence or angle of inclination.

The centre of pressure is denoted by $\bar{X}$, where

$$\bar{X} = \frac{\int_0^{2\pi} \int_{R_1}^{15} C_p \, X \, R \, dR \, d\theta}{\int_0^{2\pi} \int_{R_1}^{15} C_p \, R \, dR \, d\theta}$$

, where X is the distance in the X direction ($X = R \cos \theta$).

The upper limit of integration, $R_2 = 15$, was chosen to include as large an area of the plate surface as possible. The lateral low pressure region extends well beyond $R_2 = 15$ at moderate velocity ratios. It was felt that, by using this value, a more accurate variation of the centre of pressure at higher velocity ratios could be obtained without incurring too large an error at low velocity ratios (see Section 4.1.2.3). A positive value of $\bar{X}$ can be thought of as representing nose up pitching and a negative value as nose down pitching. The variation of the centre of pressure with increasing velocity ratio for each configuration is summarised in Figures 4.6 to 4.10. These curves can be crossplotted to give the variation of the centre of pressure with inclination and incidence.

The pitching moment coefficient is denoted by C_M, where

$$C_M = \int_0^{2\pi} \int_{R1}^{15} C_p \, X \, R \, dR \, d\theta.$$

The variation of pitching moment coefficient with the suction force coefficient (integrated over a circular area of radius 15 jet radii) is summarised in Figures 4.11 to 4.15. These curves can be thought of as the pitching moment coefficient versus lift coefficient variation.

The jet trajectories for each configuration are summarised in Figures 4.16 to 4.34. These curves can be crossplotted to show the variation of each trajectory with one independent parameter while the others remain constant. It should be noted that body axes were employed throughout this work. The jet trajectories are plotted with respect to the plate axes (defined in fig 2.2). The advantage of using these axes is that the relative deflection of the jet centre-line is more discernible.

In the following discussion the effect of increasing the angle of inclination, ϕ (section 4.1), increasing the angle of incidence, α (section 4.2) and increasing the velocity ratio, m (section 4.3) on the surface pressure distribution, surface force distribution, suction force coefficient and jet trajectory is considered. Figures 4.1 to 4.34 will be discussed in section 4.3

4.1 Effect of Increasing the Angle of Inclination, ϕ (Figures 4.35 to 4.37)

4.1.1 Surface Pressures.

4.1.1.1 Forward and Lateral Regions.

The isobar plots (fig 4.35 to 4.39 which are drawn for an incidence of zero and velocity ratio of 12) are considered first. The extent of the low pressure field to the side of the jet was reduced as the inclination increased. At the higher velocity ratios ($m > 6$), the extent of the low pressure field upstream of the jet was diminished.

At low velocity ratios ($m \leq 6$), little change was observed upstream. As the angle of inclination is increased the jet exit geometry in the plane of the plate changes. The exit dimension in the positive and negative X direction is increased and the position of any surface pressure contour (eg -2 contour) very close to the jet is changed accordingly. This occurence is localised because of the close proximity of the jet and caused little effect on the other derived quantities. The upstream centreline surface pressure distribution (fig 4.40 for $\alpha = 0^{\circ}$, $m = 12$) suggested that the flow decelerated less immediately upstream of the jet as the inclination was increased. If a stagnation point actually existed at the higher angles of inclination then it was certainly very local. It seems probable that the layers of fluid immediately above the plate surface were given a vertical component of velocity by the entrainment effect of the jet. As the inclination increased, the fluid particles retained more of their horizontal component of velocity and the induced vertical component was reduced. The deceleration of the free-stream was lessened, i.e. the blockage effect was reduced.

A comparison between the results of this work and those of Reference 19 was made in Figure 4.41 (for $\emptyset = 30^{\circ}$, $m = 8$, $\alpha = 0^{\circ}$). The qualitative agreement was reasonable. The quantitative agreement improved closer to the jet. The discrepancies were probably due to the different laboratory conditions (see Section 1.1.2 and 1.2). The data from Reference 19 appeared to have a higher effective velocity ratio than that of this work as was indicated by the more extensive low pressure field. This is the only other existing data for inclined jets.

The overall effect was an apparent movement downstream of the low pressure field as the inclination increased.

4.1.1.2 Wake Region

Allowing for the above mentioned geometry effect, the surface

pressure contours on the wake centreline have moved little with a change of inclination. Further to the sides of the wake region, because of the apparent downstream movement of the lateral low pressure field, the angle between the wake centreline and the wake contours was decreased. The low pressures occupied more of the wake region for large values of inclination. The wake and lateral region changes gave the low pressure field a 'swept back lobe' appearance (see fig 4.35 to 4.39). This characterised the effect of increasing inclination.

There was a significant change in the downstream centreline surface pressure distribution (fig 4.42) as the inclination increased. In the case of the normal jet, there was a steadily decreasing rate of pressure recovery. Initially, the rate of recovery was rapid in the close proximity of the jet but moderated with distance away from the jet. For an angle of inclination of 30 degrees and more, the initial pressure recovery rate was very rapid followed by a pressure loss in the region $3 < X < 6$ and a further pressure recovery at a more gradual rate for $X > 6$. At low velocity ratios ($m = 4$), the pressure did in fact become positive for $X > 6$ before suffering a gradual pressure loss (fig 4.90 for $\phi = 45^{\circ}$, $\alpha = 2^{\circ}$). Generally, in the close proximity of the jet, the pressures were lower for a lower angle of inclination. For $X > 6$, there was little observed change in pressure. The position of the occurrence of the pressure loss (except for low velocity ratios) appears to have coincided with the transition from the potential core to the curvilinear region (see fig 1.1 for definition of regions of jet flow). The jet is closer to the plate surface as the inclination increases. This observed effect is probably caused by the stronger interaction of the vorticity entrainment and plate boundary layer. It is expected that there would be an increasing rate of entrainment of the boundary layer especially close to the rear of the jet. The results tend to confirm this.

4.1.2 Integrated Effects

4.1.2.1 Surface Forces (Fig 4.43 - 4.52 for m = 12, $\alpha = 0^\circ$)

The most significant observation from the surface force distribution was that the position at which the minimum surface force occurred, θ_m (the angular displacement), decreased as the inclination increased. This effect was more noticeable for an inclination greater than 15 degrees. The minimum surface force, C_{Fm}, increased (i.e. became less negative), e.g. for $\alpha = 0^\circ$, m = 12, C_{Fm} changed from about -18 to -12 (R_L=10) while θ_m changed from 90° to 30° as $\emptyset$ increased. The negative surface force contribution from the wake increased while that from the forward and lateral region decreased. This was expected from the surface pressure changes.

Care must be exercised in the interpretation of the surface force distribution. The integral C_F contains the product of C_p and R. A particular ordinate could have the same value if composed of a small value of R and a large value of C_p or a large value of R and a small value of C_p.

The surface force distribution for $\emptyset$ of 0° and 15° (fig 4.43 and 44) indicated that θ_m has decreased but C_{Fm} has changed little. The increase in the negative surface force contribution from the wake region was balanced by the decrease in the lateral and forward regions. This suggested that the overall effect of a moderate deviation about the normal was small.

There were no discontinuities in the curves and the gradient at $\theta = 0^\circ$ and 180° was zero verifying the assumption that the flowfield was symmetrical about the plate centreline. The major change occurring was that the region bounded by $\theta = 0^\circ$ and 50° contributed more to the surface force distribution while the region bounded by $\theta = 60^\circ$ to 170° contributed less as the inclination increased.

The effect of varying the integration limits can be observed by comparing figs 4.43 and 4.48, 4.44 and 4.49 etc. At $\theta = 0^\circ$ and 180°, the magnitude of C_F increases as the upper limit increases. The magnitude of C_{Fm} increases and the rate of change of C_F with θ increases.

4.1.2.2 Suction Force Coefficient, C_s

The curves illustrating the variation of C_s with ϕ, at the higher velocity ratios, show that C_s decreases with increasing ϕ throughout the range of investigation (fig 4.53). At a lower ratio ($m \leq 6$), C_s changes very little over the range 0° to 15°. C_s decreases as ϕ increases beyond 15°. There appears to be an asymptotic value as ϕ approaches 90°. This is expected. A value of 90° represents the case of a propulsive jet exhausting close to, or along a horizontal surface, the only type of entrainment being that of the free jet type, vortex entrainment being zero. As the velocity ratio increases, the curves become more bunched especially at low inclination angles and do not diverge until ϕ is greater than 30°.

A practical point arises from these curves. In general C_s decreases as ϕ increases. If it is desirable to maintain a constant vertical component of thrust, the velocity ratio would have to be increased initially as the inclination is increased. In fact, the jet velocity ratio is increased proportionally to $\sqrt{\sec\phi}$. The resulting lift loss incurred from this configuration change can be less than that incurred for the corresponding lower inclination case. (e.g. by going from $m = 4$ at $\phi = 0^\circ$ to $m = 6$ at $\phi = 60^\circ$). Fig 4.53 indicates that the lift loss can be reduced by applying as much inclination as soon as possible. The additional horizontal component of velocity will create some wing borne lift reducing the need for the given level of vertical thrust. The inclined jet induces a more extensive low pressure field in the wake region. Placing the jet to the rear of the surface will reduce

the lift loss.

The suction force coefficient variation with $\not\phi$, establishes the angle of inclination as a primary parameter.

4.1.2.3 Centre of Pressure, $\bar{X}$

The most significant observation from the curves describing the variation of $\bar{X}$ with $\not\phi$ was the increase in $\bar{X}$ as $\not\phi$ increased (see fig. 4.54). Generally, an increase in $\not\phi$ did not change the sign of $\bar{X}$. A change of sign was caused by a change of velocity ratio. It is conceivable that a curve of velocity ratio between 6 and 8 could experience a sign change as the inclination increased.

The curves suggest that the lower the velocity ratio ($m \leq 6$) the more rapid the increase in the centre of pressure as $\not\phi$ increased. This could cause handling problems near to the transition to wing borne flight where the trim required is expected to be excessive. The curves show the increasing extent of the induced low pressure field within the wake.

Considerable scatter of data was evident. This arises from the value of the upper limit of integration and the above mentioned error in C_F. The further away from the jet the greater is the relative error of the pressure readings. This effect is worse for lower velocity ratios where a greater part of the pressure field under consideration consists of pressures having magnitudes little different from zero. These large relative errors are then multiplied by a large value of R (for a large distance from the jet) to form the ordinates required to evaluate C_F.

4.1.3 Jet Trajectories

The penetration decreased and the deflection decreased as the inclination increased (see fig 4.55 and 4.56). The trajectories were deflected less in the initial region from their initial inclination as $\not\phi$ increased. At lower velocity ratios ($m \leq 8$, fig 4.56) the 15° and

0^{o} curves converged downstream. This observation was also noted in ref 28. Data at the limit of experimentally determined trajectories exhibited a degree of scatter. As the jet asymptotically approached the undisturbed freestream direction, the total pressure excess decreased making it difficult to determine the centreline accurately. This situation worsened as the inclination decreased. The total pressure decay curves, presented as P_T/P_E versus S, where

$\frac{P_T}{P_E} = \frac{P_0 - P_A}{P_{OE} - P_A}$, P_0 is the total pressure at the point, P_{OE} is the total pressure at the jet exit and S is the distance along the jet centreline non-dimensionalised with respect to the jet radius.

indicated that the potential core length increased as the inclination increased reaching a maximum for the 60° jet (see Fig 4.57 drawn for m = 12, $\alpha = 0^{\circ}$). The curves also suggested that the decay rate was less as the inclination increased. Data for P_T/P_E small, exhibited scatter as mentioned above. The scatter of points for P_T / P_E of about unity arose because of the difficulty in determining the centreline within the potential core.

Comparisons with the results of ref 28 (fig 4.56 for $\alpha = 0^{\circ}$, m = 8) revealed considerable discrepancies as did the comparisons for the normal jet with other work (sect 4.3.3). The problem of comparing centreline data was the different definitions used by various authors. For instance, Patrick (ref 30) determined the centreline from a concentration profile, a velocity profile and Schlieren photographs. Keffer and Platten (ref 28) utilised the velocity profile measured with a hot wire. Jordinson (ref 24) and Mosher (ref 18) used the locus of maximum total head (as does this work) while water vapour flow visualisation was employed by Margason (ref 32). The test conditions were also variable. Patrick exhausted a normal jet through the wind tunnel floor

into a section varying from 91½ x 30½ to 282 x 94 jet radii. Keffer and Platten exhausted jets at various inclinations through a circular plate of 96 jet radii diameter mounted above the wind tunnel floor into a section 384 x 768 jet radii. Jordinson employed a plate mounted above the tunnel floor and a section of 240 x 48 and 120 x 24 jet radii while Margason suspended the jet in the wind tunnel and exhausted it into a section of 168 x 240 jet radii. It is very doubtful whether some of these sections allowed for adequate lateral spread of the jet or prevented impingement at the higher velocity ratios.

Orifices, tubes and nozzles have been employed all with differing exit profiles. The profiles of all the jets in this work were very uniform (see Appendix A). The less uniform the profiles, the more severe the initial deflection as noted in section 1.2. This does not appear to be the reason for the discrepancy. Repeat experiments were performed for the normal jet (see sect 4.3.3) at a lower freestream turbulence level (0.7%). These results compared well with those of previous works. It seems logical to argue that an increase in turbulence level of the freestream increases the deflection rate of the jet, i.e. the entrainment rate is augmented and the penetration is diminished. This suggests that the vorticity entrainment in the curvilinear region is augmented by the interaction of the jet and a turbulent freestream. This requires further investigation. The effect of this phenomenon on the surface pressures for the normal jet appears to be secondary (fig 4.89 and sect 4.3.3).

4.1.4 Interpretation.

The above observations indicate a lowering of the entrainment rate as inclination increases. The jet deflects less (fig 4.55) until, at $\phi = 60^{0}$, trajectory has hardly been deflected from its initial inclination. The total pressure decay rate at 60^{0} is lower than that

of the other jets (fig 4.57). Deflection and total pressure decay are synonymous with entrainment. It is logical to conclude that the primary effect of increasing inclination is a reduction in the entrainment characteristic of the jet.

It was stated in the introduction that a counter rotating vortex pair is produced in the flow because of the large shearing stream acting on the jet sides. For a normal jet, or one whose inclination differs little from the normal, this production of vorticity would be most pronounced in the initial stages where the uniform stream component normal to the jet is a maximum.

The increase in entrainment rate with velocity ratio is not proportional to that of momentum flux. This flux is transformed by the uniform stream flux at a lower rate and the deflection of the trajectory is less. The potential core is extended. The profile may be expected to be relatively unchanged since, generally, the potential core is not greatly deflected by the pressure field. The trajectories demonstrate that there is an initial portion which is almost linear. The linearity is most evident as the inclination increases, where freejet and vortex shear type entrainment are a minimum. This would account for the observed character change in the surface pressure field between $\phi = 15^{o}$ and 30^{o}. The total pressure decay curves indicate that the decay rates of $\phi = 15^{o}$ and 0^{o} are similar. For inclinations greater than $\phi = 15^{o}$, the decay rate is lower. This behaviour of the initial profiles indicates the importance of vorticity entrainment.

The freejet entrainment is expected to increase as the inclination is directed upstream (i.e. for negative values of ϕ, see ref 28) because the parallel freestream component is augmented. The deflection rate of the trajectory is a measure of the total entrainment rate and the profiles suggest that the vorticity entrainment in the initial

region is a minimum at $\phi = 60^{\circ}$ (and zero at 90° where the entrainment mechanism is completely freejet and no deflection occurs) and a maximum at zero. This would be consistent with the fact that the normal jet experiences a maximum crossflow shearing component for the greatest distance along the initial centreline.

Comparison of the flow exhausted normally with that at $\phi = 30^{\circ}$ and 60° suggests that the generation of vorticity is more intense for the normal jet (see also ref 28). Naturally, the greatest cross-stream shear occurs and the vortex shear entrainment should be a maximum for this configuration. The normal jet trajectory is expected to demonstrate the maximum rate of approach to the horizontal where this type of entrainment predominates. The results tend to confirm this.

4.2 Effect of Increasing the Angle of Incidence, (Figs 4.58 to 4.82.)

4.2.1 Surface Pressures (Figs 4.58-4.62 drawn for $\phi = 15^{\circ}$ and $m = 8$)

4.2.1.1 Forward and Lateral Regions

It was difficult to draw any specific conclusions from the data collected. It was apparent that the effect of a variation in the angle of incidence was of secondary importance because most of the observed pressure changes were at best only just outwith the error band of the readings. The lower pressures close to the jet were least affected. These were slightly more extensive to the front and sides of the jet. The higher pressures (contours -.5 to -.1) experienced a greater change but it must be remembered that the lower the magnitude of the pressure and the greater its distance from the jet then the greater is the shift in the contour due to the uncertainty in the pressure readings. These higher pressures were more extensive to the sides and front (see Fig 4.58-4.62). The upstream centreline pressure distribution indicated little change with increasing incidence (Fig 4.63).

A comparison of the interference surface pressure contours on

the flat plate of this work was made with the corresponding contours on the lower surface of a wing (see Fig 4.64 - 4.67), these being the only existing data illustrating the effect of incidence change (ref 22). The qualitative agreement at m= 8, α = 0° and 6° was reasonable. The quantitative agreement was poor. The wing contours were less extensive to the front of the jet but more to the side (except -.1 contour). Closer to the jet, the agreement between corresponding contours improved. The pressure in the wake recovered more rapidly for the flat plate. The comparison at m = 4, α = 0° and 6° revealed large dissimilarities. The low pressure field was far more extensive to the sides and rear of the jet of the wing. Immediately upstream of the jet, a significant spreading of the positive pressure field on the wing was evident. This spreading was localised on the flat plate to the immediate area upstream of the jet. This frontal pressure region on the wing has no counterpart on the flat plate (ref 11). It would be expected that the surface pressure distribution of the two cases would become similar as the velocity ratio increases. The jet/crossflow interference would become predominant. At high velocity ratios, the flat plate should be a reasonable representation of the lifting case. In the lifting case, the surface pressure changes with increasing incidence were more noticeable. The contours were less extensive to the sides with little change upstream. In the wake region, the contours moved closer to the jet. The wakes in the two cases bear little resemblance to each other. These changes disagreed with those of the flat plate.

There was one source of error in the wing data which would affect the interference pressures on the wing to a greater extent than those on the plate. The jet exit dynamic pressure was determined by assuming that the jet exit static pressure was the freestream static value, which in turn was the ambient. The technique employed (identical to that of

this work) in obtaining the required stagnation pressure always resulted (regardless of angle of incidence) in the same value for the plenum chamber stagnation pressure because this was referenced to the freestream static value. The static pressure at jet exit was increased by the wing/freestream interaction as α increased (symmetrical wing) causing a lower jet exit dynamic pressure and an effective velocity ratio decrease. The flat plate/freestream interaction caused a much smaller increase in the static value at exit. No allowance was made in either work for this effect which was considered to be of secondary importance. The collected data indicated that the effect of a change of incidence was secondary and this could explain the discrepancy between the results of the wing and the flat plate.

4.2.1.2 Wake Region

The surface pressure distribution within the wake was not greatly modified by an increase in incidence. As the contours in the lateral region spread, the angle between the contours and the wake centreline was decreased. The downstream centreline pressure distribution indicated a lowering of pressures immediately to the rear of the jet. The pressure recovery was more rapid for the higher incidence cases (fig 4.68). The effect of varying the incidence appeared to have little significance in the wake region.

4.2.2 Integrated Effects

4.2.2.1 Surface Forces (Fig 4.69-4.78 drawn for $\beta = 15^\circ$, $m = 8$)

There were no significant changes in the surface force distribution. The value of the minimum surface force, C_{F_m}, decreased as incidence increased from 0° to about 4° and then increased for α greater than 6°. The surface force at the centrelines ($\Theta = 0^\circ$ and 180°) showed very little, if any change. The position of the minimum surface force, Θ_m, appeared to remain constant. The gradient ($d C_F / d\Theta$) was

zero at the centrelines and no discontinuities occurred. These observations were anticipated from the above consideration of the surface pressures.

4.2.2.2 Suction Force Coefficient, C_s

The suction force coefficient, C_s, reached a maximum at an incidence of between 4^0 and 6^0 and then decreased (see fig 4.79, where the maximum occurred at 6^0). The curves became more bunched as the velocity ratio increased. The change in C_s with α was not as significant as that with ϕ as can be seen from figs 4.80 and 4.1. No data existed for the variation of the integrated suction force coefficient with incidence. The gross aerodynamic forces for the wing were measured in ref 22 but because of the above mentioned discrepancies no comparison was made.

4.2.2.3 Centre of Pressure, $\bar{X}$

The centre of pressure appeared to be independent of incidence (fig 4.81). The effects of a velocity ratio change or an inclination change were far greater (see figs 4.6 and 4.54). These results tend to confirm that the importance of incidence changes was secondary.

4.2.3 Jet Trajectories.

The results for the normal jet (fig 4.82) showed that the $\alpha = 4^0$ and 8^0 cases suffered a greater initial deflection than the normal jet at zero incidence. In fact, the $\alpha = 4^0$ case appeared to have suffered the maximum deflection in its initial region. For inclinations greater than zero, the trajectories at higher incidence tended to suffer a greater deflection in their initial regions than those at lower incidences. It must be remembered that the axes employed in the trajectory measurements were body axes. The advantage was that the rates of deflection of the various trajectories can be more easily compared. No other data existed for jet trajectories from a plate at incidence

so comparison with other work was not possible.

4.2.4 Interpretation

The results obtained can be explained by an effective change in inclination of the jet. Increasing incidence decreases the angle of inclination of the jet to the freestream direction. As mentioned in the section concerning the effects of varying jet inclination, increasing the angle of inclination decreases the freejet and vortex entrainment. In other words, as the effective jet inclination is decreased by an increase in incidence the freejet and vortex entrainment increase. This is reflected in the surface pressure contour changes. Considering the normal jet alone, an increase in incidence directs the jet upstream further.

Keffer and Platten (ref 28) observed that the trajectory of a jet directed 15° upstream suffered the maximum deflection. The vorticity entrainment was a maximum because the jet suffered the maximum cross-flow shear component for the greatest distance along the initial centre-line. The results from this work suggest that the maximum deflection occurred at $\alpha = 4^{\circ}$ to 6° upstream. This makes no allowance for the plate/freestream interaction. The initial region of the jet will be subjected to a non uniform freestream. Further out from the plate, the free-stream will be more unfform. It is expected that the jet/freestream interaction will become more predominant as the velocity ratio increases. It is also expected that the plate/freestream interaction will be more significant as incidence increases and this is probably the reason why C_s decreases for $\alpha > 8^{\circ}$ (Fig 4.79). The effect of the plate/freestream interaction would appear to cause the maximum deflection to occur at a lower upstream inclination.

The surface force distribution and suction force coefficients

give more support to this theory. The normal and $\phi = 15^{o}$ jet show a maximum value of C_s between an α of 4^{o} and 6^{o}. Results for higher inclinations did not extend to as high values of α as for $\phi = 0^{o}$ and 15^{o}. It is expected that C_s will not show a maximum at higher inclinations as the incidence will play a much less dominant role than inclination. The trend of the C_s versus α curves certainly suggest an increase in C_s with increasing α but the occurrence of a turning point cannot be dismissed until further data for high incidences at high inclinations is available.

A comparison of fig 4.82 with fig 5 of ref 28 reveals distinct similarities between the respective trajectories especially after allowing for an axes change (fig 5 uses wind axes). The deflection rate of the trajectory is a measure of the total entrainment rate and the profiles obtained suggested that the vorticity entrainment was a maximum at an α of 4^{o} - 6^{o} incidence of the normal jet configuration. This would be consistent with the observation that this configuration is subjected to the maximum crossflow shearing component for the greatest distance along the initial centreline. The other profiles for other angles of inclination give additional evidence to suggest that the jet/crossflow interaction dominates that of the plate/crossflow interaction, especially at high velocity ratios. An increase in incidence can be considered as causing an effective decrease in the inclination of the jet with respect to the freestream. The change in incidence modifies the effective entrainment rate.

4.3 Effect of Increasing the Velocity Ratio, m (fig 4.83-4.103 and 4.1-4.34)

4.3.1 Surface Pressures (fig 4.83 to 4.87 drawn for $\phi = 45^{o}$, $\alpha = 2^{o}$)

4.3.1.1 Forward and Lateral Region

The most significant change was the spreading of the low pressures to the sides and front of the jet as the velocity ratio increased. The

small high pressure region immediately upstream of the jet was diminished. This high pressure region was eventually enclosed by the low pressure field. These observations suggested an increase in entrainment as the velocity ratio increased. The upstream centreline distribution (fig 4.88 for $\phi = 45^{o}$, $\alpha = 2^{o}$) showed that a steady increase in pressure occurred as the jet was approached at low velocity ratios (m = 4). At higher velocity ratios ($m \geq 8$), a pressure loss occurred followed by a pressure recovery as the jet was approached. In general, the pressure was lowered at a given point as the velocity ratio was increased.

These observations have been noted before (ref 14,20) and a surface pressure comparison is made with these works in fig 4.89 (drawn for $\phi = 0^{o}$, $\alpha = 0^{o}$, m = 8). The agreement is good and certainly within the error bands shown in fig 3.1. The agreement is not so good close to the jet but the pressure readings are suspect because of the large pressure gradients which the pressure taps experience.

The overall effect was an apparent extension and upstream movement of the low pressure field.

4.3.1.2 Wake Region

The pressure distribution along the wake centreline indicated a decreasing rate of pressure recovery as distance increased from the jet at low velocity ratios (fig 4.90). At higher velocity ratios, the pressure recovery was very rapid close to the jet and very gradual further away from the jet. Generally, the lower velocity ratios produced lower pressures close to the rear of the jet whereas the higher velocity ratios produced lower pressures further away from the jet.

The pressure contours moved closer to the jet as the velocity ratio increased. The lateral spread of the low pressure field lessened the angle between the pressure contours and the wake centreline. The

contours were normal to the wake centreline at low velocity ratios (fig 4.83). Above a velocity ratio of 6, the angle between the centreline and the contours became less as the velocity ratio increased and typified the wake region at high velocity ratios. M = 6 was a special case for $\phi = 0^{\circ}$ and 15°. As the velocity ratio increased from 4 to 6, the wake contours spread downstream. The wake contours moved upstream as the velocity ratio increased above 6. The initial rate of pressure recovery for m = 6 was less and the contours extended much further downstream than their counterparts for other values of m for a ϕ of 0° or 15° (see fig 5.6, 5.9, 5.12, 5.15, 5.18). This effect was noted by Mikolowsky, although not directly (ref 22) and by Fearn (but for m = 4, ref 20), both for the normal jet. The reason for this observation was not known. The jet path was noticeably further away from the plate surface at higher velocity ratios ($m \geq 8$). At lower velocity ratios (m = 4) the jet was very close to the plate (fig 4.16- 4.25.) . In this latter case, the vortex entrainment must have a considerable effect on the wake boundary layer. At the higher velocity ratios this effect could be less as reflected in the wake centreline pressure close to the jet. The case of m = 6 represented the transition between these two conditions and this is possibly responsible for this observed effect.

The stagnation point observed in some previous works (ref 43) was not apparent in the wake region. The considerable quantity of data collected indicated that this stagnation point did not exist on the plate surface.

4.3.2 Integrated Effects

4.3.2.1 Surface Forces (fig 4.91-4.95 drawn for $\phi = 45^{\circ}$, $\alpha = 2^{\circ}$)

The value of the minimum surface force, C_{Fm}, and its angular displacement, Θ_m were increased for an upper limit of integration, $R_2 = 5$. The surface force in the wake region was increased and that in the

forward and lateral region was decreased (i.e. more -ve). This was anticipated from the observed surface pressure changes. The same observations applied for an upper limit of 10 except that C_{Fm} decreased in value. The distribution was continuous and the gradient approached zero at the centreline indicating the symmetry of the problem.

The surface force distribution of the normal jet exhibited a maximum value (Fig 5.11) for all incidences at m = 6 and an upper limit R_2 = 10 within the wake region. This was possibly connected with the above mentioned wake characteristics at m = 6. This maximum point also existed at approximately the same position in the data of ref 14 (but at an m of 2 and 4).

4.3.2.2 Suction Force Coefficient, C_s (Fig 4.1 to 4.5)

The suction force coefficient increased as m increased. The rate of change of C_s with m decreased for $m \geq 8$ (the curves suggested that C_s was constant in value for $m > 12$ for a normal jet). The reason why the curves for the normal and 15° inclined jet exhibited a constant value was that the upper limit of integration was sufficient to include the major part or all of the low pressure field within the wake. At higher inclinations, only part of this low pressure field was included. A comparison of the data obtained was made with that of ref 14 which used an identically defined suction force coefficient (see fig 4.1). The data from this work was of a higher magnitude and did not show the above constant value of C_s until a much higher velocity ratio. This illustrated that large differences could occur in the value of C_s for surface pressures that were in reasonable agreement. These differences arose from the error inherent in the surface force evaluation mentioned previously.

4.3.2.3 Centre of Pressure, $\bar{X}$ (Fig 4.6 to 4.10)

The centre of pressure decreased as the velocity ratio increased. The sign of the centre of pressure, $\bar{X}$ changed from positive to negative, at a velocity ratio between 6 and 7. This coincided with the change in the surface pressure distribution noted above. For $\bar{X}$ greater than zero, the rate of change of $\bar{X}$ with m was far greater than for $\bar{X}$ less than zero. The curves showed a tendency for the centre of pressure to become very large as the velocity ratio decreased (an increasing downstream movement of the centre of pressure). At low values of the velocity ratio, the wake contribution to the surface force was greater because of the close proximity of the jet and the greater entrainment incurred. The centre of pressure would be expected to move downstream. This was also supported by the surface pressure changes. Intuitively, the centre of pressure would be expected to be zero at $m = 0$ since there would be no interference effect. For this to happen, there must be a sudden decrease in the value of $\bar{X}$, i.e. a maximum turning point between $m = 0$ and 4 or a discontinuity in the variation of $\bar{X}$ with m. Large trim and large trim changes are required as the transition to wing borne flight is approached.

The curves appear to have an asymptotic value for velocity ratios greater than 12 and the centre of pressure shows a weak dependence on velocity ratio for high velocity ratios. This weak dependence indicates the attenuation of the lift loss as the entrainment causes a rise in the low pressures within the wake region. Intuitively, the centre of pressure ought to be zero as the velocity ratio becomes very large. The jet would dominate the flowfield which would effectively become that surrounding a freejet. Since the pressure distribution about a freejet is uniform, then the centre of pressure would be zero. The plate or aircraft is neutrally stable in the hover mode.

Considerable scatter of data was evident. This arose from the

error mentioned in previous discussions of the centre of pressure. A comparison of the results from this work with those of ref 18 are shown in fig 4.6. The qualitative agreement was good but the data from ref 18 was of a lower magnitude in $\bar{X}$.

4.3.2.4 Pitching Moment Coefficient (Fig 4.11- 4.15)

The pitching moment coefficient was computed so that a pitching moment coefficient variation with lift coefficient could be determined. The significant feature of these plots was the large rate of decrease of pitching moment with increasing suction force. The rate of decrease increased as C_s increased. The scatter of data observed arose from the same source as the centre of pressure scatter noted previously.

4.3.3 Jet Trajectories (Fig 4.16-4.34)

The most significant observation was that the profile underwent a less abrupt deflection on entering the freestream, or more succinctly, the penetration increased as the velocity ratio increased. The jet profiles have been investigated before and a comparison with other data is made in Fig 4.102. At first, the comparison appears to be rather poor. However, fig 18 of ref 32 shows considerable scatter which is typically of the order of 5 jet radii at a position X = 8, for tho same configuration as fig 4.102 ($\phi = 0^\circ$, $\alpha = 0^\circ$, m = 8). This scatter is not surprising considering the different definitions of the jet centreline used (as discussed in section 1.2 and 4.1.3). The data from this work lies just on the lower limit of the data shown in fig 18 of ref 32. It was thought that the discrepancy between this and other works was attributable to an effective velocity ratio change brought about by the different laboratory conditions (for instance, ref 19,24, 32 report no temperature monitoring but ref 28 does). The good agreement between ref 19,24, and 32 tends to exclude this reason. The significant condition that did differ between this work and others was the

level of turbulence of the freestream (4.4%). Data was recorded for two different configurations ($\phi = 0^{\circ}$, $\lambda = 0^{\circ}$, m = 10 and m = 12) and is shown (fig 4.103) with the corresponding results from ref 18 and 32 for a freestream turbulence level of 0.7%. The correlation of data is much improved. The higher freestream turbulence level appears to increase the rate of entrainment of the freestream fluid into the jet and, hence, the deflection increases and the jet penetrates less (see also sect 4.1.3). The data reported in ref 28 shows a smaller deflection than that of refs 19,24 and 32 (fig 4.102). The reason for this is not known. However, since the normal jet trajectory lies above that of this work, then this does explain, in part, the discrepancies noted in sect 4.1.3 and fig 4.56.

At lower velocity ratios (m = 4), the profile was not a tangent to the Z axis (fig 4.16). The potential core had been deflected by the pressure field around the jet (see ref 26). The total pressure decay curves (fig 4.101) showed a family of quite evenly spaced curves having a similar decay rate. The curves agreed with the general trend observed in ref 26 and suggested that the total pressure decay rate would be universal if a virtual origin was substituted at the end of the potential core. The potential core length increased with increasing velocity ratio. The respective values of the core length (from fig 4.101) were approximately 3.5, 4.0, 4.5 and 5.5 for velocity ratios of 6,8,10 and 12. The decay curves exhibited the familiar scatter in the initial jet region attributed to the difficulty in determining the centreline in the potential core and in the far field region attributed to the difficulty in determining the centreline where the excess total head was small.

4.3.4 Interpretation

Entrainment and jet penetration increase as the velocity ratio increases because the initial mean momentum flux of the jet has been

increased. The increase in entrainment rate with velocity ratio is not proportional to that of momentum flux. The uniform stream flux alters the greater jet momentum flux to a lesser extent in the initial region. The deflection of the jet trajectory is less severe. For the same reason the potential core is extended. Freejet entrainment increases as the difference between the jet velocity and the parallel freestream component is augmented. This will increase with increasing velocity ratio. The surface pressure contours clearly show the effect of this increasing entrainment rate and the less severe initial deflection as the velocity ratio increases. The flowfield analysis of ref 18 indicated that the effect of increasing the velocity ratio was to primarily increase the jet entrainment. It was also concluded that the effect of the change in jet trajectory was secondary. This seems contradictory because the vortex entrainment and jet deflection are synonymous and the vortex entrainment is greater than the freejet entrainment and increases with velocity ratio in the initial region (ref 28). The surface force distribution shows a decreasing contribution (i.e. force increases (less -ve)) from the wake region as the entrainment causes a rise in the low pressures in the wake as the velocity ratio increases. At low velocity ratios, the jet deflection is abrupt on entering the freestream and the effect of the vortex entrainment on the wake fluid boundary layer is greater. This process has less effect on the wake as the initial deflection becomes less severe and the jet begins to entrain more fluid from the lateral region. With further increases in velocity ratio, more and more fluid is entrained from the lateral and forward regions until the limiting condition is reached. Freejet entrainment predominates and fluid is entrained uniformly from the surrounding fluid. The results tend to confirm this.

Table 4.1. Summary of Data.

ψ	α	m	Comments
0	0	4	Figures: 3.8, 4.1, 4.6, 4.11, 4.16, 4.53, 4.54, 4.64, 4.80, 5.6, 5.7, 5.8
		6	Figures: 4.1, 4.6, 4.11, 4.16, 4.53, 4.54, 4.80, 5.9, 5.10, 5.11
		8	Figures: 4.1, 4.6, 4.11, 4.16, 4.53, 4.54, 4.56, 4.66, 4.80, 4.89, 4.102, 5.12, 5.13, 5.14
		10	Figures: 4.1, 4.6, 4.11, 4.16, 4.53, 4.54, 4.80, 4.103, 5.15, 5.16, 5.17
		12	Figures: 4.1, 4.6, 4.11, 4.16, 4.35, 4.40, 4.42, 4.43, 4.48, 4.53, 4.54, 4.55, 4.57, 4.82, 4.82, 4.103, 5.18, 5.19, 5.20
	2	4	Figures: 4.1, 4.6, 4.11, 4.17
		6	Figures: 4.1, 4.6, 4.11, 4.17
		8	Figures: 4.1, 4.6, 4.11, 4.17
		10	Figures: 4.1, 4.6, 4.11, 4.17
		12	Figures: 3.7, 4.1, 4.6, 4.11, 4.17
	4	4	Figures: 4.1, 4.6, 4.11, 4.18
		6	Figures: 4.1, 4.6, 4.11, 4.18
		8	Figures: 4.1, 4.6, 4.11, 4.18
		10	Figures: 4.1, 4.6, 4.11, 4.18
		12	Figures: 4.1, 4.6, 4.11, 4.18, 4.82
	6	4	Figures: 4.1, 4.6, 4.11, 4.19, 4.65
		6	Figures: 4.1, 4.6, 4.11, 4.19
		8	Figures: 4.1, 4.6, 4.11, 4.19, 4.67
		10	Figures: 4.1, 4.6, 4.11, 4.19
		12	Figures: 4.1, 4.6, 4.11, 4.19
	8	4	Figures: 4.1, 4.6, 4.11, 4.20

Table 4.1. Continued.

ϕ	α	m	Comments
0	8	6	Figures: 4.1, 4.6, 4.11, 4.20
		8	Figures: 4.1, 4.6, 4.11, 4.20
		10	Figures: 4.1, 4.6, 4.11, 4.20
		12	Figures: 4.1, 4.6, 4.11, 4.20, 4.82
15	0	4	Figures: 4.2, 4.7, 4.12, 4.21, 4.53, 4.54, 4.79, 4.80, 4.81
		6	Figures: 4.2, 4.7, 4.12, 4.21, 4.53, 4.54, 4.79, 4.80, 4.81
		8	Figures: 4.2, 4.7, 4.12, 4.21, 4.53, 4.54, 4.56, 4.58, 4.63, 4.68, 4.69, 4.74, 4.79, 4.80, 4.81
		10	Figures: 4.2, 4.7, 4.12, 4.21, 4.53, 4.54, 4.79, 4.80, 4.81
		12	Figures: 4.2, 4.7, 4.12, 4.21, 4.36, 4.40, 4.42, 4.44, 4.49, 4.53, 4.54, 4.55, 4.57, 4.79, 4.80, 4.81
15	2	4	Figures: 4.2, 4.7, 4.12, 4.22, 4.79, 4.81
		6	Figures: 4.2, 4.7, 4.12, 4.22, 4.79, 4.81
		8	Figures: 4.2, 4.7, 4.12, 4.22, 4.59, 4.63, 4.68, 4.70, 4.75, 4.79, 4.81
		10	Figures: 4.2, 4.7, 4.12, 4.22, 4.79, 4.81
		12	Figures: 4.2, 4.7, 4.12, 4.22, 4.79, 4.81
	4	4	Figures: 4.2, 4.7, 4.12, 4.23, 4.79, 4.81
		6	Figures: 4.2, 4.7, 4.12, 4.23, 4.79, 4.81
		8	Figures: 4.2, 4.7, 4.12, 4.23, 4.60, 4.63, 4.68, 4.71, 4.76, 4.79, 4.81
		10	Figures: 4.2, 4.7, 4.12, 4.23, 4.79, 4.81

Table 4.1. Continued.

ϕ	α	m	Comments
15	4	12	Figures: 4.2, 4.7, 4.12, 4.23, 4.79, 4.81
	6	4	Figures: 4.2, 4.7, 4.12, 4.24, 4.79, 4.81
		6	Figures: 4.2, 4.7, 4.12, 4.24, 4.79, 4.81
		8	Figures: 4.2, 4.7, 4.12, 4.24, 4.61, 4.63, 4.68, 4.72, 4.77, 4.79, 4.81
		10	Figures: 4.2, 4.7, 4.12, 4.24, 4.79, 4.81
		12	Figures: 4.2, 4.7, 4.12, 4.24, 4.79, 4.81
	8	4	Figures: 4.2, 4.7, 4.12, 4.25, 4.79, 4.81
		6	Figures: 4.2, 4.7, 4.12, 4.25, 4.79, 4.81
		8	Figures: 4.2, 4.7, 4.12, 4.25, 4.62, 4.63, 4.68, 4.73, 4.78, 4.79, 4.81
		10	Figures: 4.2, 4.7, 4.12, 4.25, 4.79, 4.81
		12	Figures: 4.2, 4.7, 4.12, 4.25, 4.79, 4.81
30	0	4	Figures: 4.3, 4.8, 4.13, 4.26, 4.53, 4.54, 4.80
		6	Figures: 4.3, 4.8, 4.13, 4.26, 4.53, 4.54, 4.80
		8	Figures: 4.3, 4.8, 4.13, 4.26, 4.41, 4.53, 4.54, 4.56, 4.80
		10	Figures: 4.3, 4.8, 4.13, 4.26, 4.53, 4.54, 4.80
		12	Figures: 4.3, 4.8, 4.13, 4.26, 4.37, 4.40, 4.42, 4.45, 4.50, 4.53, 4.54, 4.55, 4.57, 4.80
	2	4	Figures: 4.3, 4.8, 4.13, 4.27
		6	Figures: 4.3, 4.8, 4.13, 4.27
		8	Figures: 4.3, 4.8, 4.13, 4.27
		10	Figures: 4.3, 4.8, 4.13, 4.27
		12	Figures: 4.3, 4.8, 4.13, 4.27
	4	4	Figures: 4.3, 4.8, 4.13, 4.28
		6	Figures: 4.3, 4.8, 4.13, 4.28

Table 4.1. Continued.

ϕ	α	m	Comments
30	4	8	Figures: 4.3, 4.8, 4.13, 4.28
		10	Figures: 4.3, 4.8, 4.13, 4.28
		12	Figures: 4.3, 4.8, 4.13, 4.28
	6	4	Figures: 4.3, 4.8, 4.13, 4.29
		6	Figures: 4.3, 4.8, 4.13, 4.29
		8	Figures: 4.3, 4.8, 4.13, 4.29
		10	Figures: 4.3, 4.8, 4.13, 4.29
		12	Figures: 4.3, 4.8, 4.13, 4.29
45	0	4	Figures: 4.4, 4.9, 4.14, 4.30, 4.53, 4.54, 4.80,
		6	Figures: 4.4, 4.9, 4.14, 4.30, 4.53, 4.54, 4.80, 4.101
		8	Figures: 4.4, 4.9, 4.14, 4.30, 4.53, 4.54, 4.56, 4.80, 4.101
		10	Figures: 4.4, 4.9, 4.14, 4.30, 4.53, 4.54, 4.80, 4.101
		12	Figures: 3.1, 3.2, 3.3, 4.4, 4.9, 4.14, 4.30, 4.38, 4.40, 4.42, 4.46, 4.51, 4.53, 4.54, 4.55, 4.57, 4.80, 4.101
	2	4	Figures: 4.4, 4.9, 4.14, 4.31, 4.83, 4.88, 4.90, 4.91, 4.96
		6	Figures: 4.4, 4.9, 4.14, 4.31, 4.84, 4.88, 4.90, 4.92, 4.97
		8	Figures: 4.4, 4.9, 4.14, 4.31, 4.85, 4.88, 4.90, 4.93, 4.98
		10	Figures: 4.4, 4.9, 4.14, 4.31, 4.86, 4.88, 4.90, 4.94, 4.99

Table 4.1. Continued.

ϕ	α	m	Comments
45	2	12	Figures: 4.4, 4.9, 4.14, 4.31, 4.87, 4.88, 4.90, 4.95, 4.100
	4	4	Figures: 4.4, 4.9, 4.14, 4.32
		6	Figures: 4.4, 4.9, 4.14, 4.32
		8	Figures: 4.4, 4.9, 4.14, 4.32
		10	Figures: 4.4, 4.9, 4.14, 4.32
		12	Figures: 4.4, 4.9, 4.14, 4.32
60	0	4	Figures: 4.5, 4.10, 4.15, 4.33, 4.53, 4.54, 4.80
		6	Figures: 4.5, 4.10, 4.15, 4.33, 4.53, 4.54, 4.80
		8	Figures: 3.4, 3.5, 3.6, 4.5, 4.10, 4.15, 4.33, 4.53, 4.54, 4.80
		10	Figures: 4.5, 4.10, 4.15, 4.33, 4.53, 4.54, 4.80, B.2, B.3, B.4
		12	Figures: 4.5, 4.10, 4.15, 4.33, 4.39, 4.40, 4.42, 4.47, 4.52, 4.53, 4.54, 4.55, 4.57, 4.80
	2	4	Figures: 4.5, 4.10, 4.15, 4.34
		6	Figures: 4.5, 4.10, 4.15, 4.34
		8	Figures: 4.5, 4.10, 4.15, 4.34
		10	Figures: 4.5, 4.10, 4.15, 4.34
		12	Figures: 4.5, 4.10, 4.15, 4.34

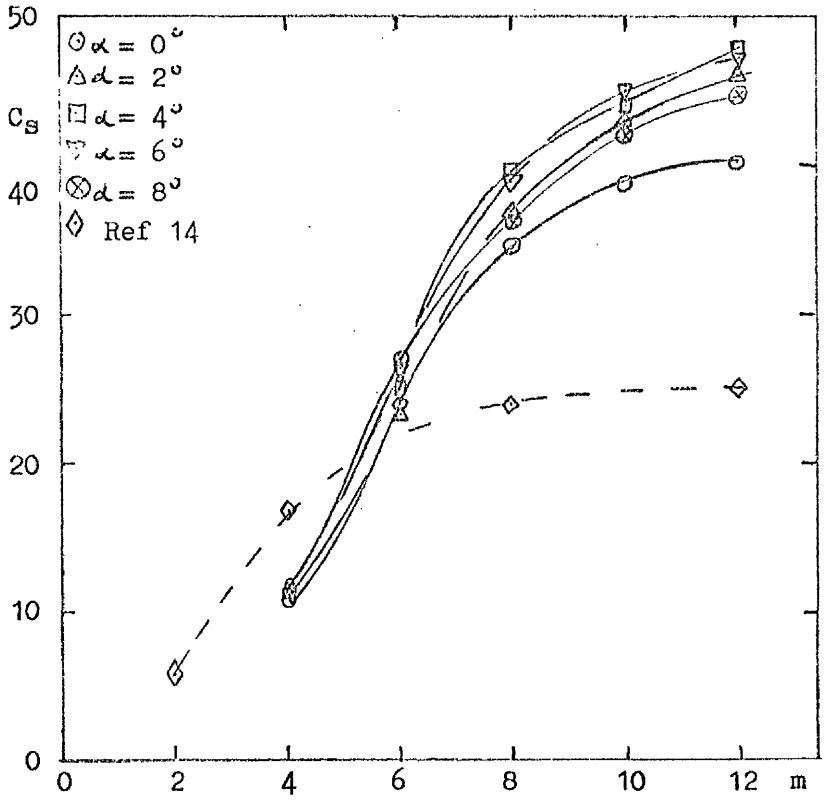

Figure 4.1. Variation of Suction Force Coefficient with Velocity Ratio ($\phi = 0^\circ$).

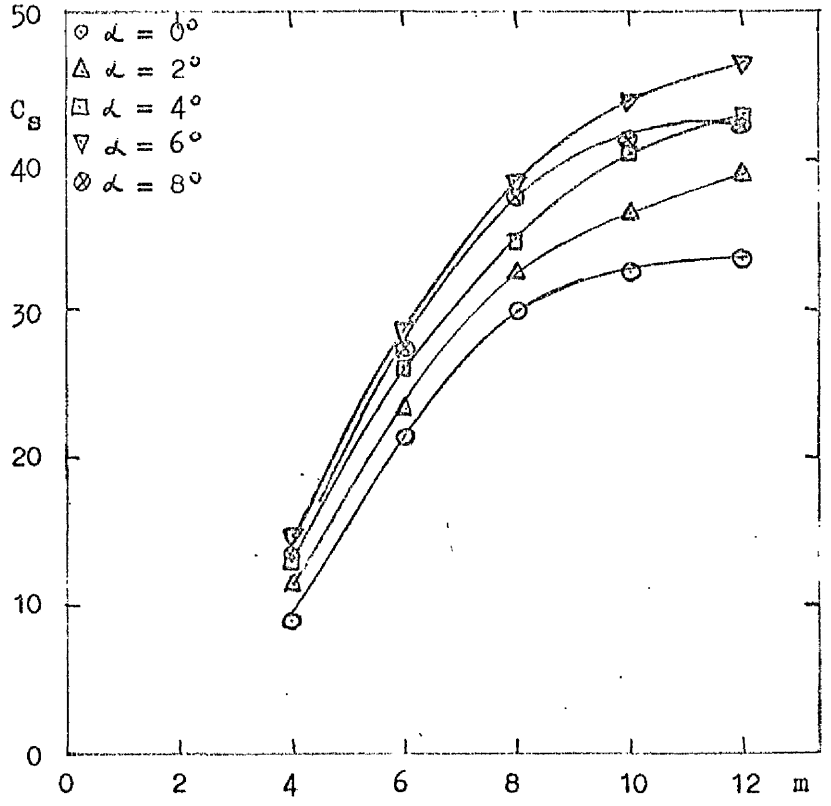

Figure 4.2. Variation of Suction Force Coefficient with Velocity Ratio ($\phi = 15^\circ$).

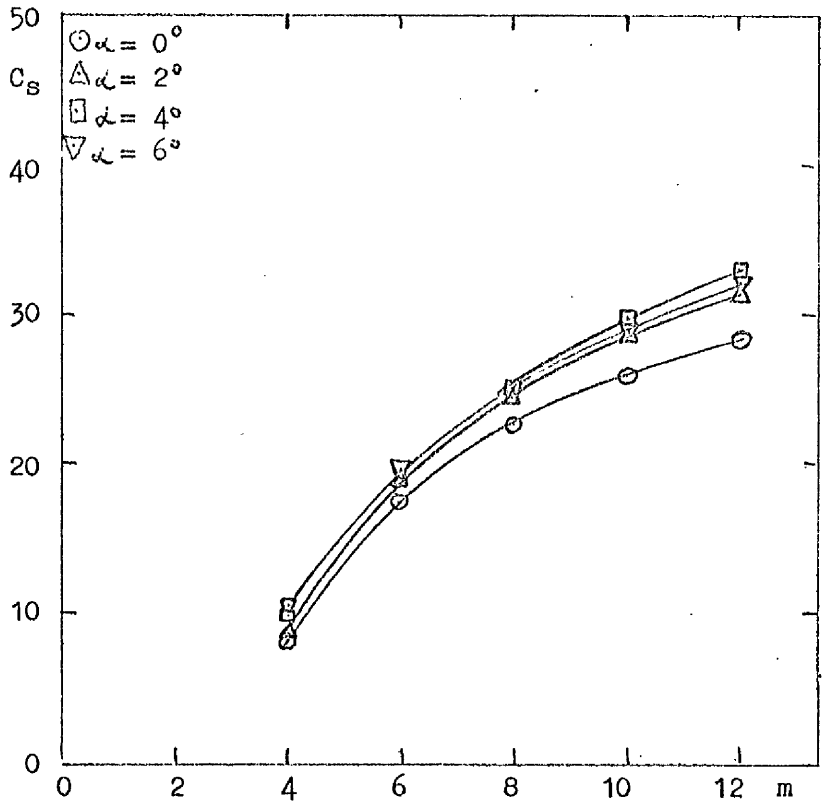

Figure 4.3. Variation of Suction Force Coefficient with Velocity Ratio (ϕ = 30°)

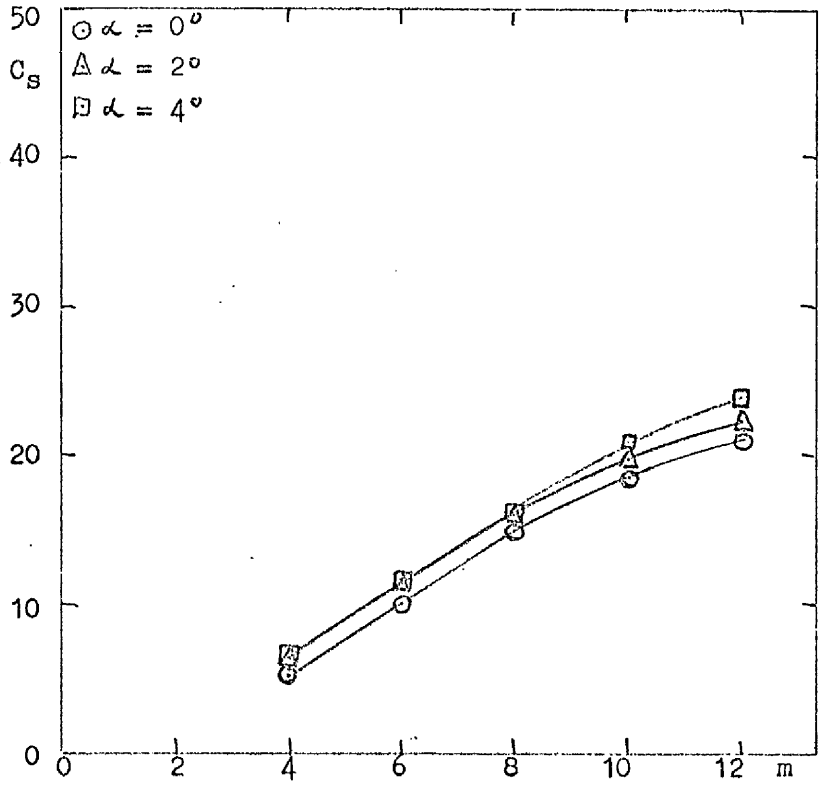

Figure 4.4. Variation of Suction Force Coefficient with Velocity Ratio (ϕ = 45°)

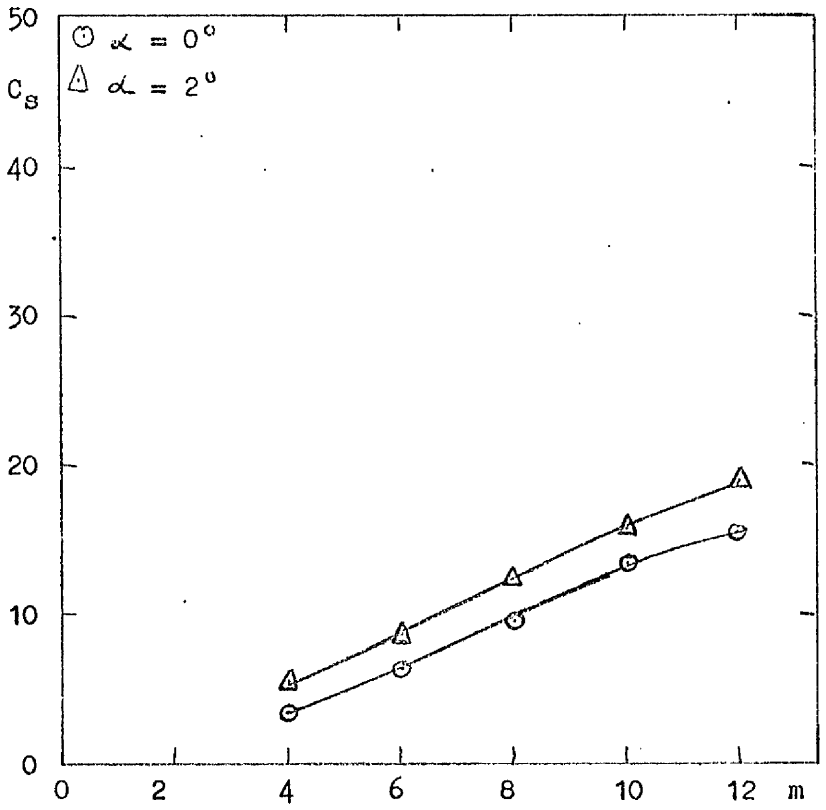

Figure 4.5. Variation of Suction Force Coefficient with Velocity Ratio ($\phi = 60°$).

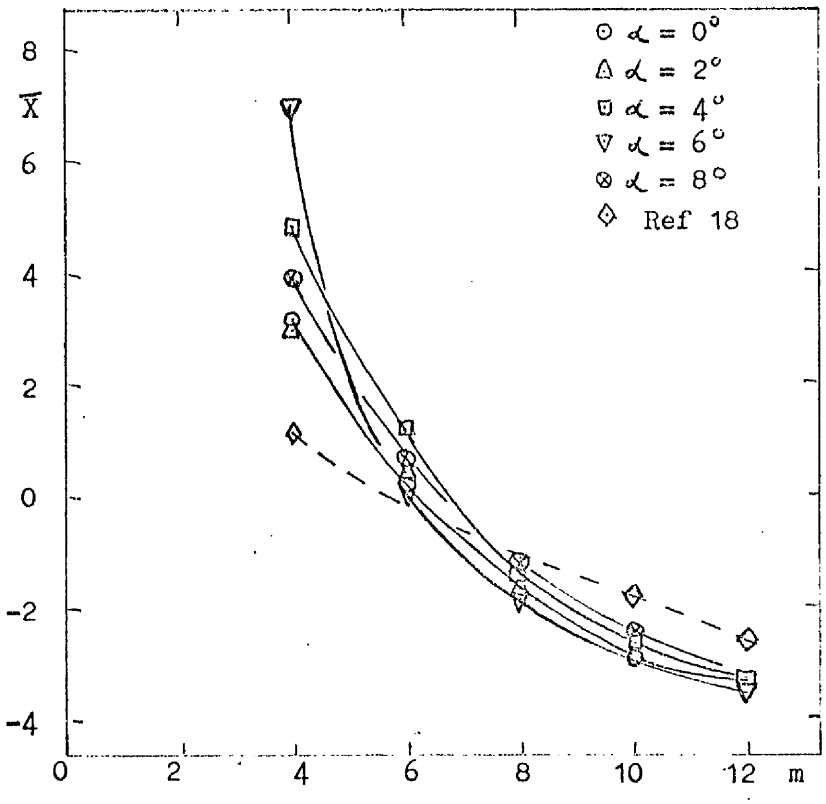

Figure 4.6. Variation of Centre of Pressure with Velocity Ratio ($\phi = 0°$).

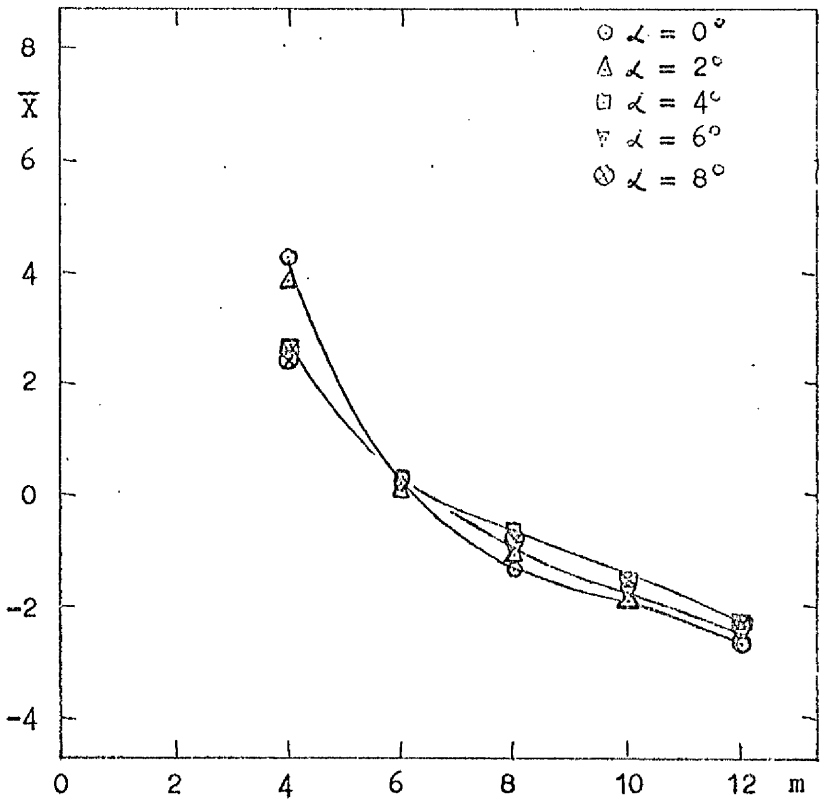

Figure 4.7. Variation of Centre of Pressure with Velocity Ratio ($\phi = 15°$).

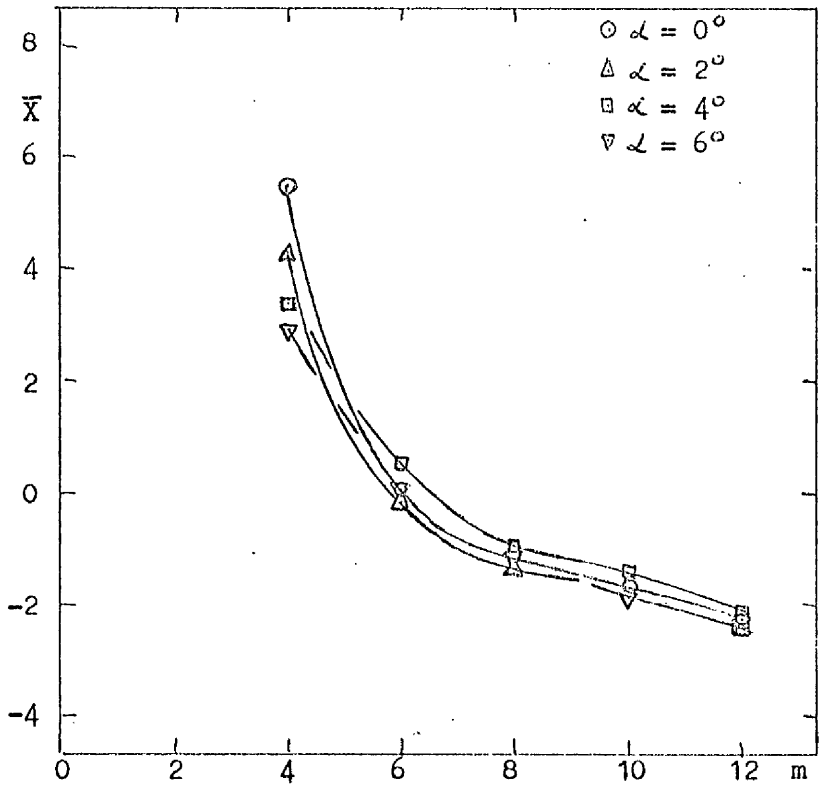

Figure 4.8. Variation of Centre of Pressure with Velocity Ratio ($\phi = 30°$).

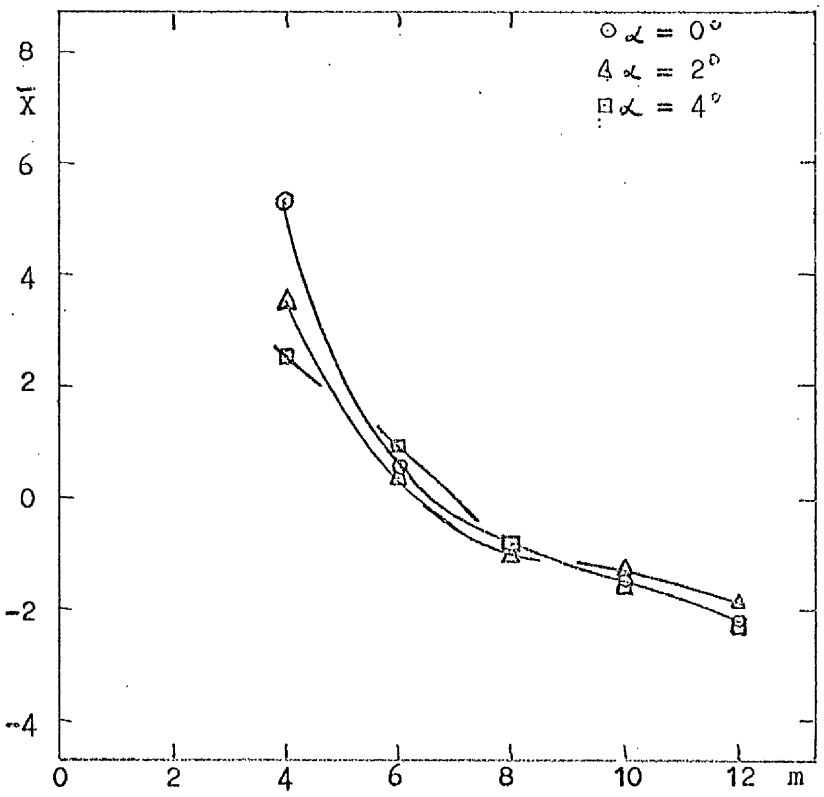

Figure 4.9. Variation of Centre of Pressure with Velocity Ratio ($\phi = 45^{\circ}$).

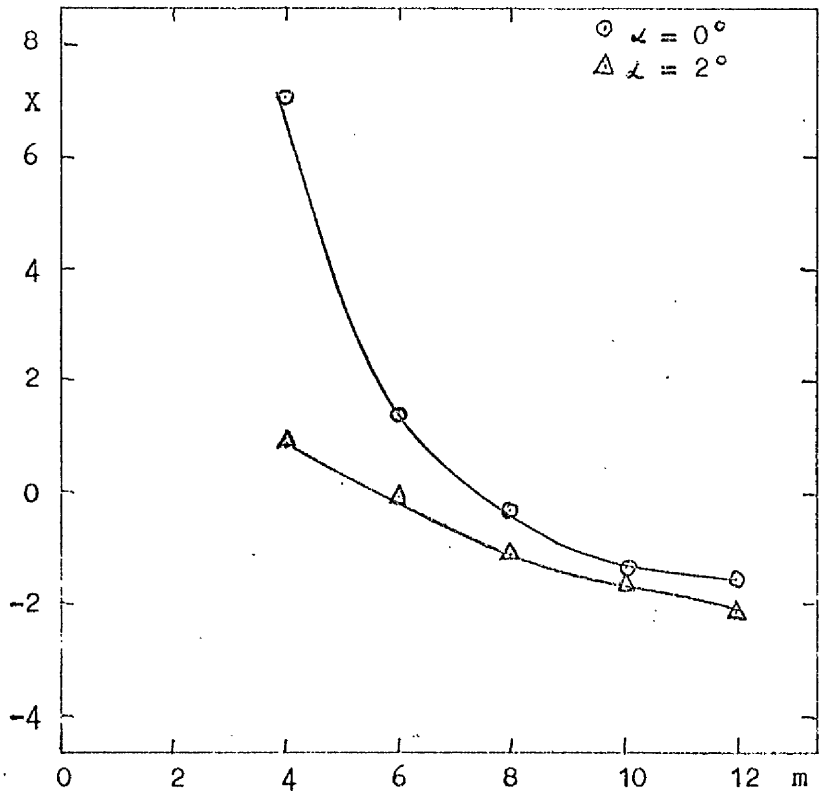

Figure 4.10. Variation of Centre of Pressure with Velocity Ratio ($\phi = 60^{\circ}$).

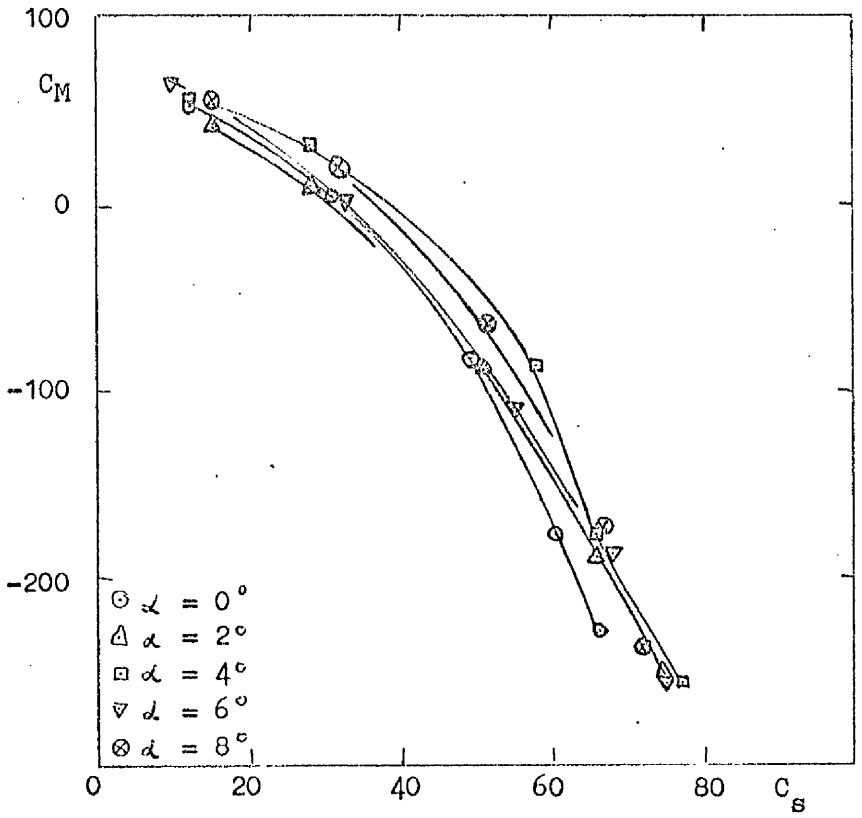

Figure 4.11. Variation of Pitching Moment Coefficient with Suction Force Coefficient ($\phi = 0°$).

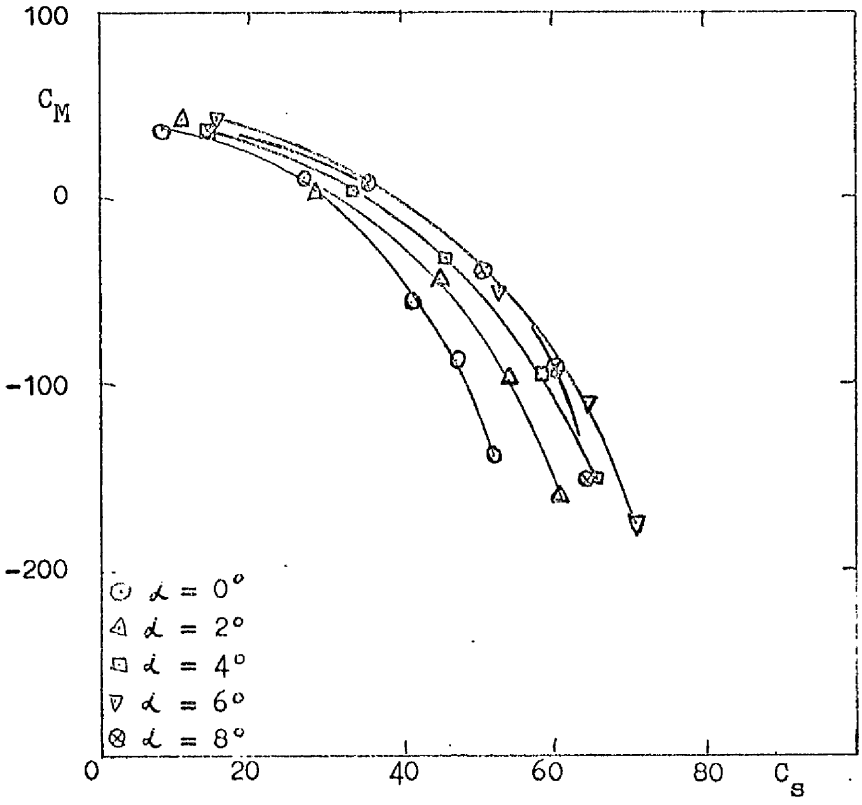

Figure 4.12. Variation of Pitching Moment Coefficient with Suction Force Coefficient ($\phi = 15°$).

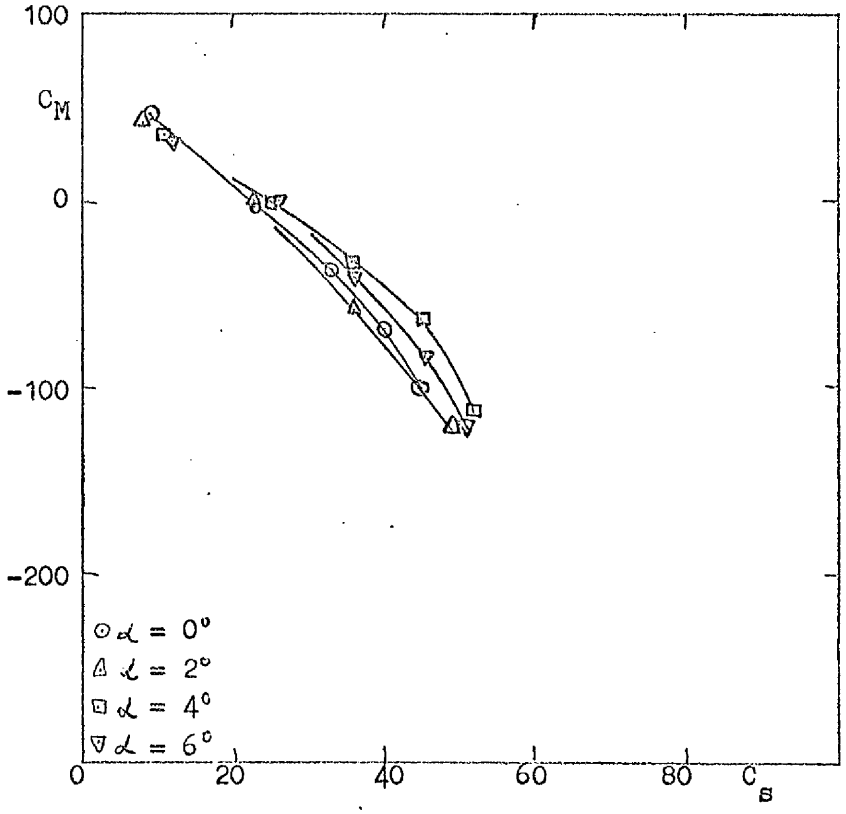

Figure 4.13. Variation of Pitching Moment Coefficient with Suction Force Coefficient ($\phi = 30°$).

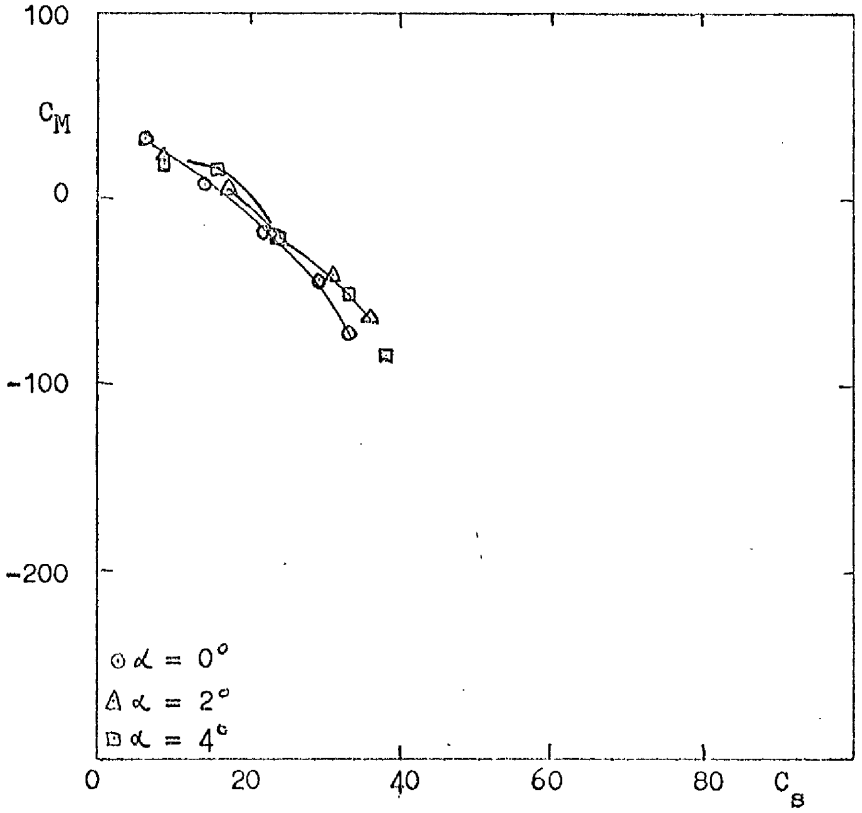

Figure 4.14. Variation of Pitching Moment Coefficient with Suction Force Coefficient ($\phi = 45°$).

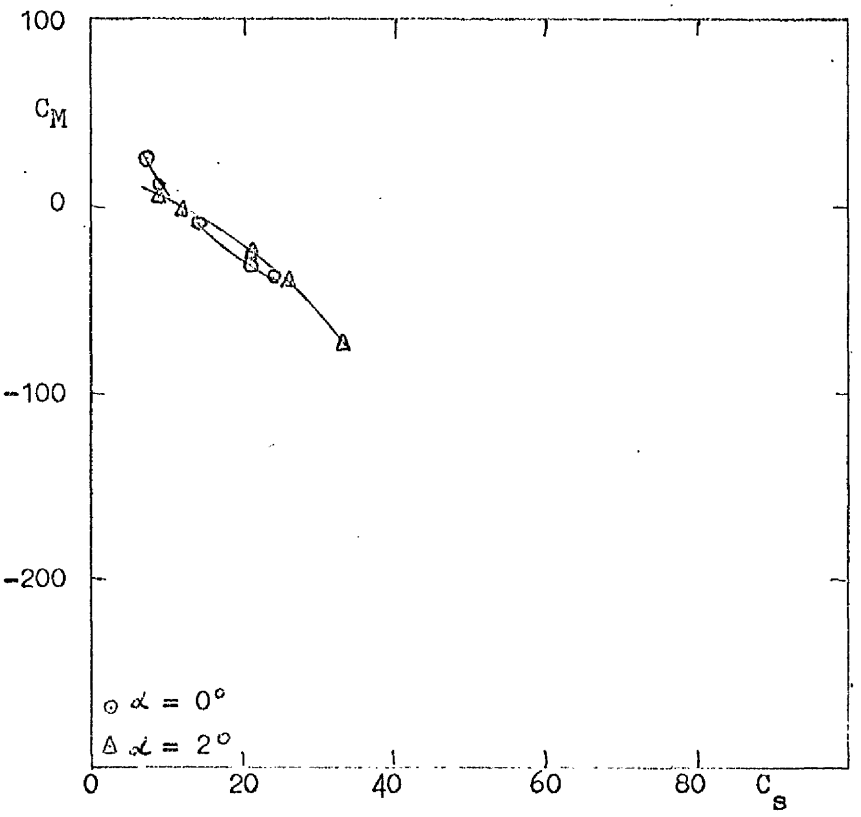

Figure 4.15. Variation of Pitching Moment Coefficient with Suction Force Coefficient ($\phi = 60°$).

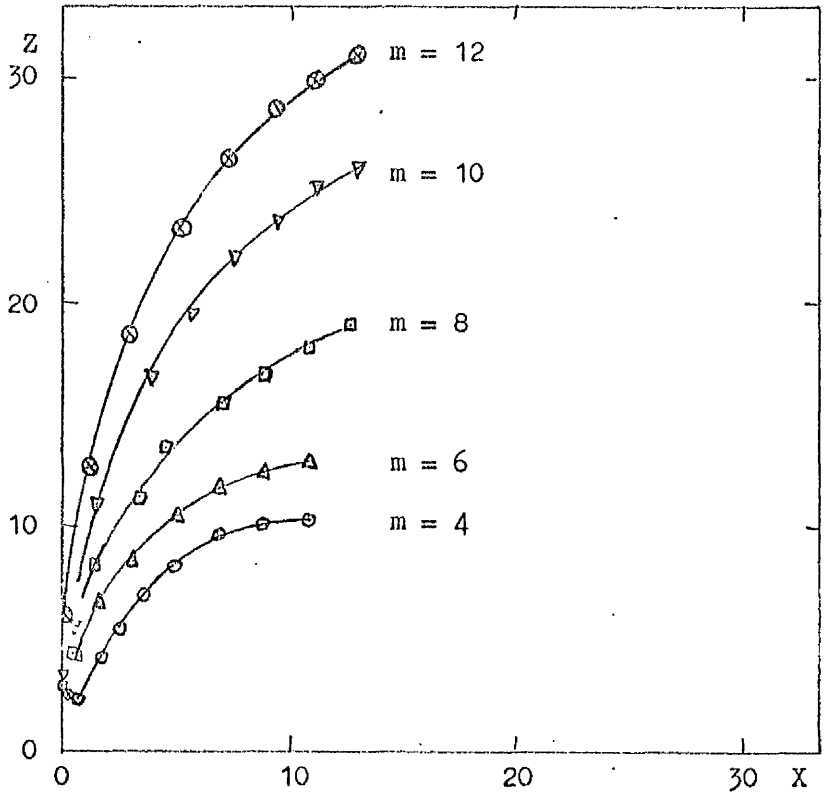

Figure 4.16. Jet Trajectory ($\phi = 0°$, $\alpha = 0°$)

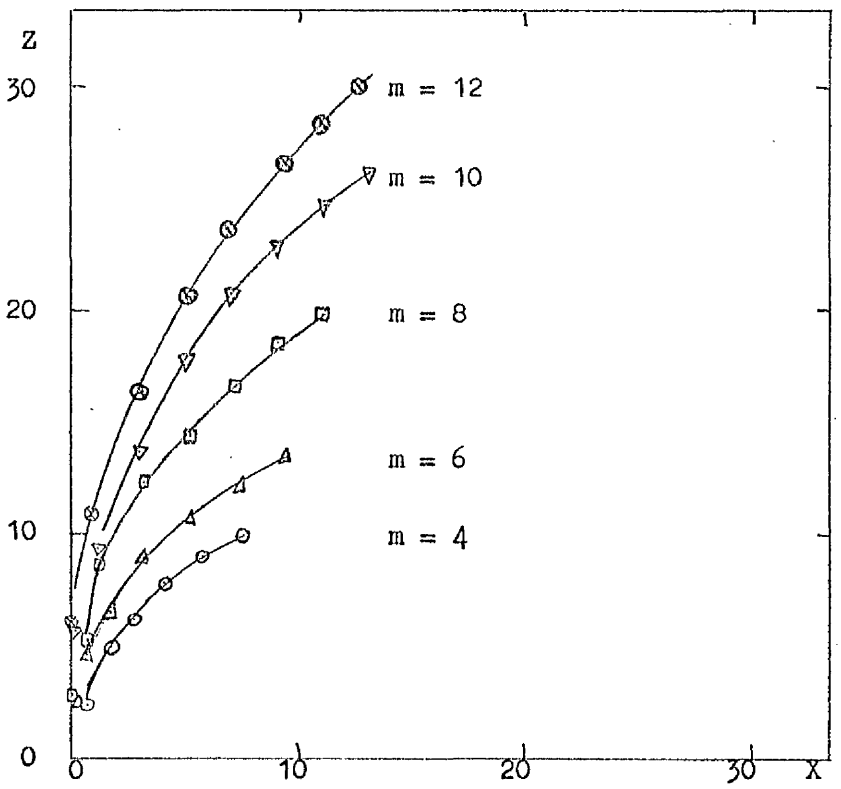

Figure 4.17. Jet Trajectory ($\phi = 0°$, $\alpha = 2°$).

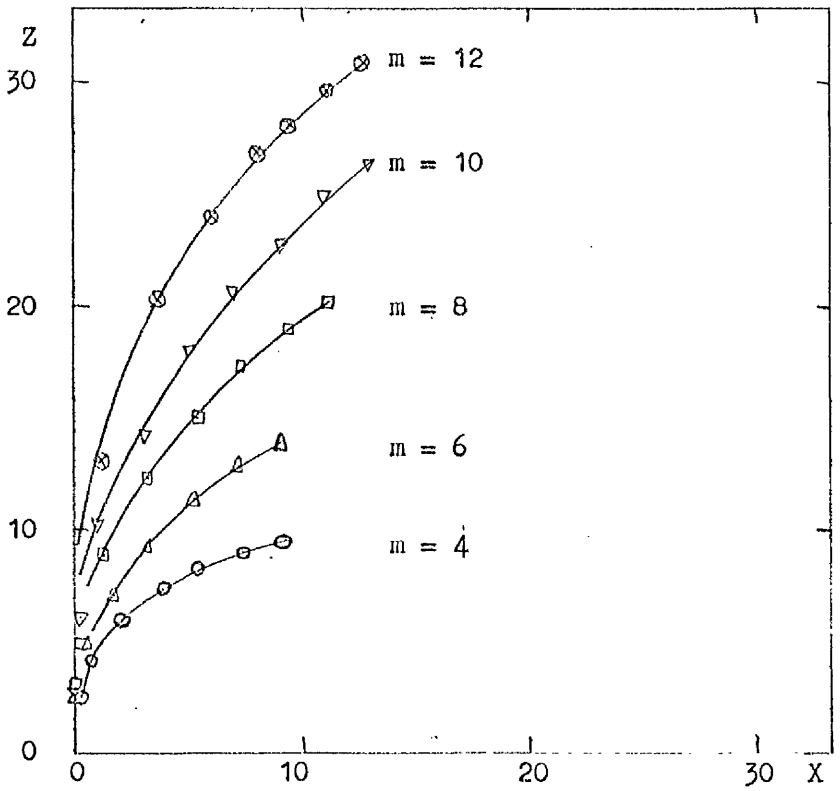

Figure 4.18. Jet Trajectory ($\phi = 0°$, $\alpha = 4°$).

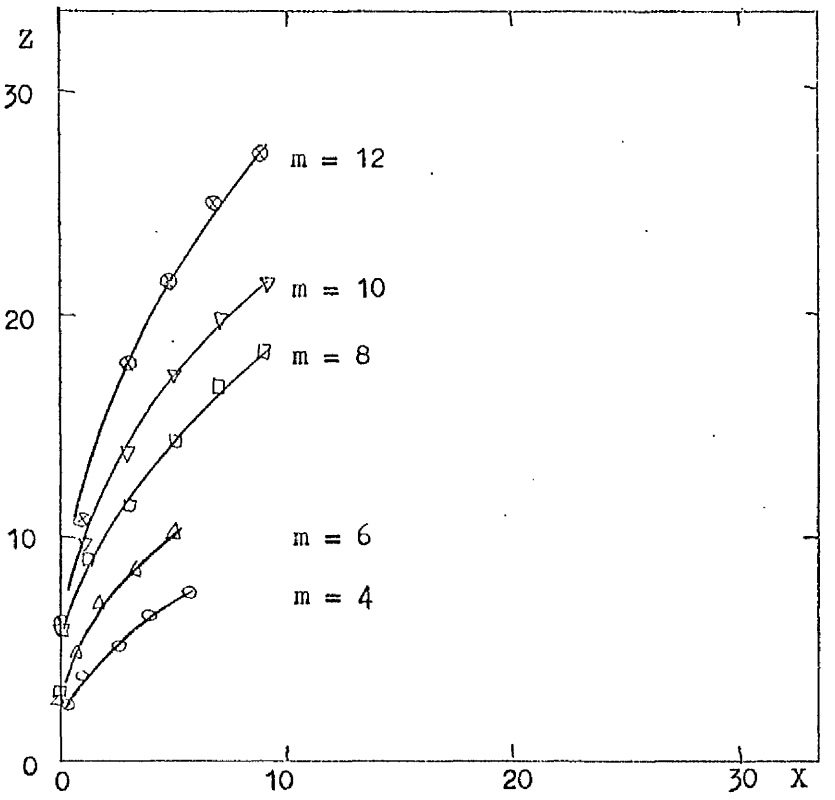

Figure 4.19. Jet Trajectory (ϕ = 0°, α = 6°).

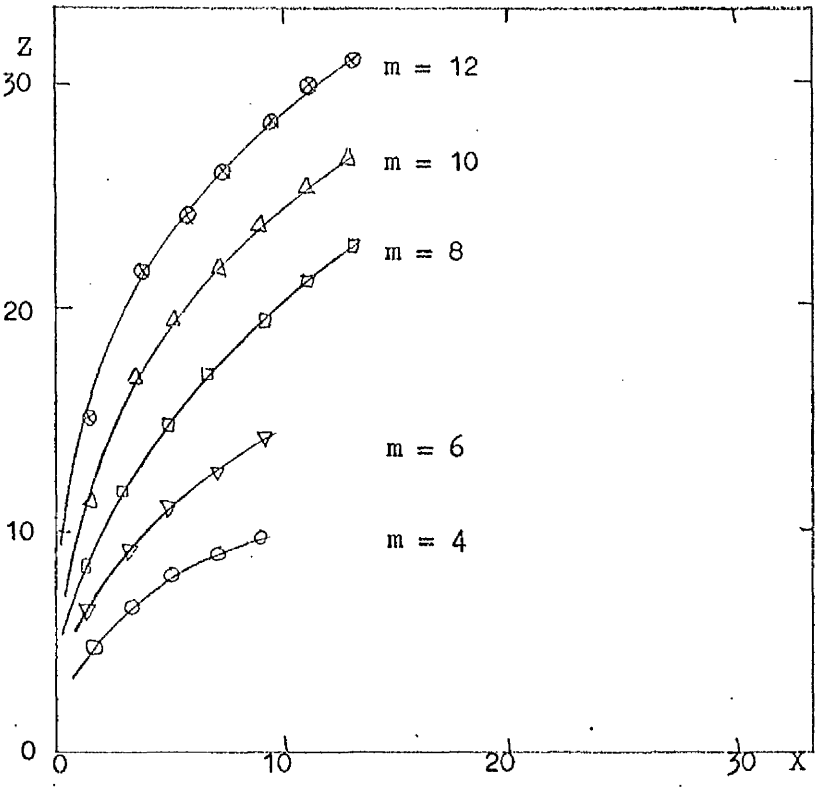

Figure 4.20. Jet Trajectory (ϕ = 0°, α = 8°).

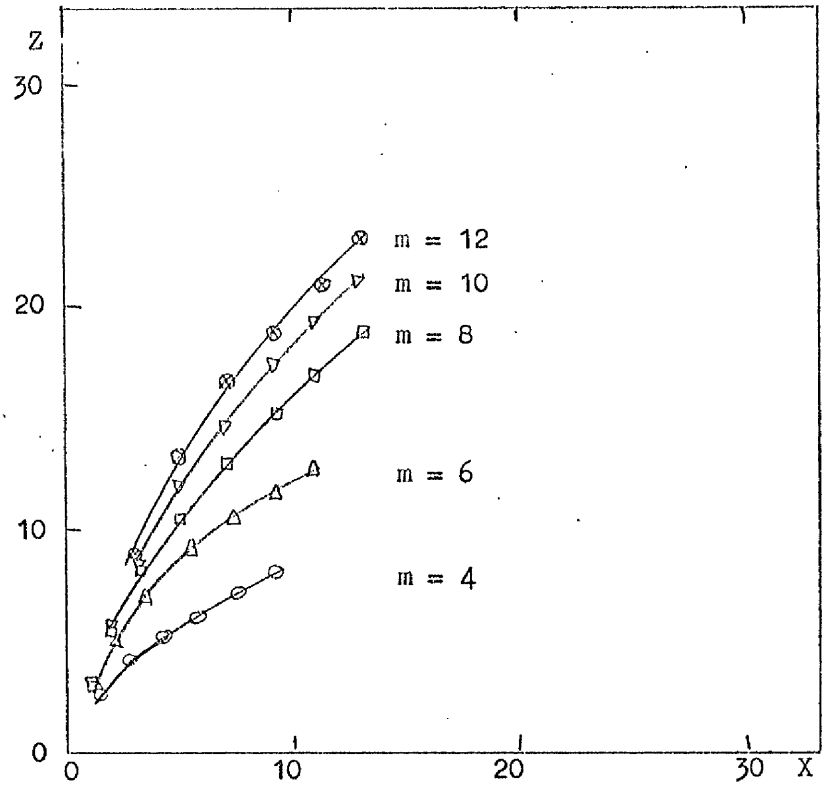

Figure 4.21. Jet Trajectory ($\phi = 15^{\circ}$, $\alpha = 0^{\circ}$).

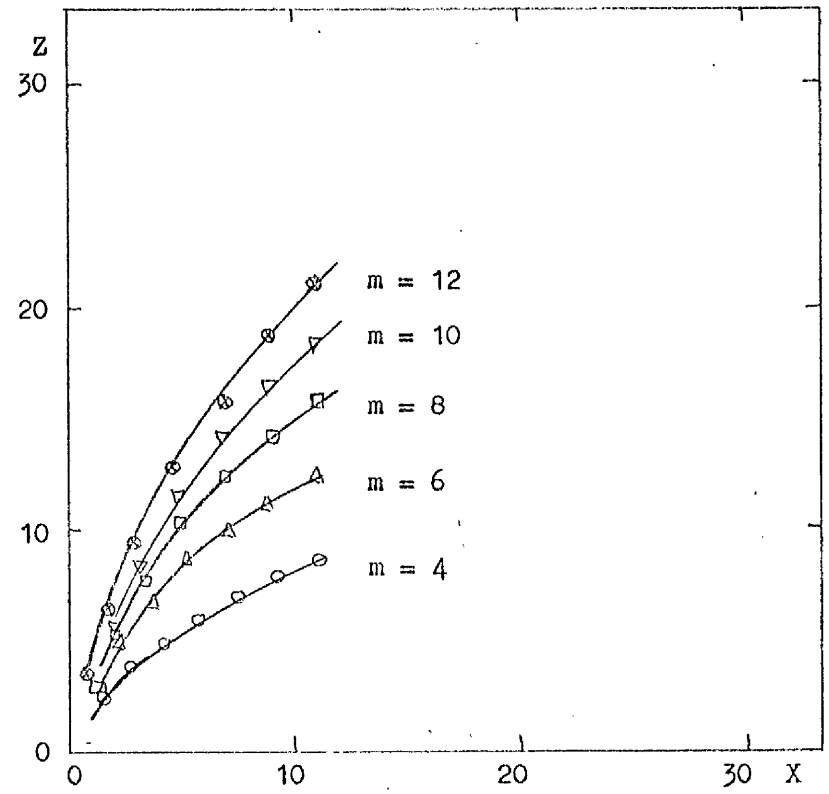

Figure 4.22. Jet Trajectory ($\phi = 15^{\circ}$, $\alpha = 2^{\circ}$).

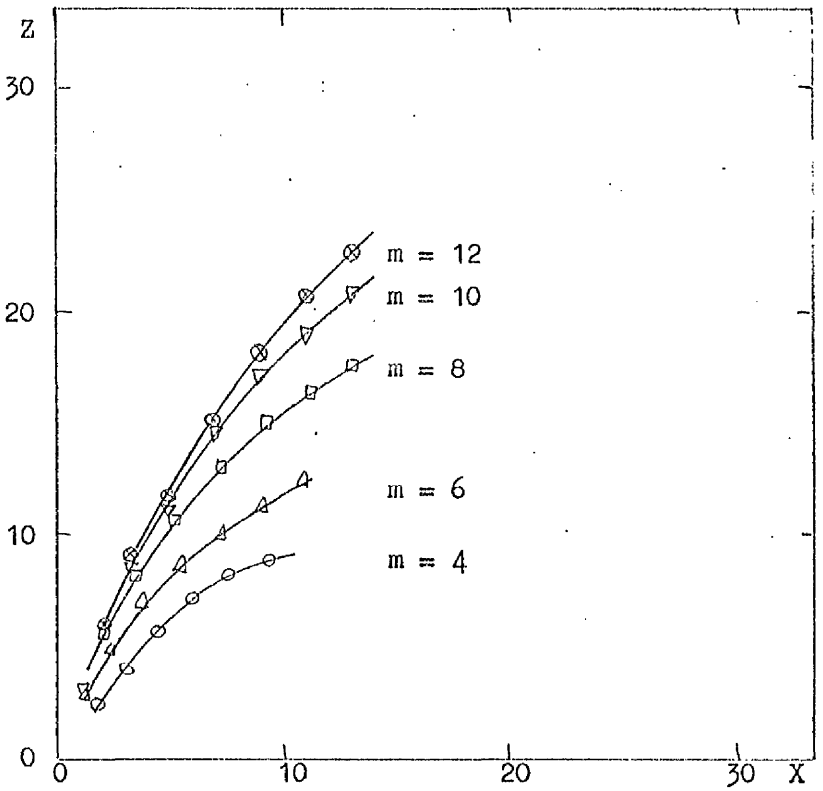

Figure 4.23. Jet Trajectory ($\phi = 15^{\circ}$, $\alpha = 4^{\circ}$).

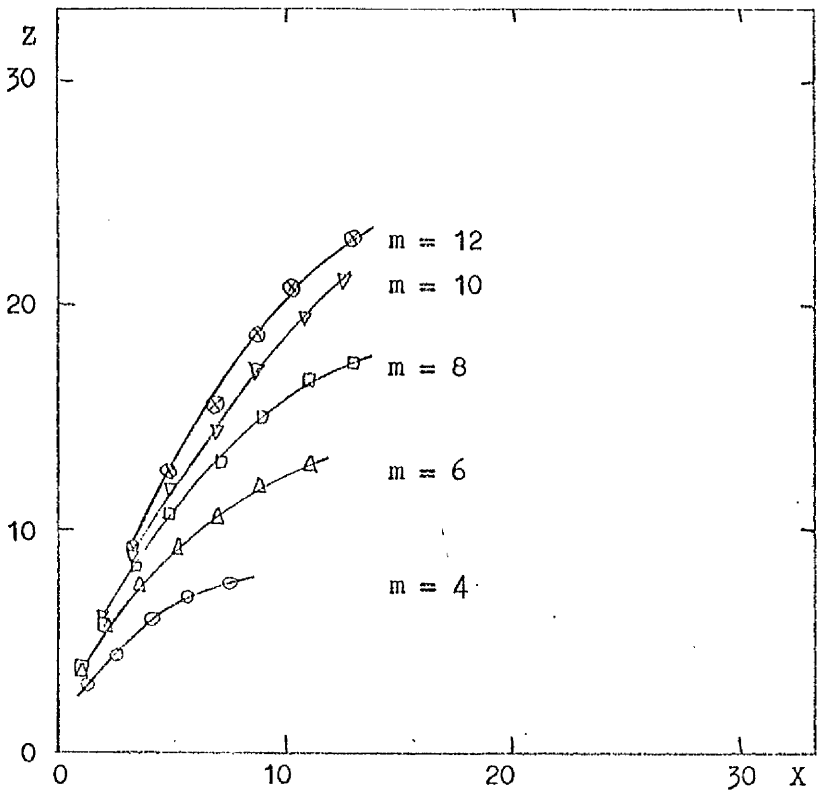

Figure 4.24. Jet Trajectory ($\phi = 15^{\circ}$, $\alpha = 6^{\circ}$).

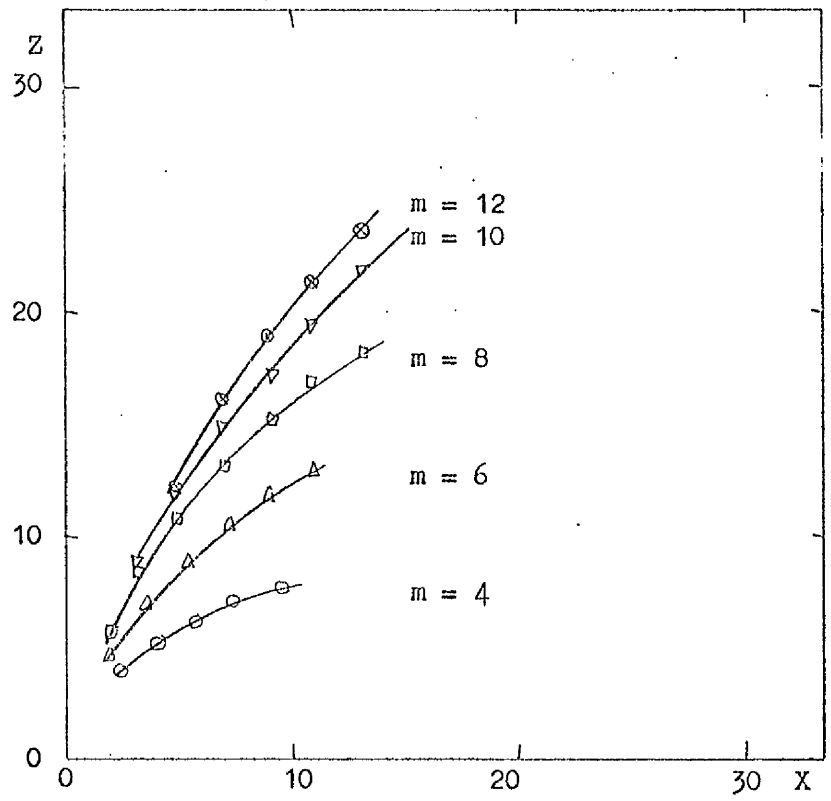

Figure 4.25. Jet Trajectory ($\phi = 15°$, $\alpha = 8°$).

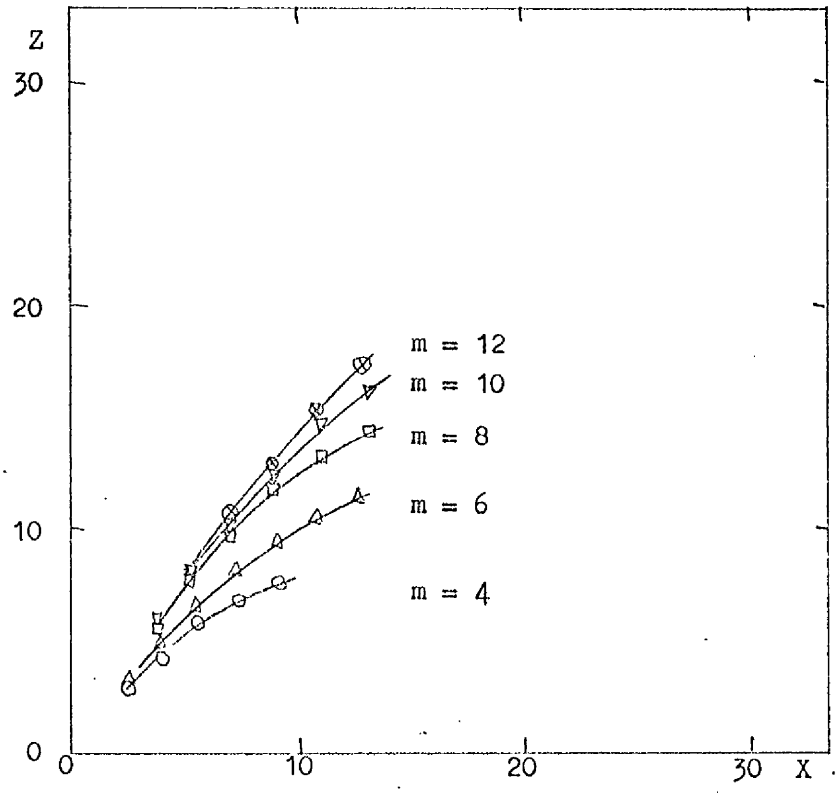

Figure 4.26. Jet Trajectory ($\phi = 30°$, $\alpha = 0°$).

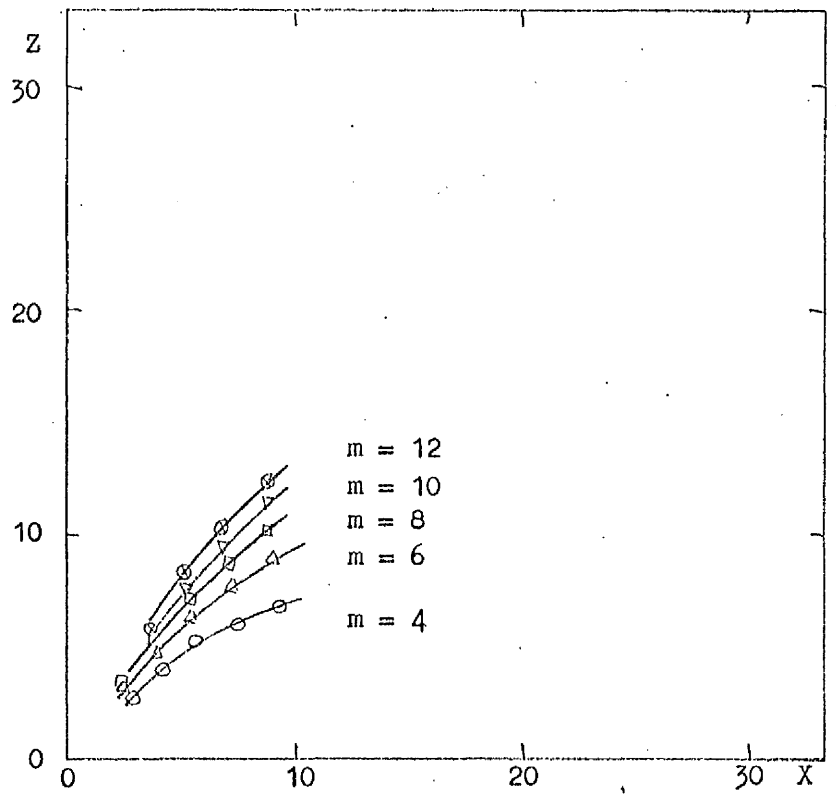

Figure 4.27. Jet Trajectory (ϕ = 30°, α = 2°).

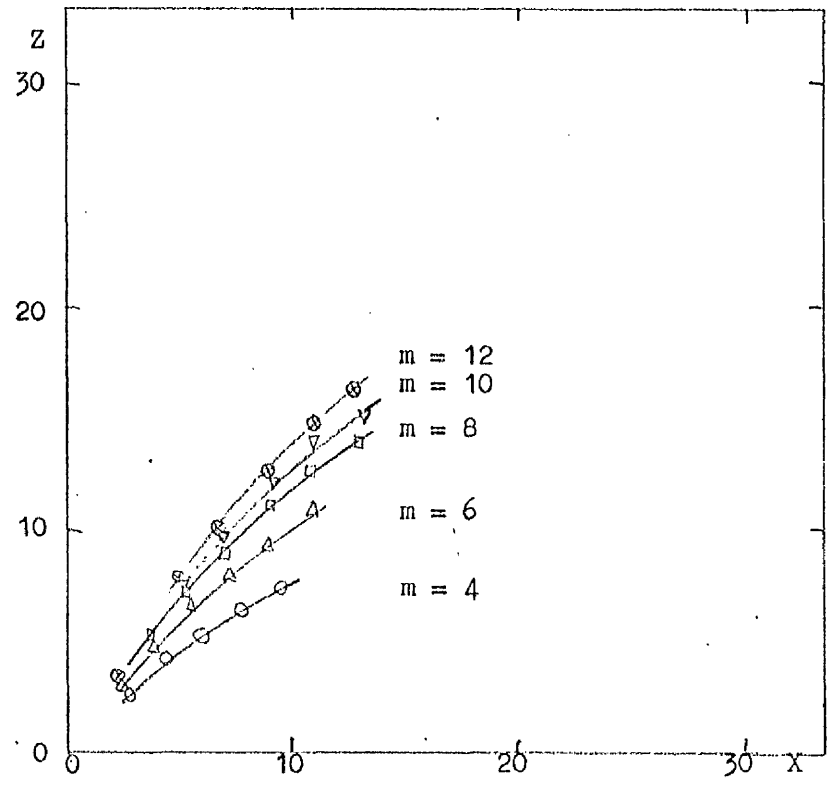

Figure 4.28. Jet Trajectory (ϕ = 30°, α = 4°).

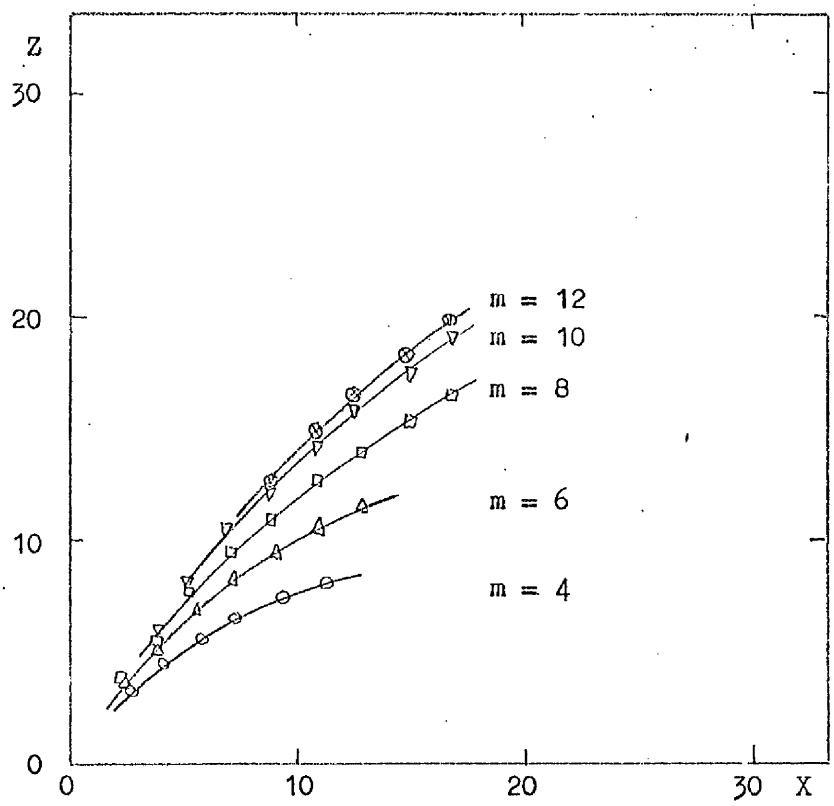

Figure 4.29. Jet Trajectory ($\phi = 30°$, $\alpha = 6°$).

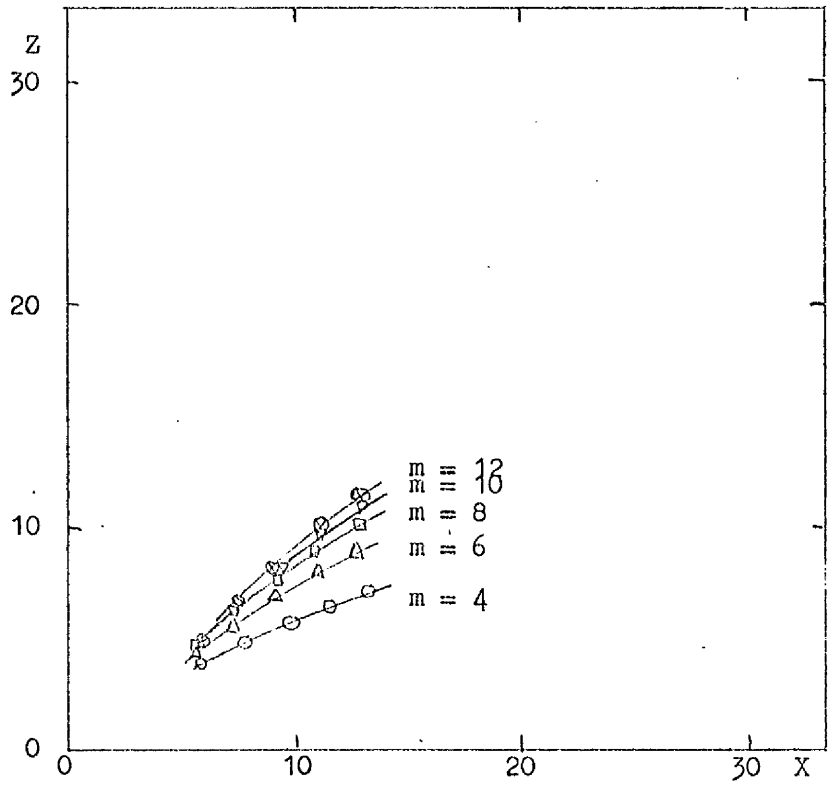

Figure 4.30. Jet Trajectory ($\phi = 45°$, $\alpha = 0°$).

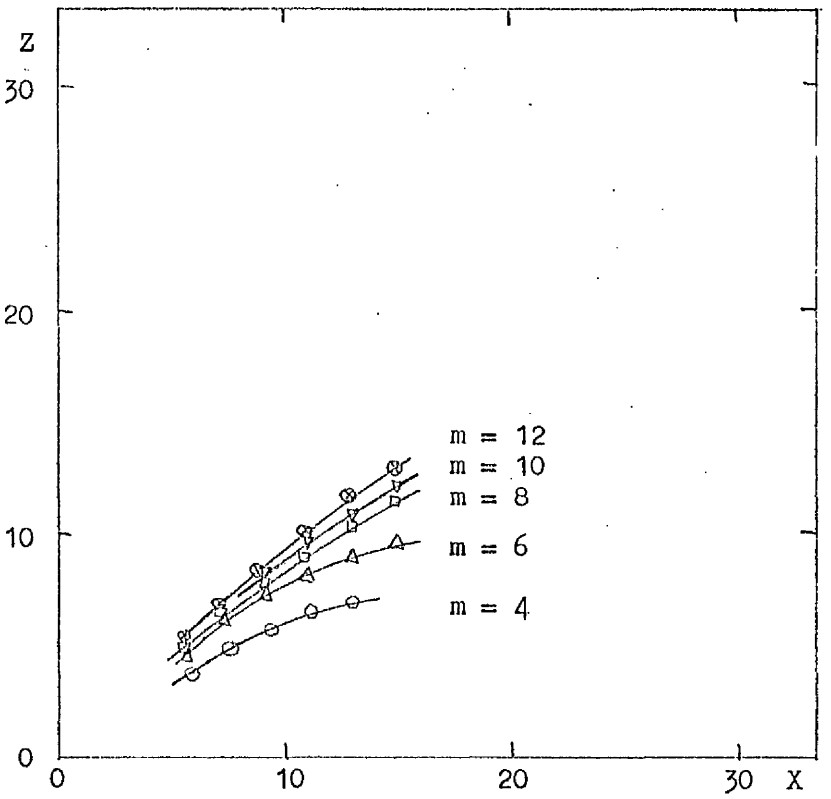

Figure 4.31. Jet Trajectory ($\phi = 45°$, $\alpha = 2°$).

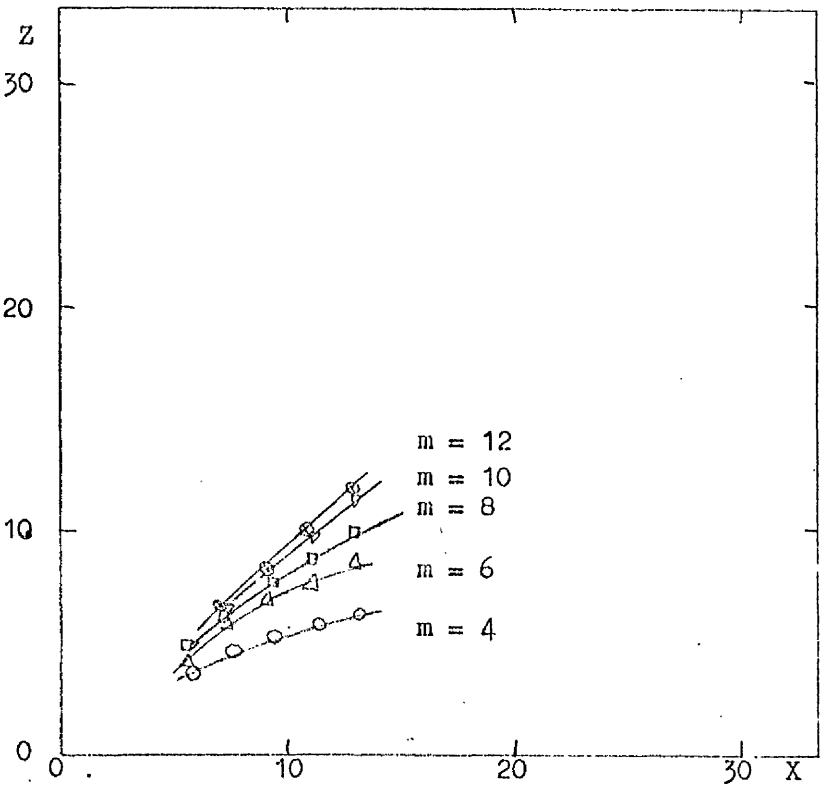

Figure 4.32. Jet Trajectory ($\phi = 45°$, $\alpha = 4°$).

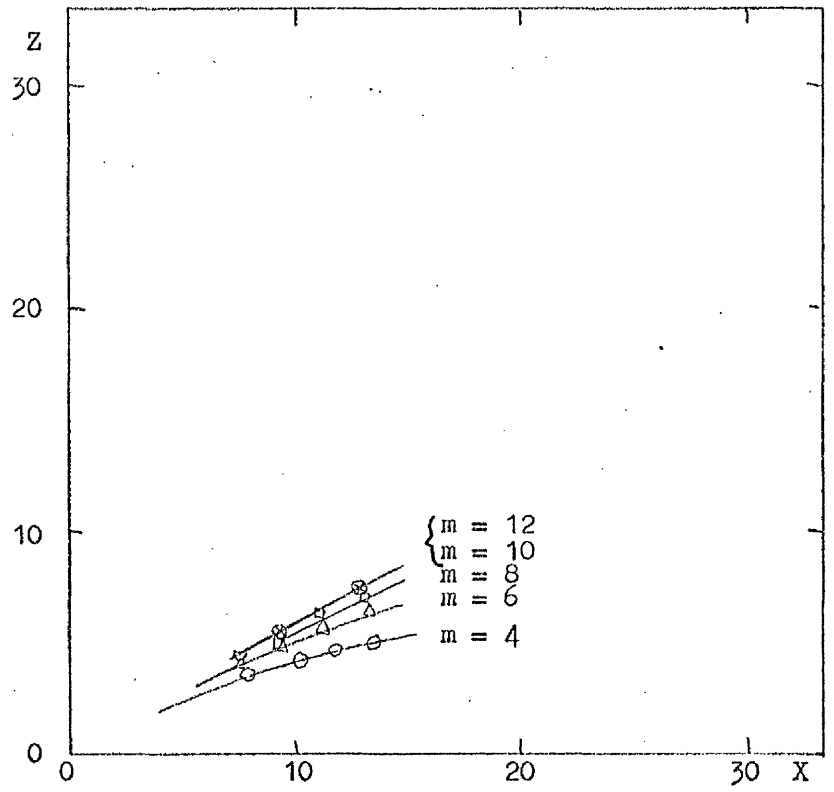

Figure 4.33. Jet Trajectory ($\phi = 60^{\circ}$, $\alpha = 0^{\circ}$).

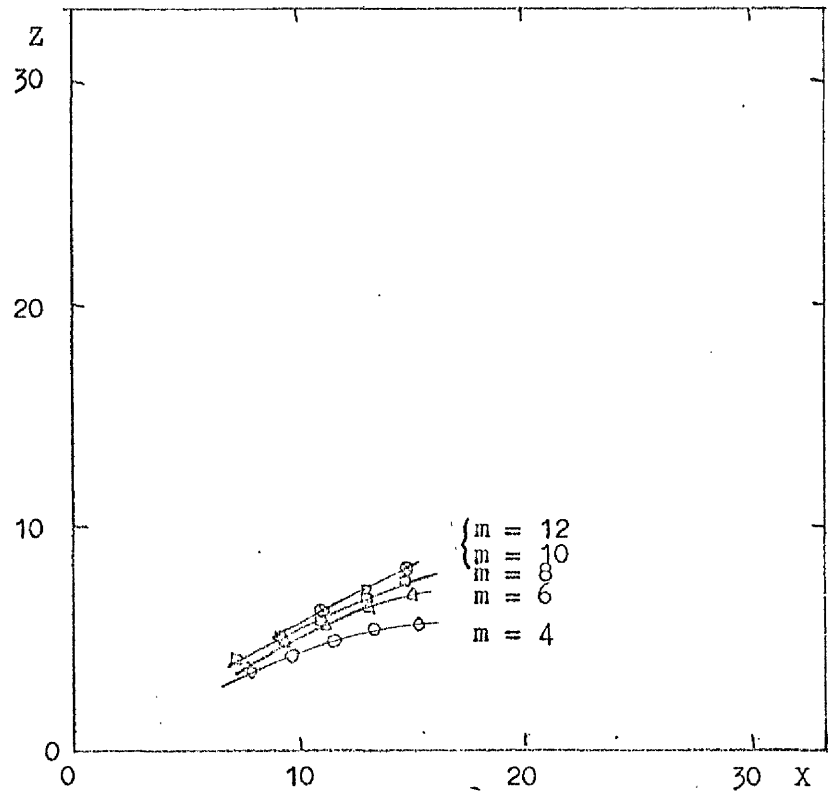

Figure 4.34. Jet Trajectory ($\phi = 60^{\circ}$, $\alpha = 2^{\circ}$).

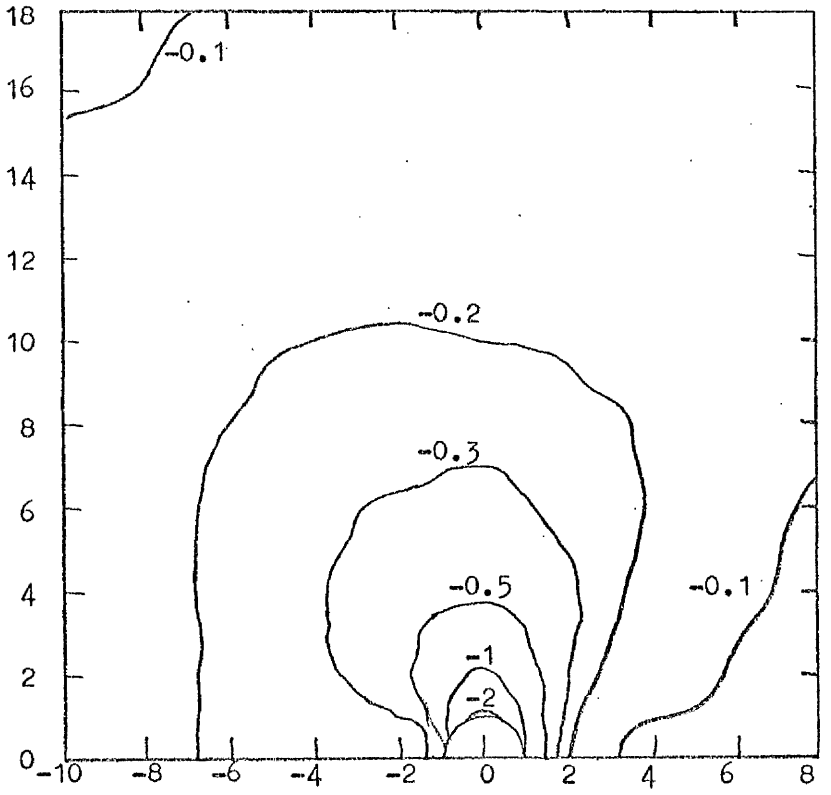

Figure 4.35. Surface Pressure Distribution (ϕ = 0°, α = 0°, m = 12).

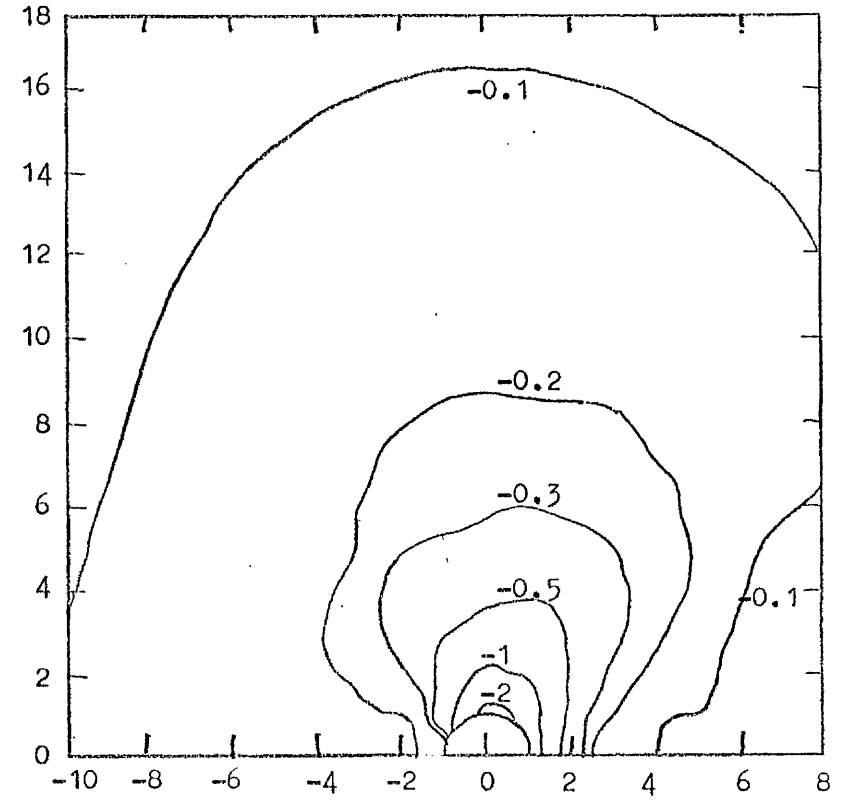

Figure 4.36. Surface Pressure Distribution (ϕ = 15°, α = 0°, m = 12).

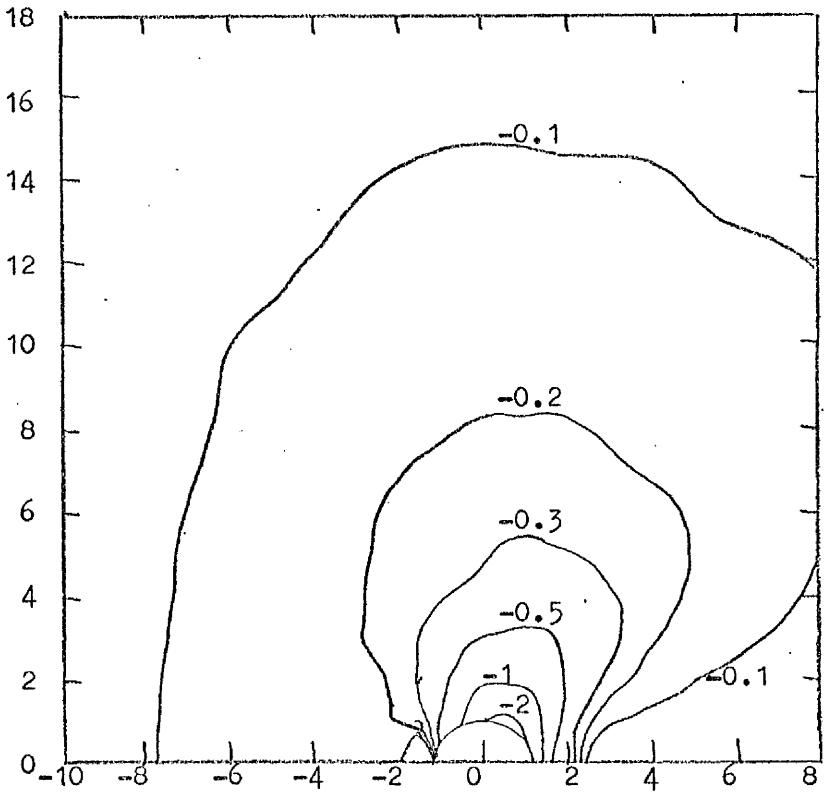

Figure 4.37. Surface Pressure Distribution ($\phi = 30°$, $\alpha = 0°$, m = 12).

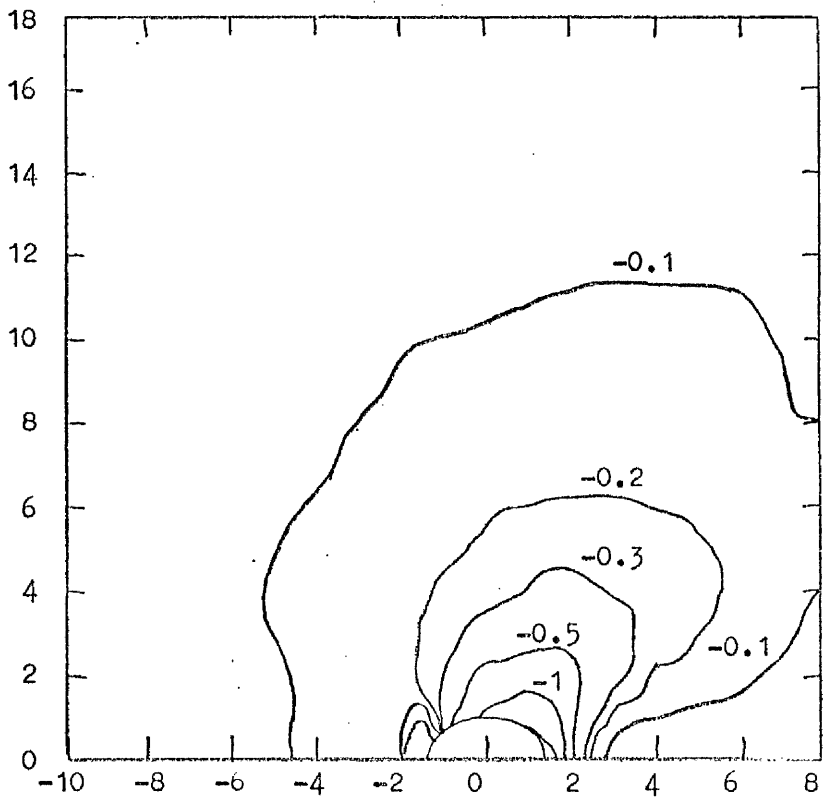

Figure 4.38. Surface Pressure Distribution ($\phi = 45°$, $\alpha = 0°$, m = 12).

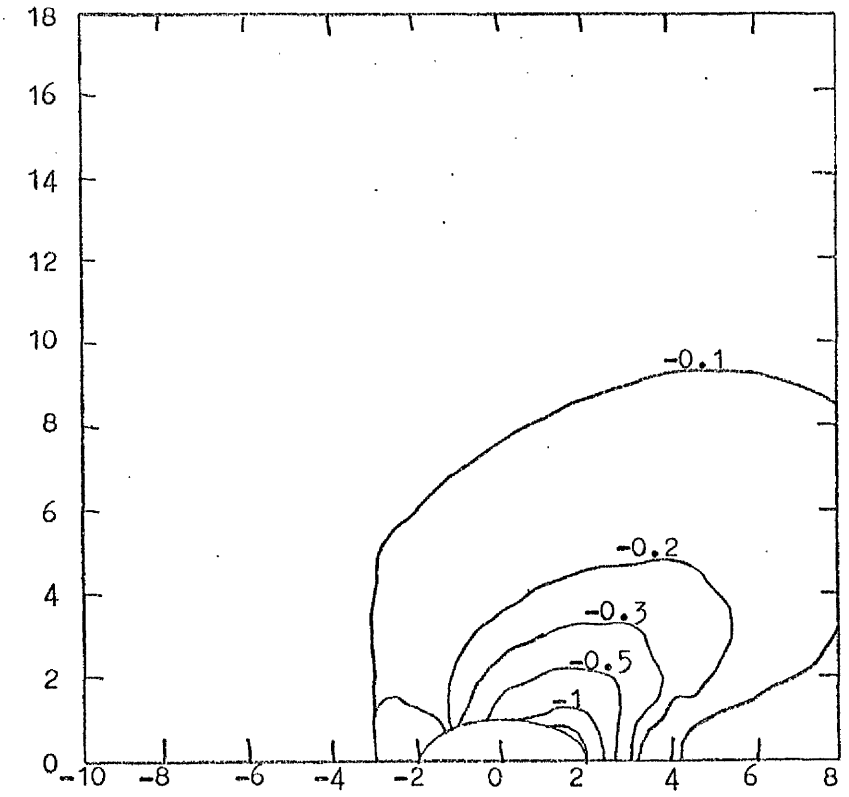

Figure 4.39. Surface Pressure Distribution ($\phi = 60^{\circ}$, $\alpha = 0^{\circ}$, m = 12).

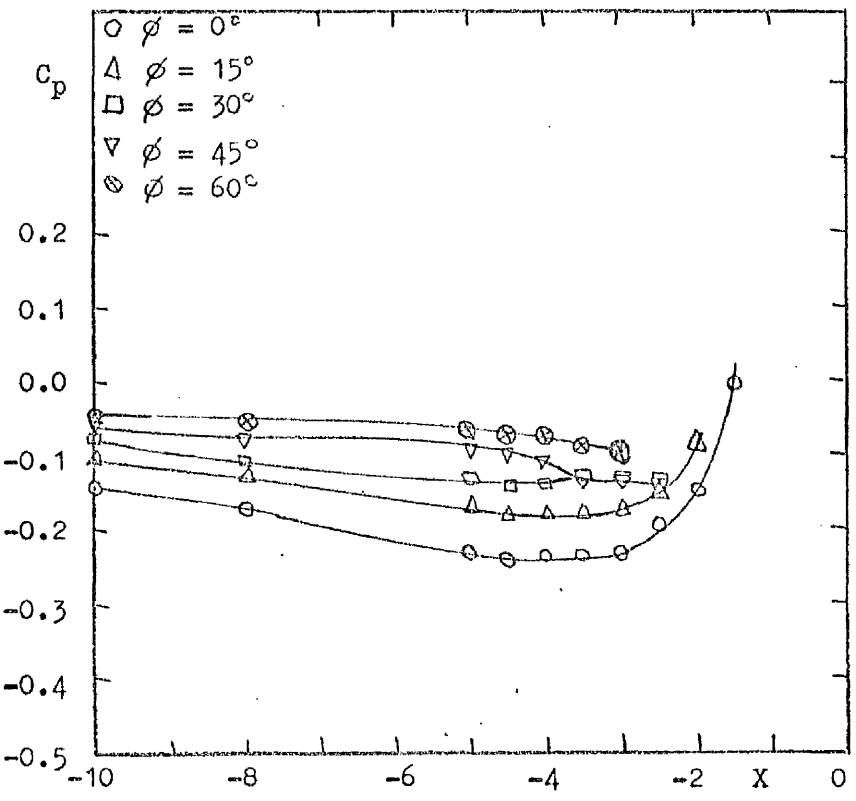

Figure 4.40. Upstream Centreline Pressure Distribution

($\alpha = 0^{\circ}$, m = 12).

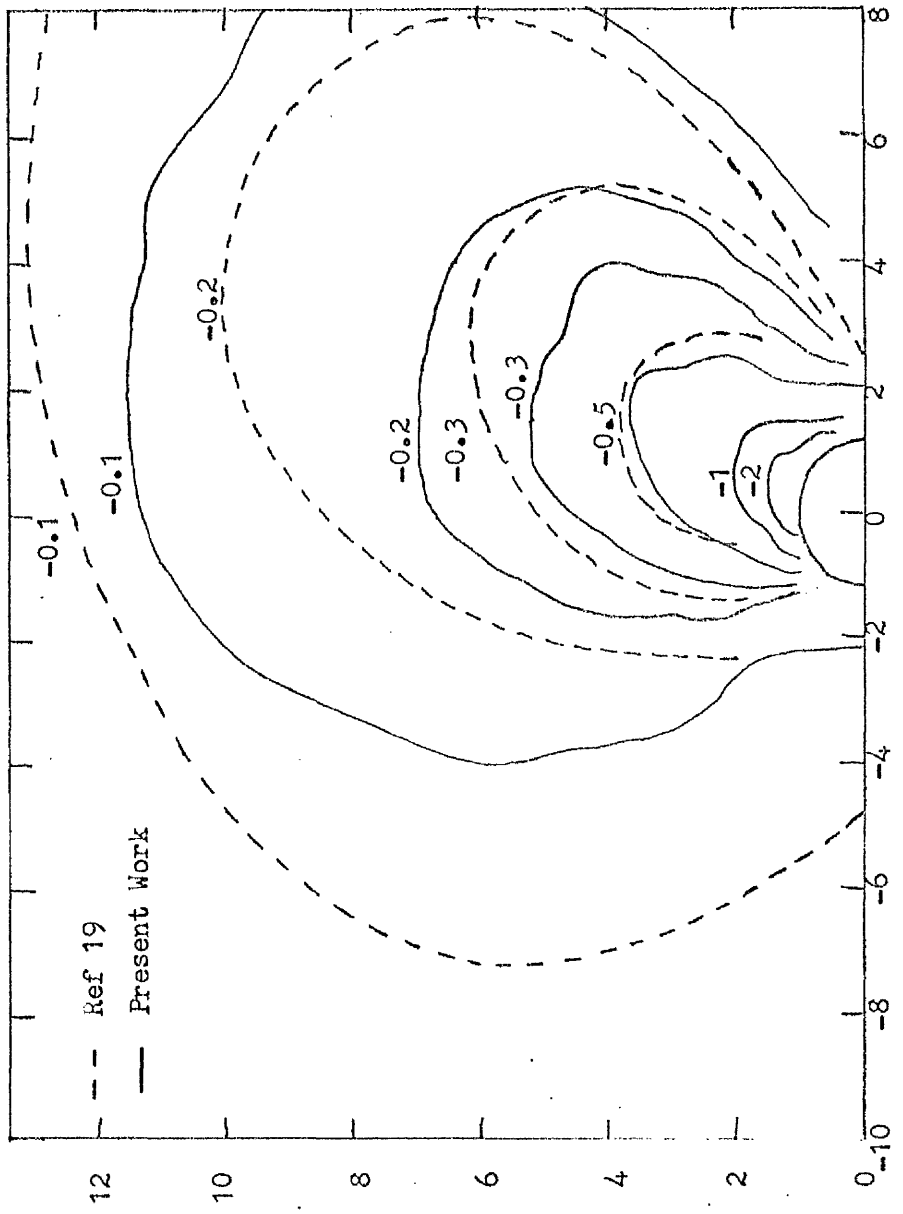

Figure 4.41. Surface Pressure Distribution ($\phi = 30^\circ, \alpha = 0^\circ$, m = 8)

A Comparison with Reference 19.

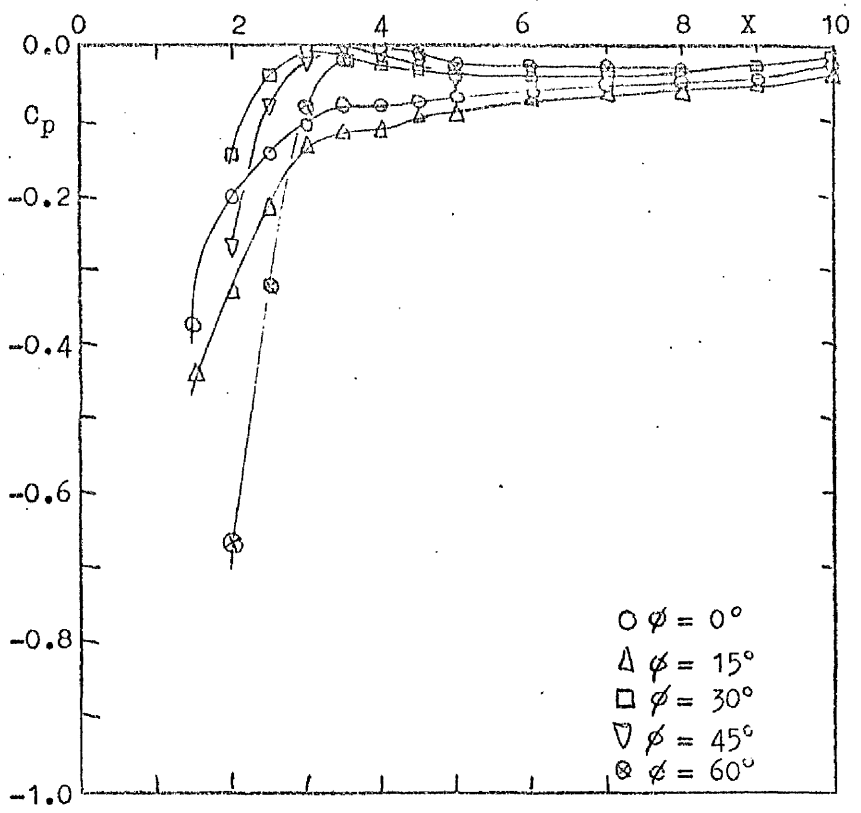

Figure 4.42. Downstream Centreline Pressure Distribution

($\alpha = 0^\circ$, m = 12).

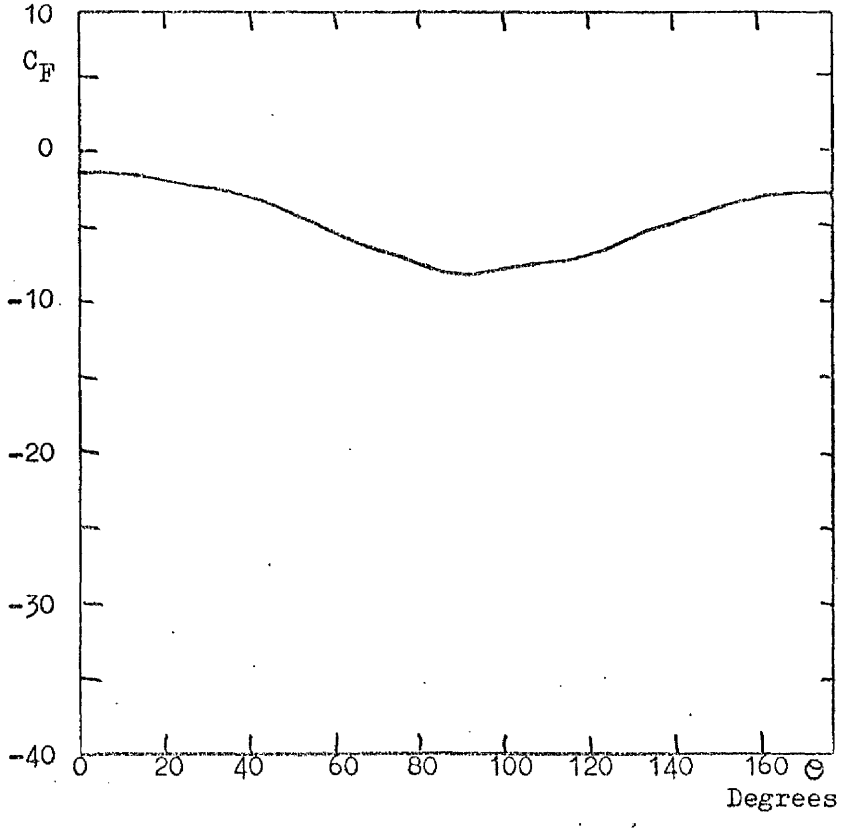

Figure 4.43. Surface Force Distribution ($\psi = 0^\circ, \alpha = 0^\circ$, m = 12, R_2 = 5)

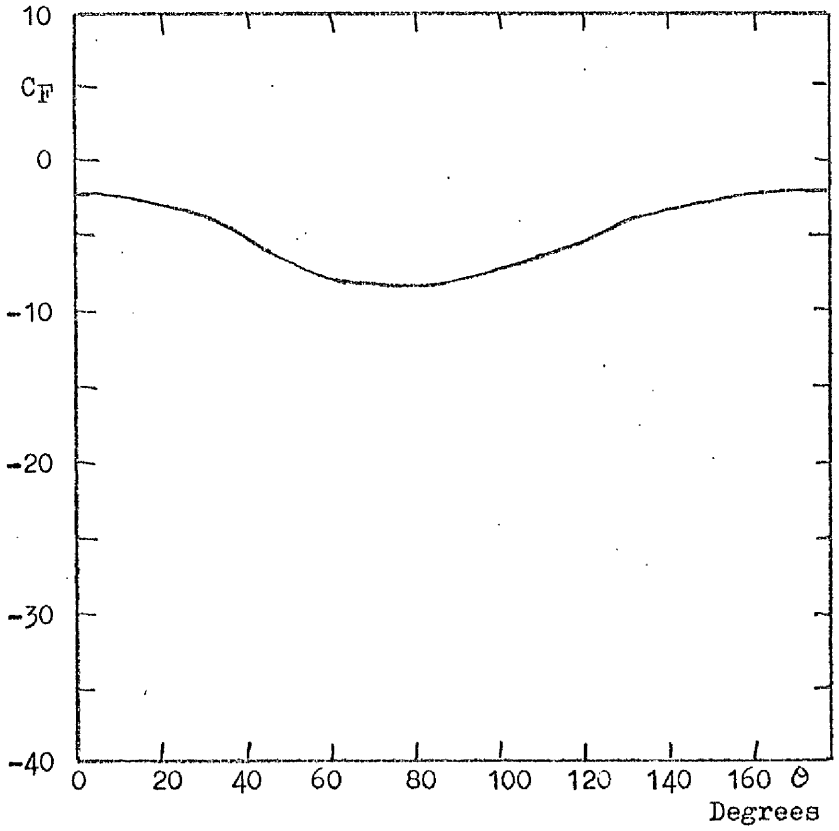

Figure 4.44. Surface Force Distribution ($\phi = 15^\circ, \alpha = 0^\circ, m = 12, R_2 = 5$)

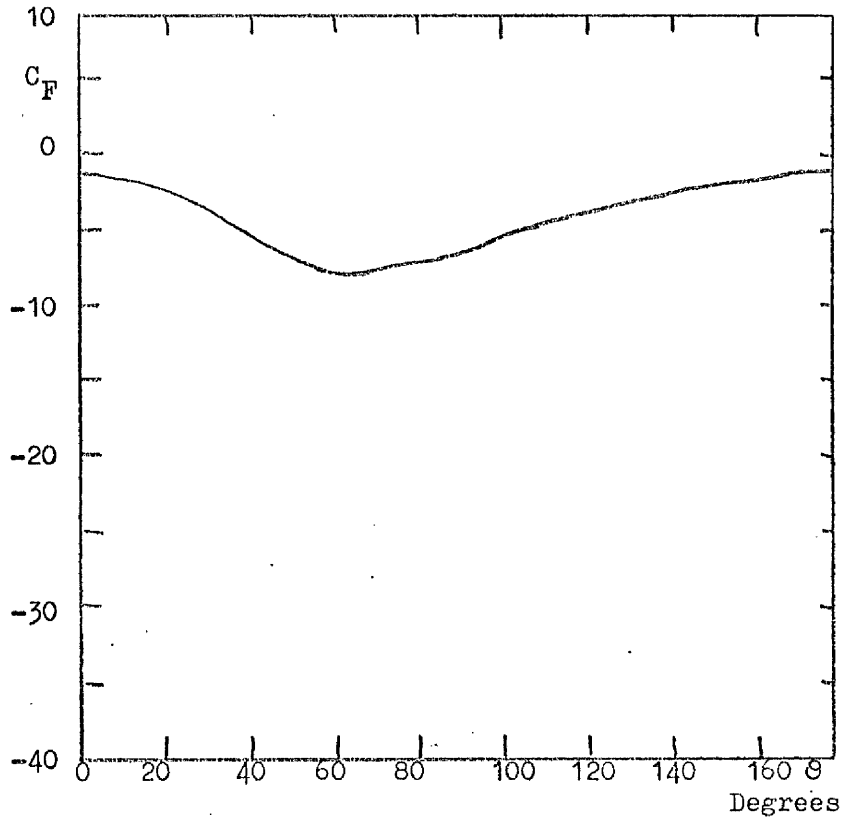

Figure 4.45. Surface Force Distribution ($\phi = 30^\circ, \alpha = 0^\circ, m = 12, R_2 = 5$)

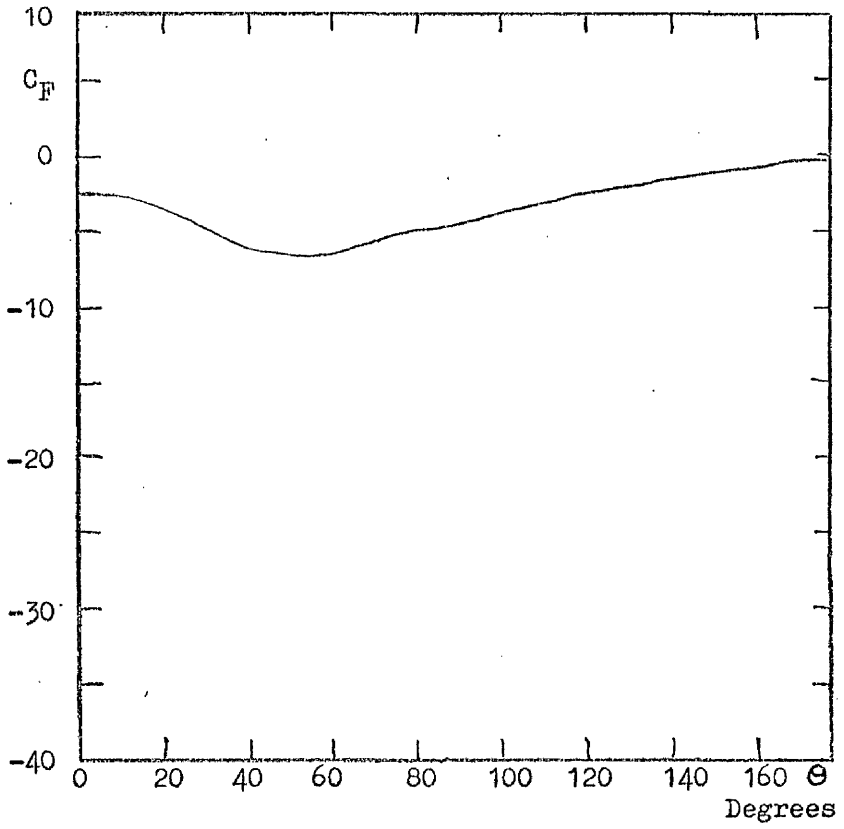

Figure 4.46. Surface Force Distribution ($\phi = 45°, \alpha = 0°, m = 12, R_2 = 5$)

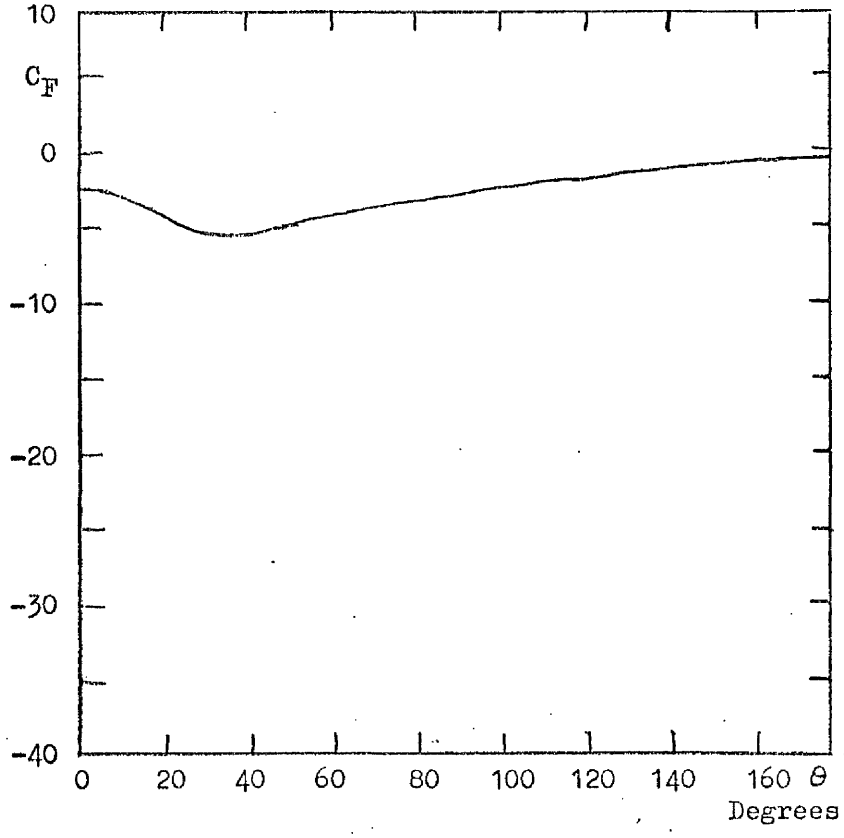

Figure 4.47. Surface Force Distribution ($\phi = 60°, \alpha = 0°, m = 12, R_2 = 5$)

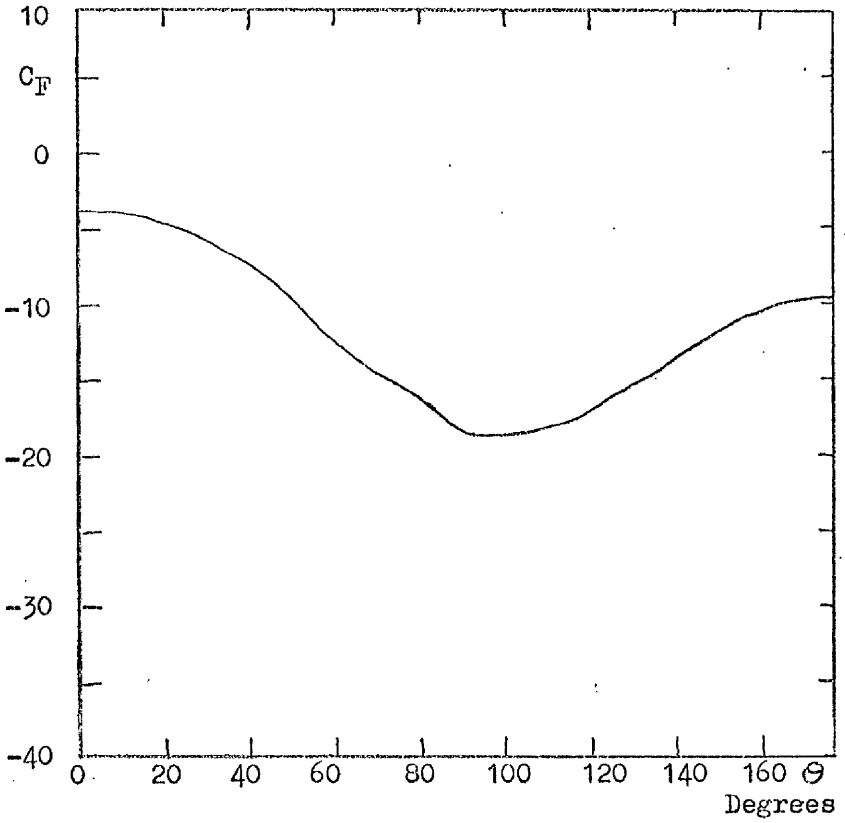

Figure 4.48. Surface Force Distribution ($\phi = 0^\circ, \alpha = 0^\circ, m = 12, R_2 = 10$)

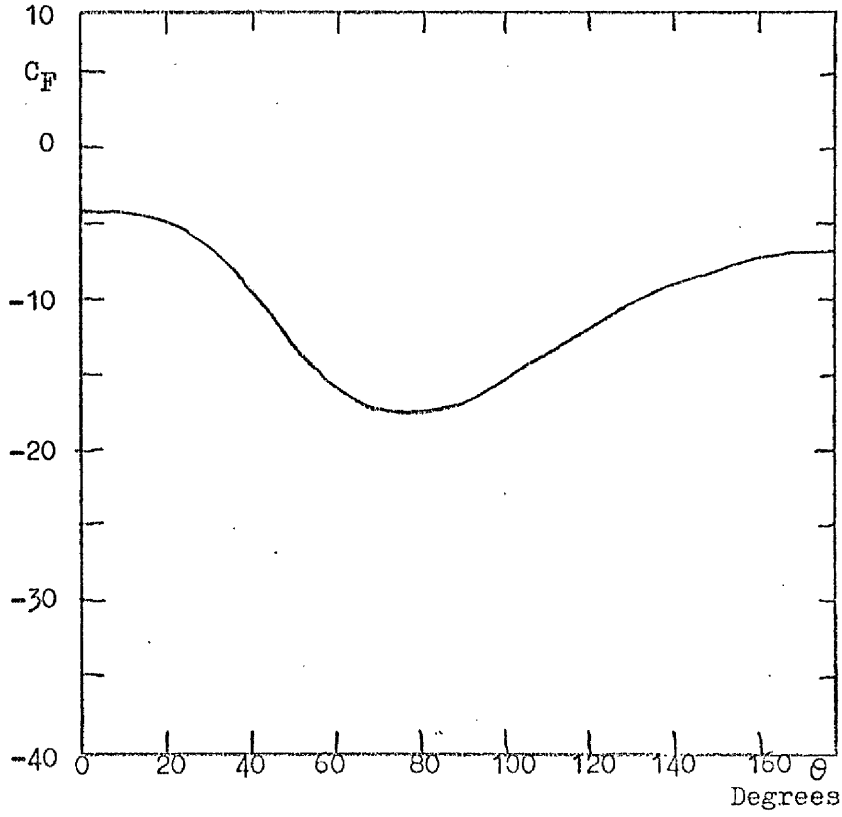

Figure 4.49. Surface Force Distribution ($\phi = 15^\circ, \alpha = 0^\circ, m = 12, R_2 = 10$)

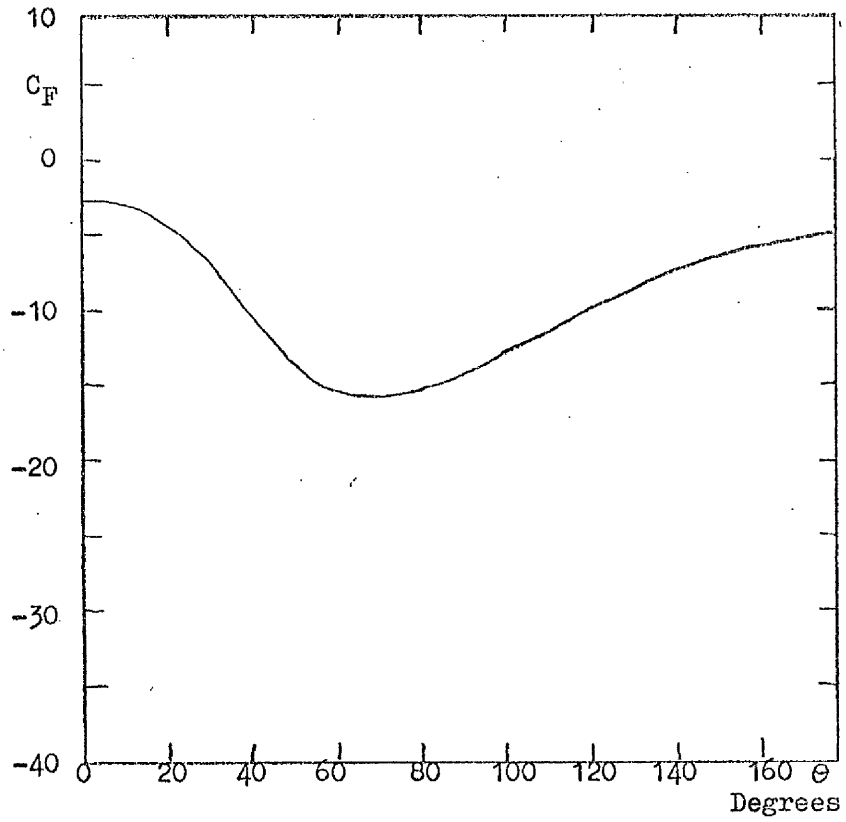

Figure 4.50. Surface Force Distribution ($\phi = 30^\circ, \alpha = 0^\circ, m = 12, R_2 = 10$)

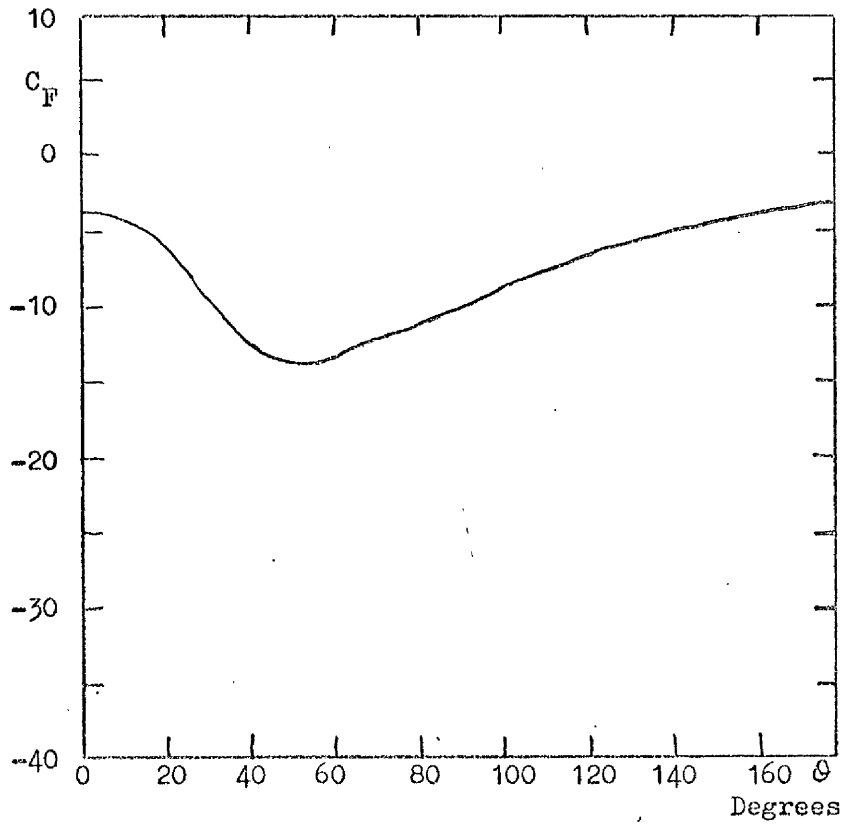

Figure 4.51. Surface Force Distribution ($\phi = 45^\circ, \alpha = 0^\circ, m = 12, R_2 = 10$)

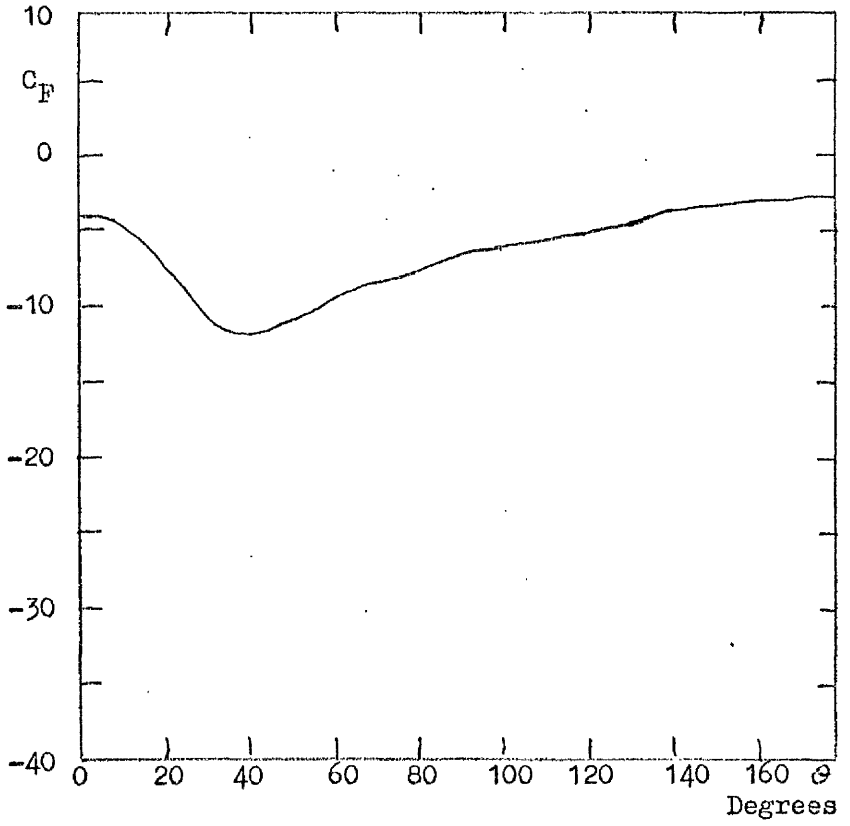

Figure 4.52. Surface Force Distribution ($\phi = 60°$, $\alpha = 0°$, $m = 12$, $R_2 = 10$)

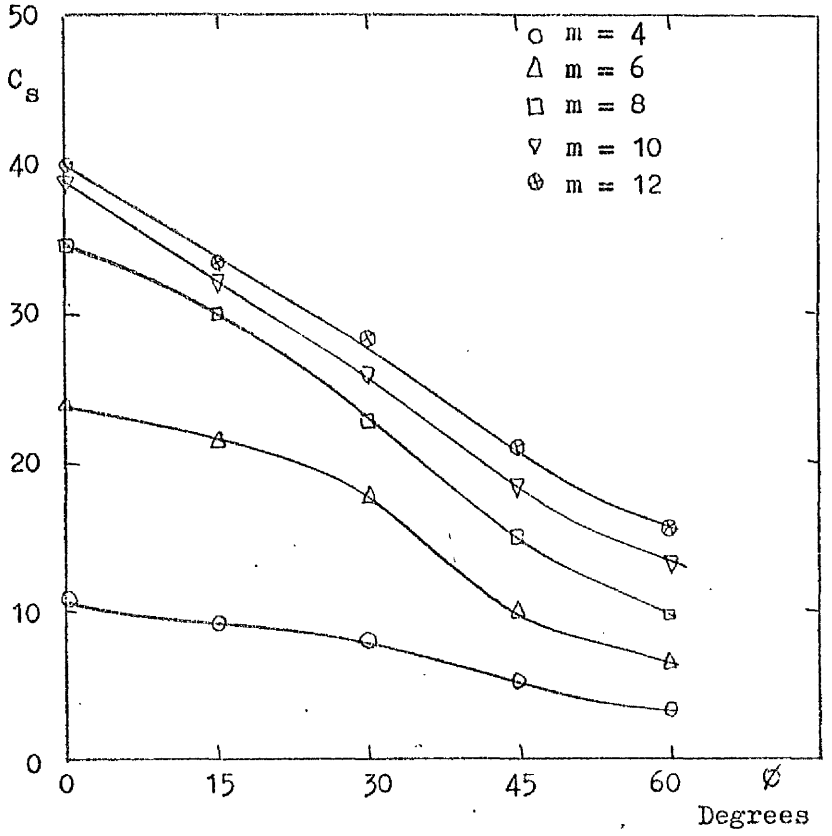

Figure 4.53. Variation of Suction Force Coefficient with Inclination ($\alpha = 0°$).

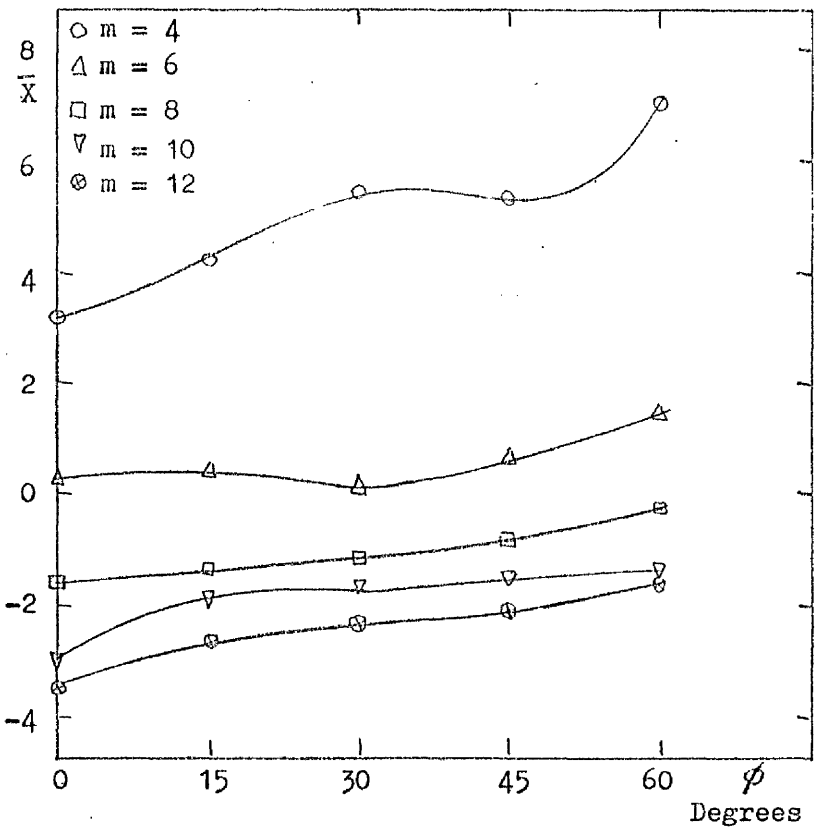

Figure 4.54. Variation of Centre of Pressure with Inclination ($\alpha = 0°$)

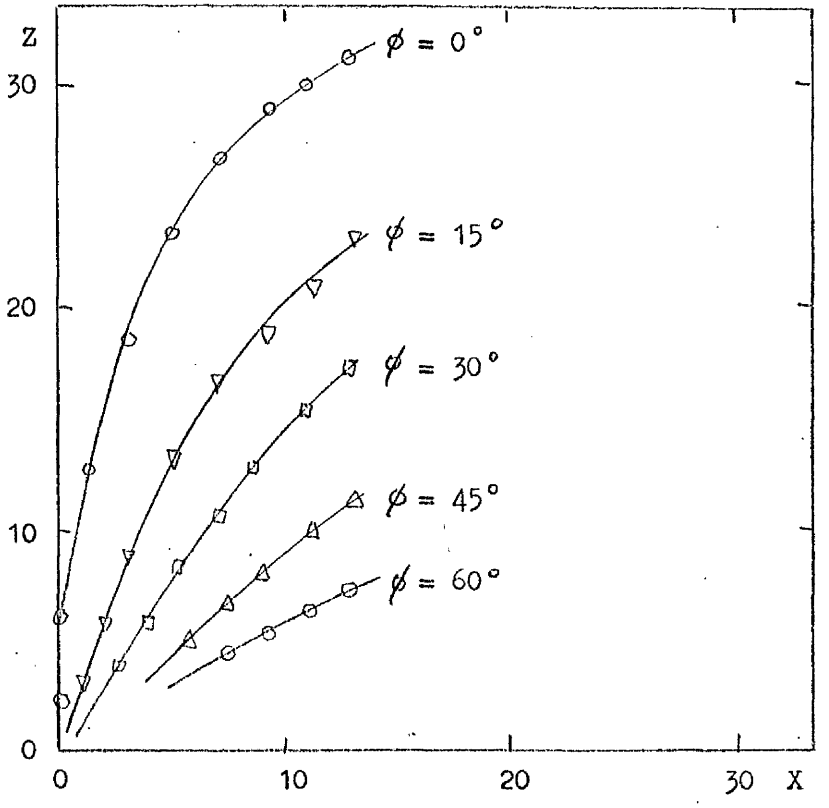

Figure 4.55. Jet Trajectory ($\alpha = 0°$, m = 12).

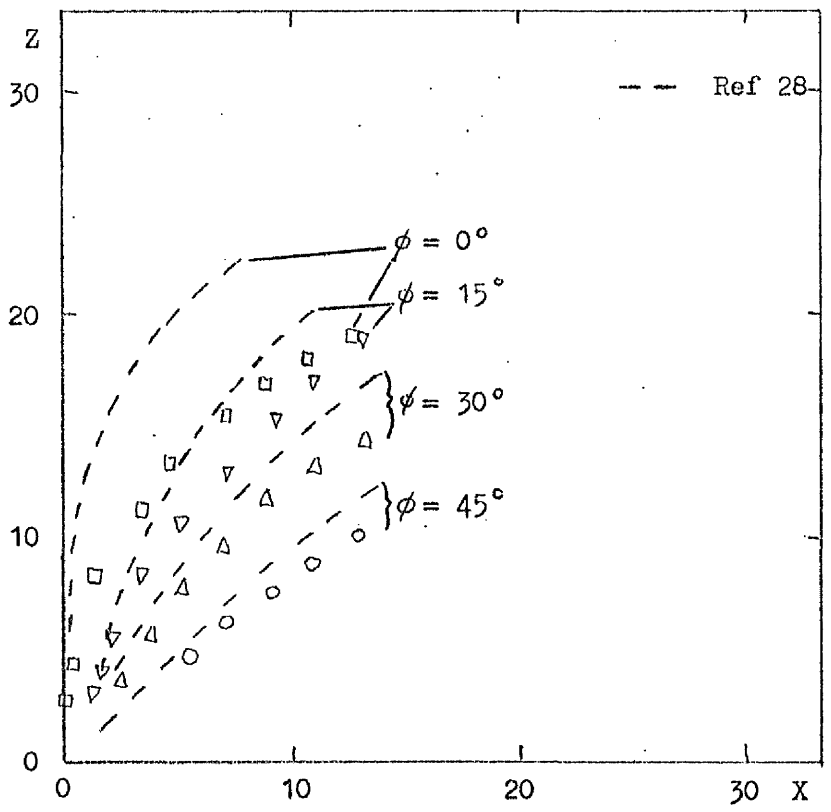

Figure 4.56. Jet Trajectory ($\alpha = 0°$, m = 8)

A Comparison with Reference 28.

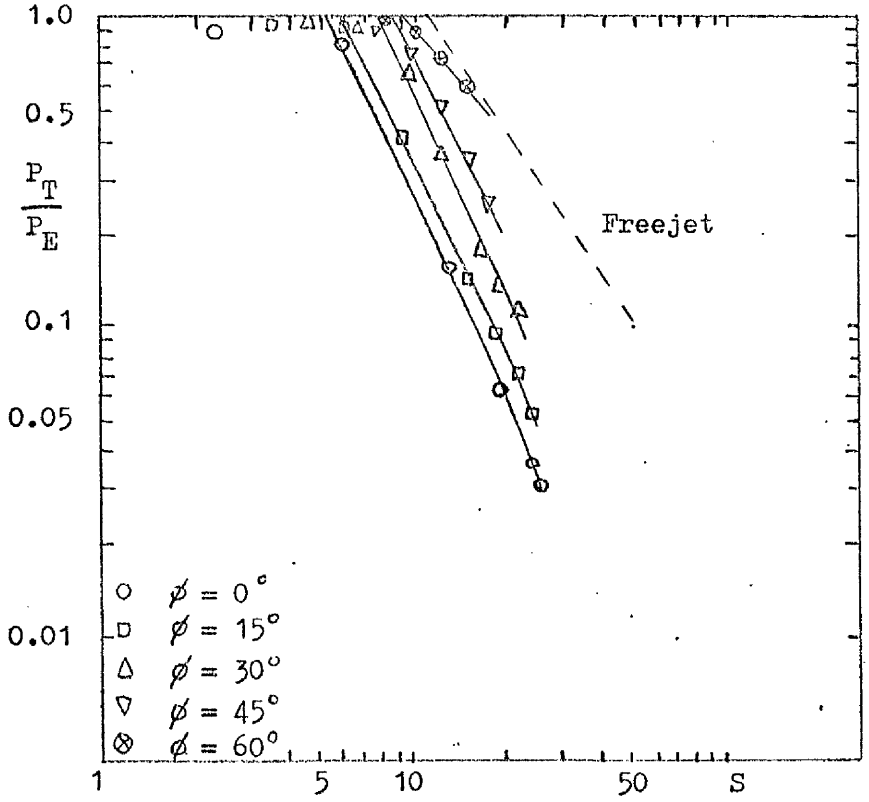

Figure 4.57. Total Pressure Decay Rate ($\alpha = 0°$, m = 12).

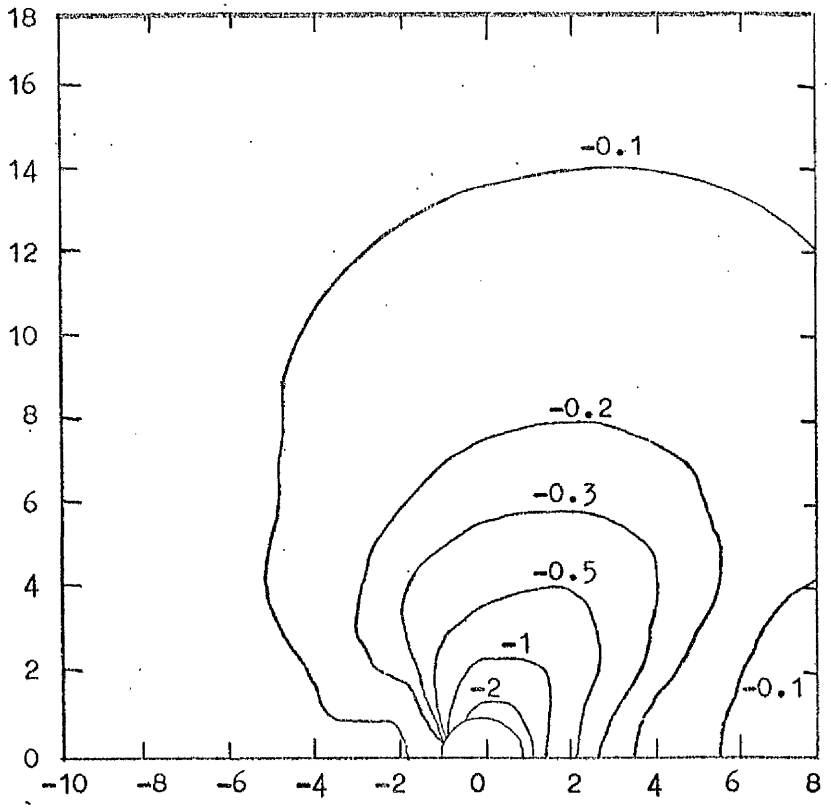

Figure 4.58. Surface Pressure Distribution ($\phi = 15^{\circ}, \alpha = 0^{\circ}$, m = 8).

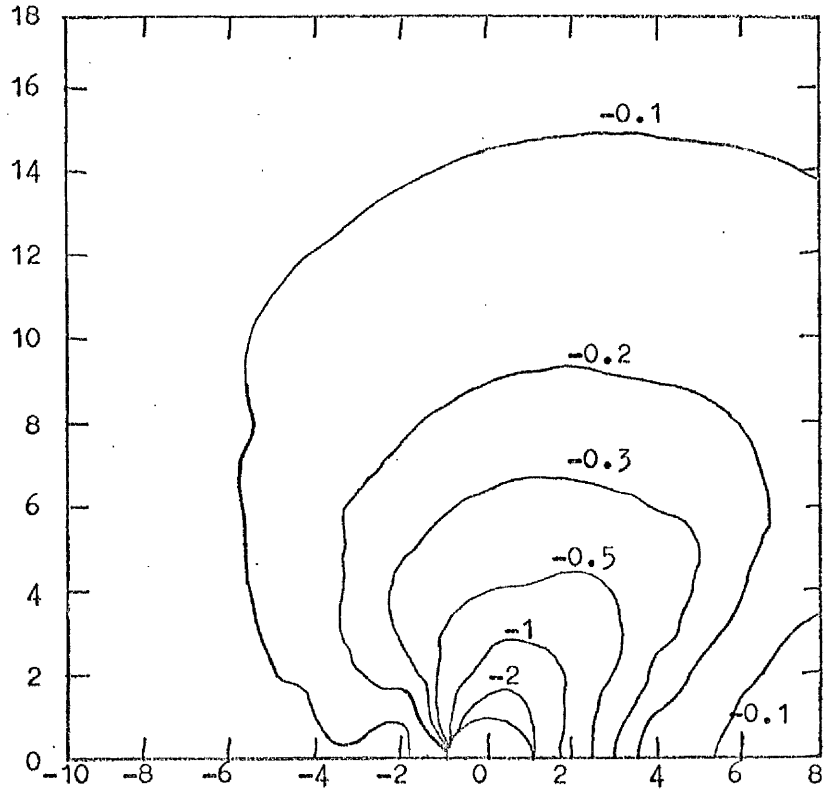

Figure 4.59. Surface Pressure Distribution ($\phi = 15^{\circ}$, $\alpha = 2^{\circ}$, m = 8).

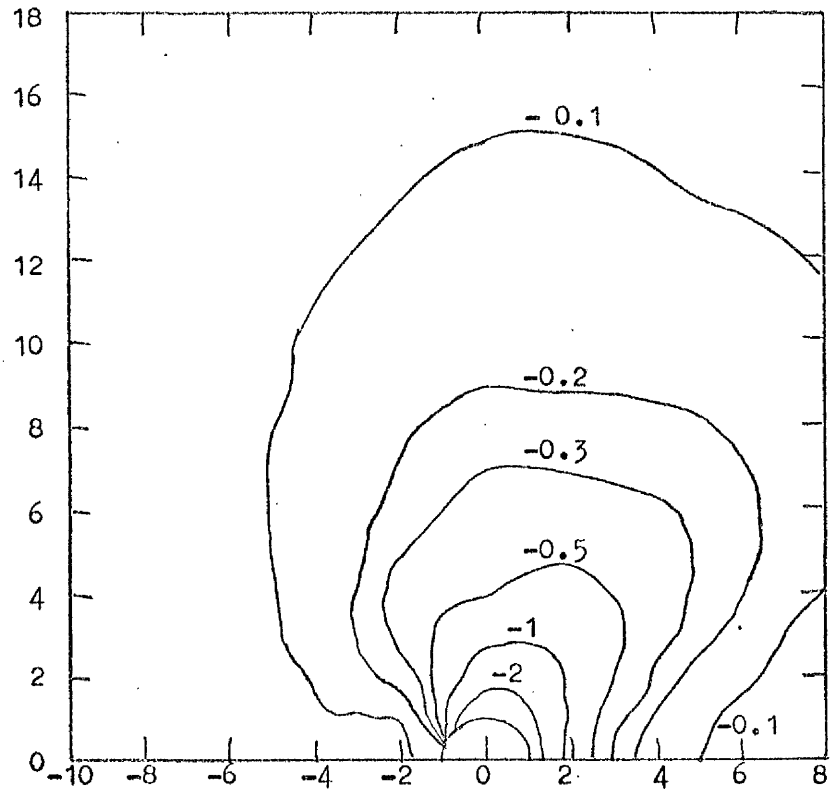

Figure 4.60. Surface Pressure Distribution ($\phi = 15^{\circ}$, $\alpha = 4^{\circ}$, m = 8).

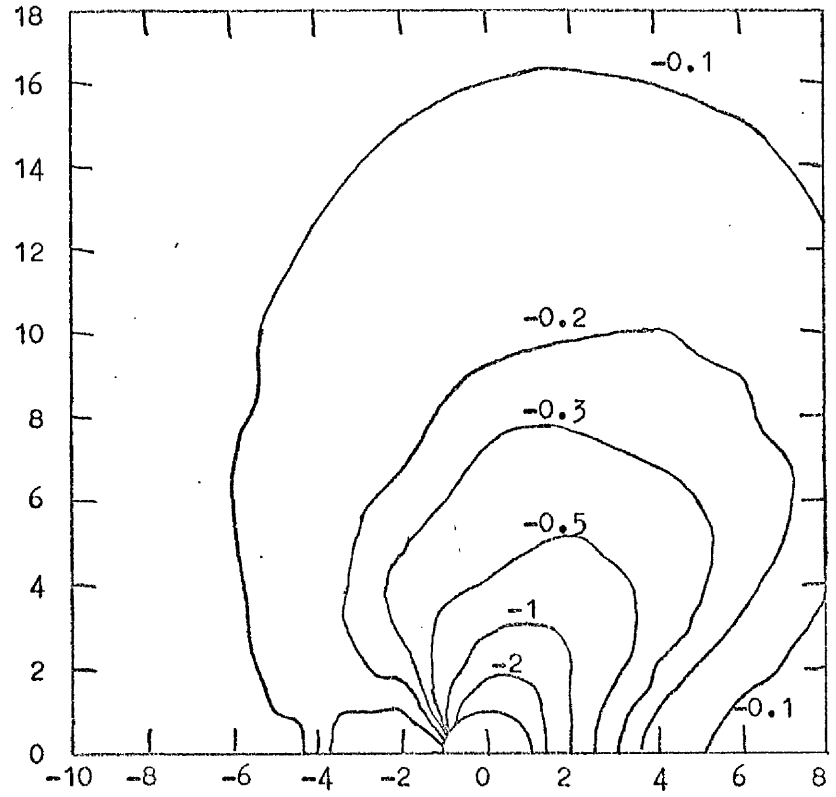

Figure 4.61. Surface Pressure Distribution ($\phi = 15^{\circ}$, $\alpha = 6^{\circ}$, m = 8).

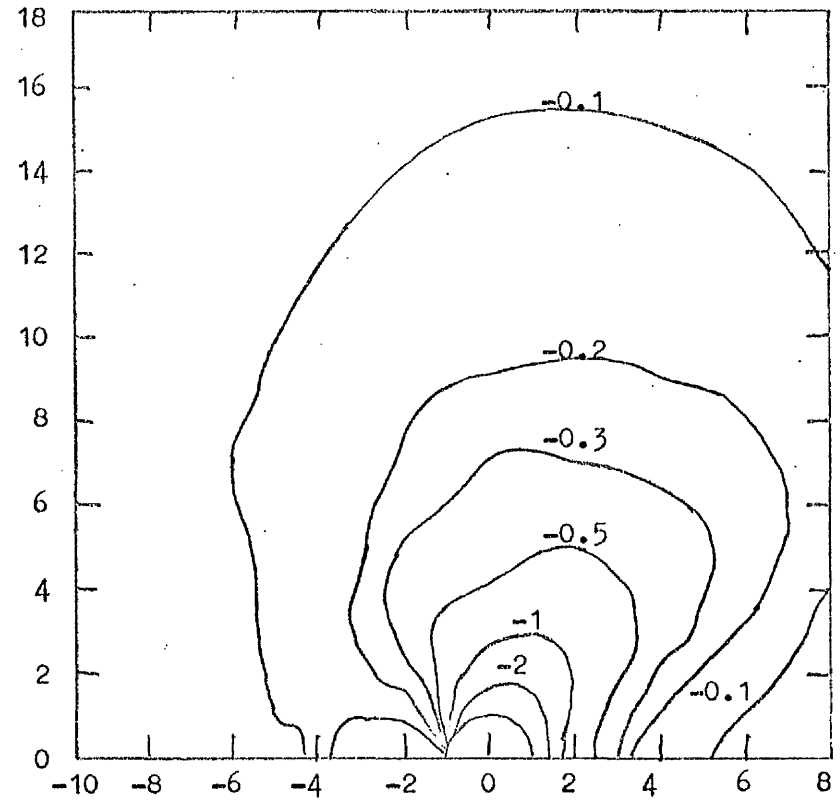

Figure 4.62. Surface Pressure Distribution ($\phi = 15^{\circ}$, $\alpha = 8^{\circ}$, m = 8).

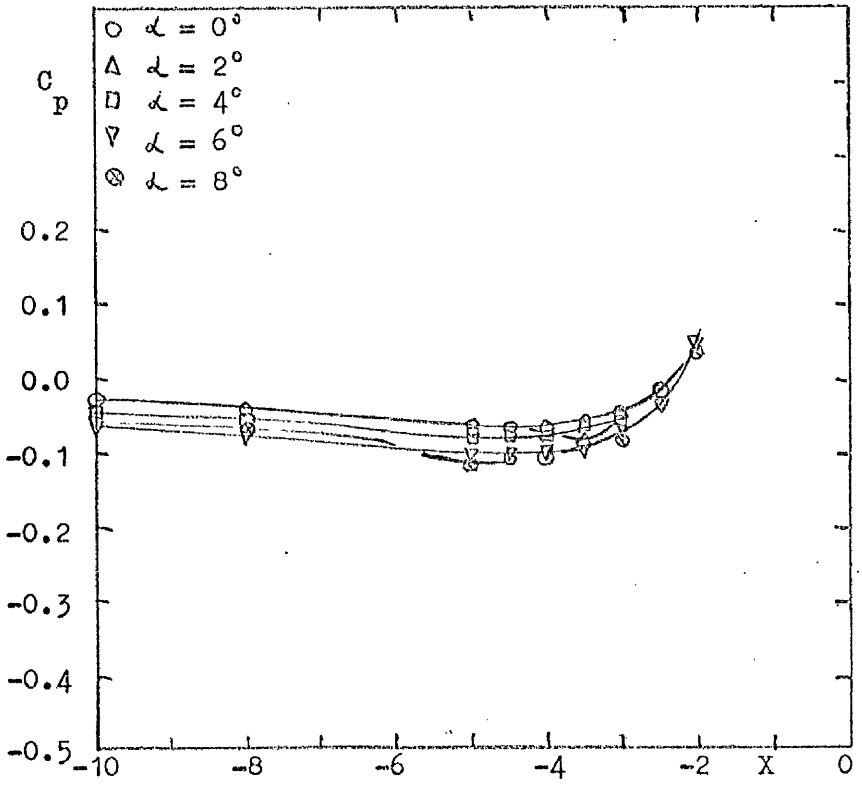

Figure 4.63. Upstream Centreline Pressure Distribution

($\phi = 15^{\circ}$, m = 8).

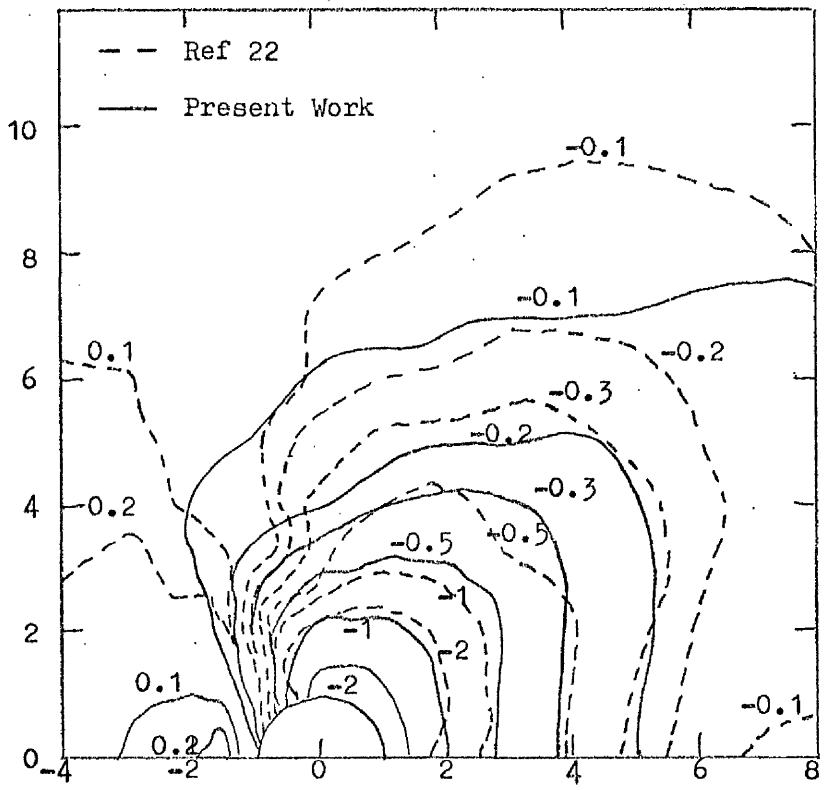

Figure 4.64. Surface Pressure Distribution ($\phi = 0°$, $\alpha = 0°$, m = 4)

A Comparison of Flat Plate with Wing.

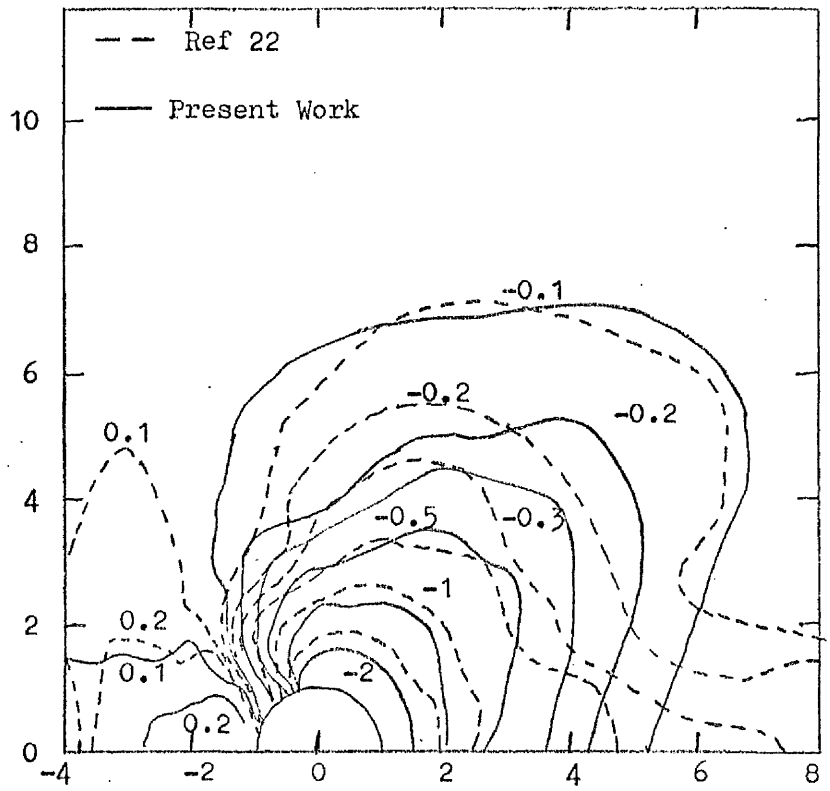

Figure 4.65. Surface Pressure Distribution ($\phi = 0°$, $\alpha = 6°$, m = 4)

A Comparison of Flat Plate with Wing.

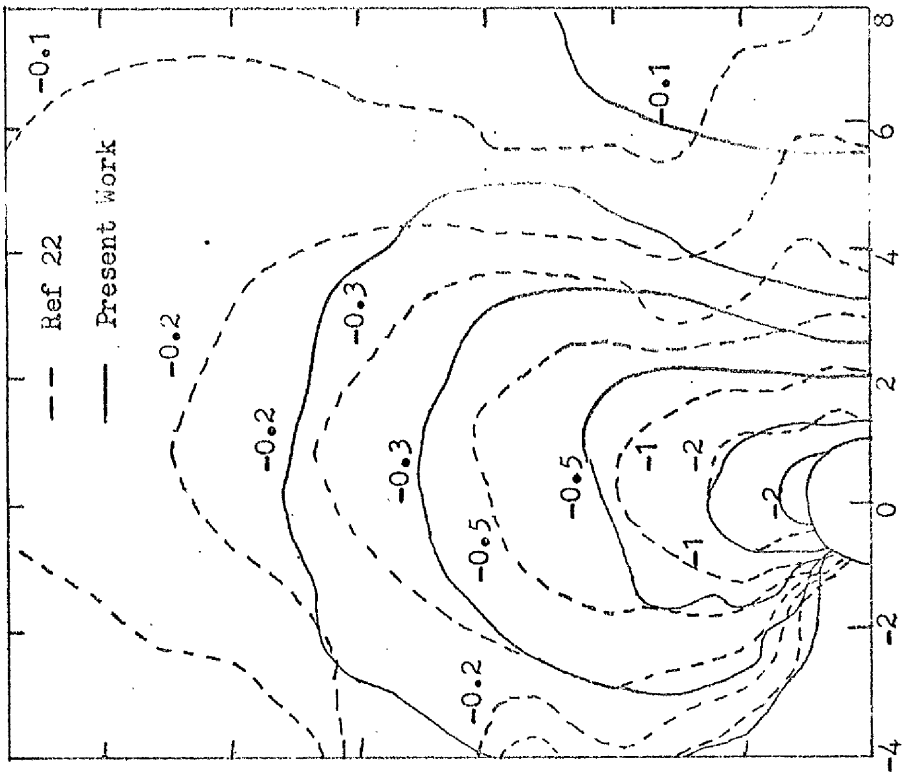

Figure 4.66. Surface Pressure Distribution ($\phi = 0°$, $\alpha = 0°$, m = 8)

A Comparison of Flat Plate with Wing.

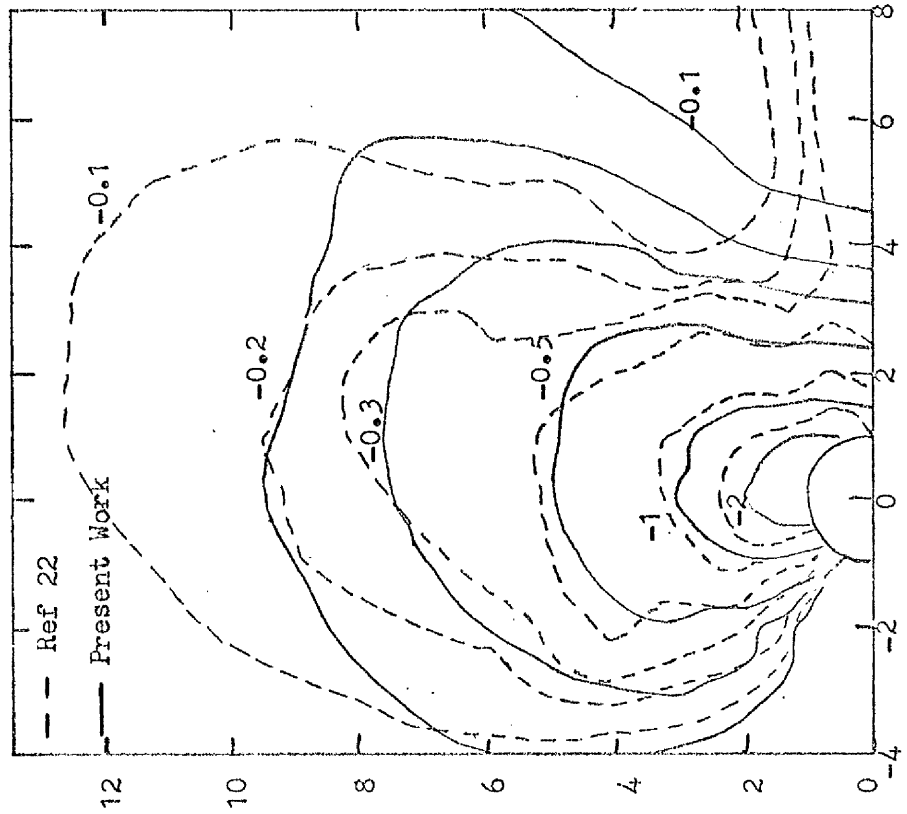

Figure 4.67. Surface Pressure Distribution ($\phi = 0°$, $\alpha = 6°$, m = 8)

A Comparison of Flat Plate with Wing.

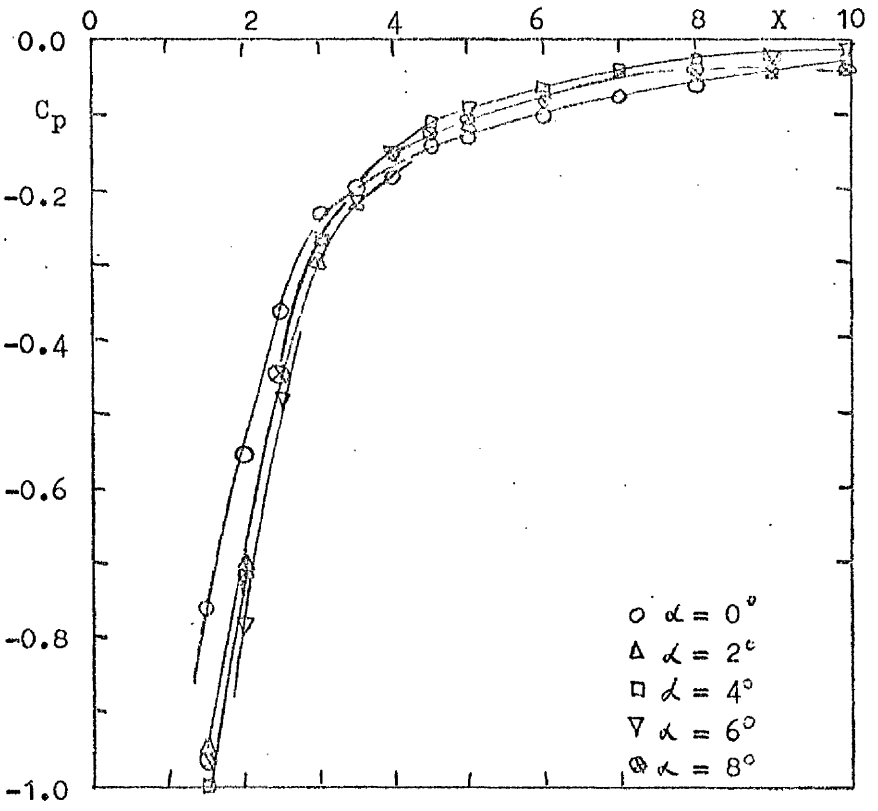

Figure 4.68. Downstream Centreline Pressure Distribution ($\phi = 15^\circ$, m = 8).

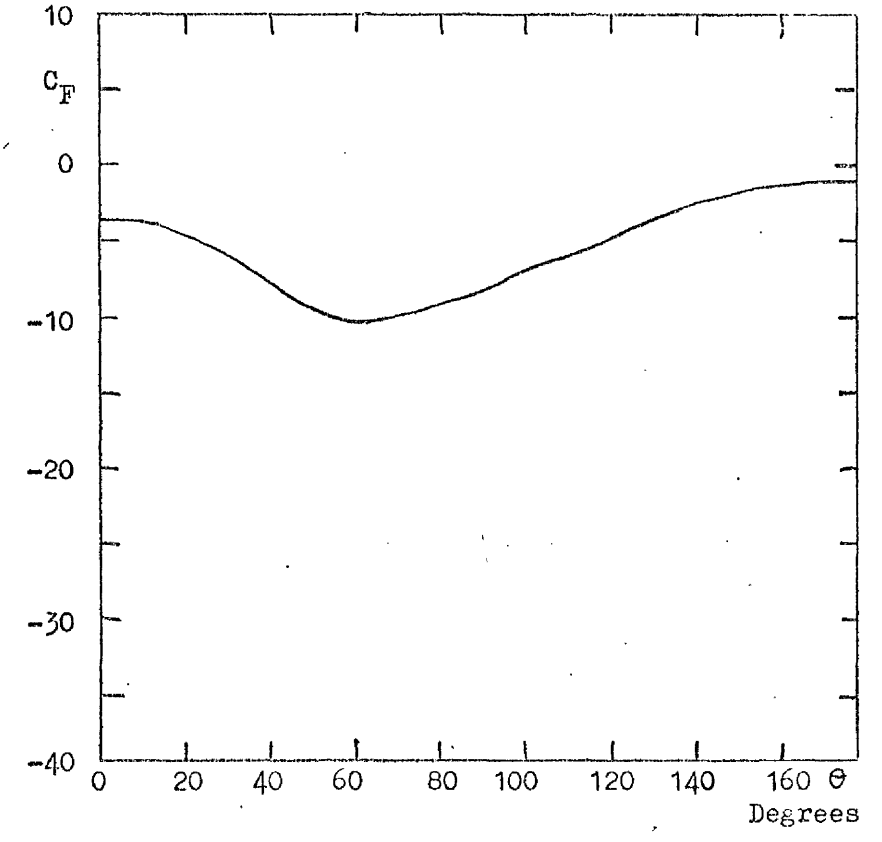

Figure 4.69. Surface Force Distribution ($\phi = 15^\circ$, $\alpha = 0^\circ$, m = 8, $R_2 = 5$)

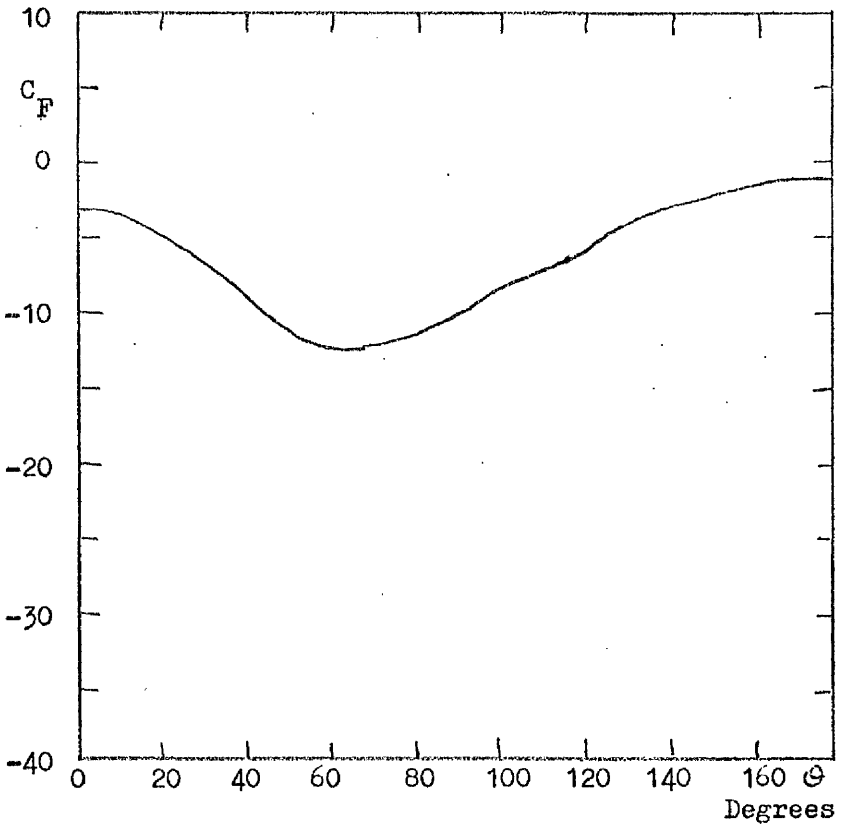

Figure 4.70. Surface Force Distribution ($\psi = 15^\circ, \alpha = 2^\circ, m = 8, R_2 = 5$).

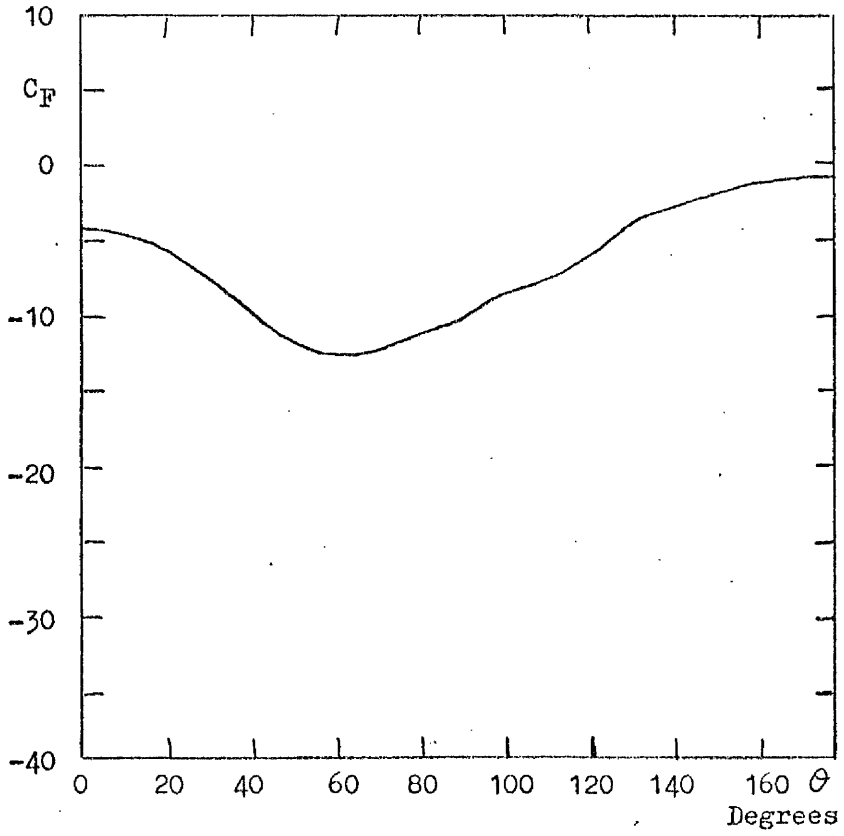

Figure 4.71. Surface Force Distribution ($\phi = 15^\circ, \alpha = 4^\circ, m = 8, R_2 = 5$).

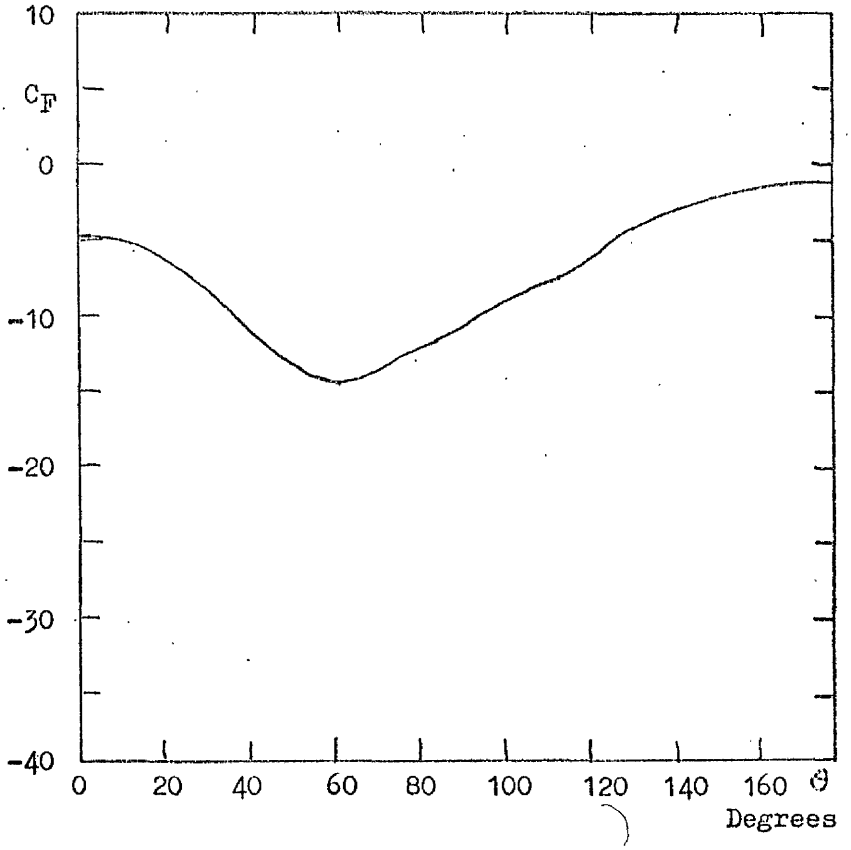

Figure 4.72. Surface Force Distribution (ϕ=15°, α= 6°, m = 8, R_2 = 5).

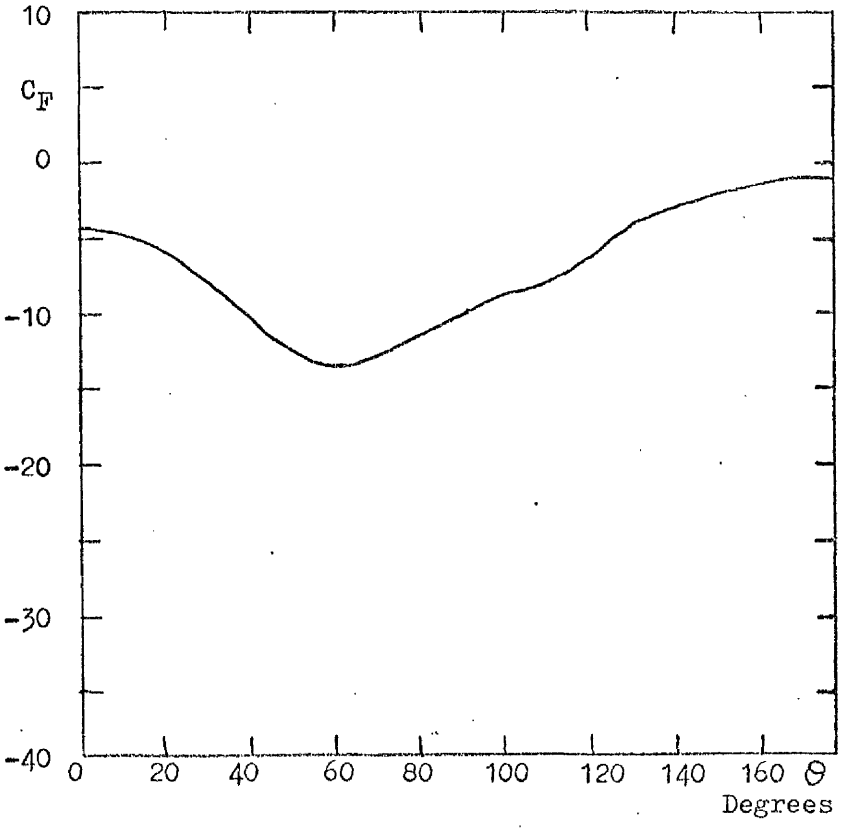

Figure 4.73. Surface Force Distribution (ϕ =15°, α= 8°, m = 8, R_2 = 5).

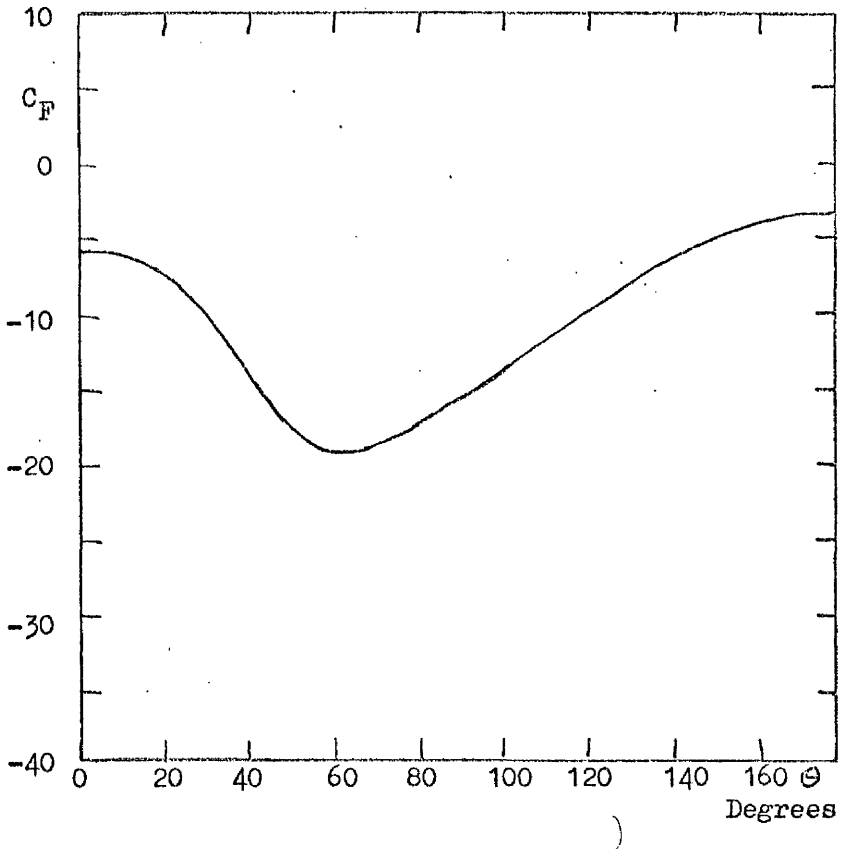

Figure 4.74. Surface Force Distribution ($\phi = 15^\circ, \alpha = 0^\circ, m = 8, R_2 = 10$).

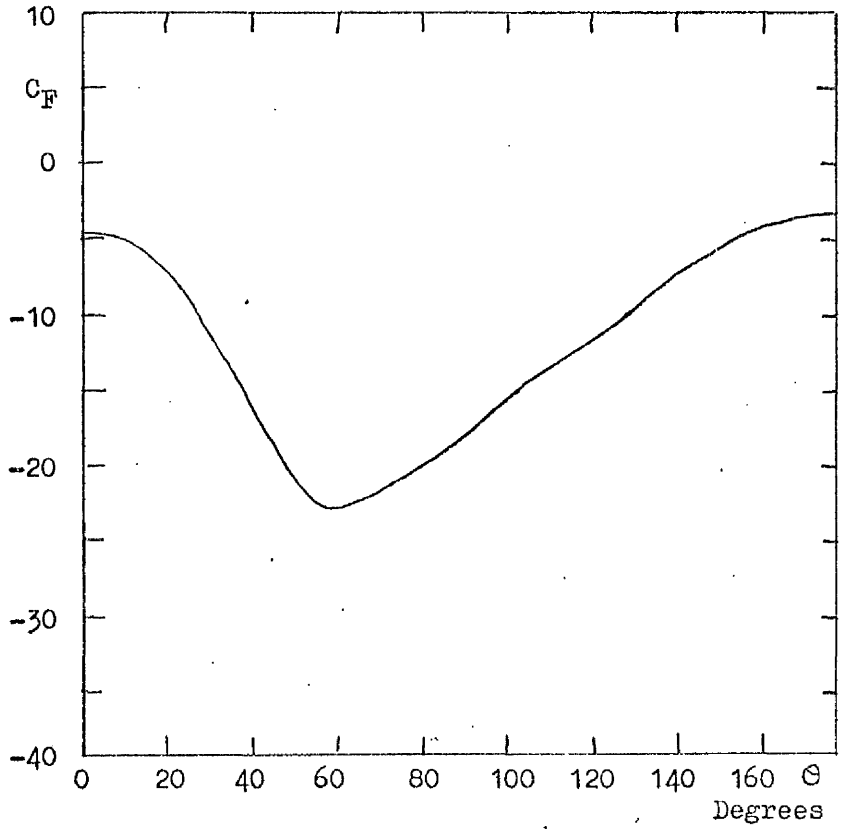

Figure 4.75. Surface Force Distribution ($\phi = 15^\circ, \alpha = 2^\circ, m = 8, R_2 = 10$).

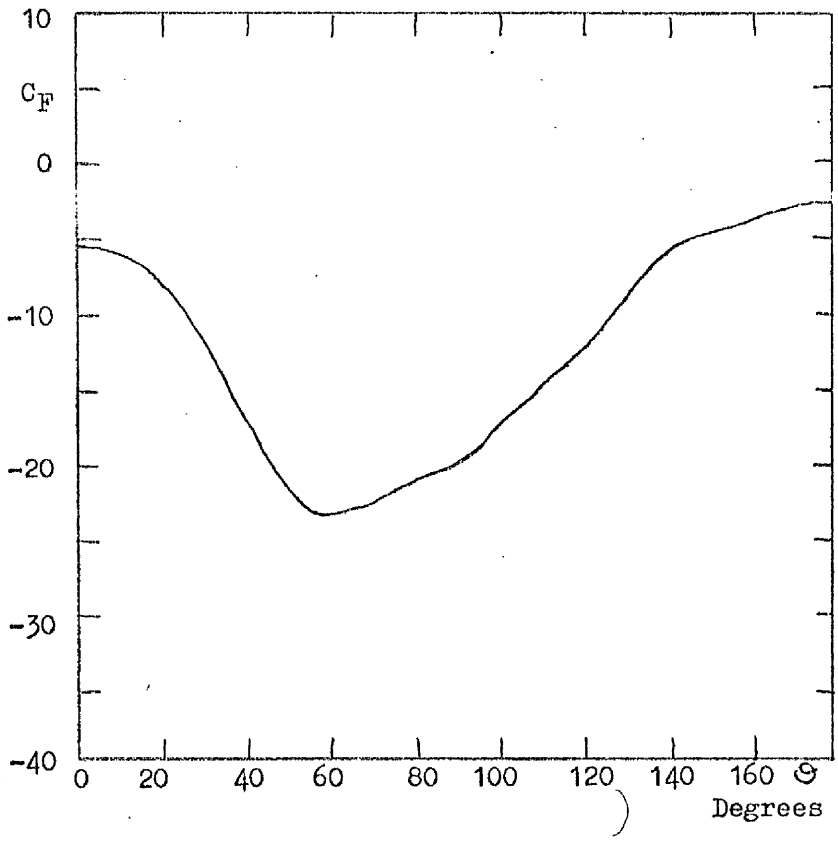

Figure 4.76. Surface Force Distribution (ϕ= 15°, α= 4°, m = 8, R_2 = 10).

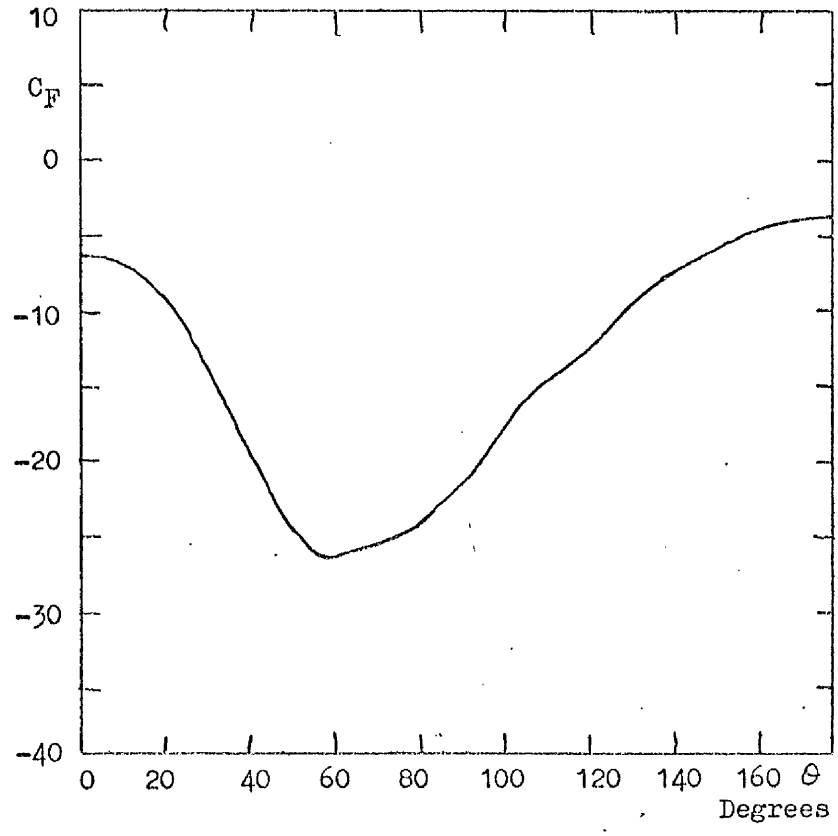

Figure 4.77. Surface Force Distribution (ϕ= 15°, α= 6°, m = 8, R_2 = 10).

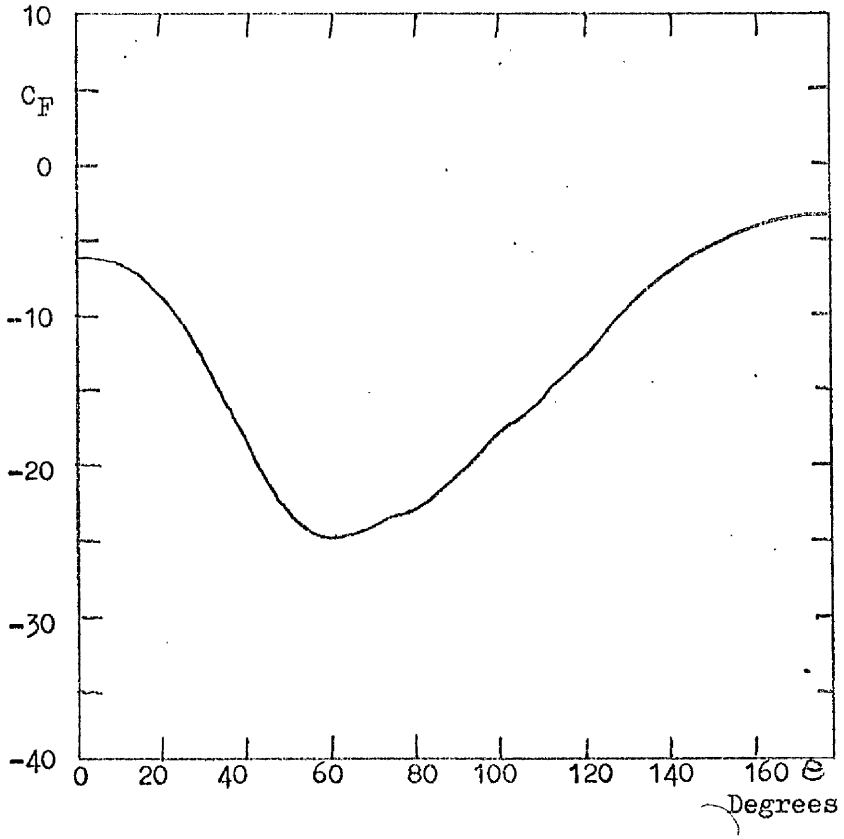

Figure 4.78. Surface Force Distribution ($\phi = 15^{\circ}, \alpha = 8^{\circ}, m = 8, R_2 = 10$).

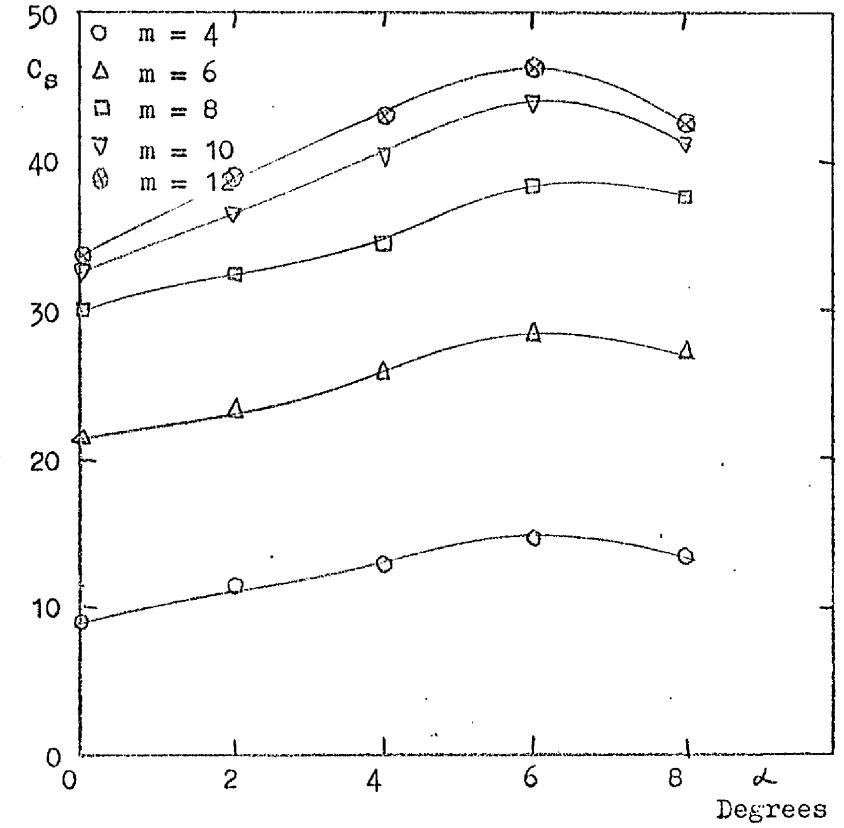

Figure 4.79. Variation of Suction Force Coefficient with Incidence ($\phi = 15^{\circ}$).

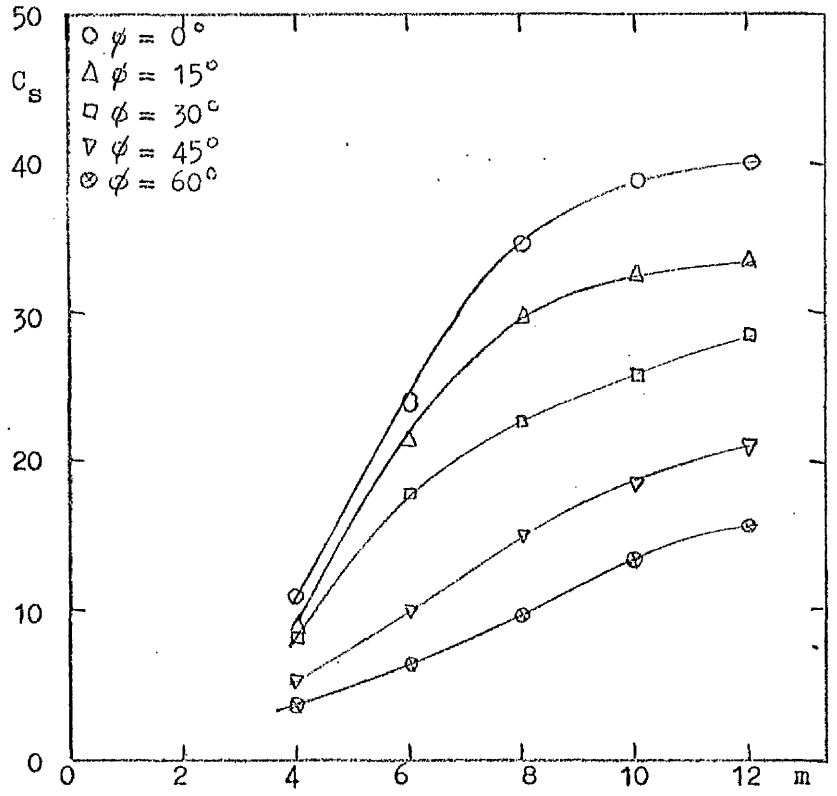

Figure 4.80. Variation of Suction Force Coefficient with Velocity Ratio ($\alpha = 0°$).

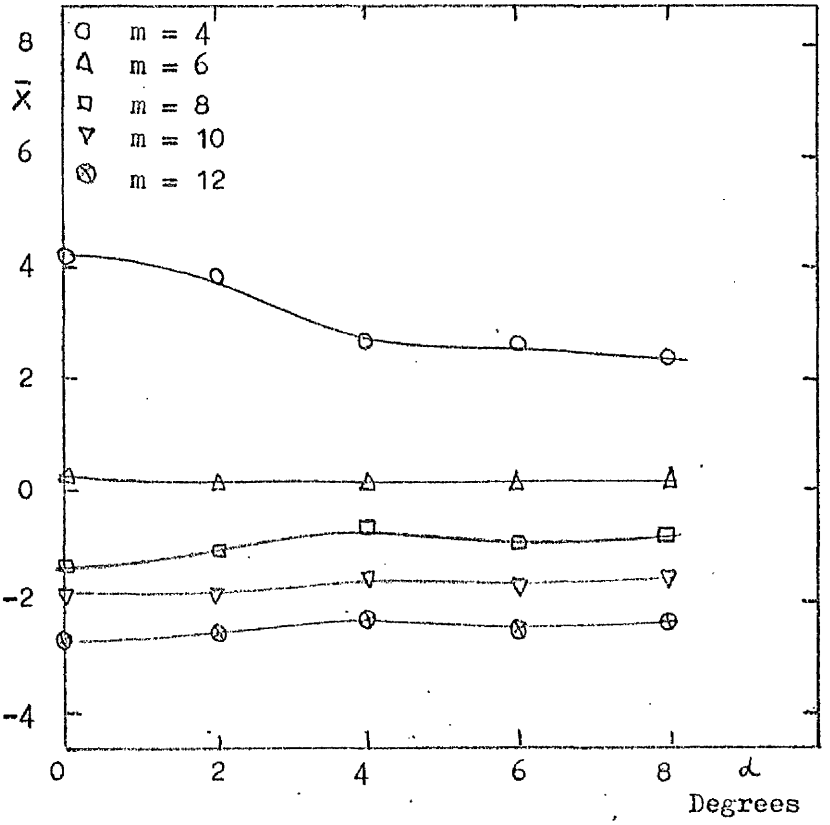

Figure 4.81. Variation of Centre of Pressure with Incidence ($\phi = 15°$).

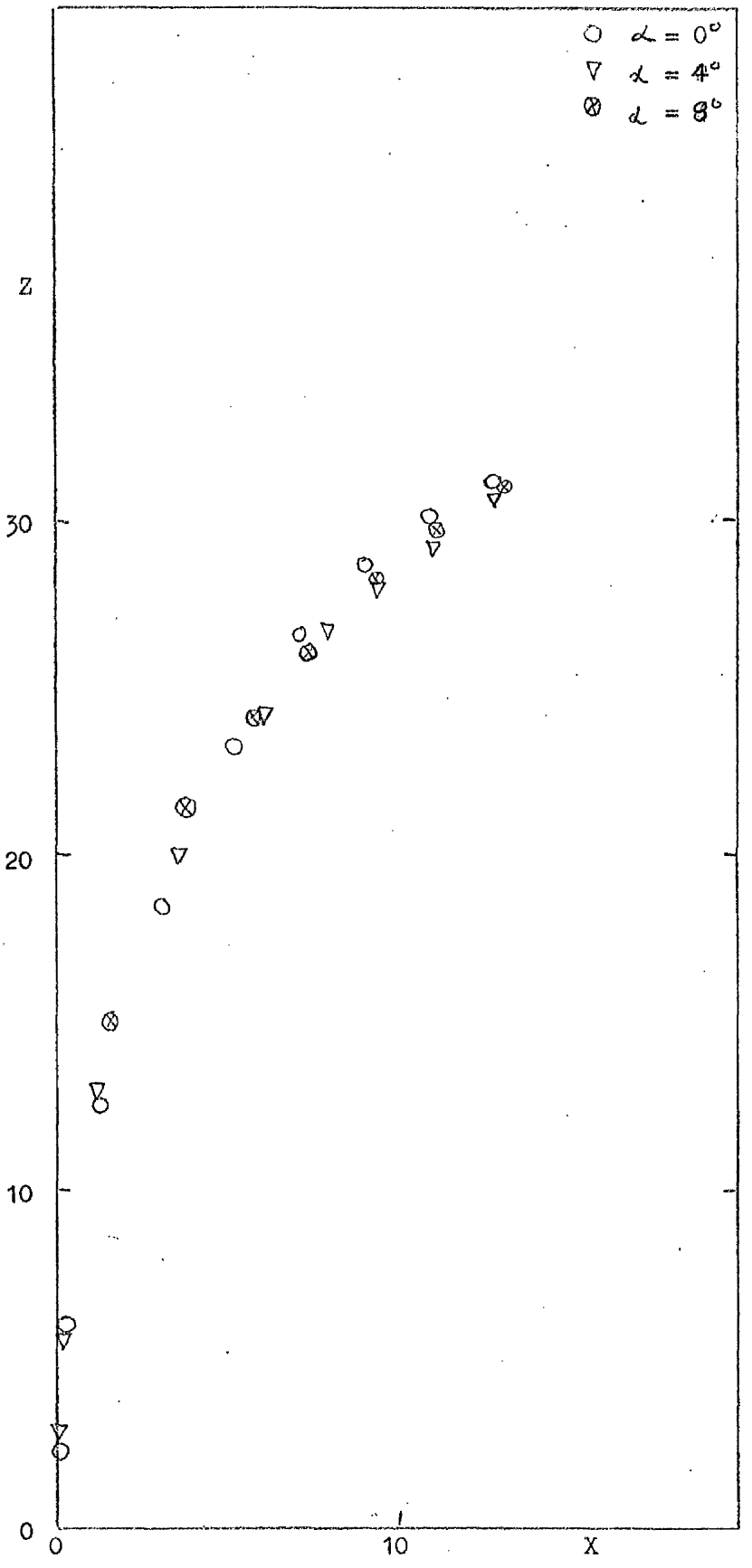

Figure 4.82. Jet Trajectory ($\phi = 0°$, m = 12).

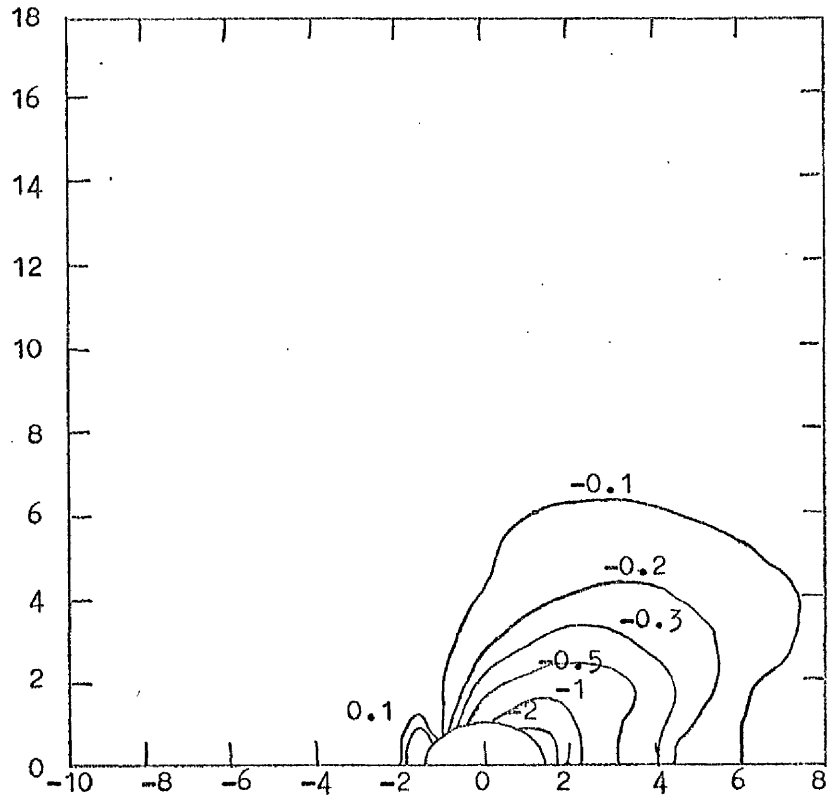

Figure 4.83. Surface Pressure Distribution ($\phi = 45^\circ, \alpha = 2^\circ, m = 4$).

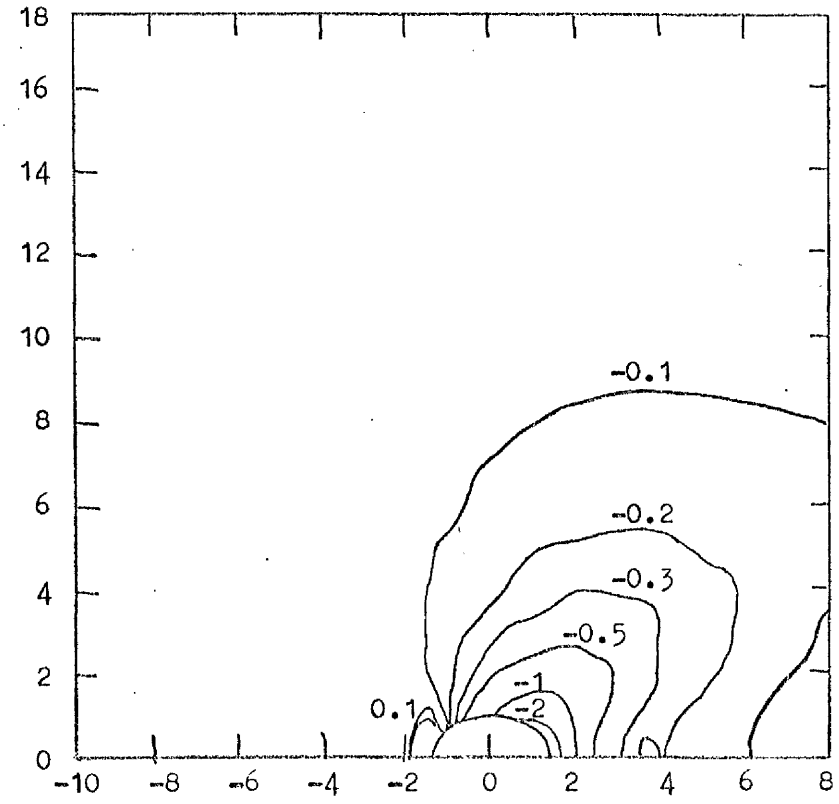

Figure 4.84. Surface Pressure Distribution ($\phi = 45^\circ, \alpha = 2^\circ, m = 6$).

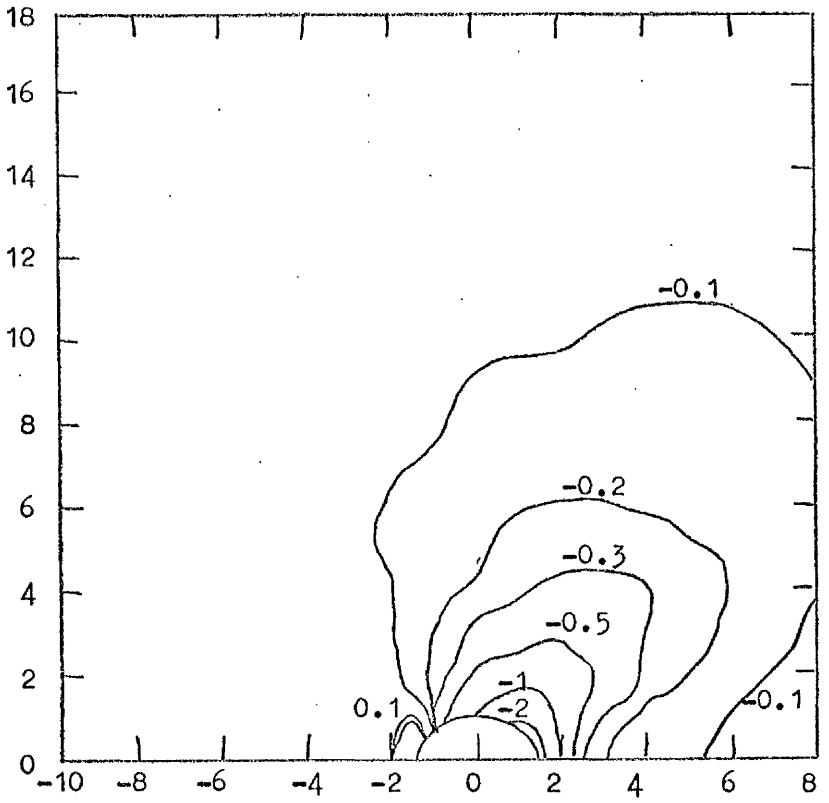

Figure 4.85. Surface Pressure Distribution ($\phi = 45^{\circ}, \alpha = 2^{\circ}, m = 8$).

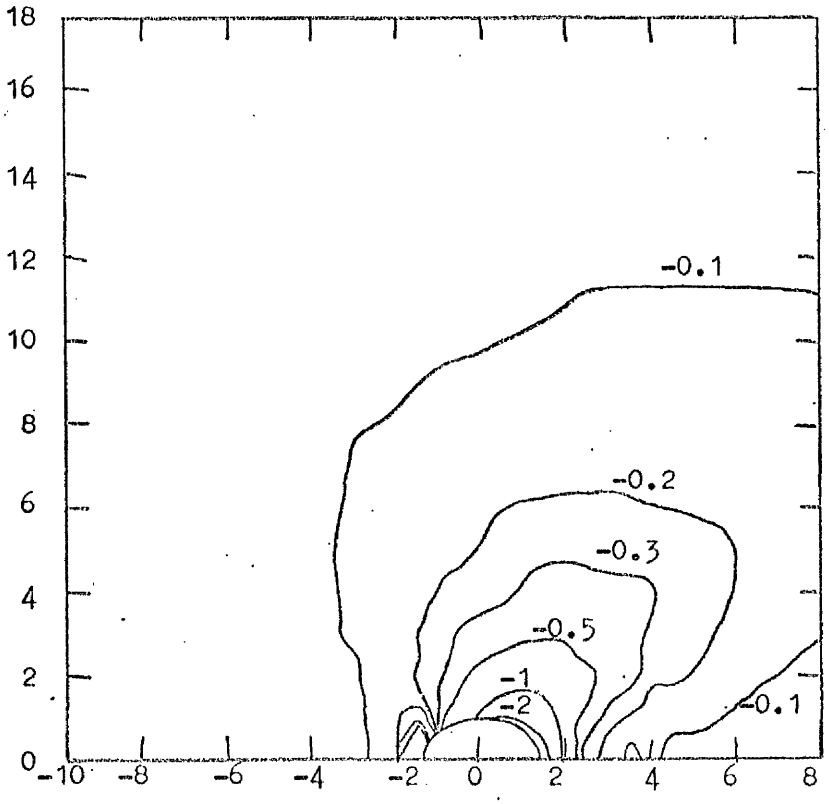

Figure 4.86. Surface Pressure Distribution ($\phi = 45^{\circ}, \alpha = 2^{\circ}, m = 10$).

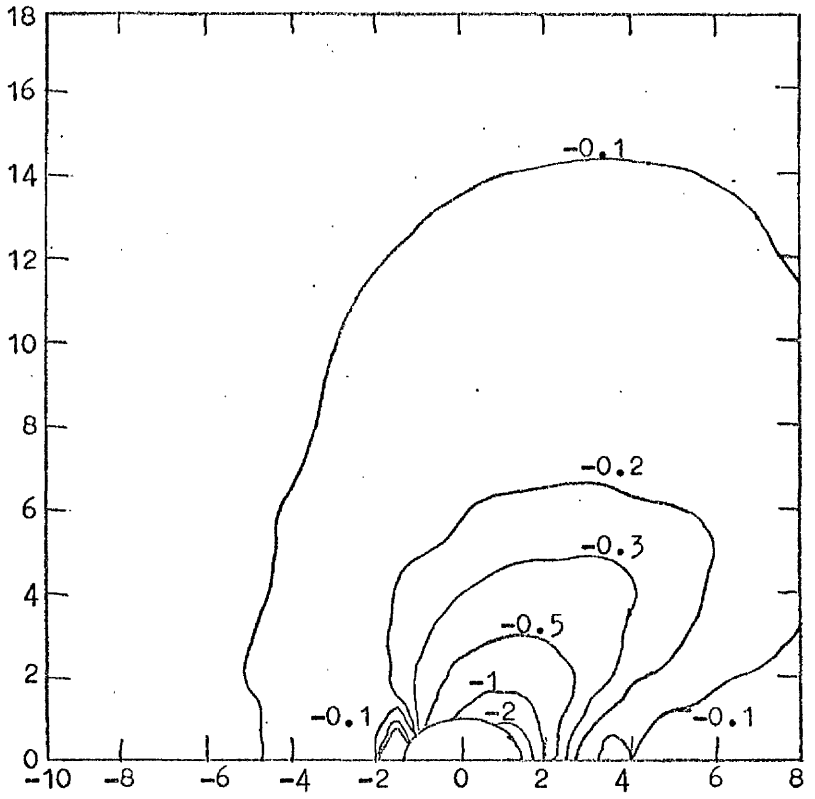

Figure 4.87. Surface Pressure Distribution ($\phi = 45^\circ, \alpha = 2^\circ, m = 12$).

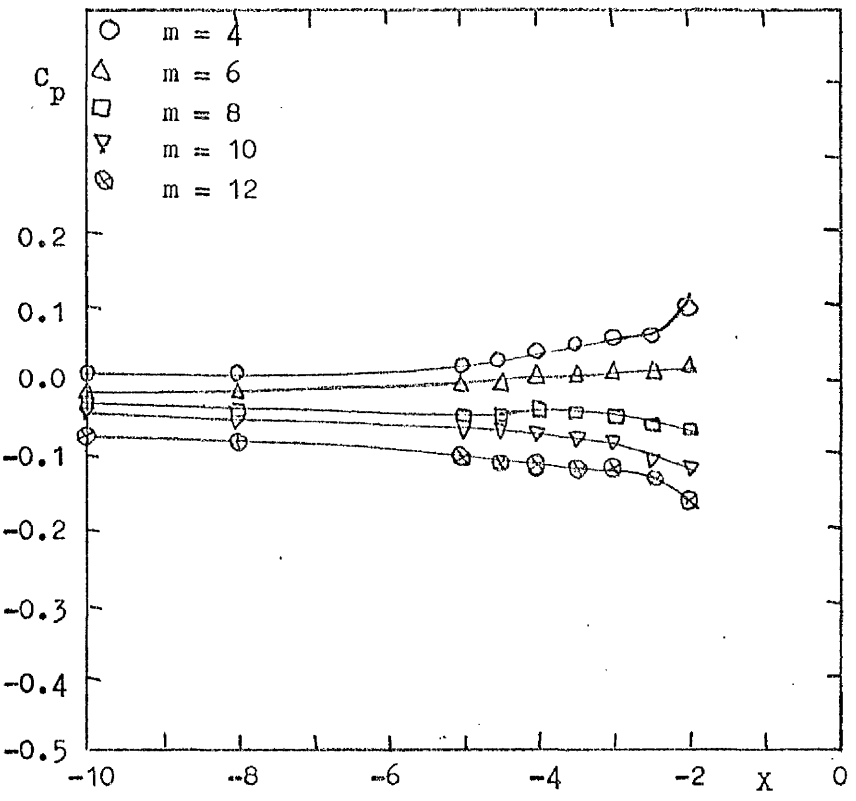

Figure 4.88. Upstream Centreline Pressure Distribution ($\phi = 45^\circ, \alpha = 2^\circ$).

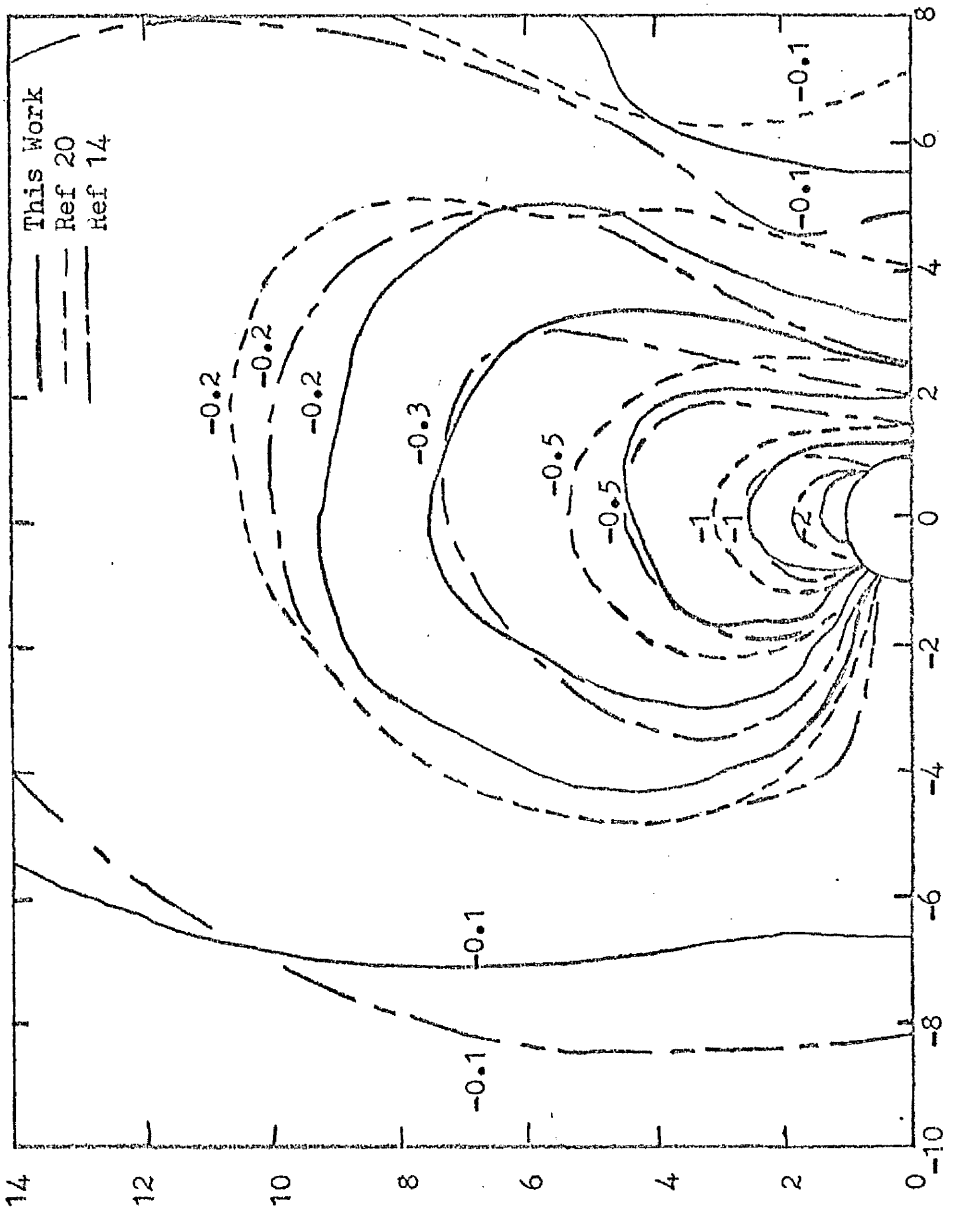

Figure 4.89. Surface Pressure Distribution ($\phi = 0^\circ$, $\alpha = 0^\circ$, $m = 8$).

A Comparison of this work with that of Ref 14 and Ref 20.

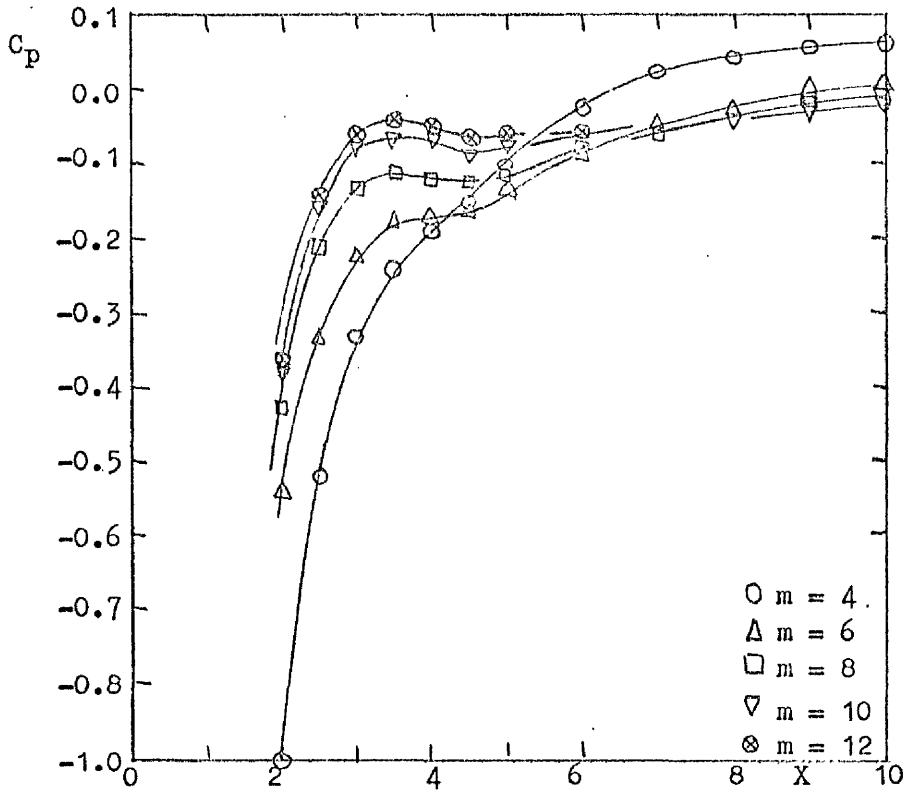

Figure 4.90. Downstream Centreline Pressure Distribution ($\phi = 45^\circ$, $\alpha = 2^\circ$).

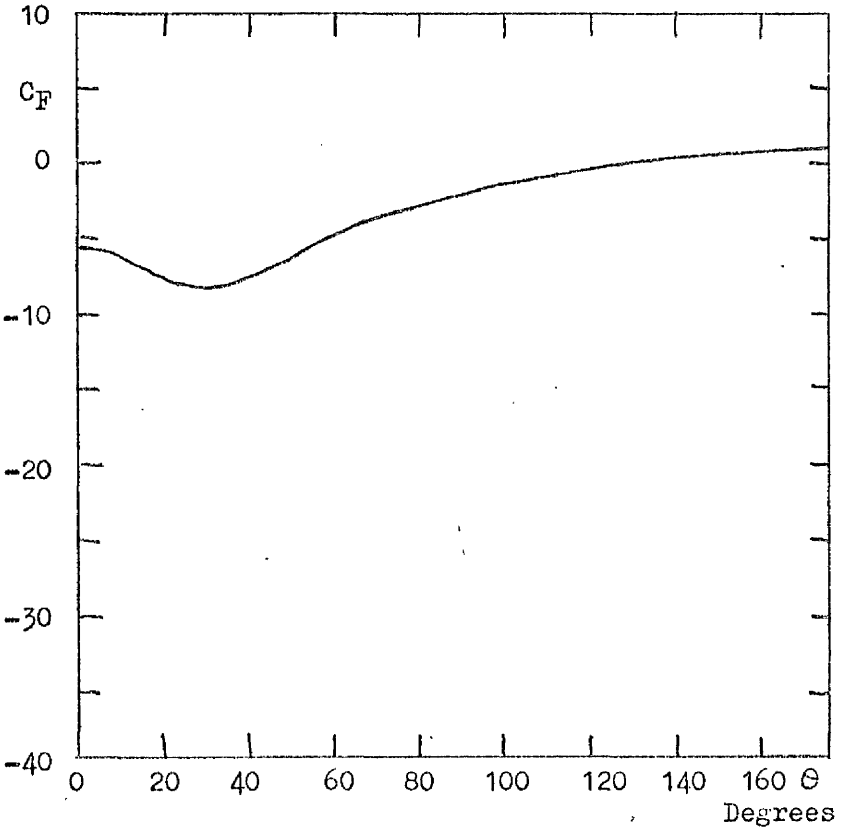

Figure 4.91. Surface Force Distribution ($\phi = 45^\circ$, $\alpha = 2^\circ$, m = 4, $R_2 = 5$).

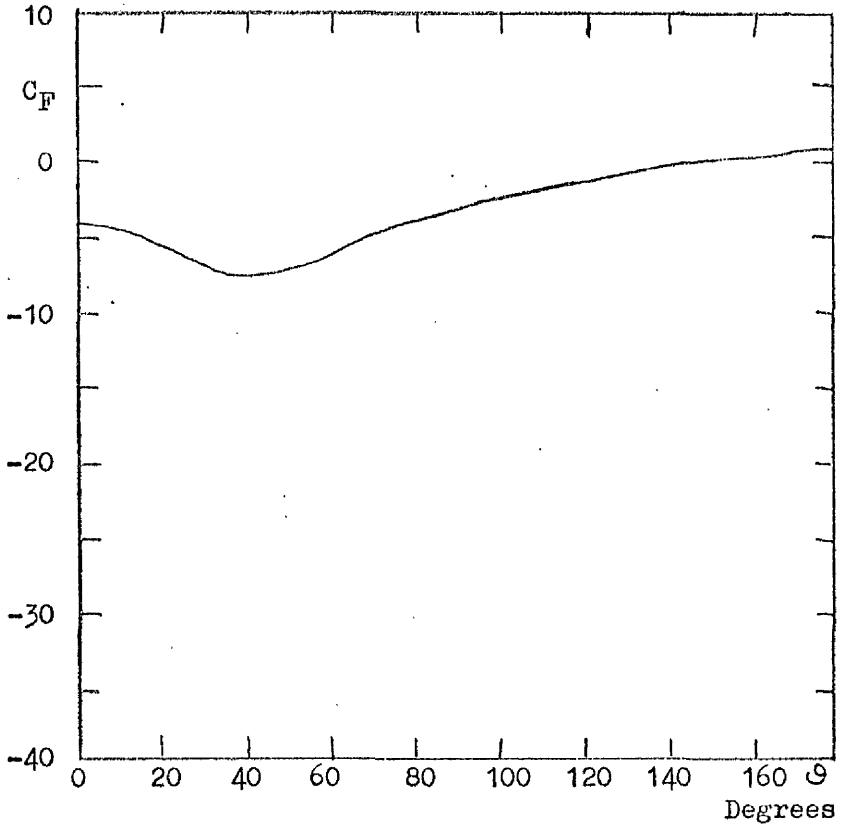

Figure 4.92. Surface Force Distribution ($\phi = 45^\circ, \alpha = 2^\circ, m = 6, R_2 = 5$).

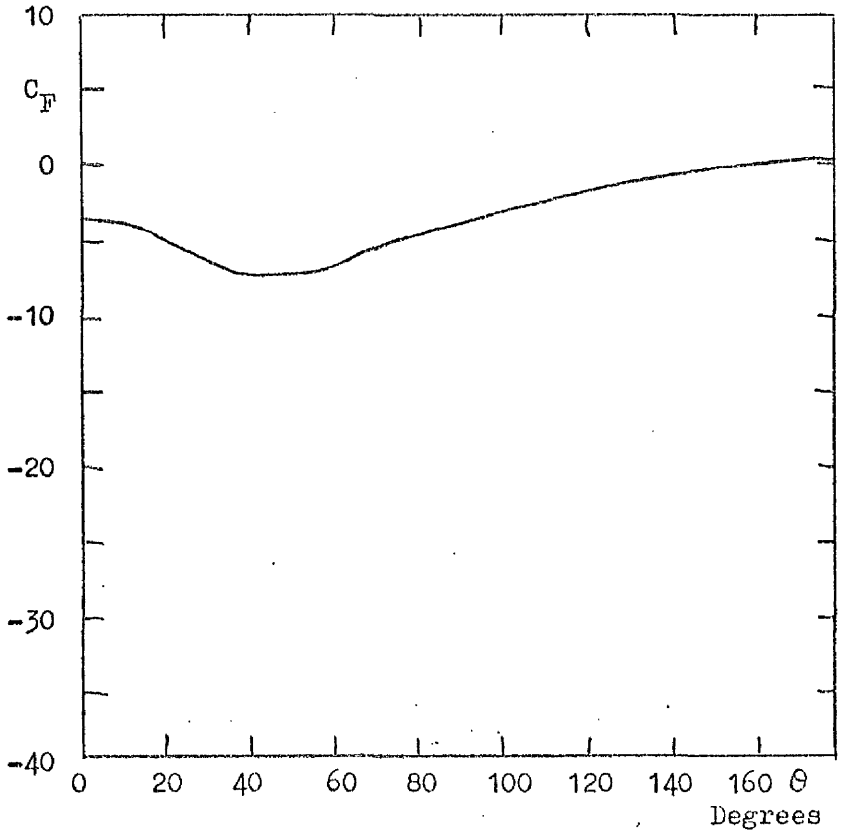

Figure 4.93. Surface Force Distribution ($\phi = 45^\circ, \alpha = 2^\circ, m = 8, R_2 = 5$).

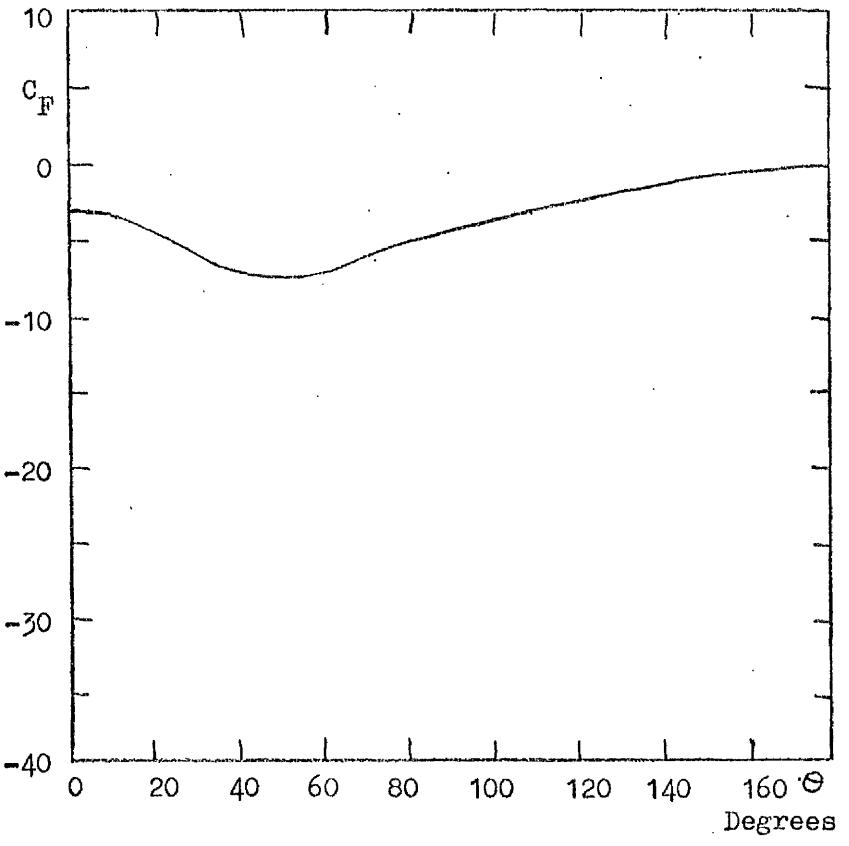

Figure 4.94. Surface Force Distribution ($\phi = 45^\circ, \alpha = 2^\circ, m = 10, R_2 = 5$).

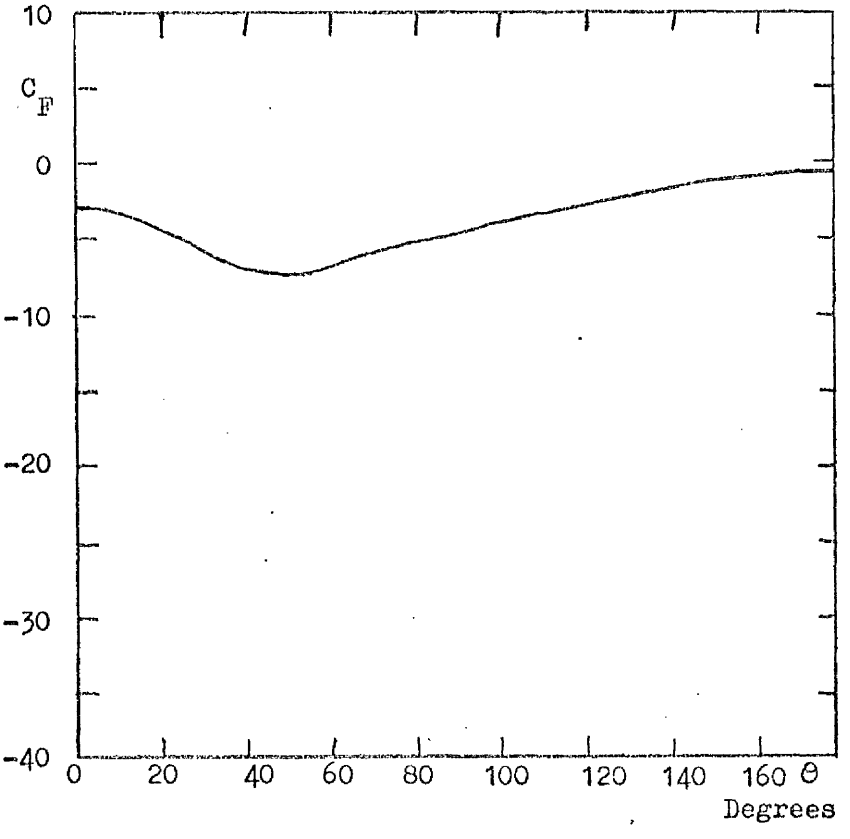

Figure 4.95. Surface Force Distribution ($\phi = 45^\circ, \alpha = 2^\circ, m = 12, R_2 = 5$).

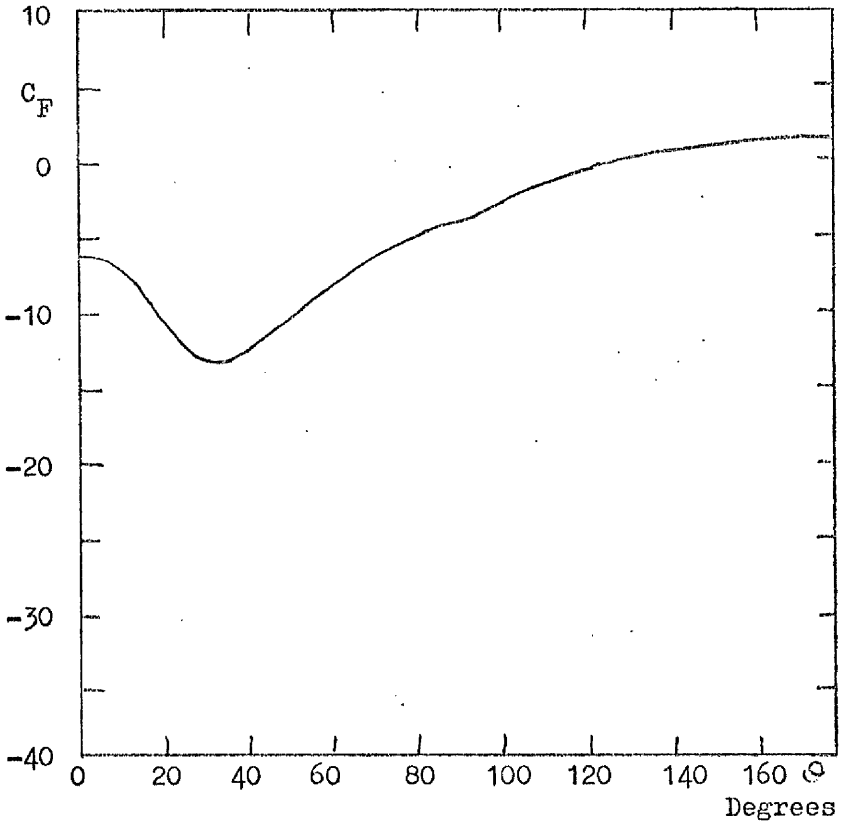

Figure 4.96. Surface Force Distribution ($\phi = 45°, \alpha = 2°, m = 4, R_2 = 10$).

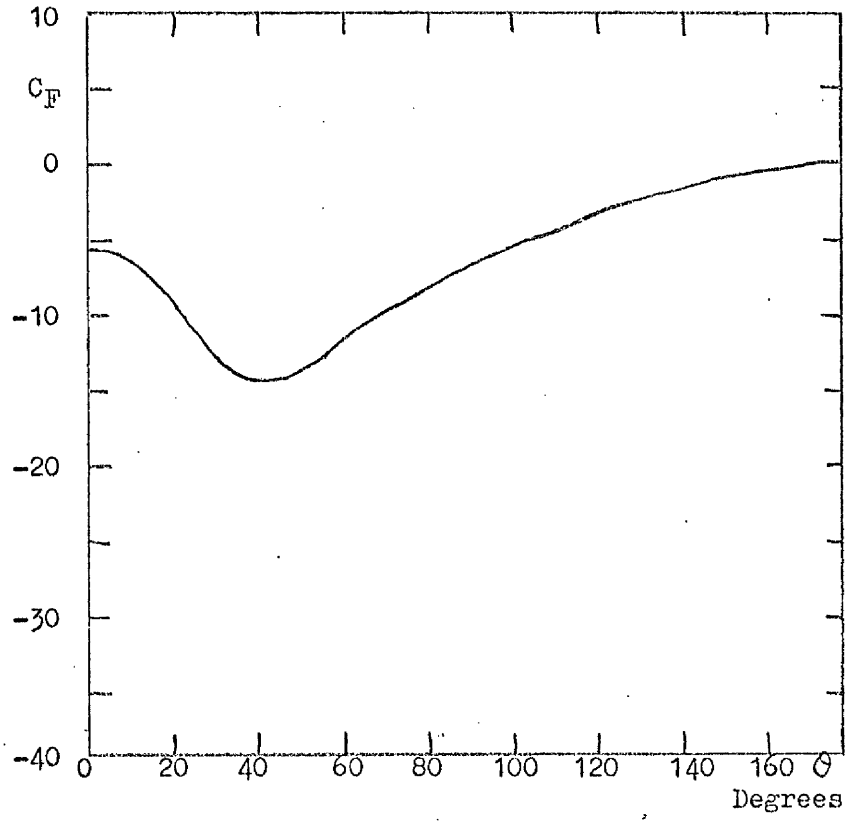

Figure 4.97. Surface Force Distribution ($\phi = 45°, \alpha = 2°, m = 6, R_2 = 10$).

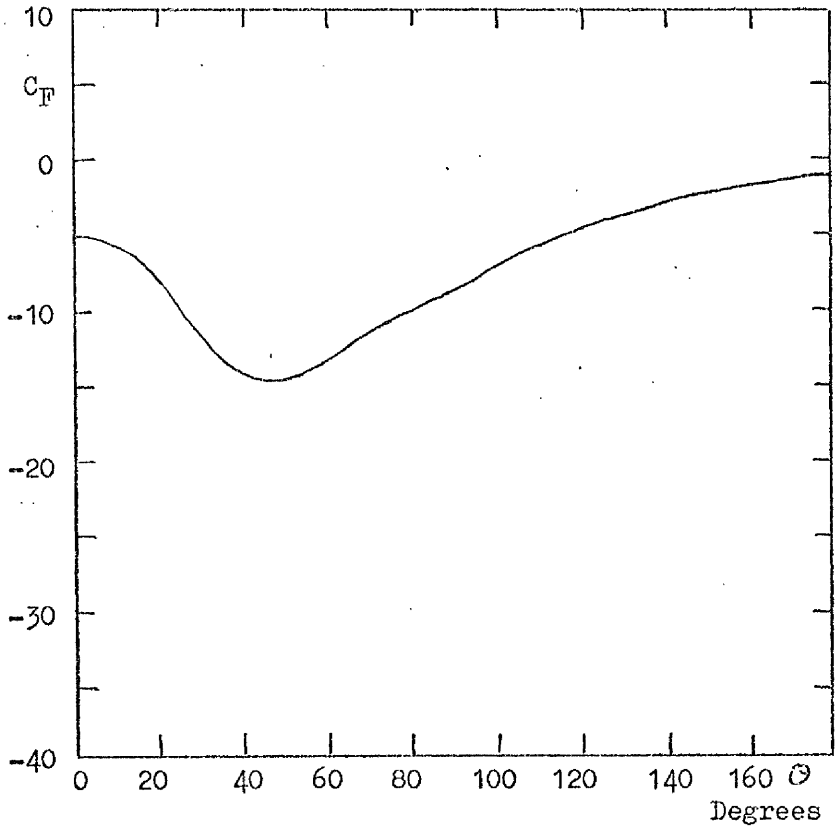

Figure 4.98. Surface Force Distribution ($\phi = 45^\circ, \alpha = 2^\circ, m = 8, R_2 = 10$).

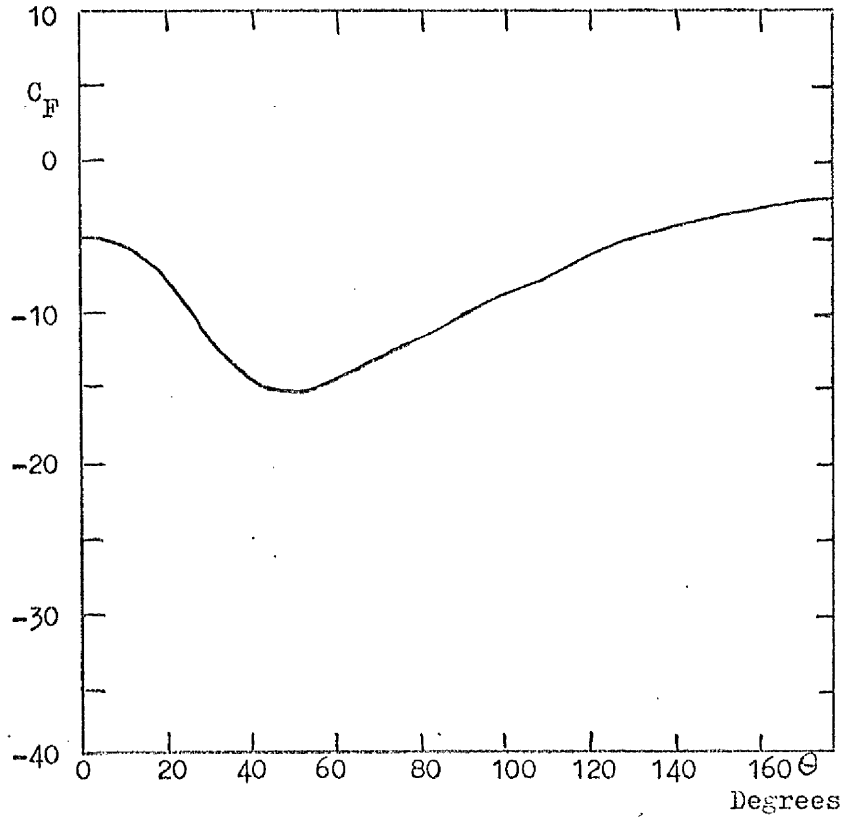

Figure 4.99. Surface Force Distribution ($\phi = 45^\circ, \alpha = 2^\circ, m = 10, R_2 = 10$).

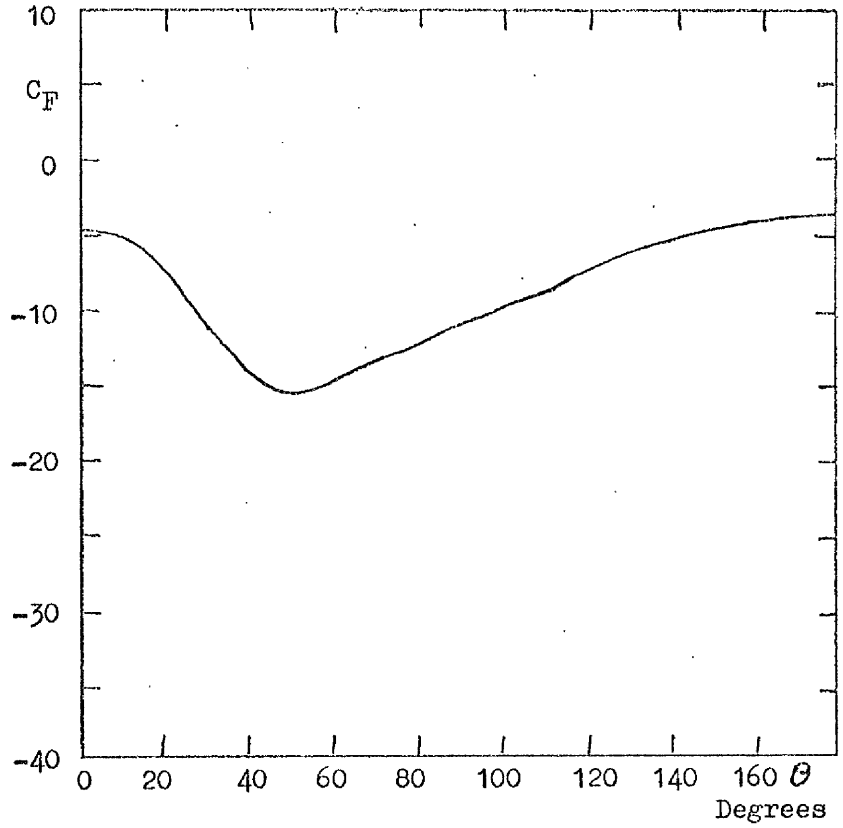

Figure 4.100. Surface Force Distribution ($\phi = 45^\circ$, $\alpha = 2^\circ$, m = 12, R_2 = 10).

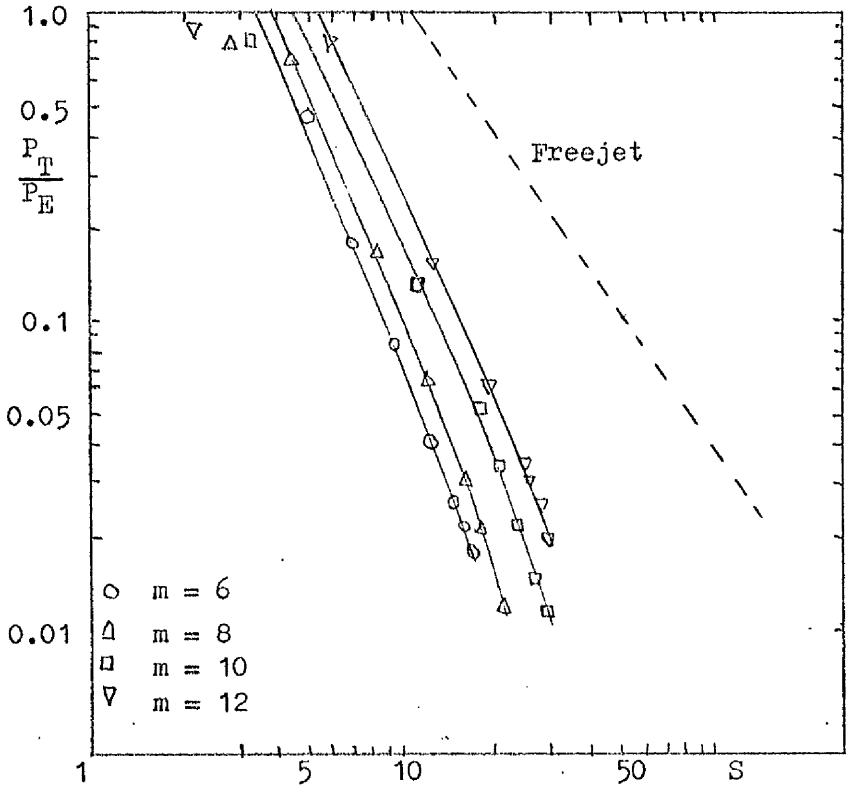

Figure 4.101. Total Pressure Decay Rate ($\phi = 45^\circ$, $\alpha = 0^\circ$).

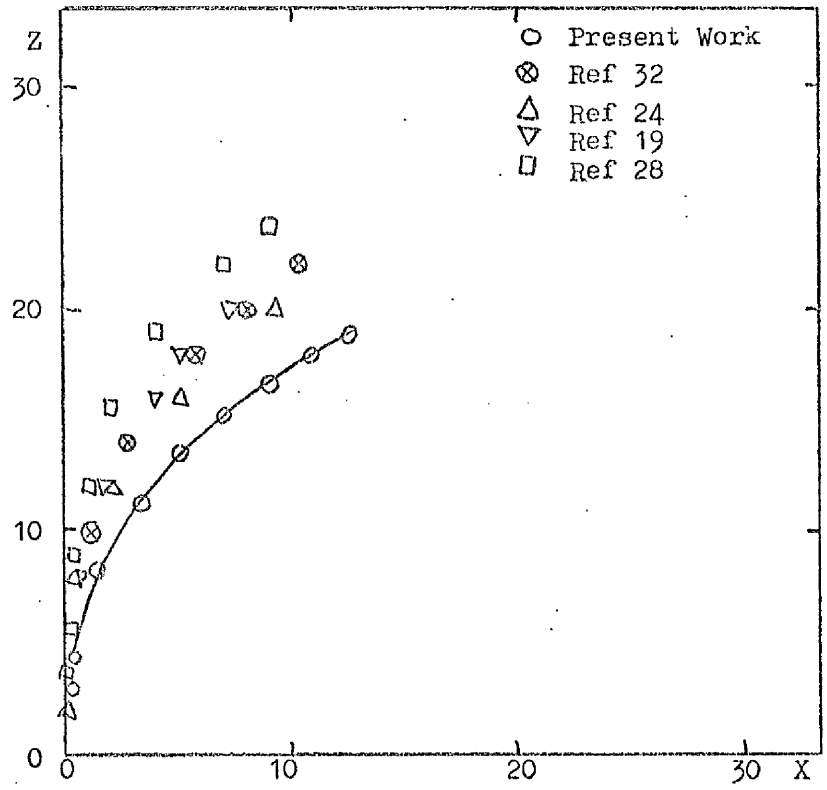

Figure 4.102. Jet Trajectory ($\phi = 0^{\circ}, \alpha = 0^{\circ}, m = 8$). A Comparison with Other Works.

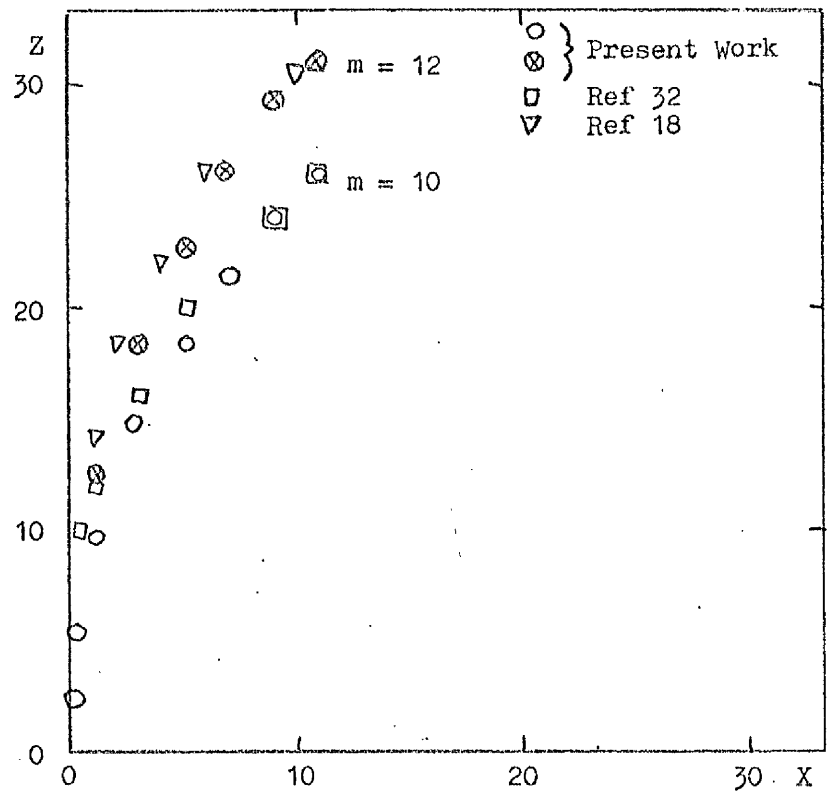

Figure 4.103. Jet Trajectory ($\phi = 0^{\circ}, \alpha = 0^{\circ}$) for a Freestream Turbulence Level of 0.7%. A Comparison with Other Works.

Chapter V

Analytical Model

5.1 Introduction

The jet interference problem is so complicated that it has defied a detailed theoretical treatment. Several analytical models have been proposed which attempted to predict the interference effect based on some empirical information concerning particular characteristics of the flow (usually the jet). These models use a potential flow representation of the interference flowfield but differ from each other in the way in which the flowfield is represented and the factors influencing the flowfield that are accounted for. References 44, 45, 46 and 47 represent the state of the art.

5.2 Initial Considerations Involved in Forming an Analytical Model

The experimental results given in Chapter IV have shown that a flat plate through which a turbulent jet exhausts experiences aerodynamic interference effects which result in lift losses and adverse pitching moment changes for velocity ratios relevant to the VTOL transition phase. Low pressures developed on the surface of the plate. The low pressures became more extensive and moved upstream while the pitching moment changed from nose up to nose down as the velocity ratio increased. It is of interest to be able to predict these trends. The objective of this chapter is to demonstrate the use of a simple two-dimensional steady potential flow model to study the interference effects resulting from a circular jet exhausting normally from an infinite plane into a crossflow.

The simplicity of a two-dimensional potential flow model makes the approach to the analysis of the problem very attractive. Potential flow singularities can be selected to represent the gross effects observed and are quite distinct so that the effect of each element can

be analysed separately. The model should aid the interpretation of the experimental results and can be used as a basis for the development of a three-dimensional model.

The experimental results show an extensive low pressure region behind the jet. The surface flow patterns of reference 14 indicate that a separated region exists behind the jet. The total pressure surveys of ref 24 show that a low total pressure region exists behind the jet and extends above the surface as well. The results of more recent experiments within the wake region (ref 31,33 and 34) suggest that a von Karman vortex street exists and that the freestream separates from the sides of the jet as in the case of a solid body. The extent of the separated region is not known. The entrainment of the freestream fluid into the jet predominates beyond the potential core region. This free-jet and vortex type entrainment is probably sufficient to prevent any separation away from the potential core and the measurements of ref 48 suggest this. It appears logical to argue that the crossflow separates around the potential core because of the adverse pressure gradient experienced around the core surface as in the case of separation about an equivalent solid body. The potential core length increases and the core presents a larger frontal area to the oncoming freestream as the velocity ratio increases. The separation point moves forward because of the increased blockage and because the potential core is less deflected than at lower velocity ratios (see ref 26). The flow photographs of ref 14 indicate a more extensive separation at higher velocity ratios.

A potential flow model cannot simulate the flow in regions of energy loss. The surface flow photographs of ref 14 indicate that the wake covers a region of at least $\pm 30^{\circ}$ either side of the wake centreline. The representation of the entire freestream by a constant total

pressure potential flow model is too strong a requirement and consequently a region downstream of the jet covering a total angle of 90° has been excluded from the analysis.

Before ending the discussion on the wake region, it is interesting to note the contribution of the wake region to the suction force coefficient obtained from experiment with the wake region excluded. The contribution from the wake is expressed as a fraction:

$$\frac{C_s(\text{Wake Included}) - C_s(\text{Wake Excluded})}{C_s(\text{Wake Included})} = \frac{\Delta C_s}{C_s}$$

The variation of this fraction with velocity ratio is illustrated in fig 5.1 covering areas up to five and ten jet radii from the jet exit. For a circular area extending up to five jet radii the maximum contribution from the wake region is 15% at a velocity ratio of 4 and decreases with increasing velocity ratio to 3% at a velocity ratio of 12. The corresponding values for the larger area are 12½% and 2½%. The exclusion of this region should still provide a useful model for studying the interference effects at all values of the velocity ratio observed in the experiments.

The experimental observations (Chapter IV) indicate that the jet plume is close to the surface downstream of the jet at low values of the velocity ratio. As the velocity ratio increases the jet penetration is increased. The proximity of the plume to the surface at low velocity ratio (i.e.m = 4) has a significant effect in the wake region. The important feature is the link between entrainment and deflection. The more rapid the deflection rate the higher the entrainment rate (see ChaptIV and ref 28). The proximity of the plume to the surface causes the entrainment of more fluid from the separated region of flow and the boundary layer than at higher velocity ratios where the

deflection is less severe. This is reflected in the positive centre of pressure observed experimentally at low values of velocity ratio. As the velocity ratio increases, the deflection of the initial centreline is less severe, the plume is less close to the surface and consequently, less fluid is entrained from the wake region. This is supported by the upstream movement of the centre of pressure observed. The three-dimensional effects of the jet deflection at low values of the velocity ratio can be expected to be confined to the excluded region and have little effect elsewhere.

The jet deforms at the end of the potential core given by $Z/m = 0.6$ (ref 24). The change in jet shape occurs further from the surface as the velocity ratio increases. The effect of the jet deformation can be expected to be less at higher velocity ratios than lower velocity ratios.

The experimental observations showed that the potential core length increased as the velocity ratio increased. The core presents a larger frontal area to the oncoming flow. As noted above, this causes a wider separation region i.e the blockage effect of the core on the oncoming freestream increases as the velocity ratio increases. This has a significant effect on the surface pressure distribution as was observed in the experiments. The blockage due to the jet plume beyond the core can be considered to be negligible because entrainment predominates in regions beyond the core. In these regions the static pressure difference across the jet is negligible and, as noted above, it seems unlikely that the freestream separates in these regions.

The only other three-dimensional effect to be considered is the increase in the vertical component of velocity close to the jet. This component increases in magnitude with increasing velocity ratio. The upstream centreline pressure distribution obtained experimentally along

with the observations of ref 24 indicate that this induced vertical component becomes significant at high velocity ratios and the two-dimensional model cannot be expected to allow for this.

The entrainment properties of the deflected jet dominate the flowfield as seen from the experiments and from other observations (ref 14 and 28). The surface flowfield photographs of ref 14 show the termination of streamlines at the jet periphery and at the wake boundary. The entrainment into the wake was also observed in refs 25, 31 and 33. It would be desirable to obtain information about the entrainment rates directly. No experiments have been devised which control the entrainment rate directly. Experimental results, which have been interpreted by matching to those results obtained from empirical models involving postulated entrainment functions, indicate that the entrainment of the jet causes the jet to deflect and deform which in turn induces the observed pressure field (ref 28). The entrainment rate increases with increasing velocity ratio and two types occur: freejet entrainment and vortex entrainment.

Analytical models proposed in the past which did not take account of entrainment showed poor correlation with experimental data. In particular the models proposed in references 49 and 50 required an excessive drag coefficient and jet spread respectively to predict the experimentally determined centreline. The results of reference 28 indicate that the freejet entrainment coefficient is roughly independant of velocity ratio and the order of magnitude agrees with that of reference 51. The vortex entrainment coefficient was found to be an order of magnitude greater than the freejet and dependent on the velocity ratio. The vortex induced velocity reached a maximum at a deflection of about 30^{o} from the initial centreline before decreasing. It appears that the entrainment rate will vary significantly in the

region close to the surface. This is also supported by the results of the analysis of reference 45 in which the entrainment coefficients were allowed to vary in the potential core region.

Finally a consideration of the effect of the surface boundary layer must be made. Fig 5 of reference 14 indicates that the surface pressure distribution is affected by the boundary layer thickness. This effect appears to be small under experimental conditions as witnessed by the comparison of various reported experimental results (see chapterIV). However, the potential flow model takes no account of the boundary layer or the changes in boundary layer thickness that occur in the vicinity of the jet. The discrepancies noted close to the jet in reference 45 and in part in reference 46 can be attributed to this change in boundary layer thickness.

The proposed model should account for these observed trends within the limitations noted above. The freestream is expected to be inviscid outside the jet, the separated region and the boundary layer. A potential flow model to describe the freestream would seem reasonable. For simplicity, the entrainment parameter is assumed to be constant. This is not correct but the overall trends predicted should agree qualitatively with those observed experimentally. The entrainment is represented by a single sink placed on the centreline downstream of the jet. This is in accordance with the experimental observation concerning the inflow of freestream fluid through the wake boundaries. This sink accounts for the gross effect of entrainment due to the vorticity and freejet effects. It seems reasonable to assume that the effects of the position of the plume relative to the surface downstream of the jet can be accounted for by varying the position of the sink. The movement of the sink as a function of velocity ratio should be in the same direction as that of the centre of pressure.

Since the wake is not amenable to analysis, the blockage effect can be simulated by a source situated on the jet periphery or downstream of the jet in the manner of reference 52. The resulting afterbody shape should represent the separation points and width of the separated region. The separation points should move upstream and the afterbody width should increase as the velocity ratio increases. The effect of the addition of an afterbody was noted in reference 47 and Wooler (ref 45) stated that some improvement was expected in the prediction by placing a source distribution at the rear of the jet periphery. Bradbury and Wood (ref 14) observed that the surface pressure distribution about a circular cylinder obtained experimentally bore little resemblance to that predicted by potential flow because of the separated region causing an area of low pressure downstream. Fig 5.3 illustrates a considerable improvement in the two-dimensional prediction outside the wake region by the use of an afterbody.

The proposed two-dimensional model can be expected to give reasonable results if the wake region is excluded. The surface pressure contours are expected to show good agreement far from the jet where the three-dimensional and boundary layer effects are very small. Poor agreement is expected near the jet where the induced vertical component of velocity is large and the effect of boundary layer thickening is measureable. The resulting surface force distribution and suction force coefficient would show very poor agreement with experiment. If the agreement of the surface pressure distribution is sacrificed then the surface force and suction force predictions can be improved considerably.

5.3 The Model.

Consider a two-dimensional, incompressible, irrotational steady flow, uniform at infinity, past a body, symmetrical with respect to the incident flow in the z_1 plane ($z_1 = x + i\,y$). The basic flow past the

circle (fig 5.2) is the familiar combination of a uniform flow in the direction of the real axis plus the flow from a suitable doublet at the origin. To this is added the flow from a source of strength $2Q_2$ located at the intersection of the circle and the positive x axis (a, 0) and from its image sink at the origin. (The combination of a double source on the circle and a sink at the origin satisfies the boundary condition on the circle. It is the limiting case of the combination of a source outside the circle and its image source and sink inside.)

Similarly the flow from a sink of strength Q_1 located on the positive x axis at a distance h from the origin (where $h \geq a$) and the flow from its image sink and source inside the circle is added. The complex potential of the resulting flow is

$$\omega(z_1) = V_\infty(z_1 + \frac{a^2}{z_1}) + \frac{Q_1}{2\pi}(\ln z_1 - \ln(z_1 - \frac{a^2}{h}) - \ln(z_1 - h))$$

$$+ \frac{Q_2}{2\pi}(2\ln(z_1 - a) - \ln z_1)$$

and the complex velocity in the z_1 plane is

$$q(z_1) = u(z_1) - iv(z_1) = \frac{d\omega(z_1)}{dz_1}$$

$$= V_\infty(1 - \frac{a^2}{z_1^2}) + \frac{Q_1}{2\pi}(\frac{1}{z_1} - \frac{1}{(z_1 - \frac{a^2}{h})} - \frac{1}{(z_1 - h)}) + \frac{Q_2}{2\pi}(\frac{2}{(z_1 - a)} - \frac{1}{z_1})$$

The upstream flow from the source creates symmetrical stagnation points on the circle located at S_1 and S_2. These are found by setting $q(z_1)$ and $Q_1 = 0$ from which a relation between θ_s and Q_2 is obtained. The complex potential is non-dimensionalised with respect to the jet radius a and the freestream velocity V_∞. Hence

$$\Omega(Z) = (Re^{i\theta} + \frac{e^{-i\theta}}{R}) + K_1(\ln(Re^{i\theta}) - \ln(R_3 e^{i\gamma}) - \ln(R_2 e^{i\beta})) +$$

$$K_2(2\ln(R_1 e^{i\alpha}) - \ln(Re^{i\theta}))$$

where $K_1 = \dfrac{Q_1}{2\pi V_\infty a}$, represents the sink entrainment

$K_2 = \dfrac{Q_2}{2\pi V_\infty a}$, represents the source outflow or blockage

and in the usual notation

$Z = Re^{i\theta}$ where $R = r/a$ and $\theta = \arctan(Y/X)$,

$Z_1 = R_1 e^{i\alpha}$ where $R_1 = \sqrt{(X-1)^2 + Y^2}$ and $\alpha = \arctan(Y/(X-1))$

$Z_2 = R_2 e^{i\beta}$ where $R_2 = \sqrt{(X-H)^2 + Y^2}$ and $\beta = \arctan(Y/(X-H))$

$Z_3 = R_3 e^{i\gamma}$ where $R_3 = \sqrt{(X-\frac{1}{H})^2 + Y^2}$ and $\gamma = \arctan(Y/(X-1/H))$

The stagnation points S_1 and S_2 are found to occur at

$Z^2 + Z(K_2 - 2) + 1 = 0$

or $Z = -\dfrac{(K_2-2)}{2} \pm i\sqrt{1 - \dfrac{(K_2-2)^2}{4}}$ for $K_2 \leq 4$

and $\theta_s = \arctan(Y_s/X_s)$ where $Y_s = \pm\sqrt{1 - \dfrac{(K_2-2)^2}{4}}$

$$X_s = -\frac{(K_2-2)}{2}$$

The variation of θ_s with K_2 is illustrated in fig 5.4. The stream function is given, in non-dimensional form, by

$\psi(Z) = \sin\theta(R - 1/R) + K_1(\theta - \beta - \gamma) + K_2(2\alpha - \theta) + \pi(K_1 - K_2)$

The additional constant $\pi(K_1 - K_2)$ ensures that the value of ψ for $\theta = \pi$ is zero. A grid of values of the stream function can be generated and the streamlines S_1S_1' and S_2S_2' can be found (see Appendix B). These streamlines, passing through the stagnation points S_1 and S_2, correspond to the boundary of the afterbody representing the wake effect on the freestream. It is analagous to the representation of the wake behind a circular cylinder (ref 52). S_1 and S_2 are the equivalent separation points. To keep the model simple no transformation is performed so that the resulting intersection of the afterbody and the jet occurs

at right angles instead of at a tangent. The flow close to the stagnation points will be affected and irregularities will occur in the surface force distribution especially when $\theta_s \gtrsim 45$, i.e. S_1 and S_2 are outside of the excluded region.

The complex pressure coefficient can be determined at any point and is given by Bernouilli's equation

$$p + \tfrac{1}{2}\rho\left|q(z_1)^2\right| = p_\infty + \tfrac{1}{2}\rho V_\infty^2$$

$$\text{or } C_p = \frac{p - p_\infty}{\frac{1}{2}\rho V_\infty^2} = 1 - \frac{\left|q(z_1)^2\right|}{V_\infty^2}$$

Or in non-dimensional form where $Q(Z) = U(Z) - iV(Z)$

$$C_p = 1 - U(Z)^2 - V(Z)^2$$

$$\text{where } U(Z) = 1 - \frac{\cos 2\theta}{R^2} + K_1\left(\frac{\cos\theta}{R} - \frac{\cos\beta}{R_2} - \frac{\cos\gamma}{R_3}\right) + K_2\left(\frac{2\cos\alpha}{R_1} - \frac{\cos\theta}{R}\right)$$

$$\text{and } V(Z) = -\frac{\sin 2\theta}{R^2} + K_1\left(\frac{\sin\theta}{R} - \frac{\sin\beta}{R_2} - \frac{\sin\gamma}{R_3}\right) + K_2\left(\frac{2\sin\alpha}{R_1} - \frac{\sin\theta}{R}\right)$$

The pressure coefficient can be determined at any point in the flow field. The region bounded by $|Z| = 1$ and $\theta = \pm\pi/4$ is excluded. The position of the surface contours can be found using Isomet (see Appendix B).

If values of K_2 and H are supplied then the average value of K_1 can be obtained by comparison with the experimentally determined press-coefficients along the radial $\theta = \pi$. For this condition $V(Z) = 0$ and $U(Z)^2 = 1 - C_p$. From the above equation for C_p and $U(Z)$

$$K_1 = -\frac{F}{2} \pm \sqrt{\frac{F^2}{4} - C}$$

where $F = (2(1 - 1/R^2) + 2K_2(2/R_1 - 1/R))/D$

$$C = ((1 - 1/R^2)^2 + C_p - 1 + K_2^2(1/R - 2/R_1)^2 + 2K_2(1 - 1/R^2) \times (1/R - 2/R_1))/D^2$$

and $D = 1/R_2 + 1/R_3 - 1/R$

only the root $K_1 > 0$ is physically meaningful. The value of K_1 is determined at each point, considered from the experimental value of C_p at that point, and the average value of K_1 is computed (see Table 5.1).

The surface force is given by direct integration from

$$C_F = \int_1^{RR} C_p \, R \, dR \qquad \text{where RR has the values 5 and 10}$$

and the suction force coefficient is given by direct integration of

$$C_s = \frac{-2}{\pi} \int_{\pi/4}^{\pi} C_F \, d\Theta$$

5.4 Model Parameters.

The method of choosing the model parameters which portrayed the experimentally observed results was as follows:

1. A speed ratio was selected.

2. Avalue of K_2 was chosen by referring to the flowfield photographs of ref14 and obtaining an estimate of Θ_s. The value of K_2 was determined from fig 5.4.

3. A value of H was selected.

The entrainment parameter K_1 was calculated by matching the experimental upstream centreline pressure distribution ($\Theta = \pi$) (see Section 5.3). This method was chosen because the resulting calculations were greatly simplified by the fact that the flow direction for $\Theta = \pi$ is in the X direction (i.e. V(Z) = 0).

If the plate pressures predicted by the model are to correlate with the experimental data then the velocity u must equal the local test velocity along $\Theta = \pi$. However, as mentioned in Section 5.2, there is a vertical component of velocity induced in the vicinity of the jet. The pressure coefficient predicted must try and represent this additional

component.

Ideally, the calculated value of K_1 should be the same for all X. However, there was a variation of K_1 with X, K_1 increasing as the jet was approached (see table 5.1). Table 5.1 indicates the increasing effect of entrainment as the jet is approached. The value of K_1 used to calculate the induced surface pressure distribution was taken to be the average of the values calculated from the experimental data. Better results were obtained by considering points closely spaced near the jet and sparsely spaced far from the jet. This is reasonable because the three-dimensional effects are more influential close to the jet. Fig 5.5 illustrates the comparison between predicted and experimental data.

The model predicts lower pressures far from the jet ($|X| > 5$) and higher pressures near the jet for $|X| < 5$. These higher pressures result because the flow stagnates at the front of the jet whereas the experimental data suggests that the real flow does not. This is caused by the additional component of velocity which contributes to the surface pressures. If this vertical component did not exist and the real flow was truly two-dimensional then it seems likely that the real flow would also stagnate i.e. the model can only represent the horizontal and lateral components of velocity of the real flow and to match the surface pressures the values of the magnitude of these components must be increased to allow for the additional contribution from the vertical component.

After the model parameters had been selected, the surface pressure distribution, the surface force distribution and the suction force coefficients were calculated and compared to the experimentally determined results. Generally, the calculated distribution did not correlate with the experimental data. The values of the parameters (K_1, K_2, H) were adjusted until good agreement with experiment was obtained. The

criterion for a 'best fit' model was that the surface force distribution and suction force coefficient over an area up to five jet radii from the origin agreed well with the experimental measurements. When this agreement was obtained, the parameters were adjusted slightly to improve the surface pressure distribution as much as possible without losing the good surface force and suction force correlation. The 'best' model obtained was the result of considering a wide range of sink strengths, sink positions and source strengths.

The constitution of a'best fit' model is difficult to define. A direct comparison of detailed pressures may appear to be the most direct means but the experimental uncertainty of the pressure far from the jet could result in differences between the prediction and the measurements of several hundred per cent. The experimental error band increases as the magnitude of the pressure decreases (see Chapter 111). If the same experimental error band is considered based on the boundaries of the experimental band in Chapter 111 i.e. the new error band is twice that of the experimental band, then this band seems a reasonable measure by which the prediction can be compared to the measurements far from the jet. An error band criterion appears to be the only direct means of assessing the results. However, there will be regions where the agreement can never be good. The obvious example is immediately upstream of the jet or close to the wake region. Since the accuracy of the model decreases with distance from the jet, all assessments of the predicted integrated distributions were based on an area covering a radial distance of five jet radii. The problem with these integrated quantities is that the inaccuracies occurring far from the jet are multiplied by the corresponding radial distance (see Chapter 1V) to form the product $C_p R$. The larger the area of integration the more suspect these quantities become and hence the restriction to the area

basedon five jet radii. The'best fit' model finally produced predicts regions in which the agreement with the experimental data is bad because of the inability of the two-dimensional model to represent three-dimensional effects.

5.5 Results

The surface pressure distributions and surface force distributions resulting from the 'best fit' models are shown in Figures 5.6 to 5.20 where the solid curves represent the predicted results from the model and the broken curves represent the corresponding experimental data. The values of the entrainment parameter, K_1, the blockage parameter, K_2, and the sink position, H , are shown as functions of the velocity ratio in Figures5.22, 5.23 and 5.24. The predicted suction force coefficients are compared to the corresponding experimental values, both evaluated over a circular area of radius five jet radii and excluding the wake region $(45^o \leq \Theta \leq 180^o,)$in Figure 5.21.

The surface pressure distributions (Figs 5.6,5.9,5.12,5.15,5.18) show a fair correlation with the experimental results for a range of Θ, $90^o \leq \Theta \leq 180^o$, and for $R \leq 5$, especially the contours of value -1, -.5 and -.3. Contours of value -.2 and -.1 generally lie outside this region and show poor agreement. The model is unable to predict the lateral spread of the low pressure region and the agreement far from the jet worsens as the velocity ratio increases. This poor agreement was anticipated because of the inability of the model to describe the three-dimensional effects (see Sect 5.2) and because the good agreement of the surface pressure distribution in regions far from the jet was sacrificed to improve the agreement close to the jet so that the surface forces and the suction force coefficients (for upper limits of integration, RR = 5) showed a good correlation with the experimental values. The surface pressure distribution is greatly affected in the region 90^o

$\leq \theta \leq 45^{\circ}$ by the close proximity of the singularities. The results show poor agreement in this region. The use of a distribution of singularities rather than the use of discrete singularities would probably improve the agreement in this region but would also make the model more complicated.

The surface force distribution (Fig 5.7, 5.10, 5.13, 5.16, 5.19) for an upper limit of integration, RR = 5, shows good correlation between the model and experiment in the lateral and forward regions and for velocity ratios less than 10. The results for the near wake region do not agree well with experiment because of the close proximity of the singularities. As the velocity ratio increases above 8, the agreement between the model and experiment worsens (Fig 5.16, 5.19). The first reason for this poor agreement is the expected inability of the model to allow for the large induced vertical component of velocity, close to the jet (see Section 5.2). The second reason is the inability of the model to predict adequately the diminishing region of low pressures in the near wake region as the velocity ratio increases. This arises because the sink has too great an effect on this region and the values of the entrainment parameter required to predict the surface pressures in the lateral and forward regions, over predicts the surface pressures in the near wake region.

The surface force distribution (Fig 5.8, 5.11, 5.14, 5.17, 5.20), for RR = 10, shows a poor agreement between experiment and the predicted results for velocity ratios less than 10. For velocity ratios greater than 10, the correlation of data between experiment and the model improves (see Fig 5.20).

The predicted suction force coefficients, integrated over an area of 5 jet radii, show excellent agreement with the corresponding experimental results for velocity ratios less than 12 (Fig 5.21), For

velocity ratios greater than 10, the model appears to be unable to predict the weak dependence of the suction force coefficient on the velocity ratio. The reason for this excellent agreement is not difficult to find. The surface force distribution curves (see above) show that the predicted curves lie above and below the experimental curves and the summation involved in the evaluation of the suction force coefficient cancels or hides the regions of poor agreement.

The variation of the entrainment parameter, K_1, with velocity ratio (Fig 5.22) shows that the value of the entrainment parameter is an order of magnitude greater than that of the equivalent freejet. This arises because the entrainment parameter represents the overall entrainment and consists of the vorticity entrainment, which is an order of magnitude greater than that of the freejet (Ref 28), and the freejet entrainment. The value of the entrainment parameter increases with increasing velocity ratio and shows a weak dependence on velocity ratio at high velocity ratios ($m > 8$). As the velocity ratio increases the vorticity entrainment will have a reduced effect on the plate surface because the jet is deflected less and the vortices are further away from the plate surface. In the limiting case, the only entrainment mechanism will be the freejet type and it is expected that the entrainment parameter will rapidly approach the equivalent freejet value as the velocity ratio becomes large. Fig 5.22 tends to confirm this.

The blockage parameter, K_2, increases with increasing velocity ratio (Fig 5.23) and, like the entrainment parameter, shows a weak dependence on velocity ratio for high values of the velocity ratio. The blockage increases as the velocity ratio increases because the length of the potential core increases (see Fig 4.101 and Section 5.2). The increase in potential core frontal area causes a larger separated region to form behind the jet (see Sect 5.2 and the flowfield photo-

graph of ref 14). The potential core length approaches that of the freejet at high velocity ratios and the blockage parameter can be expected to show a weak dependence on velocity ratio, Fig 5.23 shows this to be so although possibly a little prematurely.

The variation of the sink position, H, with velocity ratio (Fig 5.24) shows that the sink position approaches the rear of the jet as the velocity ratio increases. This is in accordance with the experimentally observed shift in the centre of pressure (Fig 4.6) arising from the diminishing contribution to the surface force from the wake region as the velocity ratio increases.

An interesting comment arises from a consideration of Figures 5.22, 5.23 and 5.24. It appears that two separate functions could be used to relate the change in model parameter with velocity ratio: one function would describe the changes for a velocity ratio less than 8 and the other would describe the changes for a velocity ratio greater then 8 with a discontinuity existing between 6 and 8. This observation coincides with the experimental observation concerning the change in surface pressure distribution for velocity ratios below and above 8 (Section 4.3.1.2). Figure 5.9 shows very poor agreement between the predicted and experimental position of the -0.1 contour which arises because the model attempts to predict the effect of the more extensive low pressure region in the near wake and wake regions observed at a velocity ratio of 6. The agreement of the higher magnitude contours is generally good along with the prediction of the surface force distribution (Fig 5.10) and suction force coefficient (Fig 5.21).

Despite the limitation of the two-dimensional model it is capable of predicting the surface force distribution and suction force coefficient (both for upper limits of integration, k = 5) for a velocity ratio less than 10 with good agreement between experiment and prediction. The correlation

of data for the surface pressure distribution is good in the region R $\leq$ 5 and $90^{0} \leq \Theta \leq 180^{0}$. The trend in the variation of the model parameters with increasing velocity ratio accord with the experimentally observed trend in those physical characteristics which the parameters represent.

5.6 Parametric Study.

It is interesting to examine the effect of varying the parameters of the model in a controlled manner. The values of the parameters obtained for the 'best fit' model to predict the experimental data for a velocity ratio of 8 were chosen as the reference values. The values were: $K_1 = 1.82$; $K_2 = 0.71$; $H = 3$; $C_s = 14.95$. These will be denoted by the subscript 0. K_1 and K_2 were varied by $\pm$ 10 per cent of the value of K_{10} anf K_{20} respectively. The effective sink location, H, was varied between 1 and 5 (i.e. $\pm 66\frac{2}{3}$ % of H_0.) For a particular variation in one parameter, the others remained fixed at their respective reference value. The surface force distribution (Figs 5.25,26 and 27) and the suction force coefficient, C_s (both integrated to an upper limit of 5), were calculated, neglecting the wake region as before. The values of C_s obtained are compared to the reference value C_{s0} by the fraction A, where

$$A = \frac{\Delta C_s}{C_{s0}} \times 100 = \frac{C_s - C_{s0}}{C_{s0}} \times 100$$

The percentage change in C_s is then divided by the corresponding percentage change in the parameter under consideration. These values are presented as a fraction B, where

$$B = \frac{A}{\frac{\Delta(\text{Parameter})}{(\text{Parameter})_0} \times 100}$$ for example, if K_1 was being considered then

$$B = \frac{C_s - C_{s0}}{C_{s0}} \times \frac{K_1}{K_1 - K_{10}}$$

These values are presented in Table 5.2

The entrainment parameter, K_1, has the greatest influence on the suction force coefficient. The value of the suction force coefficient increases as the entrainment increases. The surface force distribution (Fig 5.25) shows that the sink has a greater effect in the near wake region and a lesser effect upstream. This is expected because the sink induced velocity is proportional to the inverse of the distance from the sink.

The blockage parameter, K_2, is the next most influential parameter (see Col B, Table 5.2). The suction force coefficient decreases in value as the blockage increases. The source induced velocity is also inversely proportional to distance from the source and consequently the effect of the source is greater in the near wake region than upstream (Fig 5.26).

The sink position has the least effect on the suction force coefficient. The suction force coefficient decreases as the sink moves downstream (Col A and B, Table 5.2). The surface force distribution (Fig 5.27) shows the greatest effect of a change in H occurs in the near wake and lateral region. This is expected since a forward movement of the sink will influence the near wake and lateral region more than the upstream region because the sink induced velocity is inversely proportional to the distance from the sink. The change in slope of the surface force distribution (Fig 5.27) as the sink moves away from the jet appears to be caused by irregularities in the pressure distribution around the afterbody/jet intersection and Figure 5.27 suggests that some form of coupling between the sink position and the blockage is responsible.

In practice, it was found that the sink strength and position were more important than the blockage. The source outflow, K_2, was of an

order of magnitude less than that of K_1. A ten per cent change in K_1 will therefore have a greater effect on the predicted flowfield than a ten per cent change in K_2 and this is reflected in column A of Table 5.2. Generally, the actual changes in K_1 and K_2 were less than 10%, whereas the change in H was greater than 10% when determining the 'best fit' models. K_1 and K_2 were used as fine adjustments to the predicted flowfield and H was a coarse adjustment. Column A of Table 5.2 reflects the 'practical' changes in C_s with the various parameters rather than Column B which shows the actual changes.

TABLE 5.1. VARIATION IN CALCULATED VALUES OF K1

X	K1
=14.00	0.99
=12.00	1.07
=10.00	1.09
=8.00	1.19
=5.00	1.45
=4.50	1.50
=4.00	1.55
=3.00	1.70
=3.50	1.63
=2.50	1.91
=2.00	2.36
=1.50	3.84

AVERAGE K1 = 1.69

MODEL PARAMETERS= CIRCULAR JET EXIT

THETAS = 50.0 DEGREES

K2 = 0.71

N = 3.00

TEST CONDITIONS= CIRCULAR JET EXIT

VJ/V0 = 8.0

PHI = 0.0 DEGREES

ALPHA = 0.0 DEGREES

Table 5.2. Effect of the Variation in Model Parameters on the Suction Force Coefficient.

Comments	C_s	A	B
Increase k1 by 10%	17.56	17.4	1.74
Decrease k1 by 10%	12.45	-16.7	1.67
Increase k2 by 10%	13.84	-7.4	-0.74
Decrease k2 by 10%	16.09	7.6	-0.76
Increase H by 66⅔%	10.49	-29.8	-0.45
Decrease H by 66⅔%	20.08	34.4	-0.52

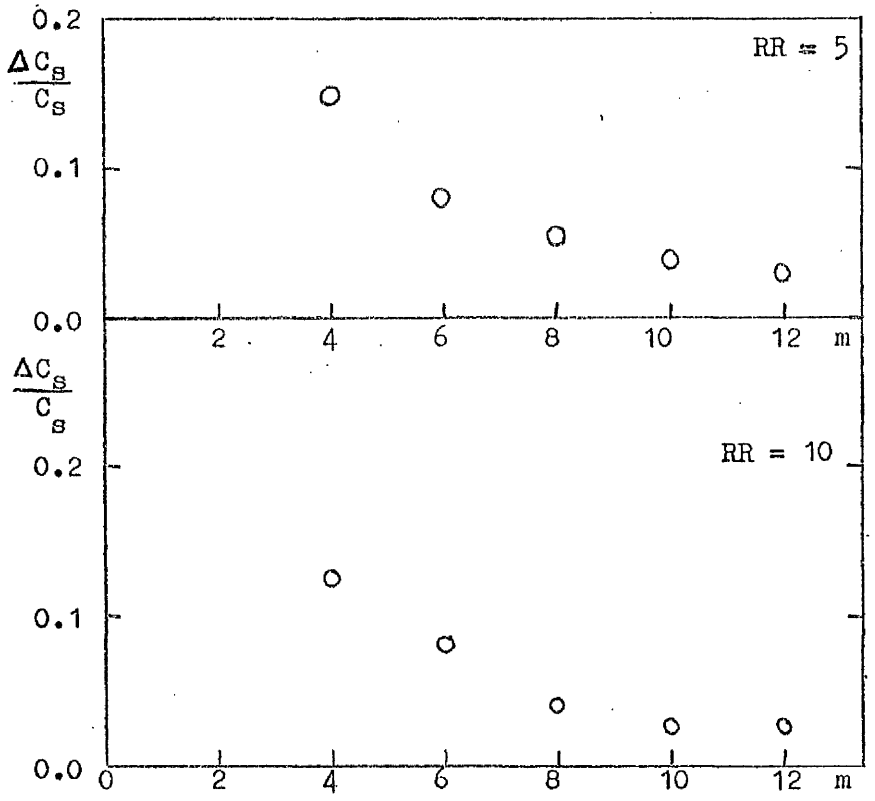

Figure 5.1. Contribution to Suction Force Coefficient from Wake Region.

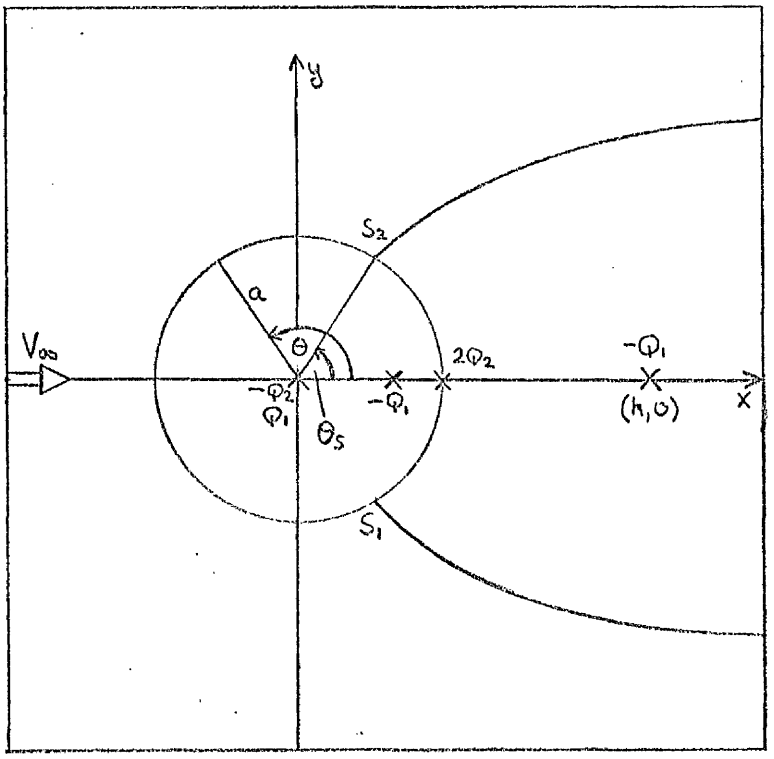

Figure 5.2. 2D Potential Flow Model.

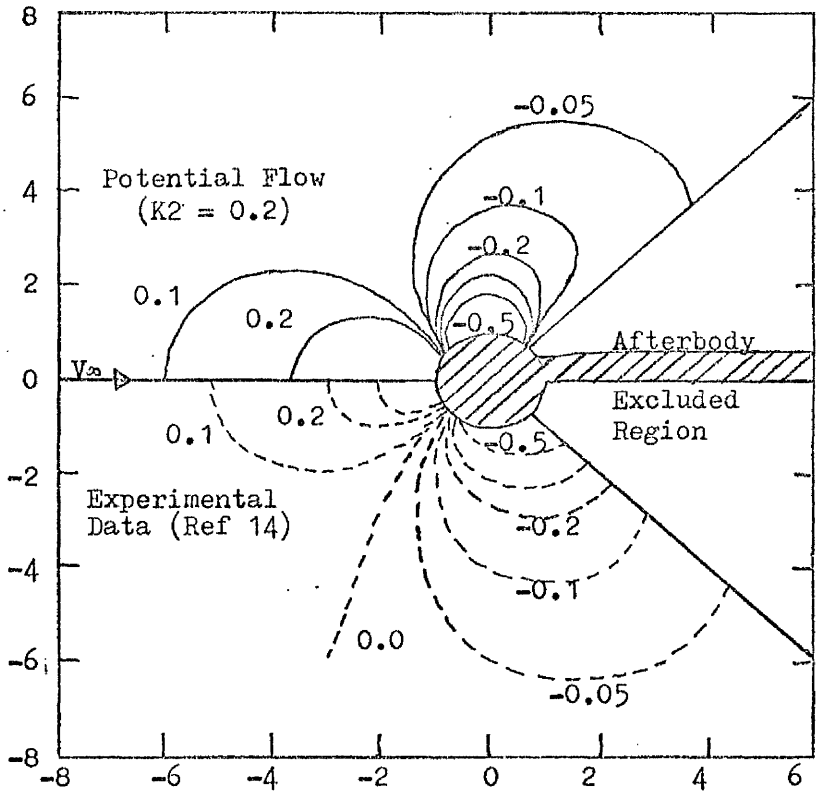

Figure 5.3. Comparison between Experimental Data and Potential Flow Model for Circular Cylinder.

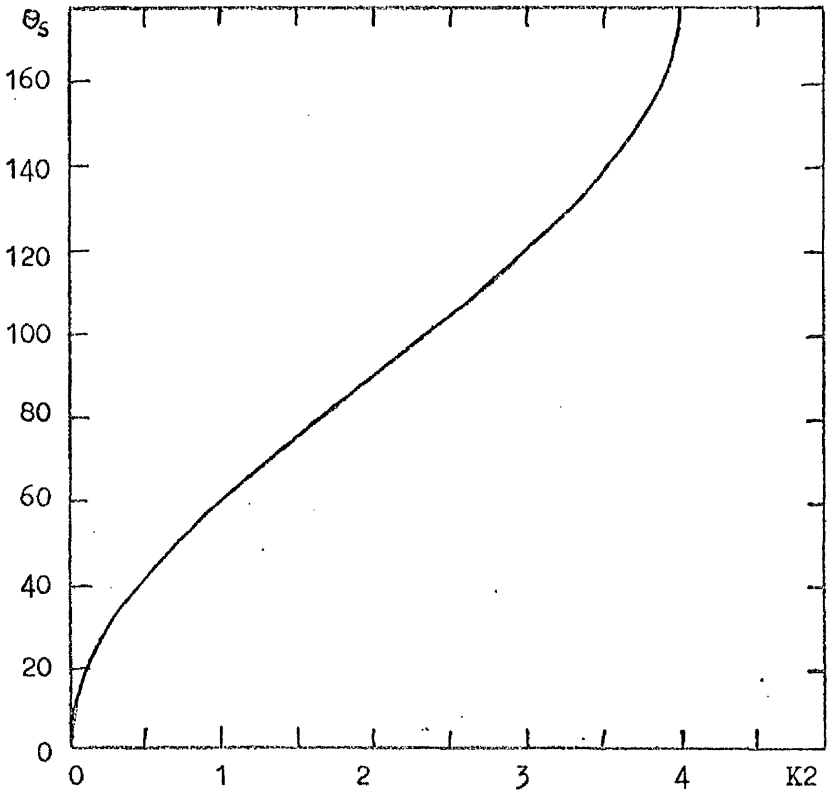

Figure 5.4. Variation of Θ_s with K2.

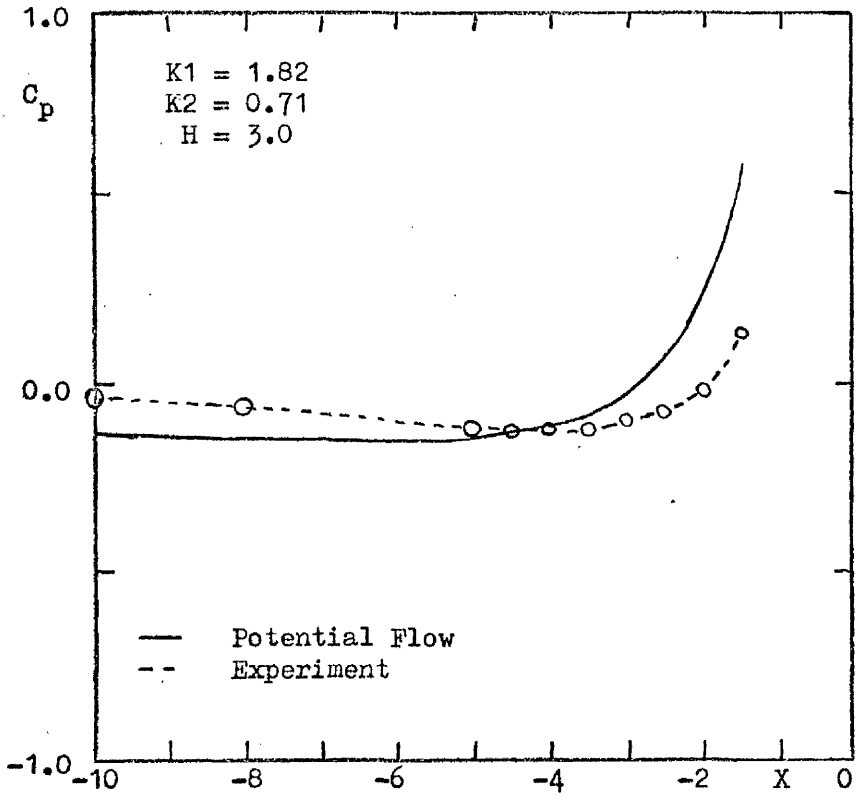

Figure 5.5. Example of Upstream Pressure Distribution Matching ($\phi = 0^o$, $\alpha = 0^o$, m = 8).

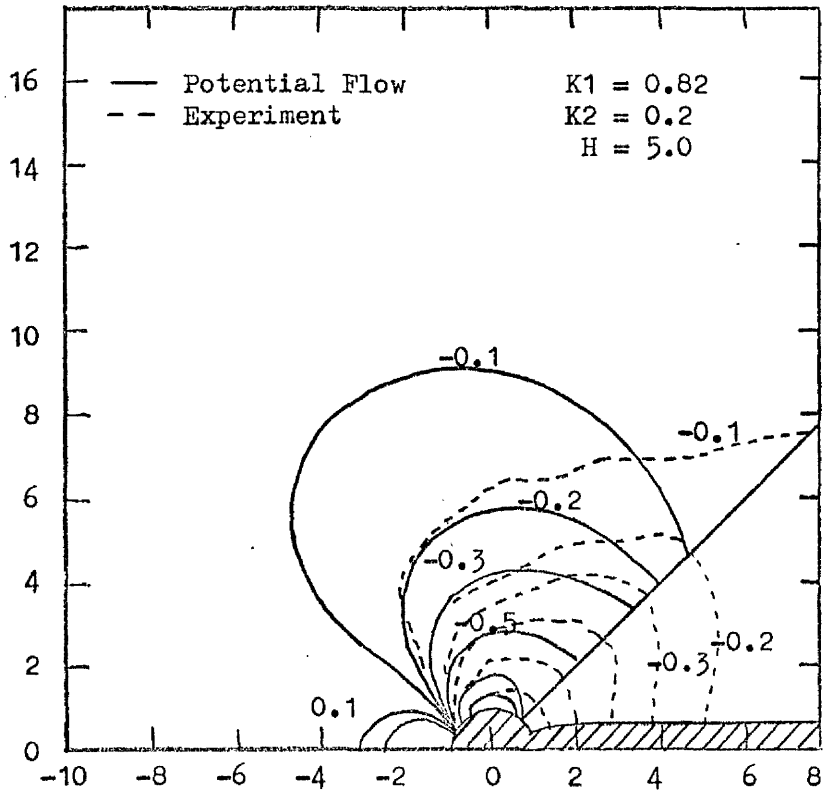

Figure 5.6. Surface Pressure Distribution ($\phi = 0^o$, $\alpha = 0^o$, m = 4).

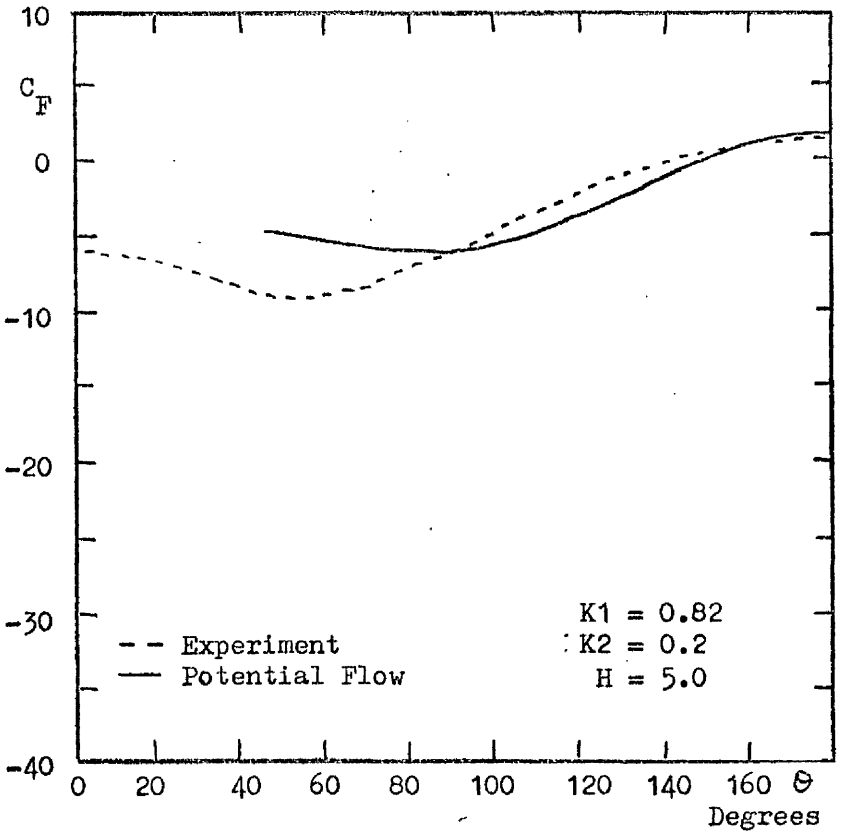

Figure 5.7. Surface Force Distribution ($\phi = 0^\circ, \alpha = 0^\circ, m = 4, RR = 5$).

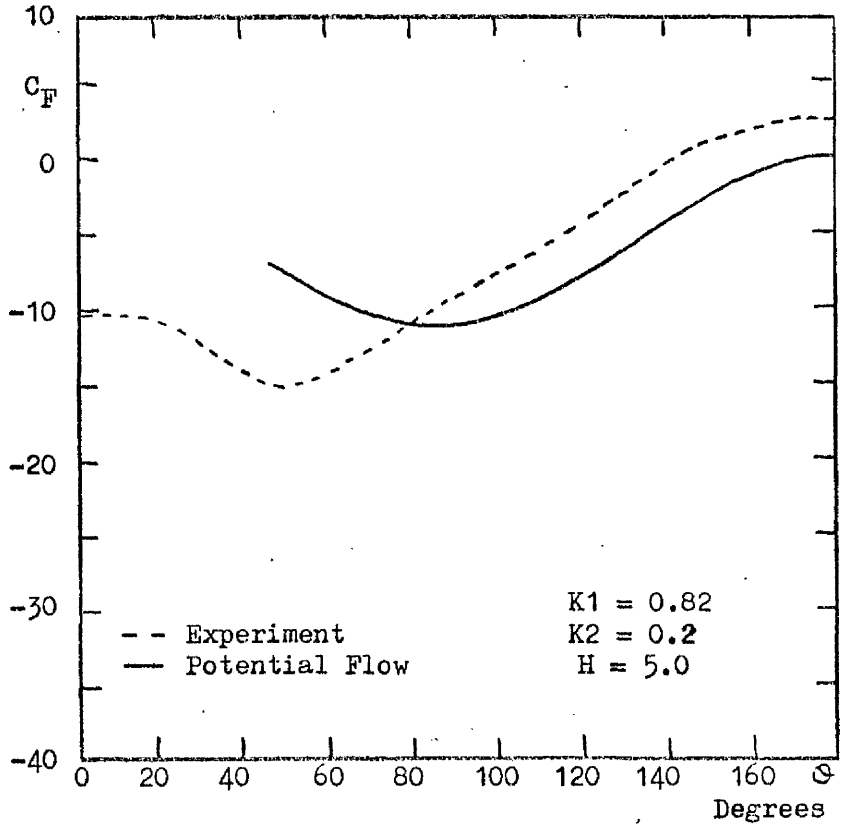

Figure 5.8. Surface Force Distribution ($\phi = 0^\circ, \alpha = 0^\circ, m = 4, RR = 10$).

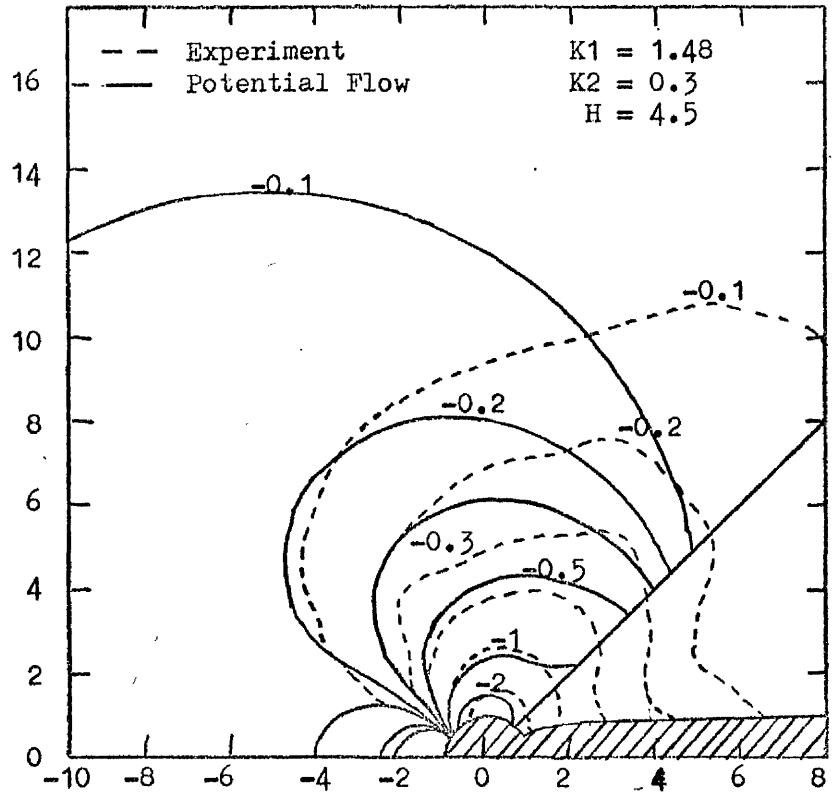

Figure 5.9. Surface Pressure Distribution ($\phi = 0^{\circ}, \alpha = 0^{\circ}, m = 6$).

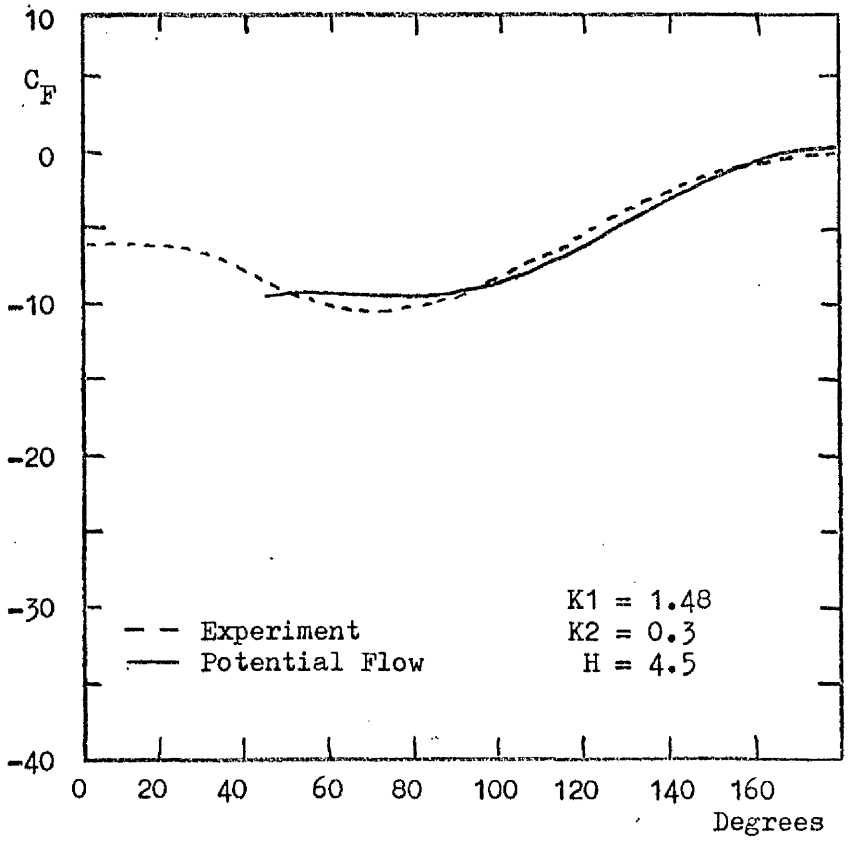

Figure 5.10. Surface Force Distribution ($\phi = 0^{\circ}, \alpha = 0^{\circ}, m = 6, RR = 5$).

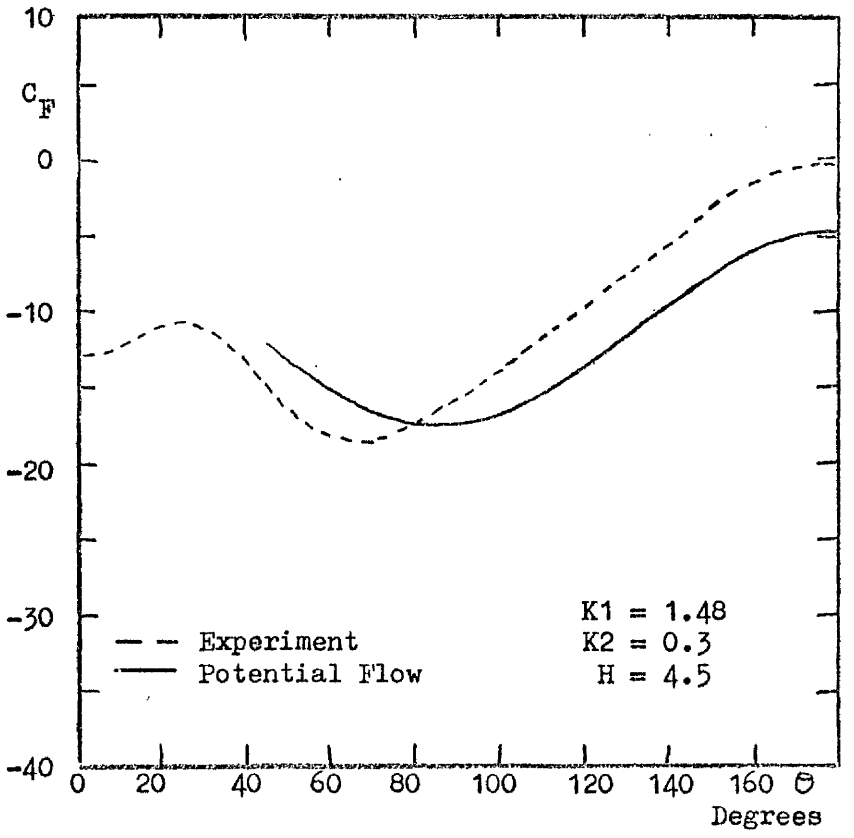

Figure 5.11. Surface Force Distribution ($\phi = 0°$, $\lambda = 0°$, m = 6, RR = 10).

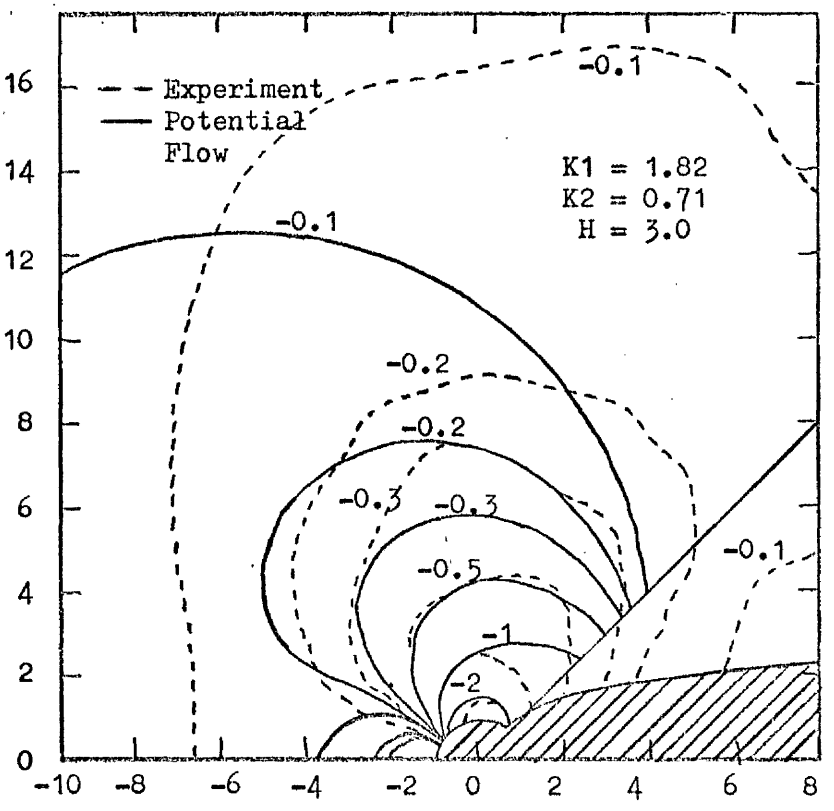

Figure 5.12. Surface Pressure Distribution ($\phi = 0°$, $\lambda = 0°$, m = 8).

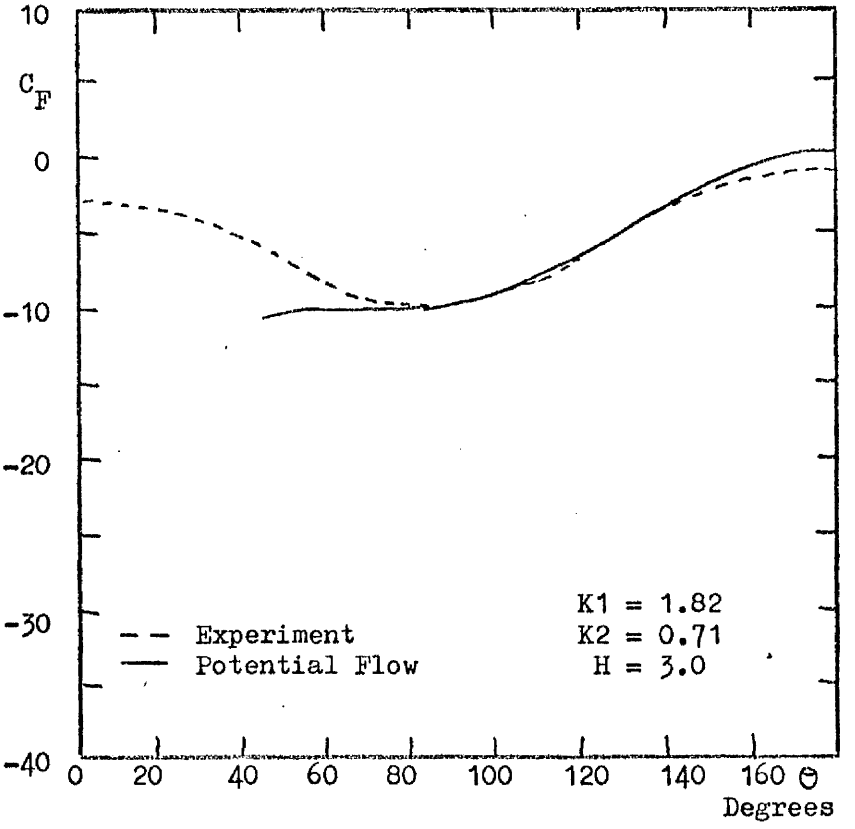

Figure 5.13. Surface Force Distribution ($\phi = 0°, \alpha = 0°, m = 8, RR = 5$).

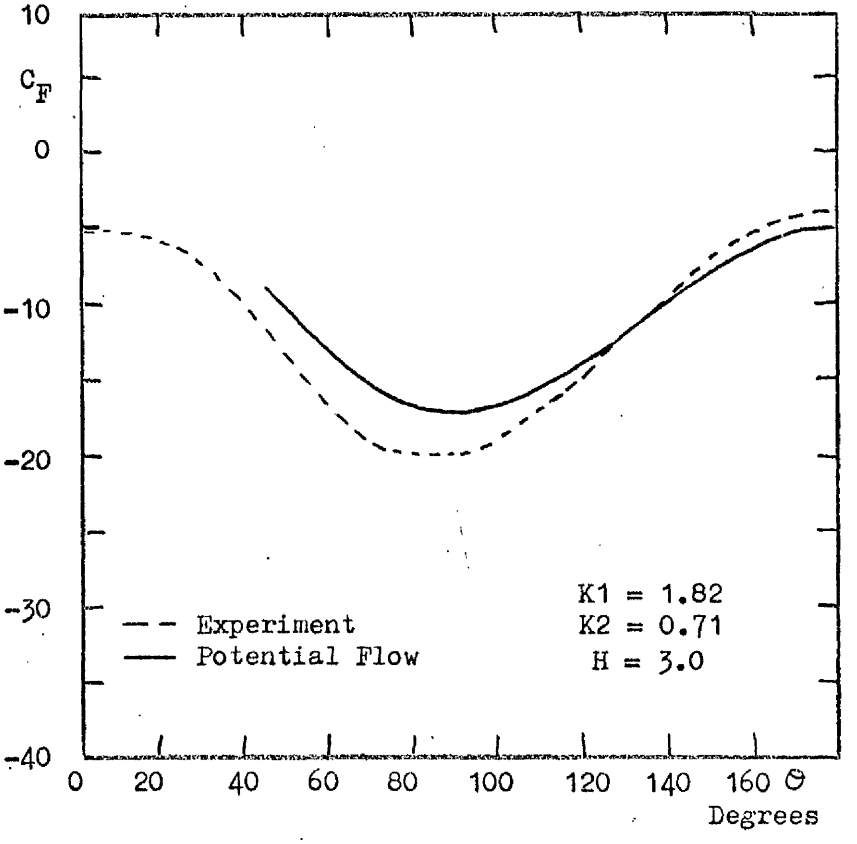

Figure 5.14. Surface Force Distribution ($\phi = 0°, \alpha = 0°, m = 8, RR = 10$).

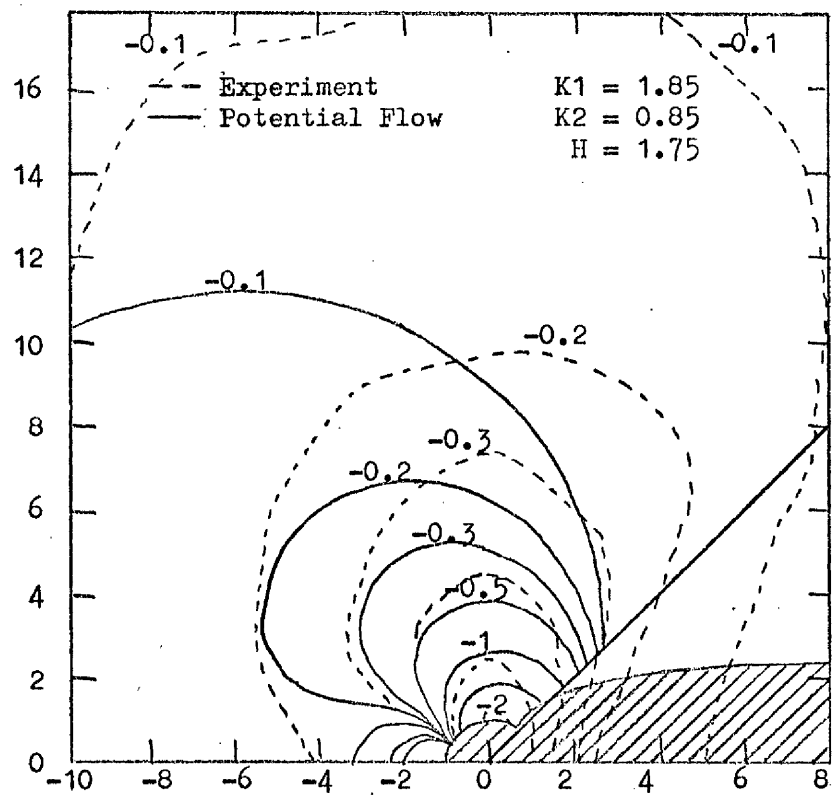

Figure 5.15. Surface Pressure Distribution ($\phi = 0°, \alpha = 0°, m = 10$).

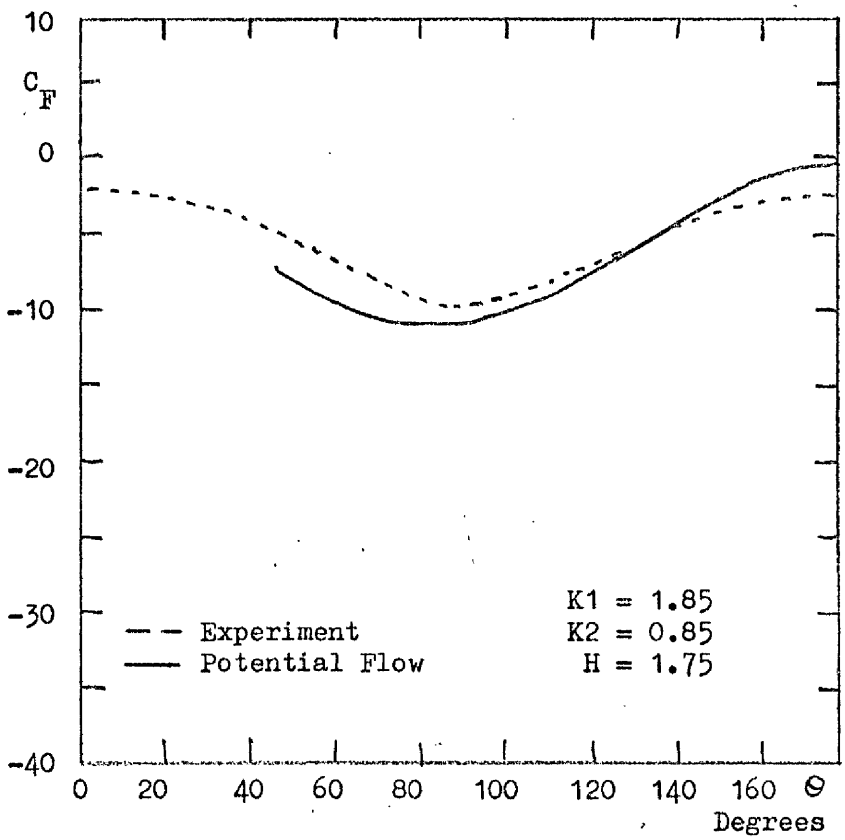

Figure 5.16. Surface Force Distribution ($\phi = 0°, \alpha = 0°, m = 10, RR = 5$).

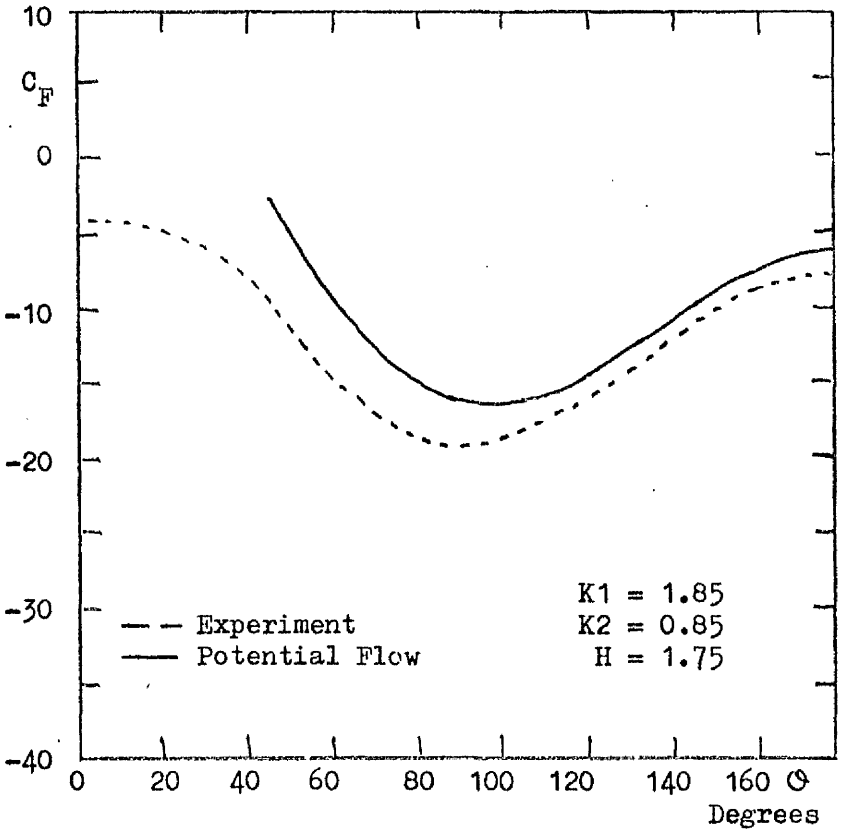

Figure 5.17. Surface Force Distribution ($\phi = 0^\circ, \alpha = 0^\circ$, m = 10, RR = 10).

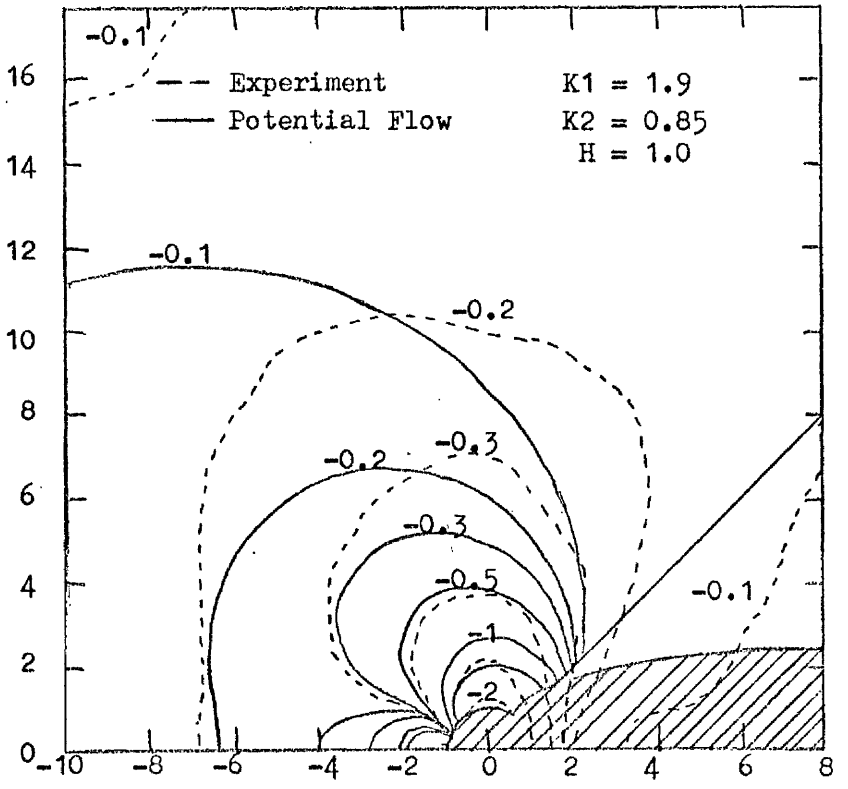

Figure 5.18. Surface Pressure Distribution ($\phi = 0^\circ, \alpha = 0^\circ$, m = 12).

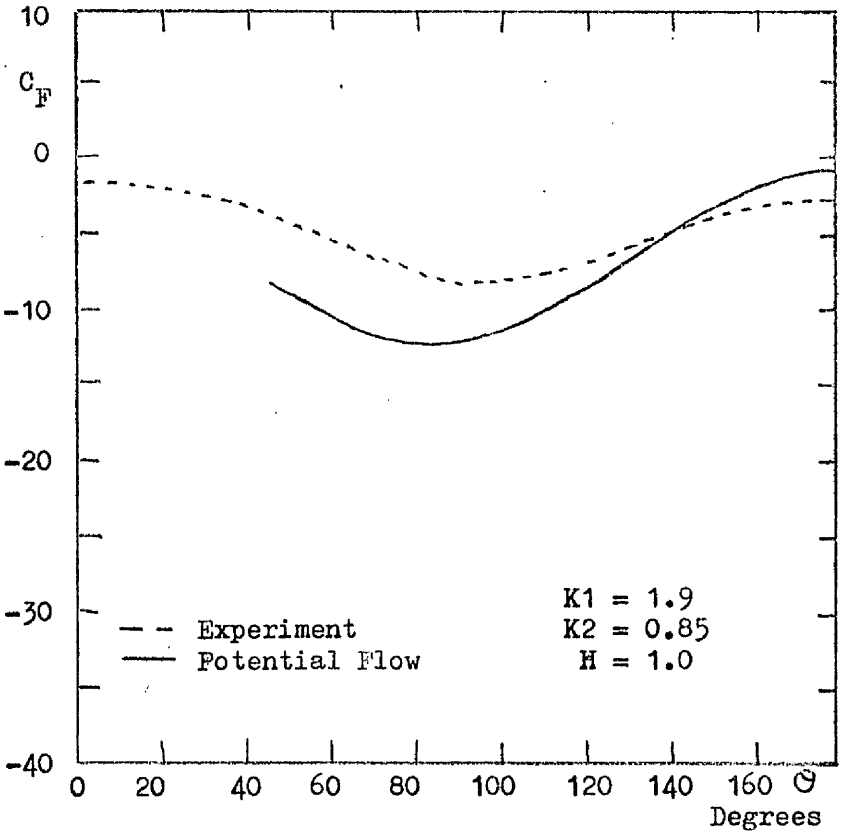

Figure 5.19. Surface Force Distribution ($\phi = 0^\circ, \alpha = 0^\circ, m = 12, RR = 5$).

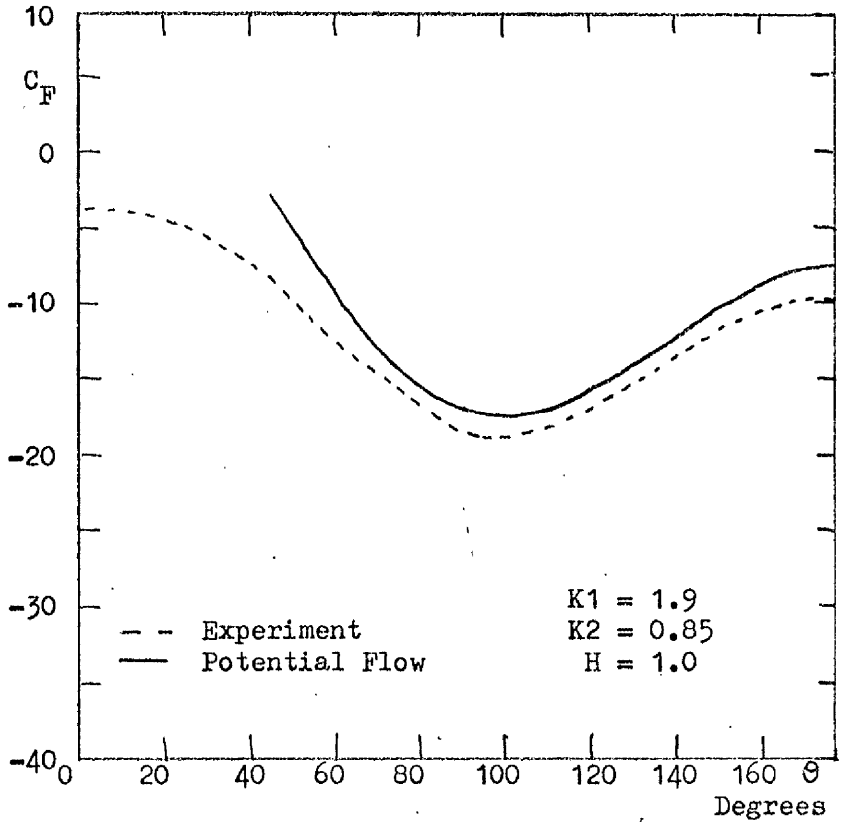

Figure 5.20. Surface Force Distribution ($\phi = 0^\circ, \alpha = 0^\circ, m = 12, RR = 10$).

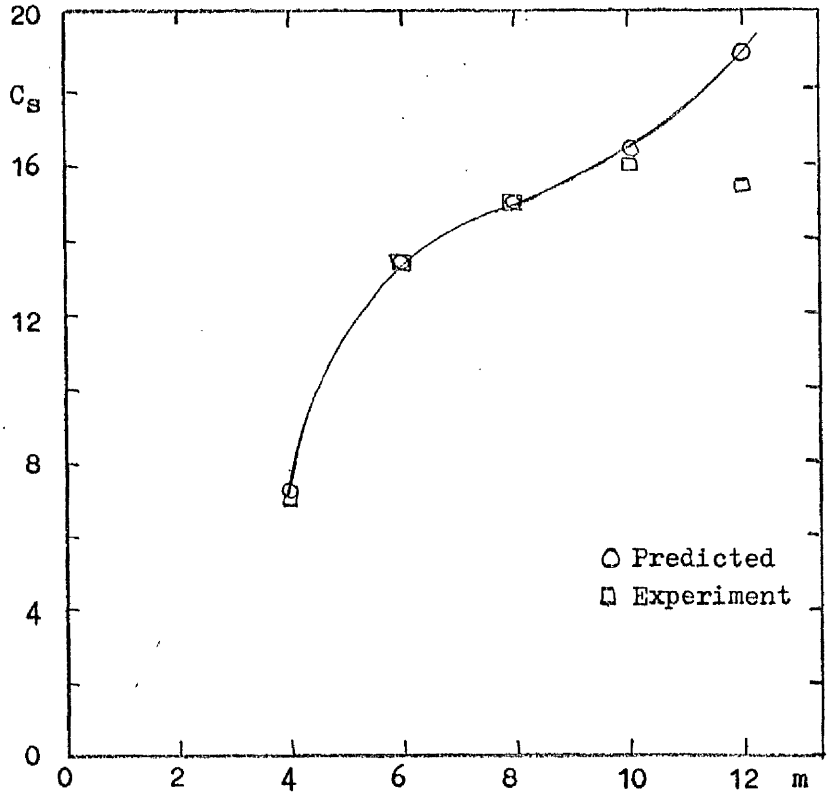

Figure 5.21. Variation of Suction Force Coefficient with Velocity Ratio ($\phi = 0^\circ$, $\alpha = 0^\circ$).

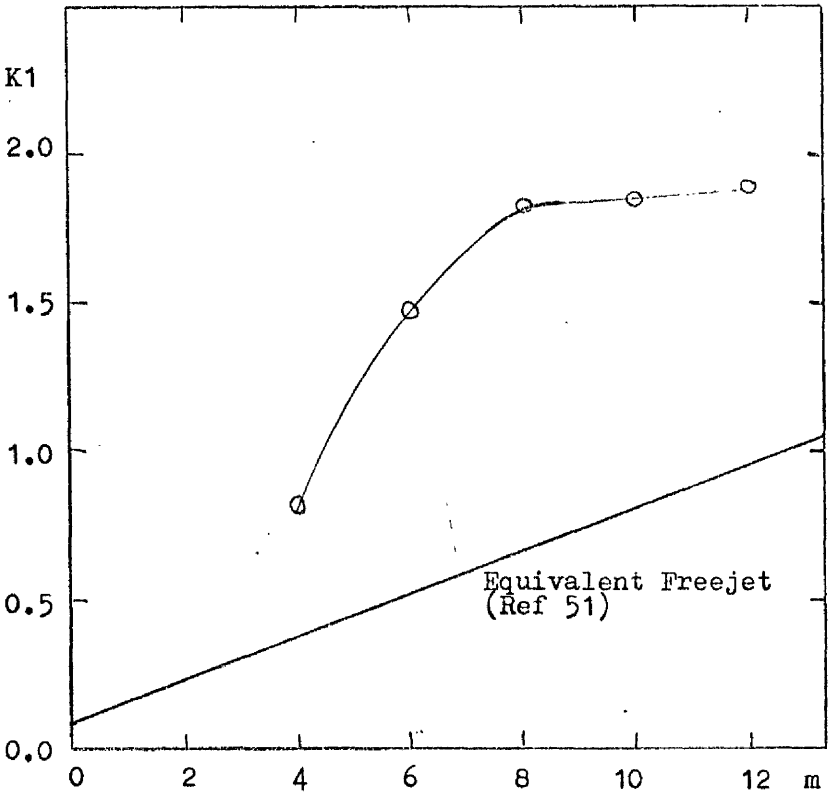

Figure 5.22. Variation of Entrainment Parameter with Velocity Ratio.

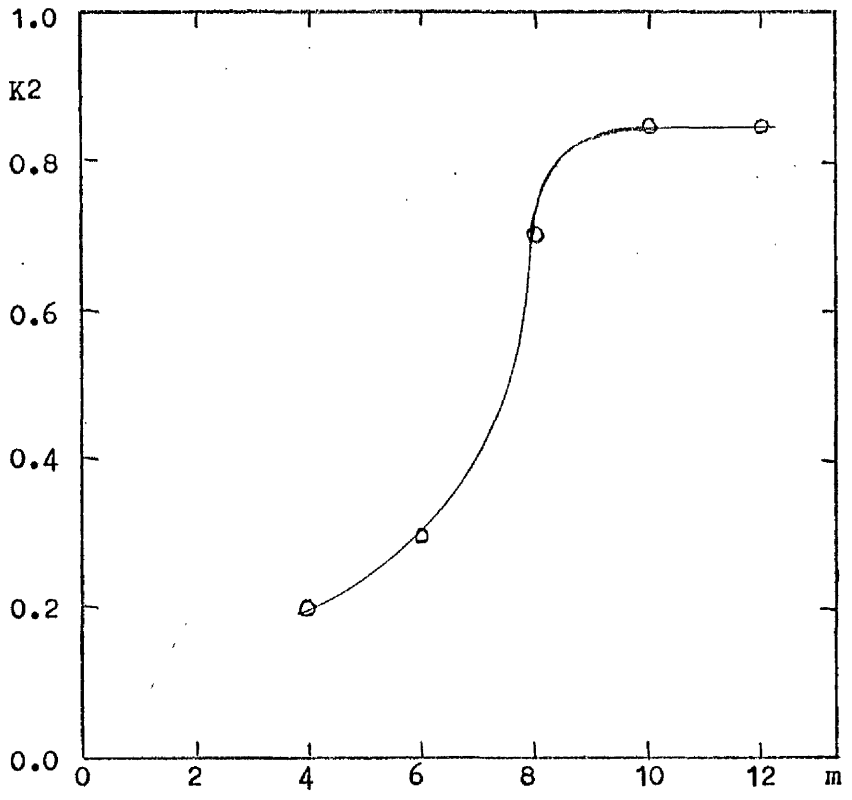

Figure 5.23. Variation of Blockage Parameter with Velocity Ratio.

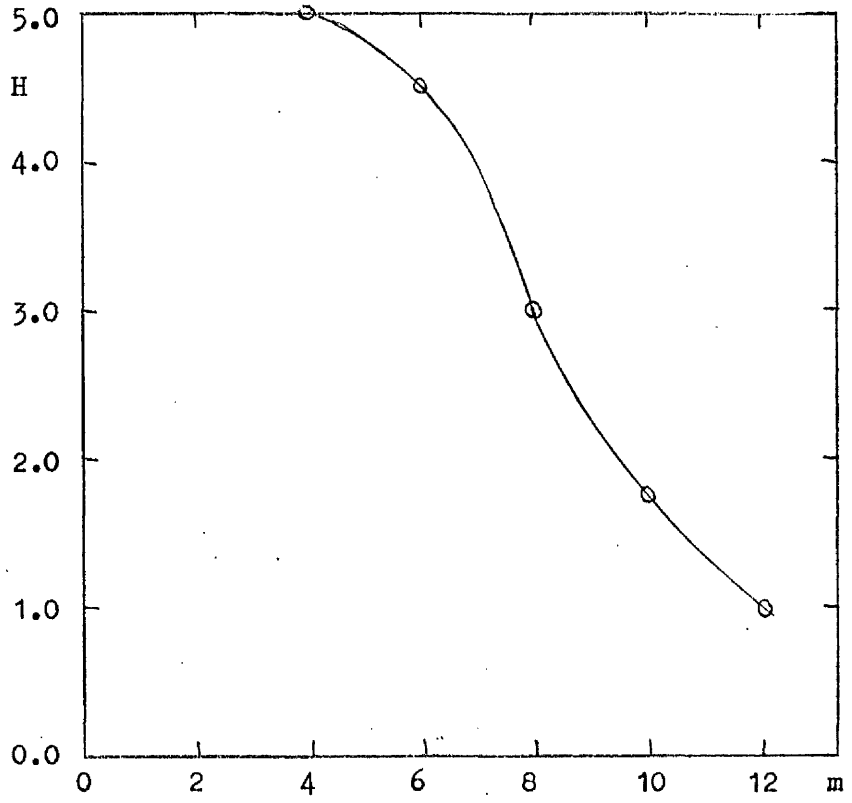

Figure 5.24. Variation of Sink Position with Velocity Ratio.

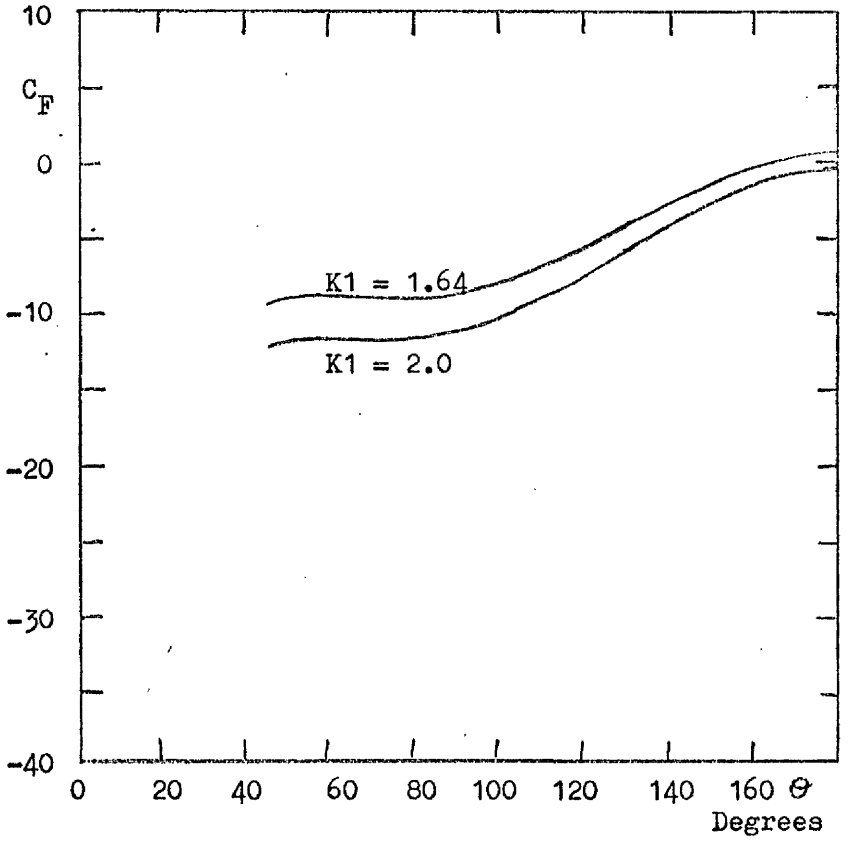

Figure 5.25. Effect of Variation in K1 on Surface Force.

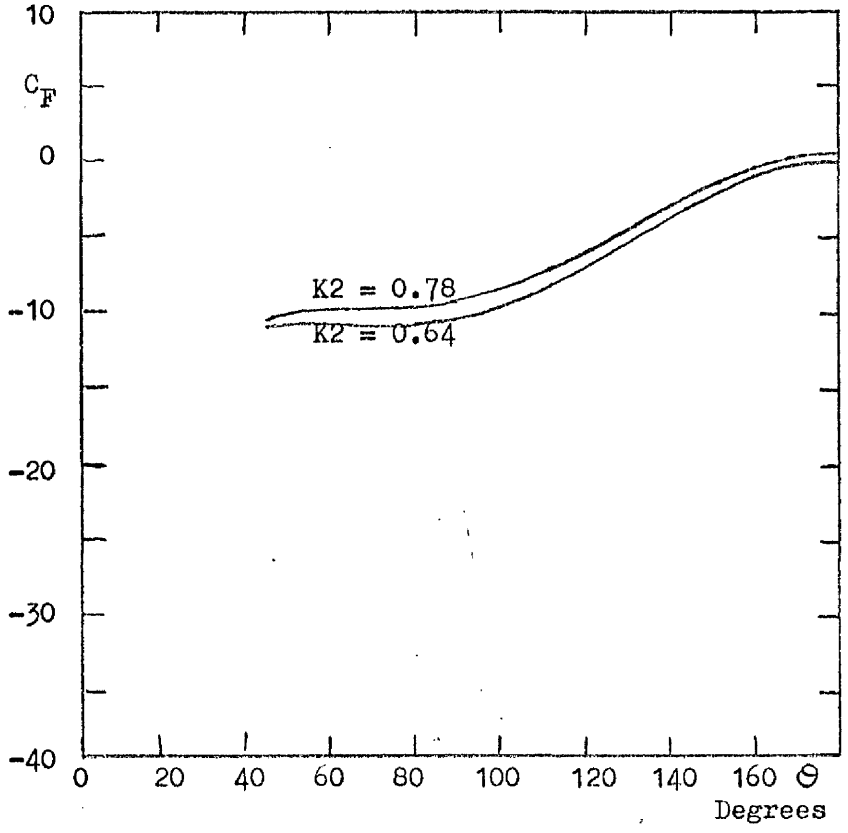

Figure 5.26. Effect of Variation in K2 on Surface Force.

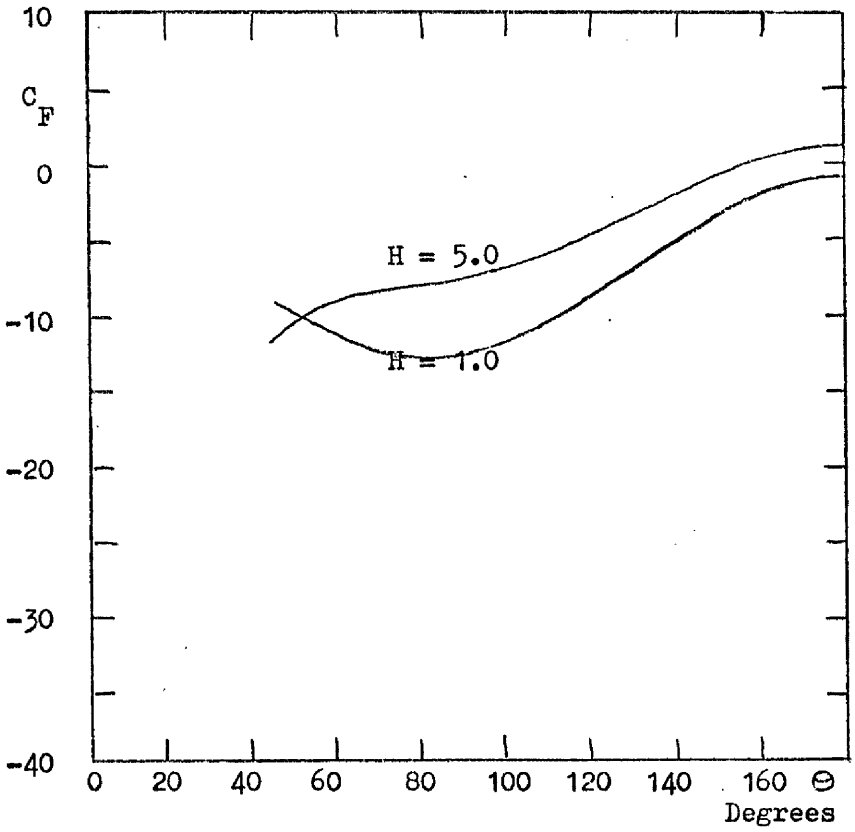

Figure 5.27. Effect of Variation of Sink Position on Surface Force.

Chapter VI

Conclusions and Recommendations.

6.1 Conclusions.

The experimental data collected has identified the jet inclination angle and the velocity ratio as being of primary importance in determining the interference characteristics of a turbulent jet exhausting into a subsonic freestream. The incidence of the surface through which the jet exhausted was of secondary importance.

The extent of the low pressure field to the sides and front of the jet was decreased as the jet inclination increased downstream. The surface force was increased (ie. became less negative) in the upstream and lateral regions. The suction force coefficient was decreased and the centre of pressure moved downstream. The jet penetrated the freestream less and the deflection of the jet was decreased as the jet inclination increased. The potential core length of the jet increased and approached the freejet value and the total pressure decay rate along the jet centreline was lowered. The entrainment rate of the jet was decreased as the jet inclination increased.

An increase in the incidence of the surface through which the jet exhausted caused changes in the surface pressure distribution and the surface force distribution which were within the error band arising from the uncertainty in the pressure readings. The variation of the suction force coefficient with incidence exhibited a maximum at an incidence of between 4^{o} and 6^{o}. The variation of the centre of pressure was independent of incidence. The deflection of the jet trajectory generally increased as incidence increased except for the normal jet where the incidence caused the jet to be directed upstream and the 4^{o} case suffered the maximum deflection.

An increase in incidence caused an effective change in the jet

inclination and modified the entrainment rate accordingly, At small incidences the jet flow dominated the flowfield. At relatively large incidences, the plate/jet interaction became more important and caused the effective entrainment rate to fall.

A comparison between the surface pressure distribution on the flat plate with that on the lower surface of a two-dimensional wing for the case of the normal jet showed that the flat plate data was not entirely applicable to the wing. The qualitative agreement was reasonable and the quantitative agreement improved closer to the jet for velocity ratios greater than 8. At lower velocity ratios, a large increase occurred in the extent of the high pressure region upstream of the jet which had no counterpart on the flat plate.

The low pressures spread to the lateral and forward regions of the flowfield as the velocity ratio increased. The surface force was increased in the wake region and was decreased (i.e. became more negative) in the lateral and forward regions. The suction force coefficient increased with increasing velocity ratio but showed a weak dependence on velocity ratio at high values of the velocity ratio. The centre of pressure moved upstream and also showed a weak dependence on velocity ratio at large values of velocity ratio. The jet penetrated the free-stream more and suffered a less abrupt initial deflection as the velocity ratio increased. The potential core length increased but the total pressure decay rate along the jet centreline remained about the same. The entrainment rate was increased as the velocity ratio increased.

A two-dimensional potential flow model was developed to represent the important physical characteristics of the jet interference problem which governed the surface pressure distribution. The characteristics represented were the entrainment and the blockage arising from the potential core of the jet and the separated region behind the

jet. The surface forces and the surface pressures predicted close to the jet and in the lateral and upstream regions correlated well with the corresponding experimental data for velocity ratios less than 10. The resulting suction force coefficient was found to agree very well with the experimental value. For velocity ratios greater than 10, the two-dimensional model was unable to allow for the three-dimensional effects which began to dominate the flowfield. The trends in the variation of the model parameters with increasing velocity ratio were similar to the trends in the variation of their physical counterparts with increasing velocity ratio.

6.2 Recommendations.

1. The extent of the low pressure field induced on the surface by the jet causes serious lift losses and handling problems. Where the aircraft allows for a STOL capability, the problem can be partially overcome by employing as large an angle of jet inclination as possible with the jet exit placed to the rear of the surface. However, the close proximity of the plume, which penetrates the freestream less in this case, to the aircraft could induce an adverse flowfield about the tailplane. For a direct jet lift VTOL aircraft, this solution is not possible. A method of reducing the extent of low pressure field is required. The investigation could take two different forms. The first approach could investigate ways of reducing the spread of the low pressure field by providing attachments to the surface; the second approach could investigate ways of modifying the jet flow such that the effective entrainment rate is reduced. This approach could also include methods of suppressing the low pressure region formed behind the jet.

2. The effect of turbulence characteristics of the freestream on the jet flow require further investigation. The surface pressure distribution appears not to be affected. The jet appears to penetrate less

as the turbulence level increases. The atmospheric turbulence level is greater than that of the freestream in the experimental tests and it is important to know how much less the penetration will be because the plume will be closer to the tailplane.

3. There is a need for a comprehensive survey of the flowfield, in the forward as well as the lateral and wake regions, induced by inclined jets and jets exhausting through surfaces at incidence to aid the development of any future mathematical modelling.

References.

Number	Author	Title
1	Trebble, W.J.G. Williams, J.	Exploratory Wind-Tunnel Investigation on a Bluff Body Containing a Lifting Fan. RAE TN AERO 2754, 1961.
2	Spreeman, K.P.	Investigation of the Interference of a Deflected Jet with the Freestream and Ground on the Aerodynamic Characteristics of a Semispan Delta Wing VTOL Model. NASA TN D 915, 1961.
3	Trebble, W.J.G.	Wind Tunnel Experiments on a Simple Lifting Jet Body with and without Wings. RAE AERO TN 2882, 1963.
4	Wyatt, L.A.	Tests on the Loss of Vertical Jet Thrust due to Ground Effect on Two Simple VTOL Planforms, with Particular Reference to the Short SC 1 Aircraft. ARC 20369, R & M 3313, 1963.
5	Vogler, R.D.	Interference Effects of Single and Multiple Round or Slotted Jets on a VTOL Model in Transition. NASA TN D 2380, 1964.
6	Vogler, R.D.	Ground Effects on Single Jet and Multiple Jet VTOL Models at Transition Speeds over Stationary and Moving Ground Planes. NASA TN D 3213, 1966.
7	Trebble, W.J.G.	Wind Tunnel Experiments on a Lifting Jet in a Bluff Body with and without Wings. RAE TN AERO 2971, 1966.

Number	Author	Title
8	Hackett, J.E.	Wind Tunnel Tests on a Streamlined Fan Lift Nacelle. R & M 3470, 1967.
9	Carter, A.W.	Effects of a Jet Exhaust on the Longitudinal Aerodynamic Characteristics of a Jet V/STOL Model. NASA TN D 5333, 1969.
10	Vogler, R.D.	Wind Tunnel Investigation of a VTOL Jet Transport Model with Powered Lift Engines in Pods at the Wing Midspan or Inboard. NASA TN D 5770, 1970.
11	Williams, J. Wood, M.N.	Aerodynamic Interference Effects with Jet-Lift V/STOL Aircraft under Static and Forward Speed Conditions. RAE TR 66403, 1966.
12	Margason, R.J.	Review of Propulsion Induced Effects on the Aerodynamics of Jet V/STOL Aircraft. NASA TN D 5617, 1970.
13	Vogler, R.D.	Surface Pressure Distributions Induced on a Flat Plate by a Cold Air Jet Issuing Perpendicularly from the Plate and Normal to a Low Speed Free Stream Flow. NASA TN D-1629, 1963.
14	Bradbury, L.J.S. Wood, M.N.	Static Pressure Distribution around a Circular Jet Exhausting Normally from a Plane Wall into an Airstream. RAE TN AERO 2978, 1964.

Number	Author	Title
15	Gelb, G.H. Martin, W.A.	An Experimental Investigation of the Flow Field about a Subsonic Jet Exhausting into a Quiescent and a Low Velocity Airstream. Canadian Aeronautics and Space Journal, Vol 12, No 8, October 1966.
16	Wu, J.C. McMahon, H.M. Mosher, D.K. Wright, M.A.	Experimental and Analytical Investigations of Jets Exhausting into a Deflecting Stream. AIAA Paper No 69-223, February 1969.
17	McMahon, H.M. Mosher, D.K.	Experimental Investigation of Pressures Induced on a Flat Plate by a Jet Issuing into a Subsonic Crosswind. Paper 4, NASA SP 218, September 1969.
18	Mosher, D.K.	An Experimental Investigation of a Turbulent Jet in a Crosswind. Ph D Thesis, Georgia Institute of Technology. 1970.
19	Fricke, L.B. Wooler, P.T. Ziegler, H.	Wind Tunnel Investigations of Jets Exhausting into a Crossflow. Volume 1. Test Description and Data Analysis. Volume 2. Additional Data for One Jet Configuration. Volume 3. Additional Data for Two Jet Configuration. Volume 4. Additional Data for three Jet Configuration. Air Force Flight Dynamics Laboratory TR 70-154, December 1970.

Number	Author	Title
20	Fearn, R.L. Weston, R.P.	Induced Pressure Distribution of a Jet in a Cross Flow. NASA TN D 7916, 1975.
21	Peake, D.J.	The Pressures on a Surface Surrounding a Jet Issuing Normal to a Mainstream. NRC LR 410, November 1964.
22	Mikolowsky, W.T.	Experimental Investigation of a Jet Issuing from a Wing in Crossflow. Ph D Thesis, Georgia Institute of Technology, 1972.
23	Mikolowsky, W.T. McMahon, H.	An Experimental Investigation of a Jet Issuing from a Wing in Crossflow. Journal of Aircraft, Vol 10, No 9, 1973.
24	Jordinson, J.	Flow in a Jet Directed Normal to the Wind. R & M 3074, 1956.
25	Gordier, R.L.	Studies of Fluid Jets Discharging into a Moving Liquid. St Anthony Falls Hydro Laboratory, University of Minnesota, TP 28, Series B, 1959.
26	Keffer, J.F. Baines, W.D.	The Round Turbulent Jet in a Cross Wind. Journal Fluid Mechanics, Vol 15, 1963.
27	Pratte, B.D. Baines, W.D.	Profiles of a Round Turbulent Jet in a Cross Flow. Journal Hydraulics Division, ASCE 92 HY6, November 1967.
28	Platten, J.L. Keffer, J.F.	Entrainment in Deflected Axisymmetrical Jets at Various Angles to the Stream. University of Toronto, Mechanical Engineering TP 6808, June 1968.

Number	Author	Title
29	Pratte, B.D. Keffer, J.F.	Swirling Turbulent Jet Flows. Pt 1. Single Swirling Jet. University of Toronto, Mechanical Engineering TP 6901, March 1969.
30	Patrick, M.A.	Experimental Investigation of the Mixing and Penetration of a Round Turbulent Jet Injected Perpendicularly into a Transverse Stream. Trans Institute Chemical Engineers, Vol 45 February 1967.
31	Reilly, R.S.	Investigation of the Deformation and Penetration of a Turbulent Subsonic Jet Issuing Transversely into a Uniform, Subsonic Main Stream. Ph D Thesis, University of Maryland, 1968.
32	Margason, R.J.	The Path of a Jet Deflected at Large Angles to a Subsonic Free Stream. NASA TN D 4919, 1968.
33	McAllister, J.D.	A Momentum Theory for the Effects of Cross Flow on Incompressible Turbulent Jets. Ph D Thesis, University of Tennessee, 1968.
34	McMahon, H.M. Hester, D.D. Palfery, J.G.	Vortex Shedding from a Turbulent Jet in a Crosswind. Journal Fluid Mechanics, Vol 48, Pt 1, 1971.
35	Kamotani, Y. Greber, I.	Experiments on a Turbulent Jet in a Cross Flow. AIAA Journal, Vol 10, NO 11, November 1972.

Number	Author	Title
36	Fearn, R. Weston, R.P.	Vorticity Associated with a Jet in a Crossflow. AIAA Journal, Vol 12, No 12, December 1974.
37	Riegels, F.W.	Aerofoil Sections. Butterworths, 1961.
38	Smith, R.H. Wang, C.T.	Contracting Cones giving Uniform Throat Speed. Journal of Aeronautical Sciences, Vol 11, No 4, October 1944.
39	Bryer, D.W. Pankhurst, R.C.	Pressure Probe Methods for Determining Wind Speed and Flow Direction. NPL HMSO, 1971.
40	Rainbird, W.J.	Errors in Measurement of Mean Static Pressures of a Moving Fluid due to Pressure Holes. DME/NAE Quarterly Bulletin, No 1967(3), October 1967.
41	Ower, E. Pankhurst, R.C.	Measurements of Air Flow. Pergamon, 1966.
42	Tyler, R.A. Williamson, R.G.	Observations of Tunnel Flow Separation Induced by an Impinging Jet. NRC Aero Report LR 537, April 1970.
43	Rubbert, P.E.	Calculation of Jet Interference Effects on V/STOL Aircraft by Nonplanar Potential Flow Method. Paper 12, NASA SP 218, September 1969.
44	-	Analysis of a Jet in a Subsonic Crosswind. Papers 6 - 15, NASA SP 218, September 1969.

Number	Author	Title
45	Wooler, P.T. Kao, H.C. Schwendemann, M.F. Wasson, H.R. Ziegler, H.	V/STOL Aerodynamic Prediction Methods Investigation. Volume 1. Theoretical Development of Prediction Methods. Volumell. Application of Prediction Methods. Volume lll. Manual for Computer Programmes. Volume lV. Literature Survey. Air Force Flight Dynamics Laboratory TR 72 - 76, January 1972.
46	Snel, H.	A Method for the Calculation of the Flow Field Induced by a Jet Exhausting Perpendicularly into a Crossflow. Paper 18, AGARD CP 143, April 1974.
47	Wright, M.A.	A Two-Dimensional Representation of the Crosswind for the Jet Interference Problem. Ph D Thesis, Georgia Institute of Technology, 1971.
48	Mehmel, D.	Untersuchungen über das Strömungsfeld eines schräg angeblasenen Strahles. Teil I, AVA (Göttingen) Bericht 67 A 53, 1967.
49	Abramovich, G.N.	Theory of Turbulent Jets. Cambridge, MIT Press, 1963.
50	Crowe, C.T. Riesebieter, H.	An Analytical and Experimental Study of Jet Deflection in a Cross Flow. Paper 16, AGARD CP 22, 1967.

Number	Author	Title
51	Ricou, F.P. Spalding, D.B.	Measurements of Entrainment by Axisymmetrical Turbulent Jets. Journal Fluid Mechanics, Vol 11, Pt 1, August 1961.
52	Parkinson, G.V. Jandali, T.	A Wake Source Model for Bluff Body Potential Flow. Journal Fluid Mechanics, Vol 40, Pt 3, 1970.

Appendix A

Jet Characteristics

Initial experiments were conducted to determine the freejet characteristics of the five jets. The total pressure distribution across each jet exit and the total pressure decay along each jet centreline were investigated. These initial tests were motivated by the conclusion of ref A1 which stated that the jet induced effects were strongly influenced by the jet pressure decay characteristics. It was considered desirable to ensure that the characteristics of all the jet exit geometries were similar.

The jet plenum chamber was placed on a cradle positioned in the working section of the tunnel such that the jet centreline and tunnel centreline were coincident. The jet could exhaust some 12 to 15 feet before encountering any obstruction. The air supply was identical to that described in Section 2.2.

The traversing rig was installed in the working section complete with the total pressure probe (Section 2.8, Plate 2.2). The first experiment was to calibrate the reading of the static pressure tap within the jet plenum chamber ($p_s - p_A$) against that of the exit total pressure ($p_{OE} - p_A$). The total pressure probe was positioned at the centre of the jet exit plane. The second experiment determined the jet exit total pressure distribution in the exit plane normal to the jet centreline. Using the calibration from the first experiment, the desired exit conditions were set (usually V_J = 200ft/sec). The exit plane was traversed. The results are given in fig A.1 to A.5. In fig A.1 an additional traverse is given for a jet exit velocity of 600ft/sec. The results are presented in the form of a total pressure coefficient:

$$\frac{p_T}{p_E} = \frac{p_0 - p_A}{p_{OE} - p_A}$$

where p_0 is the total pressure at any point and p_{OE} is the exit total pressure at the jet centre-line.

The jet exit total pressure profiles were uniform to within 1% for $-0.6 \leq D \leq 0.6$ or $R \leq 0.6$. This was considered to be satisfactory especially as the jet exit geometries were dissimilar.

The third experiment measured the jet total pressure decay along the jet centreline. The results are presented in fig A.6 to A.10 using the above total pressure coefficient. The freejet total pressure decay curves were very similar for all geometries. The potential core length was about 11 jet radii which agreed well with the results of ref A2 (potential core length quoted as about 12 jet radii).

A.1 Jet Dynamic Pressure

The method of determing the jet dynamic pressure was as follows: the freestream dynamic pressure was selected (in this work $q_\infty = 1.07$mm of mercury). The jet exit dynamic pressure was given by

$q_J = m^2 q_\infty$ where $m = \sqrt{\dfrac{\int_{A_J} \rho_J V_J^2 dA}{\rho_\infty V_\infty^2 A_J}}$

now if the jet and crossflow fluid are the same and obey the ideal gas equation of state and the pressure at the jet exit is the same as the freestream pressure (static) and if the jet is unheated (i.e. $\rho_\infty = \rho_J$) then m simply becomes, for V_J constant, $m = V_J/V_\infty$.

Using the isentropic pressure ratio at the jet exit

$$p_{OE} = p_E\left(1 + \frac{\gamma - 1}{2} M_E^2\right)^{\frac{\gamma}{\gamma - 1}}$$

Assuming $p_E = p_\infty = p_A$ (wind tunnel breather should give $p_\infty = p_A$)

where $M_E^2 = V_J^2/a_J^2$ and a_J is the acoustic velocity at the jet exit

$= m^2 V_\infty^2 \rho_\infty / \gamma p_\infty$

$= 2m^2 q_\infty / \gamma p_\infty$

Hence $p_{OE} - p_A = p_A\left(1 + (\gamma - 1) m^2 q_\infty / \gamma p_\infty\right)^{\frac{\gamma}{\gamma - 1}} - p_A$

using a value of 1.4 for γ

$$p_{OE} - p_A = p_A(1 + m^2 q_\infty / 3.5 p_\infty)^{3.5} - p_A$$

From this last equation, curves of $p_{OE} - p_A$ versus p_A for various values of the velocity ratio, m, with q_∞ = 1.07mm of mercury were constructed. These curves showed a very linear relationship between $p_{OE} - p_A$ and p_A, the discrepancy being less than any errors incurred experimentally. No allowance was made for the non-isentropicity of the jet flow.

References

A1	Ousterhout, D.S.	An Experimental Investigation of a Cold Jet Emitting from a Body of Revolution into a Subsonic Free Stream. NASA CR 2089, August 1972.
A2	Albertson, M.L. Dai, Y.B. Jensen, R.A. Rouse, H.	Diffusion of Submerged Jets. Trans. ASCE 115(1950) Paper 2409.

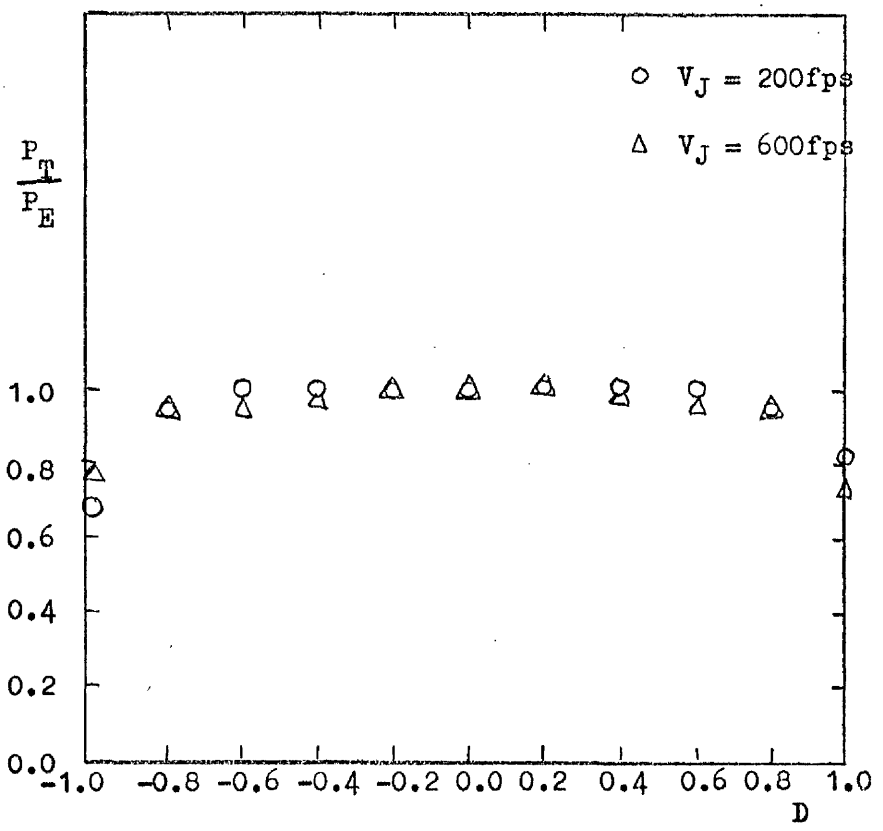

Figure A.1. Total Pressure Profile of Nozzle Exit ($\phi = 0^c$).

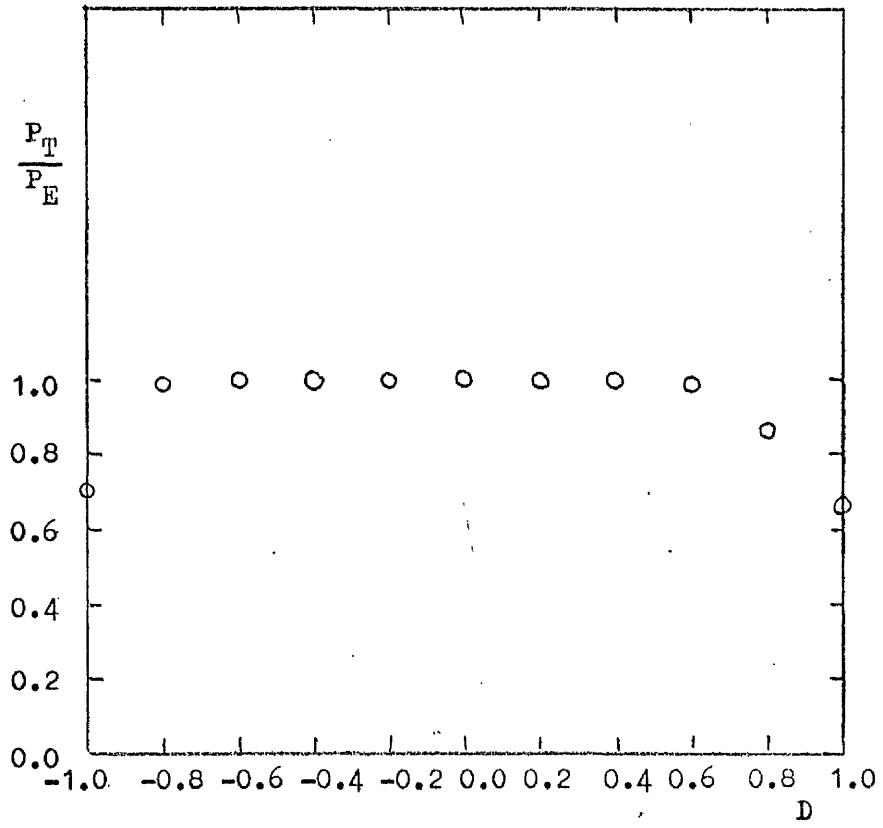

Figure A.2. Total Pressure Profile of Nozzle Exit ($\phi = 15^c$).

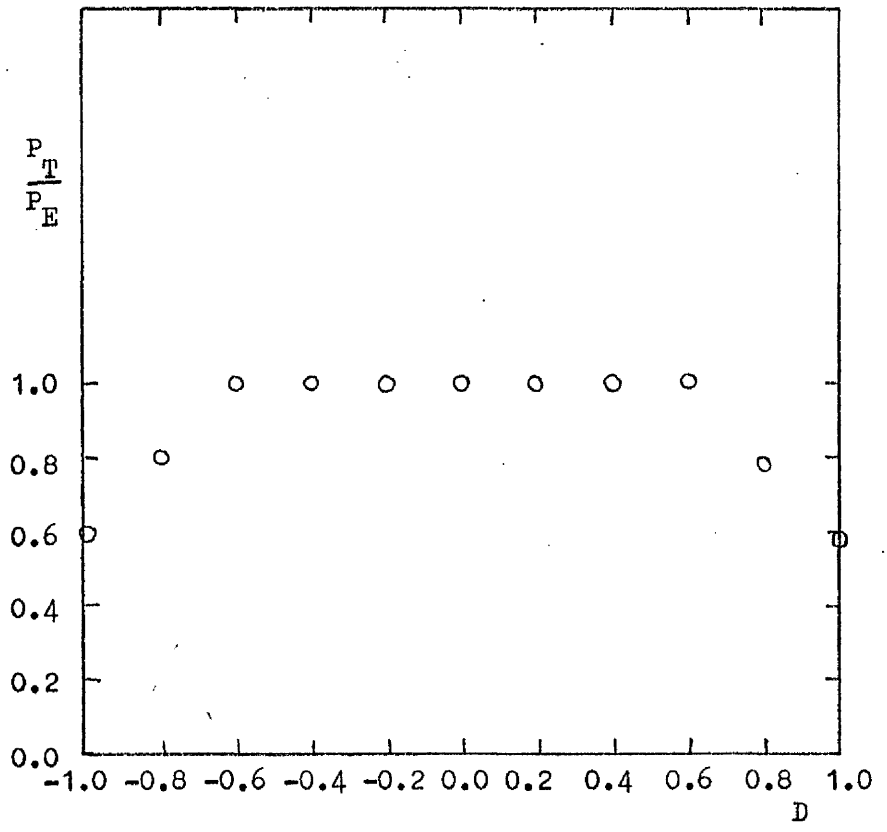

Figure A.3. Total Pressure Profile of Nozzle Exit ($\phi = 30^{\circ}$).

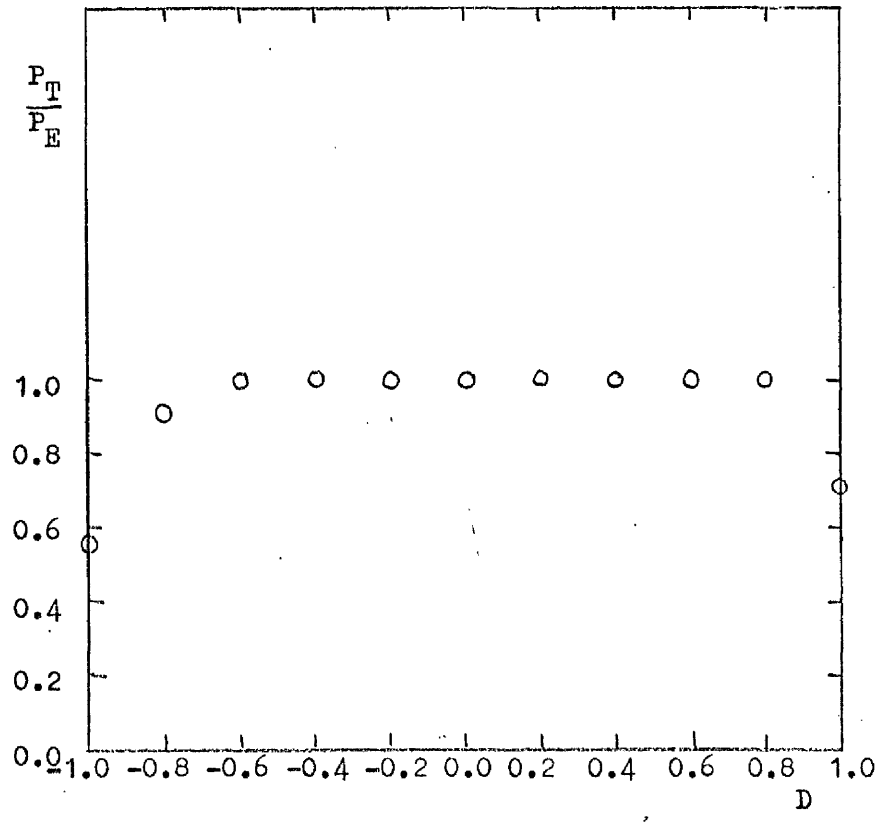

Figure A.4. Total Pressure Profile of Nozzle Exit ($\phi = 45^{\circ}$).

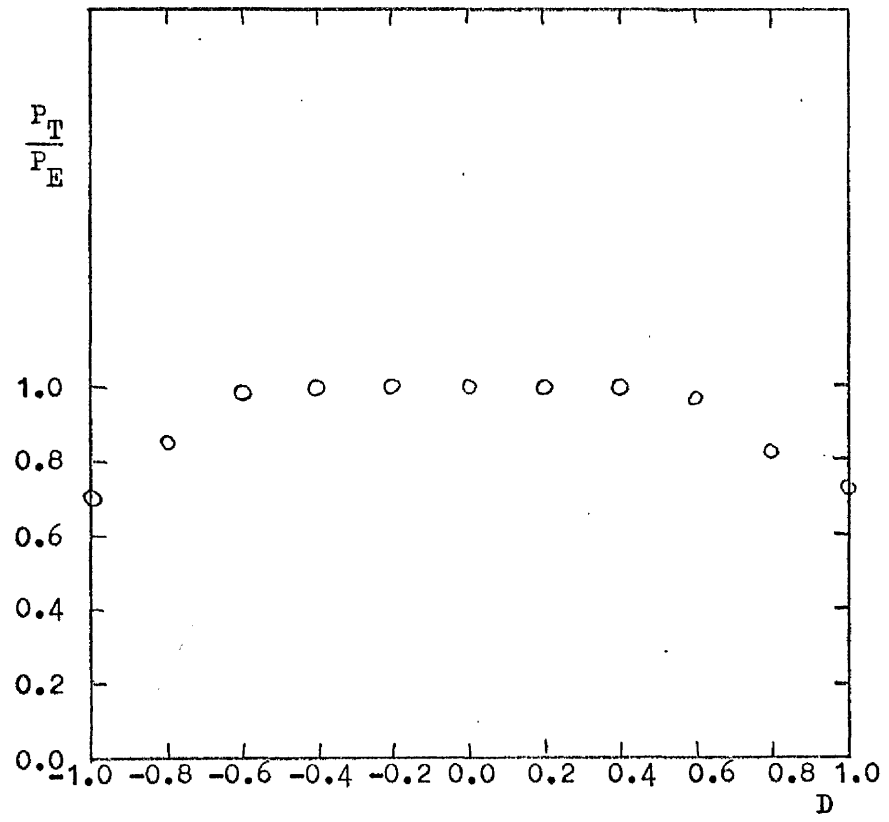

Figure A.5. Total Pressure Profile of Nozzle Exit ($\varphi = 60°$).

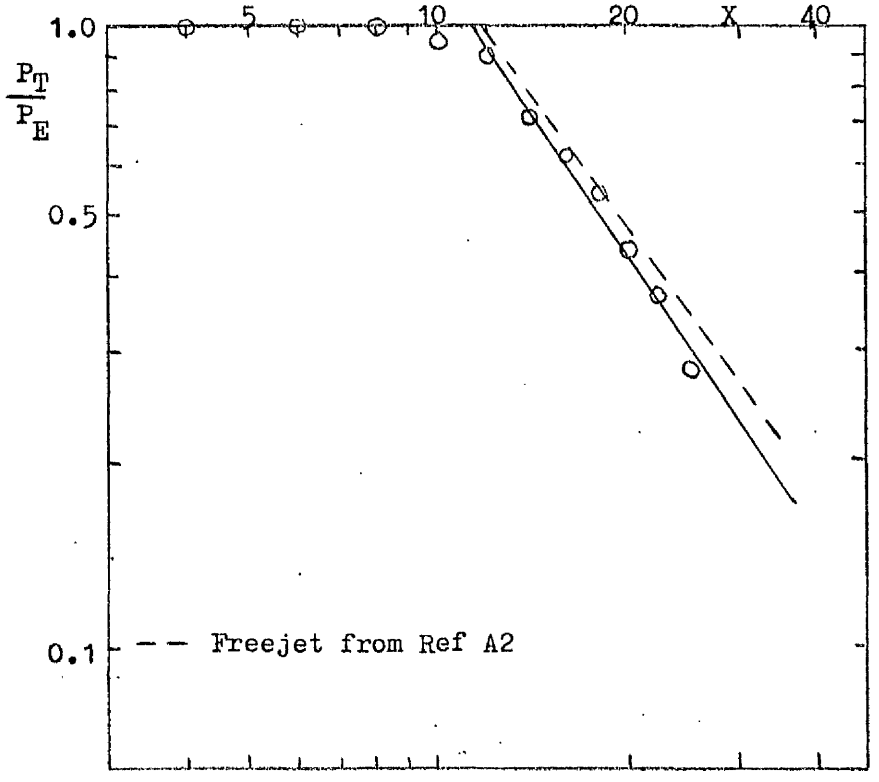

Figure A.6. Freejet Total Pressure Decay Rate ($\phi = 0°$).

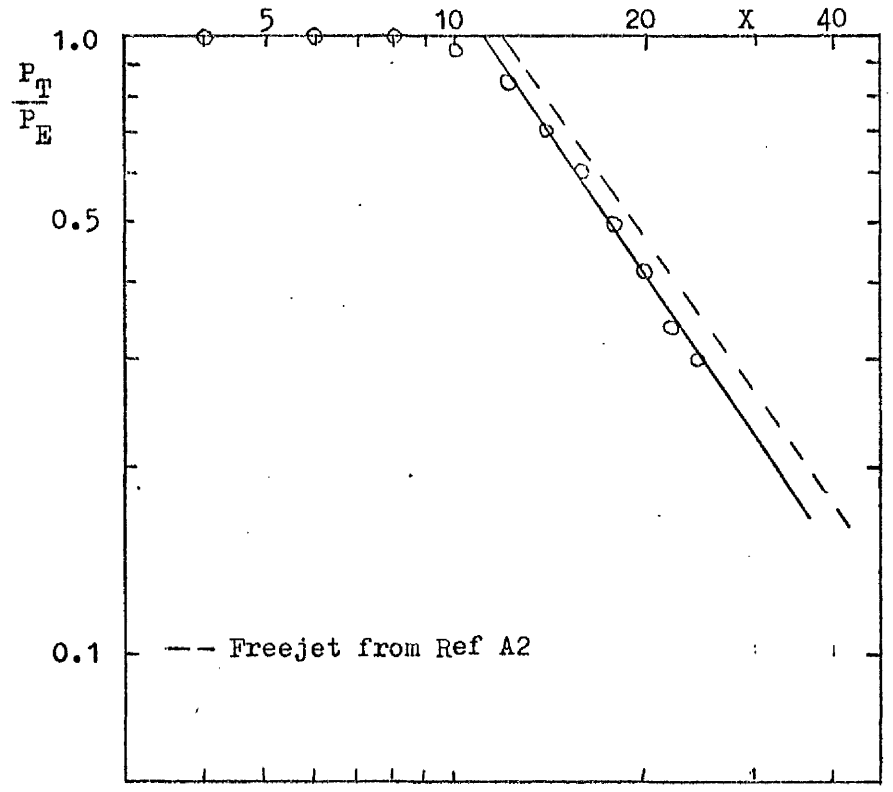

Figure A.7. Freejet Total Pressure Decay Rate (ϕ = 15°).

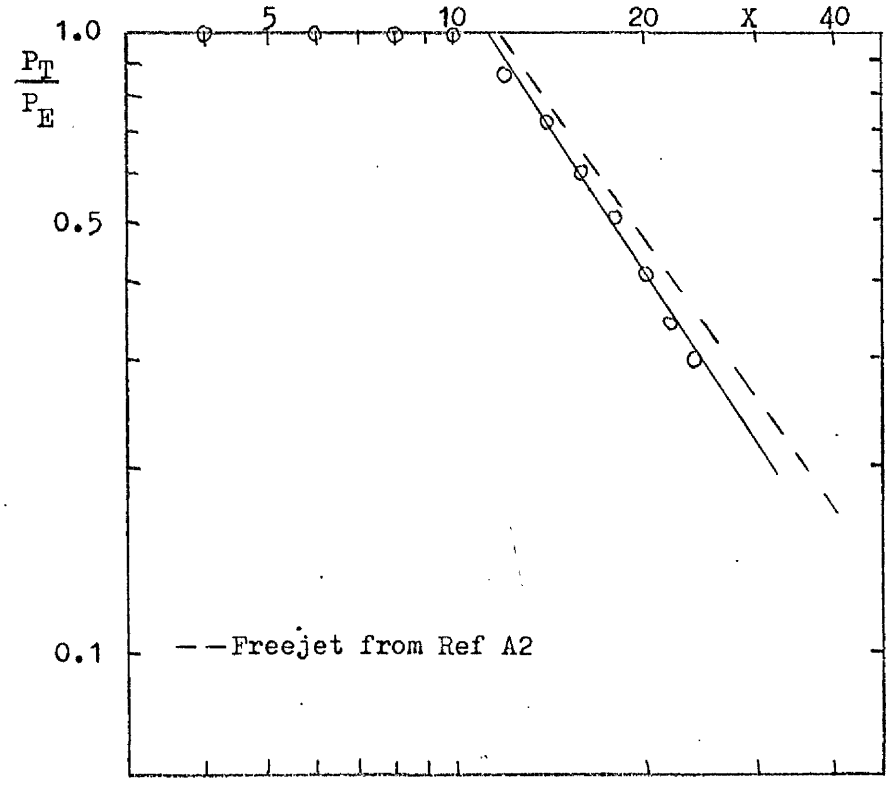

Figure A.8. Freejet Total Pressure Decay Rate (ϕ = 30°).

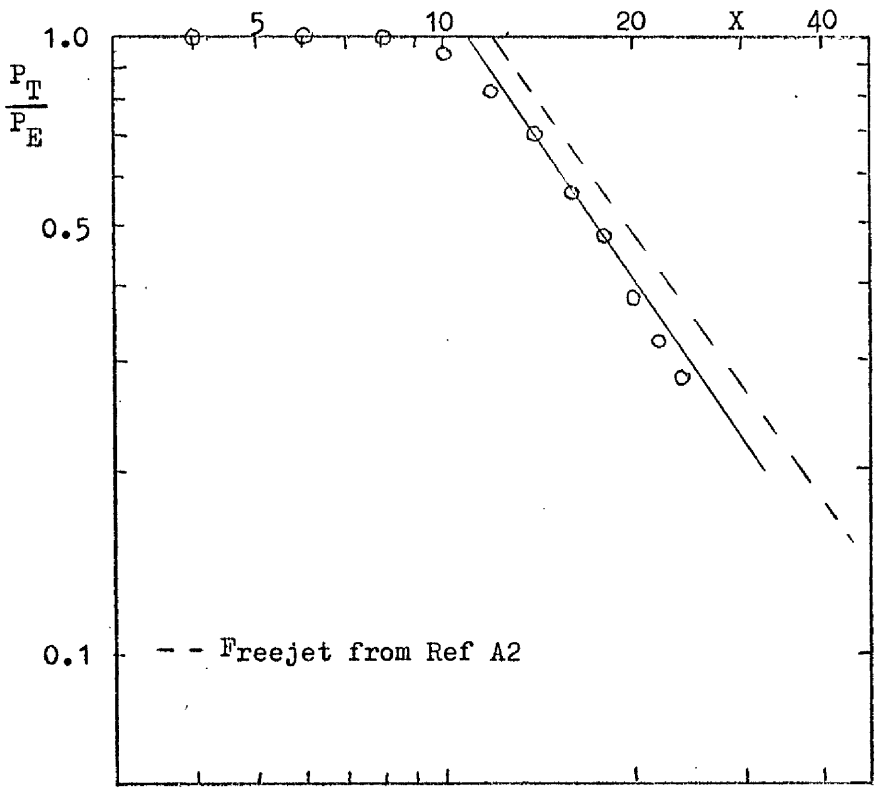

Figure A.9. Freejet Total Pressure Decay Rate ($\phi = 45^\circ$).

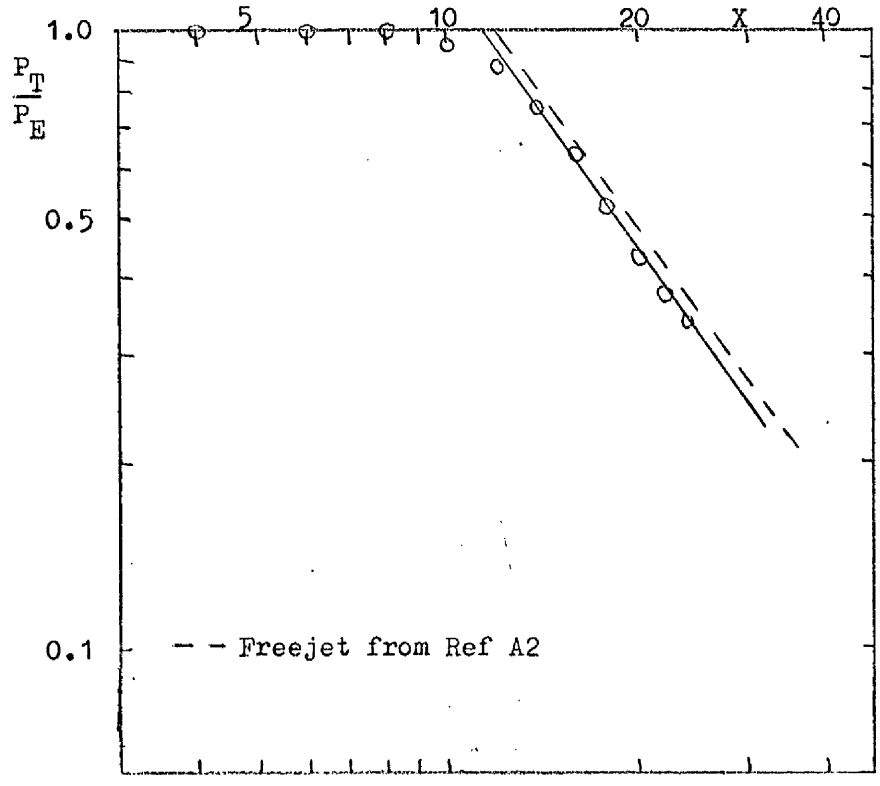

Figure A.10. Freejet Total Pressure Decay Rate ($\phi = 60^\circ$).

Appendix B

Computer Programmes

B.1 Experimental Programme

A multistep programme written in PL1 was implemented on the ERCC system 370/158 and latterly the NUMAC System 370/168. This programme processed the data generated from the wind tunnel tests, evaluated the surface force distribution, suction force coefficient, centre of pressure and pitching moment coefficient (for definitions see Chapter IV) and presented certain of the results in a graphical manner. The input data consisted of the values of the parameters (see Table B.1 for an example of the input data) which defined the wind tunnel test followed by a stream of data consisting of the height of hexane recorded at a pressure tap (measured from the melinex sheet see Section 3.3) along with the coordinates defining the location of that pressure tap. These coordinates (I and J) defined the position within the array receiving the data. The relationship between the physical position and array position was

$X = (I - 65)/2$ for $0 \leq I \leq 113$

$Y = (J - 1)/2$ for $0 \leq J \leq 81$

The pressure heights were converted into interference pressure coefficients. The pressure coefficients were smoothed using an orthogonal least squares curve fitting routine (Forsythe's Method see ref B 1). This routine was also employed to 'fill the holes', by interpolation, in the static pressure tap distribution caused by the constraints on a particular configuration. (e.g. missing tap at $X = -6$, $Y = 0$ and generally upstream of the inclined nozzles in the region $-6 < X < -1$, see also Table 2.1). The input array of pressure coefficients was completed by interpolation between the existing values to form a grid of values with a mesh size of $\frac{1}{2}$ (jet radii) for $-32 \leq X \leq 24$,

$0 \leq Y \leq 40$.

Certain columns and rows of the input array consisted of data showing the chracteristics of the flat plate with the jet off and of data showing the symmetry of the problem. These pressure distributions were presented in graphical form (see figs B.5 - B.11 and end of Table 2.1.6)

The pressure coefficient array was passed as input to a procedure called Isomet (ref B2). This procedure generated the coordinates of isometric contours from the data consisting of values on a rectangular grid and of the value for which the contours were required. The contours of constant pressure were presented in graphical form (see fig B.1 and B.2)

The definition of the surface force and suction force involved a polar coordinate system (see Chapter IV). It was decided, for computational simplicity, to generate pressure coefficients based on a regular polar coordinate system by interpolation from the Cartesian system used by the pressure tap distribution. A tabular interpolation routine was used. All numerical integrations were performed using Simpson's rule. The lower limit of integration, R_1, was taken to be the jet periphery ($R_1 = 1$ for the normal jet) and the radial stepsize was taken to be one twentieth of the difference between the upper and lower limits of integration. The angular stepsize was three degrees. The suction force coefficient to upper limits of integration, $R_2 = 5$ and 10(including and excluding the wake region (see Chapter V)), the centre of pressure and the pitching moment coefficient were calculated (see Table B.2). The surface force distribution was presented in graphical form (see figs B.3 and B.4 and also Table B.2).

The graphs plotted were as follows:

the surface pressure distribution for the range $-20 \leq X \leq 24$, $0 \leq Y \leq 40$

(Fig B.1);

the surface pressure distribution for the range $-10 \leq X \leq 8$, $0 \leq Y \leq 18$ (Fig,B.2);

the surface force distribution for an upper limit, $R_2 = 5$, (fig B.3);

the surface force distribution for an upper limit, $R_2 = 10$, (Fig B.4);

the interference pressure distribution along the Y axis (Fig B.5);

the pressure distribution along the Y axis (jet off) (Fig B.6);

the pressure distribution at the leading edge (jet on)(Fig B.7);

the pressure distribution at the trailing edge (jet on) (Fig B.7);

the interference pressure distribution along the X axis (Fig B.8);

the pressure distribution along the X axis (jet off) (Fig B.9);

the pressure distribution along the plate tips ($Y = \pm 60$, jet on) (FigB.10);

and the pressure distribution along $X = 48$ (jet on) (Fig B.11).

The distribution along the X and Y axis recorded the flat plate distributions. These were used to ensure that no adverse effects occurred on the plate in the region of interest ($-20 \leq X \leq 24$, $0 \leq Y \leq 40$ and in particular the area included in a radial distance of about 15 jet radii from the jet centre). In fact, all the above distributions were used to check the pressure distribution on the flat plate (jet off), whenever a configuration change dictated adjustment to the plate, prior to an experimental test. Fig B.9 shows a fall in pressure over the leading edge which affects the region $X < -25$. Fig B.10 shows a fall in pressure towards the rear of the plate along the tips. This is caused by the rear fairings interfering with the lower surface flow. This appears to be confined to the tips and of no consequence. The conditions in the region of interest appear to be uniform as stated in Section 2.3. The jet induced flow appeared not to affect the leading edge, trailing edge or tip distribution and these can be considered as representative of the flat plate pressure distribution. The pressure distribution along the Y axis and $X = 48$ shows the symmetry of the problem.

The complete programme required 100 CPU seconds for execution.

B.2 Theory Programme

This programme was written in PL1 and implemented on the ERCC system 370/158 and the NUMAC System 370/168. The programme was similar to the experimental programme described above. The input step of that programme was replaced by a procedure which generated the array of pressure coefficients and stream function values (to determine the afterbody shape) from the theory given in Chapter V. The stagnation points were computed to give the separation angle, θ_s. Isomet computed the afterbody shape and the constant pressure contours.

The numerical integration of the surface force and suction force coefficients employed Simpson's Rule. The radial stepsizes were 0.5, 0.25, 0.125 and 0.0625 and the surface force value was converged more rapidly using Richardson's Extrapolation. The integration converged after four iterations. The angular stepsize was 3 degrees.

The surface pressure distribution and surface force distribution were presented in graphical form (see figs 5.6, 5.7 and 5.8 for example). The complete programme required 40 CPU seconds for execution.

References.

B1	Fox, L. Mayers, D.F.	Computing Methods for Scientists and Engineers. OUP, 1968.
B2	Nonweiler, T.R.F.	Isomet. Private Communication, September 1974.

RUN NUMBER 117

TEST CONDITIONS- CIRCULAR JET EXIT

VJ/VO = 10.00

JET INCLINATION ANGLE = 60.00 DEGREES

PLATE INCIDENCE = 0.00 DEGREES

DYNAMIC PRESSURE = 0.576 IN OF WATER

MANOMETER TILT ANGLE = 20.00 DEGREES

MANOMETER LIQUID SP. GR. = 0.68

TOTAL NUMBER OF DATA POINTS = 527

INPUT DATA

I	J	H	CP
1	1	-0.0630	-0.0254
1	17	-0.0630	-0.0254
1	33	-0.0470	-0.0190
1	49	-0.0310	-0.0125

Table B.1. Example of Input Data.

Table B.1. Continued.

101	5	0.0160	0.0065
101	9	-0.0010	-0.0004
101	13	-0.0630	-0.0254
101	17	-0.0780	-0.0315
105	1	0.0310	0.0125
105	5	0.0160	0.0065
105	9	0.0010	0.0004
105	13	-0.0630	-0.0254
105	17	-0.0630	-0.0254
105	25	-0.0630	-0.0254
105	33	-0.0470	-0.0190
105	41	-0.0310	-0.0125
105	49	-0.0310	-0.0125
109	1	0.0310	0.0125
109	5	0.0310	0.0125
109	9	0.0010	0.0004
109	13	-0.0160	-0.0065
109	17	-0.0470	-0.0190
113	1	0.0310	0.0125
113	5	0.0630	0.0254
113	9	0.0310	0.0125
113	13	-0.0010	-0.0004
113	17	-0.0310	-0.0125
113	25	-0.0310	-0.0125
113	33	-0.0310	-0.0125
113	41	-0.0160	-0.0065
113	49	-0.0160	-0.0065
113	65	-0.0010	-0.0004
113	81	0.0010	0.0004

Table B.2. Example of the Evaluation of the Surface Forces, Suction Force Coefficient, Centre of Pressure and Pitching Moment Coefficients.

VJ/V0 = 10.00 PHI = 60.00 DEGREES ALPHA = 0.00 DEGREES RUN NO. = 17

THETA(DEGREES)	CF1	CF2
0.0000E+00	-2.3688E+00	-4.2745E+00
3.0000E+00	-2.4297E+00	-4.4381E+00
6.0000E+00	-2.6251E+00	-4.8259E+00
9.0000E+00	-2.8609E+00	-5.3587E+00
1.2000E+01	-3.1582E+00	-6.0690E+00
1.5000E+01	-3.5649E+00	-6.9787E+00
1.8000E+01	-3.9441E+00	-7.9040E+00
2.1000E+01	-4.2326E+00	-8.7780E+00
2.4000E+01	-4.7176E+00	-9.7899E+00
2.7000E+01	-4.9312E+00	-1.0461E+01
3.0000E+01	-5.1629E+00	-1.1012E+01
3.3000E+01	-5.2161E+00	-1.1230E+01
3.6000E+01	-5.1721E+00	-1.1183E+01

Table B.2. Continued.

1.5900E+02	-5.9329E-01	-2.4051E+00
1.6200E+02	-5.6196E-01	-2.3817E+00
1.6500E+02	-5.3121E-01	-2.3560E+00
1.6800E+02	-4.6689E-01	-2.2935E+00
1.7100E+02	-3.9477E-01	-2.2228E+00
1.7400E+02	-3.1013E-01	-2.1403E+00
1.7700E+02	-2.4708E-01	-2.0810E+00
1.8000E+02	-2.5645E-01	-2.0937E+00

SUCTION FORCE COEFFICIENT(WAKE INCLUDED)

R=5 IS 5.3520E+00
R=10 IS 1.3382E+01

SUCTION FORCE COEFFICIENT(WAKE EXCLUDED)

R=5 IS 4.5607E+00
R=10 IS 1.1718E+01

CENTRE OF PRESSURE IS -1.4374E+00

PITCHING MOMENT COEFFICIENT IS -2.9943E+01

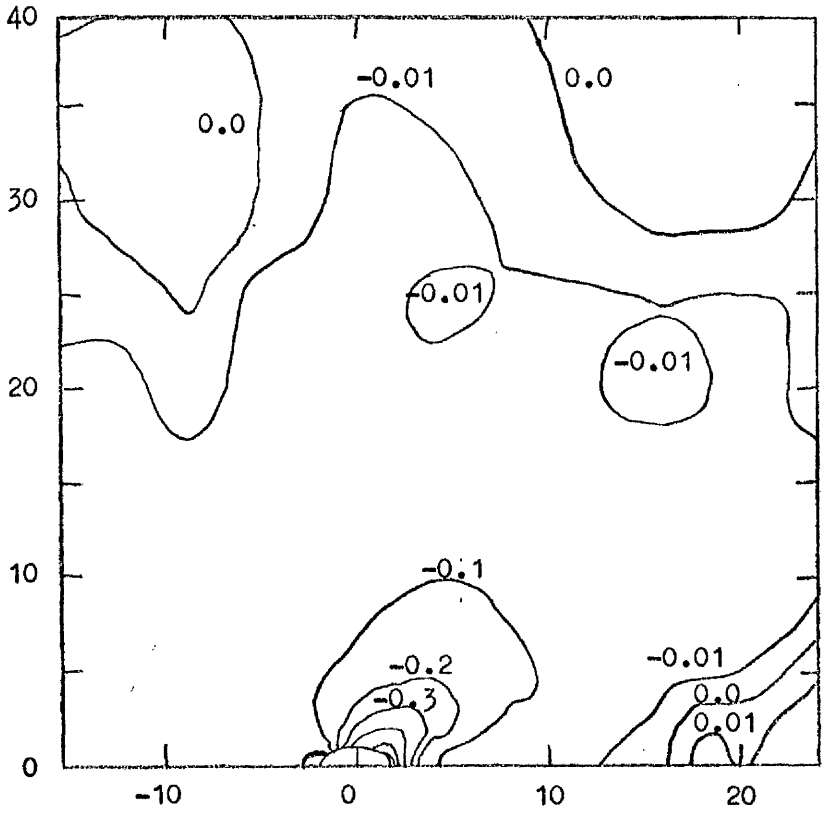

Figure B.1. Surface Pressure Distribution ($\phi = 60^{\circ}, \alpha = 0^{\circ}, m = 10$).

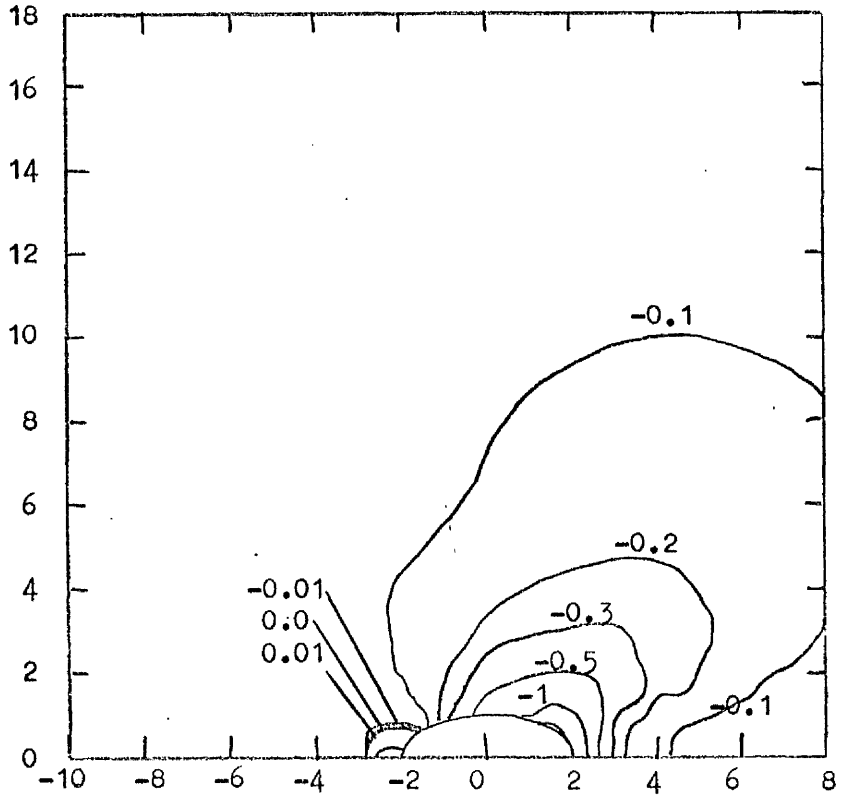

Figure B.2. Surface Pressure Distribution ($\phi = 60^{\circ}, \alpha = 0^{\circ}, m = 10$).

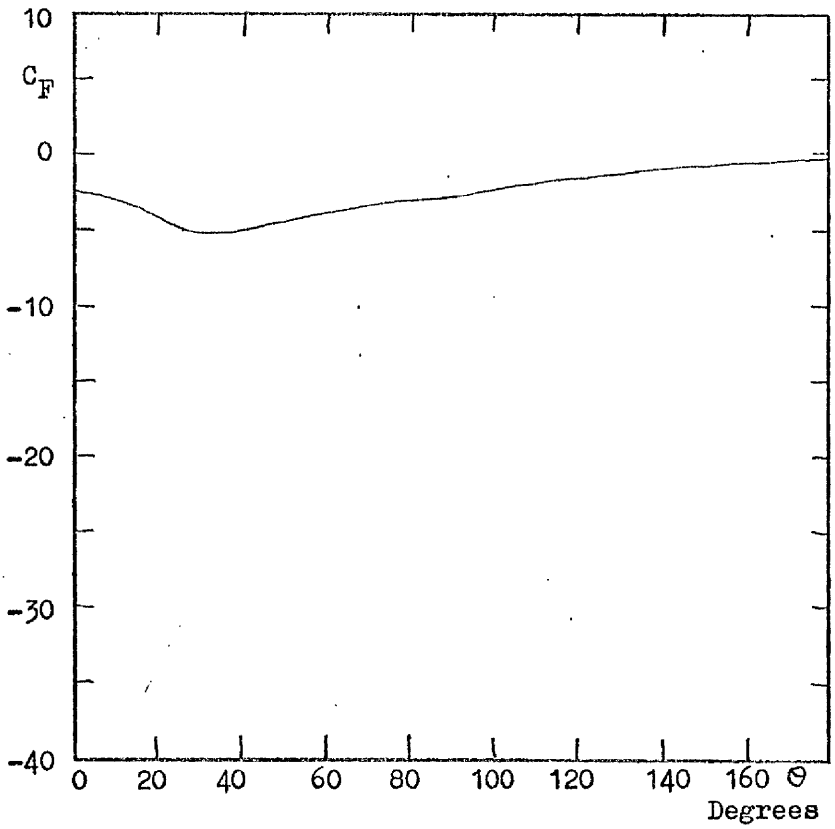

Figure B.3. Surface Force Distribution ($\phi = 60^{\circ}, \alpha = 0^{\circ}, m = 10, R_2 = 5$).

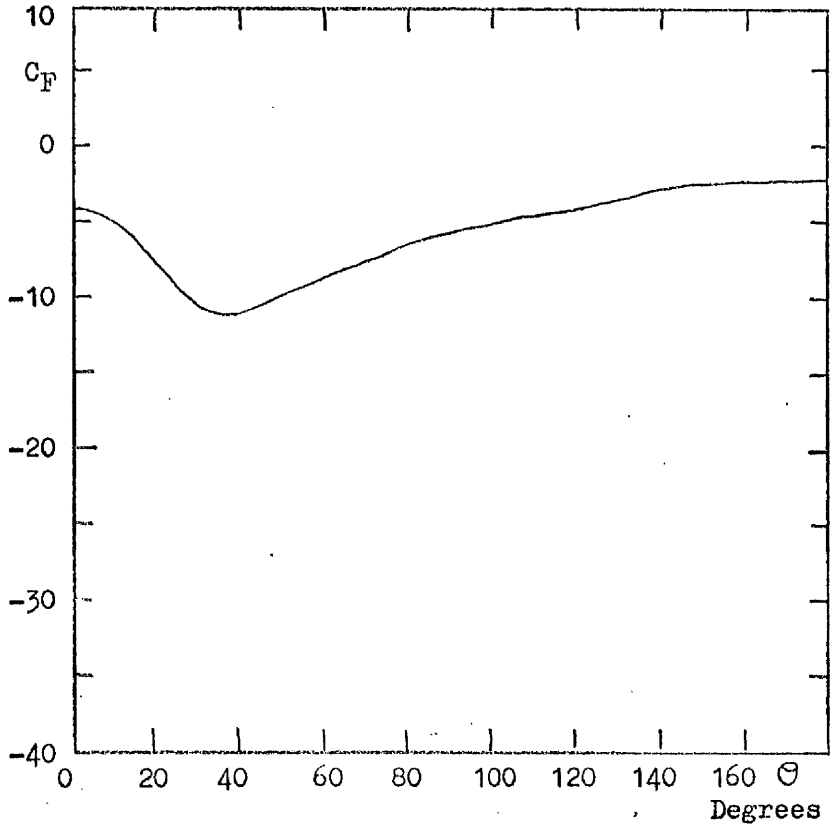

Figure B.4. Surface Force Distribution ($\phi = 60^{\circ}, \alpha = 0^{\circ}, m = 10, R_2 = 10$).

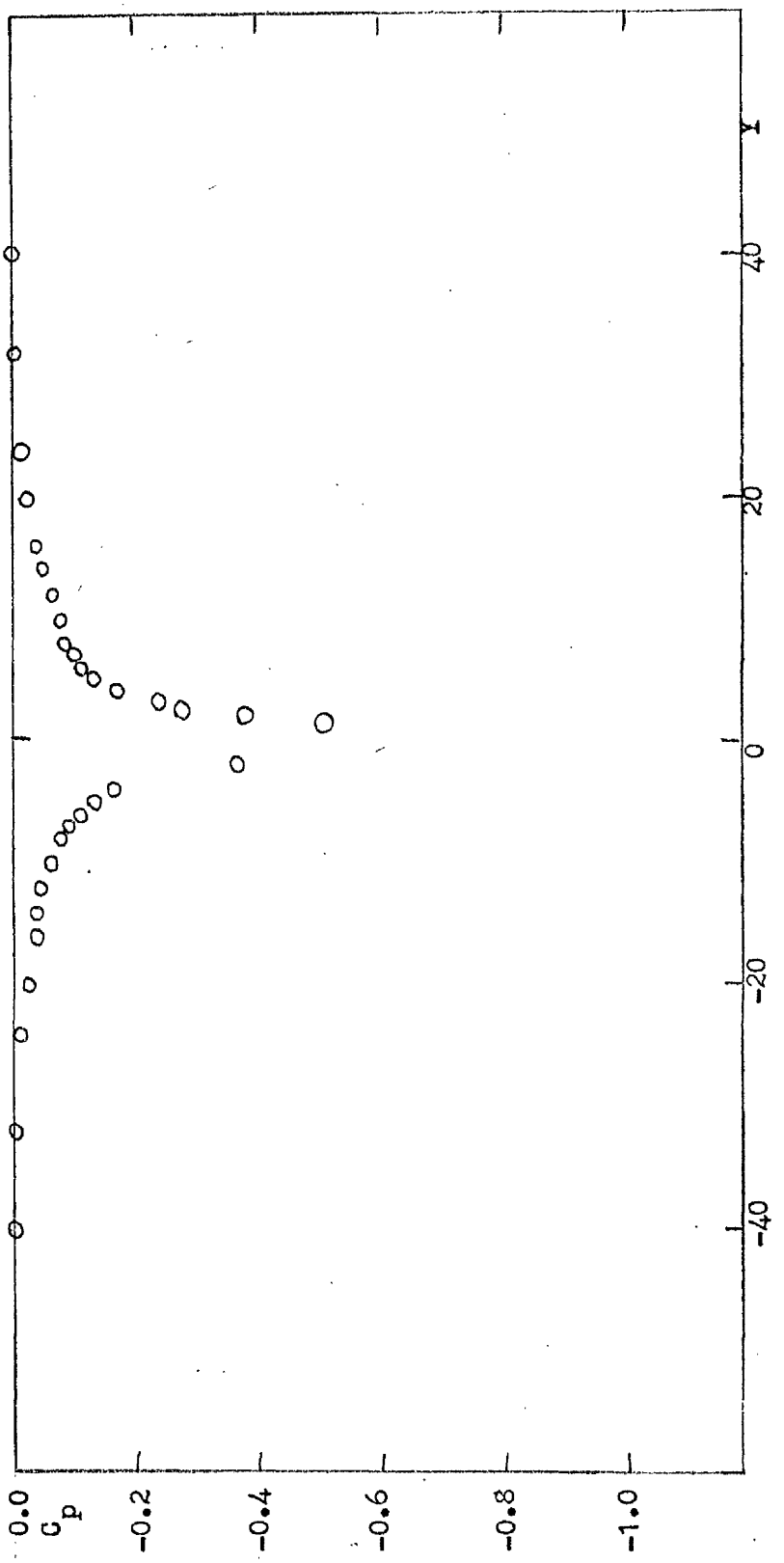

Figure B.5. Interference Pressure Distribution along the Y Axis

(ϕ = 60°, α = 0°, m = 10).

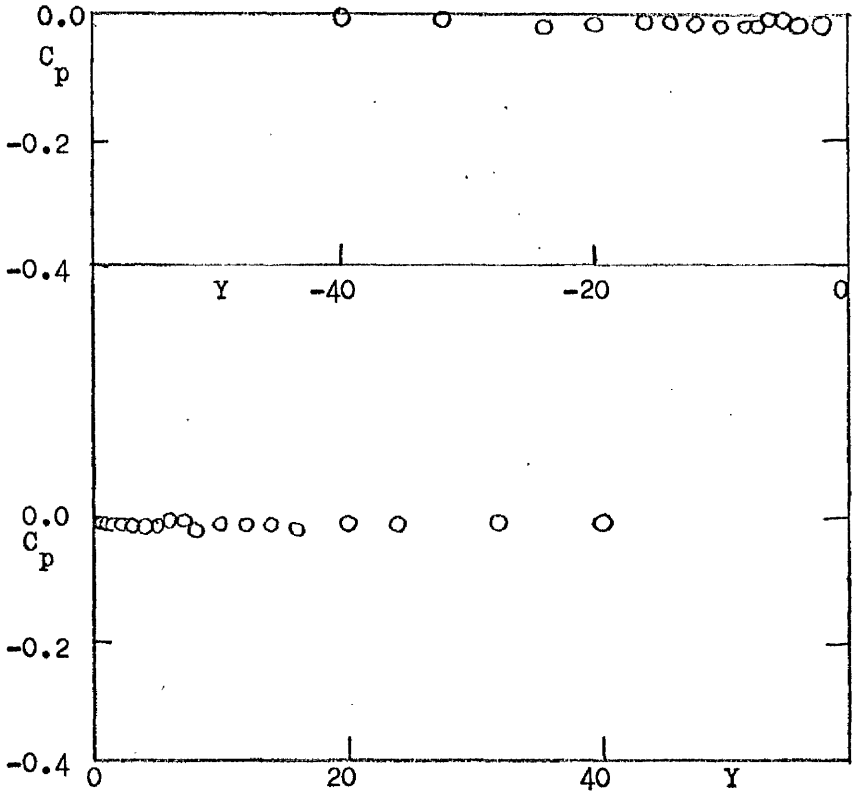

Figure B.6. Pressure Distribution along the Y Axis (Jet Off)

(ϕ = 60°, α = 0°, m = 10).

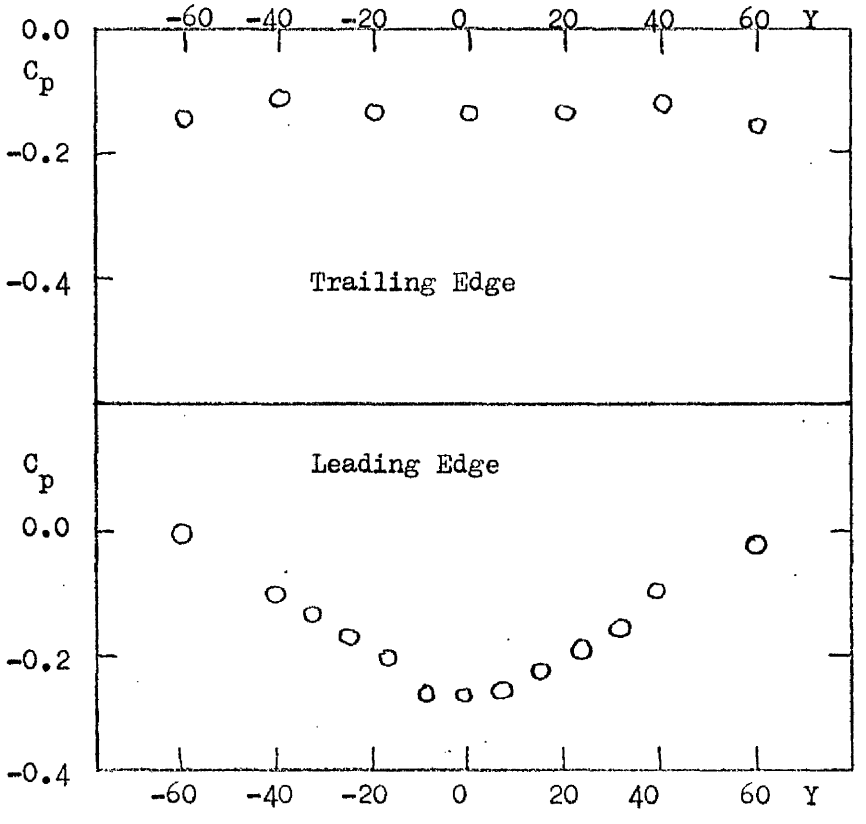

Figure B.7. Pressure Distribution at the Trailing Edge (above) and Leading Edge (below) for Jet On (ϕ = 60°, α = 0°, m = 10).

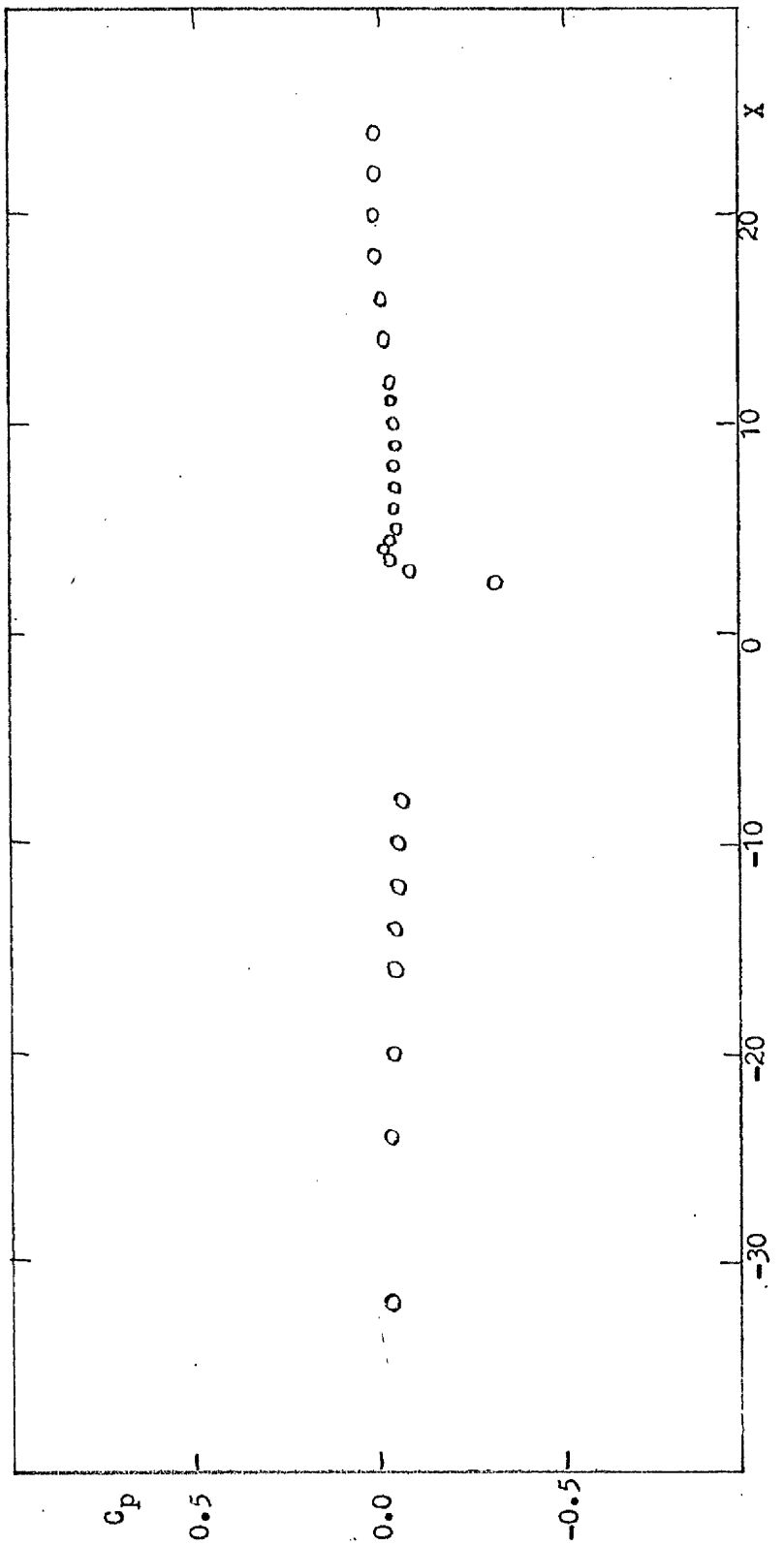

Figure B.8. Interference Pressure Distribution along the X Axis

($\phi = 60°$, $\alpha = 0°$, m = 10).

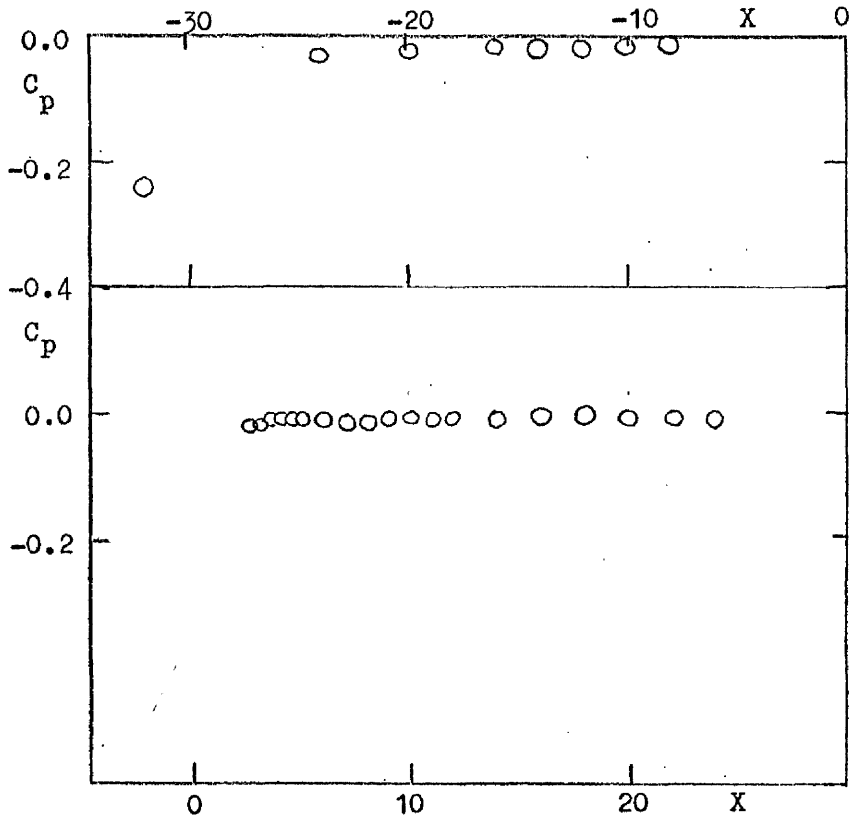

Figure B.9. Pressure Distribution along X Axis (Jet Off)

($\phi = 60^\circ$, $\alpha = 0^\circ$, m = 10).

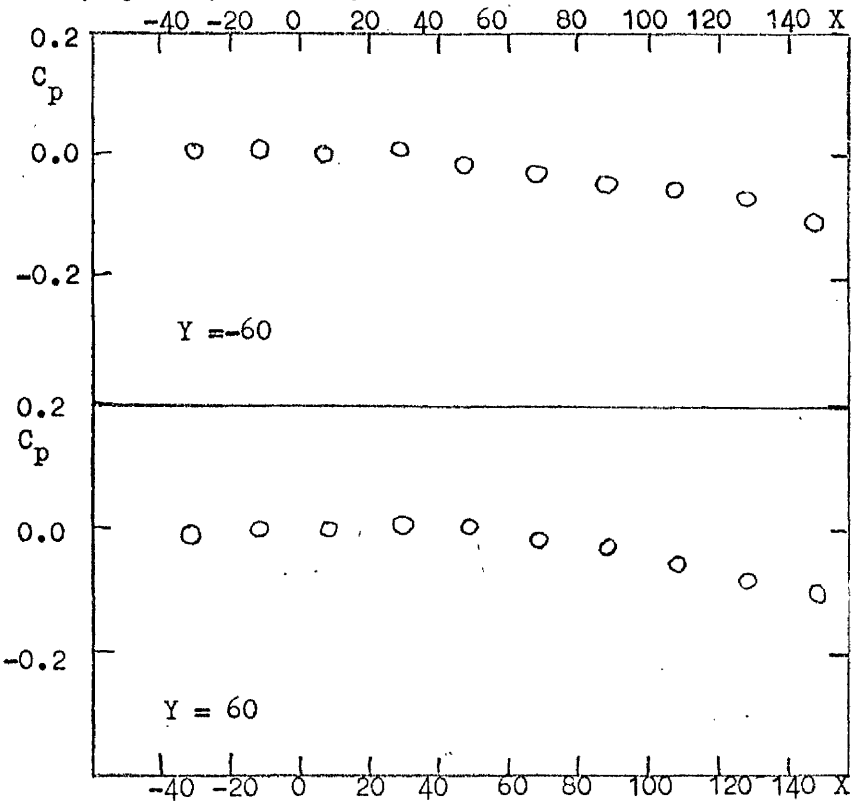

Figure B.10. Pressure Distribution along Plate Tips Y = -60 (above) and Y = 60 (below) for Jet On ($\phi = 60^\circ$, $\alpha = 0^\circ$, m = 10).

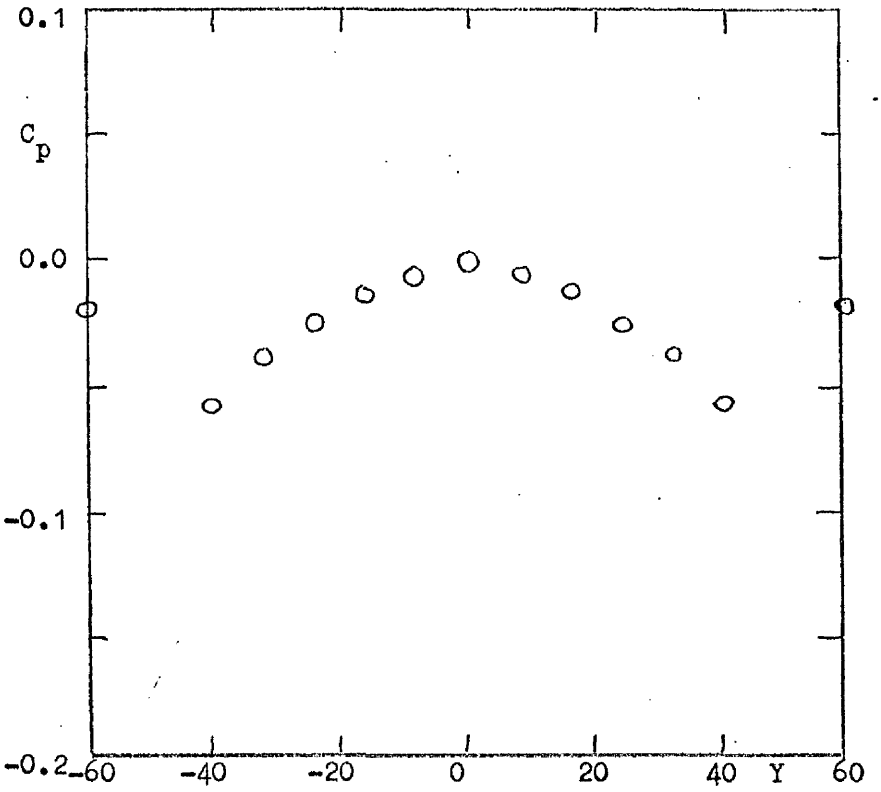

Figure B.11. Pressure Distribution along Span X = 48 (Jet On)
($\phi = 60^\circ$, $\alpha = 0^\circ$, m = 10).